Treatment of low-grade meningiomas with protons and helium ions

Thomas Tessonnier

München 2017

Treatment of low-grade meningiomas with protons and helium ions

Thomas Tessonnier

Dissertation
an der Fakultät für Physik
der Ludwig-Maximilians-Universität
München

vorgelegt von
Thomas Tessonnier
aus Marseille

München, den 13.02.2017

Erstgutachter: Prof. Dr. Katia Parodi
Zweitgutachter: Prof. Dr. Werner Rühm
Tag der mündlichen Prüfung: 17.03.2017

Content

List of figures

List of tables

Abbreviations

AVM	Arterio-veinous-malformation
BAMS	Beam applications and monitoring system
BED	Biologically effective dose
BEV	Beam eye view
BL	Beamline
BME	Boltzmann master equation
BP	Bragg peak
CCE	Charge Collection Efficiency
CERN	European center for nuclear research
CT	Computed tomography
CTV	Clinical target volume
ddds	Depth dose distributions
DFO	Distal fall-off
DG	Double Gaussian
DNA	Deoxyribonucleic acid
DSB	Double strand break
DVH	Dose volume histogram
EPLR	Entrance-to-plateau ratio
EPR	Entrance-to-peak ratio
FO	Fall-off
FWHM	Full-width at half-maximum
GTV	Gross tumor volume
Gy	Unit (Gray) for absorbed dose
GyRBE	Unit for RBE-weighted dose / biological dose
HIT	Heidelberg ion beam therapy center
HU	Hounsfield unit
IC	Ionization chamber
Ipot	Ionization potential
INFN	Italian national institute for nuclear physics
LBL	Lawrence Berkeley Laboratory
LET	Linear energy transfer

LEM	Local effect model
LFO	Lateral fall-off
LIBC	Library of ion beam characteristics
LQ	Linear quadratic
MC	Monte Carlo
MCTP	Monte Carlo Treatment planning tool
MKM	Microdosimetric kinetic model
MRI	Magnetic resonance imaging
MWPC	Multiple wires proportional chamber
NTCP	Normal tissue complication probability
OAR	Organ at risk
OER	Oxygen enhancement ratio
PET	Positron emission tomography
PEANUT	Pre-Equilibrium Approach to Nuclear Thermalization
PKF	Peakfinder water column
PS	Phase space files
PSI	Paul Scherrer Institut
PTCOG	Particle Therapy Co-Operative Group
PTV	Planning target volume
PW	Peak-width
RBE	Relative biological effectiveness
RiFi	Ripple filter
ROI	Region of interest
RQMD	Relativistic quantum molecular dynamics
SG	Simple Gaussian
SOBP	Spread-out Bragg peak
SSB	Single strand break
TCP	Tumor control probability
TG	Triple Gaussian
TPS	Treatment planning system
TPLR	Tail-to-plateau ratio
TPR	Tail-to-peak ratio
WEPL	Water equivalent path length

Zusammenfassung

Während der vergangen Jahrzehnte hat die Anwendung von Teilchentherapie zur Behandlung von Krebspatienten rasant zugenommen. Durch die physikalischen Eigenschaften der Ionenstrahlen, hauptsächlich das invertierte Tiefendosisprofil und die steilen longitudinalen und lateralen Dosisgradienten, wird Teilchentherapie zu einer vielversprechenden Modalität zur Behandlung von tiefliegenden Tumoren nahe an Risikostrukturen. Heutzutage werden nur Protonen und Kohlenstoffionen klinisch angewandt, jedoch könnten auch neue Ionenarten im klinischen Bereich Vorteile bringen. Heliumionen werden dafür in Erwägung gezogen, da ihre physikalischen und biologischen Eigenschaften zwischen derer von Protonen und Kohlenstoffionen liegen. Am Heidelberger Ionenstrahl Therapiezentrum (HIT) sind neben den etablierten Protonen und Kohlenstoffionen auch Helium- und Sauerstoffionen für experimentelle Zwecke vorhanden, deren klinische Anwendung in der nahen Zukunft angestrebt wird. Allerdings müssen für den klinischen Einsatz neuer Teilchen die dosimetrischen und biologischen Eigenschaften der Teilchen genau bestimmt werden und weiterhin ausführliche Vergleiche zwischen Bestrahlungsplänen mit bekannten und neuen Teilchen durchgeführt werden.

In dieser Arbeit wurden die Therapie von gut differenzierten, bösartigen Meningiomas mit Protonen und Heliumionen verglichen. Dafür wurden am HIT ausführliche Studien zu den dosimetrischen Eigenschaften aller verfügbaren Ionenarten im therapeutischen Energiebereich hinsichtlich der Tiefendosisverteilung und der lateralen Dosisprofile durchgeführt. Anschließend wurden für Heliumionen ausführliche Vergleiche und Validierungen der Monte Carlo (MC) Simulationen FLUKA mit Tiefendosismessungen durchgeführt, welche auf Experimenten zur Bestimmung der Strahlcharakteristika in Vakuum, die bisher kaum erforscht wurden, aufbauen. Als nächster Schritt wurde dazu der detaillierte Strahlverlauf in die Simulationen eingebaut („phase space approach“). Anschließend wurde das FLUKA-basierte Monte Carlo „Monte Carlo Treatment Planning Tool“ (MCTP) für Bestrahlungsfelder mit unterschiedlichen Größen und Tiefen in Wasser für alle verfügbaren Ionenarten am HIT verifiziert. In Verbindung mit validierten biologischen Modellen wurde das MCTP für Vergleiche zwischen Protonen- und Heliumionenplänen für Bestrahlungen von Meningioma benutzt.

Die experimentellen Ergebnisse der dosimetrischen Charakterisierung lassen darauf schließen, dass die Behandlung mit Heliumionen zu einer gleichmäßigeren Dosisverteilung als bei Behandlung mit Protonen führt, hauptsächlich wegen geringerer lateraler Streuung und geringerer Reichweitenunsicherheit. Dabei sind außerdem die distalen und lateralen Dosiskanten schärfer und der Dosisschwanz weniger ausgeprägt als bei Kohlenstoffionen. Es wurde eine gute Übereinstimmung zwischen der MC FLUKA Vorhersage und den experimentellen Messungen gefunden, was deren Anwendbarkeit als Strahlenmodell zur Vorbereitung des klinischen Einsatzes von Heliumionen bestätigt. Daraus folgend stellt das MCTP Tool validiert gegen Dosismessungen auch für anspruchsvolle Zielvolumina eine solide Forschungsbasis für Behandlungsplan-Vergleiche am HIT dar. Weiterhin wird die Anwendung verschiedener state-of-the-art-Modelle für die relative biologische Wirksamkeit damit unterstützt. Die Ergebnisse dieser Arbeit für die Vergleiche verschiedener

Behandlungspläne unter verschiedenen Bedingungen zeigen, dass Heliumionen eine Alternative zur Protonentherapie sein können, basierend auf ihren vorteilhaften physikalischen und biologischen Eigenschaften. Damit könnten sie insbesondere für gut differenzierte, bösartige Meningioma eine vielversprechende, neue Behandlungsmethode sein. Um die klinische Anwendung voranzutreiben sind weitere Planungs-Studien und biologische Untersuchungen geplant.

Abstract

Particle therapy for cancer patient treatments has gained in popularity over the last decades. The physical characteristics of ion beams over conventional radiotherapy with photons, mainly the inverted depth dose profile, with sharp longitudinal and lateral dose gradient, make ion therapy an interesting modality for treatment of deep-seated tumors near critical structures. Nowadays, only protons and carbon ions are used in clinical routine. The introduction of other ions species in clinical practice is foreseen as potential asset for improving clinical outcomes. Helium ions, with physical and biological properties in between protons and carbon ions, have been pointed out as potential candidates. At the Heidelberg ion beam therapy center (HIT), helium and oxygen ions, which are currently only used for experiments, are foreseen to be employed clinically in the near future in addition to the established protons and carbon ions. The introduction of ion species in the clinical practice needs to be supported by a thorough assessment of their dosimetric and biological properties, and subsequently by treatment planning comparisons with clinically used proton and carbon ion beams.

This thesis aimed at comparing the treatment of low-grade meningiomas with protons and helium ions. To achieve this goal, an extensive study of the basic dosimetric features of the different ions available at the HIT was performed in the entire therapeutic energy range, comparing depth dose distributions and lateral profiles in water. Subsequently, thorough comparisons and validations of the Monte Carlo (MC) code FLUKA for helium ion beams was conducted against in-depth dosimetric measurements, after an experimentally-driven tuning of the less known initial beam characteristics in vacuum. After integration of the detailed beamline model into a simulation framework with a new original phase space approach, a dosimetric verification of the FLUKA-based Monte Carlo Treatment Planning tool (MCTP) for spread-out Bragg peaks of different sizes and at different depths in water was performed for all ion species available at HIT. Using this engine coupled to a validated biological model, plan comparisons between protons and helium ions were investigated for meningioma patient treatments.

The experimental results of the dosimetric characterization indicate that helium ions could afford a more conformal treatment, due to a smaller lateral scattering and longitudinal straggling than with protons, leading to better lateral and distal fall-off, as well as a lower fragmentation tail compared to carbon and oxygen ions. Overall, good agreements were found between MC FLUKA predictions and measurements of helium ions, confirming the suitability of the code for beam modeling in preparation of clinical establishment at HIT. Subsequently, the MCTP tool was validated against dosimetric measurements for challenging targets, to provide a solid research engine for treatment planning comparisons at HIT, supporting the usage of multiple state-of-the-art models of relative biological effectiveness. The final results of the thesis for treatment plan comparisons under different treatment conditions indicate than helium ions could be an alternative to proton therapy due to their favorable physical and biological characteristics, and thus could provide promising treatment for low-grade meningioma in the head. Future treatment planning studies and biological investigations with helium ions are foreseen to proceed toward clinical implementation.

Chapter 1. Introduction

Cancer is one of the leading causes of death worldwide with the second largest morbidity in the European Union. According to the world health organization 2012 report, there are 14 million new cases and 8.2 million cancer-related deaths worldwide annually. By 2030, the prevalence of cancer is expected to rise by nearly 70% due to the ageing population and endogenous factors, as well as external risks such as tobacco-use, pollution, chemical agents, and other environmental factors. Cancer is a broad term to characterize cell degeneration and abnormal cell proliferation. The first tumor cells to localize are called the primary cancer and can, at later stages, invade other parts of the body (metastatic). The main approach to treating cancer is with either surgery, radiotherapy, chemotherapy or a combination of these treatments. Other systematic therapy like chemotherapy can also be proposed such as hormonotherapy. While surgery and radiotherapy focus on treating the primary cancer alone, chemotherapy aims at curing metastatic disease as well. Roughly 50% of patients with malignant tumors are undergoing radiotherapy in combination with surgery and/or chemotherapy (Durante and Löffler 2010).

Radiotherapy seeks to deliver enough energy to the primary tumor to damage deoxyribonucleic acid helix (DNA) within the tumorous cells by the process of ionization. Thus, the goal is to eradicate the malignant cells while sparing the surrounding tissues and critical organ at risks. A trade-off then has to be considered to satisfy this balance between an effective treatment and avoiding/decreasing complications probability and risk of secondary cancer in the normal tissue. In order to achieve this goal, conventional radiotherapy techniques using high energy photons evolved to provide a more conformal dose delivery to the tumor. However, limitations from physical interaction properties of photons can be overcome when instead using ions, due to their more favorable physical properties. So far over 150,000 patients have been treated with ions, mainly with protons, since the first clinical applications of ion therapy at the Lawrence Berkeley Laboratory (LBL) in the 1950's (Lawrence *et al* 1964, Lyman and Howard 1977, Phillips *et al* 1977, Jermann 2015). Ions can provide a superior treatment to photons for different cancer localization such as inoperable tumors in the head and neck region, chordomas or chondrosarcomas (Schulz-Ertner *et al* 2007, Tsujii *et al* 2007, Durante and Löffler 2010, Löffler and Durante 2013). Several clinical trials are necessary to obtain hard evidence of the advantage of ions over photons. Furthermore, ions could enhance clinical outcome for pediatric cases and tumors near highly functional structures by reducing the normal tissue complication probability (NTCP) and in turn decrease the risk of radiation-induced secondary cancer and damage to organs at risk (D'Avila Nunes 2015). One example is skull base meningioma (Gudjonsson *et al* 1999, Vernimmen *et al* 2001), where ion therapy could better spare critical organs (e.g. chiasma,

brainstem, optical nerves …) in comparison to conventional radiotherapy and was experimented with promising results in several proton therapy centers (Weber *et al* 2011, Austin-Seymour *et al* 1990, Noel *et al* 2005).

In addition to the clinically used protons and carbon ions, helium ions could be beneficial for patient treatments as well. After their introduction at the Lawrence Berkeley National Laboratory in 1975 and clinical use until 1992 for skull base tumor (Kaplan *et al* 1994) and uveal melanoma (Castro *et al* 1994, Char *et al* 1998), a renewed interest in helium ions grew over the last decade with the rising number of related publications (Kempe *et al* 2007, Knäusl *et al* 2016, Grün *et al* 2015, Burigo *et al* 2015), and their recent availability at the Heidelberg ion beam therapy center (HIT, Haberer *et al* 2004, Combs *et al* 2010a) with a state-to-the-art delivery system (Tessonnier *et al* 2017a, Tessonnier *et al* 2017b), as it will be presented in the following chapters. From a theoretical standpoint, helium ions can in principle provide better conformity to the tumor than protons and carbon ions due to their physical properties, i.e. reduced straggling (both lateral and distal) compared to protons and lower dose fragmentation tail than carbon ions. Regarding biological outcome, the relative biological effectiveness (RBE) of helium is higher than that of protons. Compared to carbon ions the RBE is lower but presents less variability, thus decreasing the uncertainty in the dose delivered to the patient. For these reasons, helium ions may be of particular use in pediatrics and cases with tumors close to critical structures such as low-grade meningiomas. Additionally, it could be of interest in high-risk meningiomas for dose escalation in complement to radiotherapy with photons as investigated at HIT for carbon ions (Combs *et al* 2010b).

The aim of this thesis is to introduce the necessary elements for the treatment of low-grade meningiomas with helium ions compared to protons. This work is organized as follows:

- Chapter 2 describes the rationale of the use of ions through a general description of their physical and biological properties. An overview of current clinical implementation and treatment planning in ion therapy will be presented.

- Chapter 3 presents detailed measurements and comparisons of the four ions available at HIT: protons, helium, carbon and oxygen ions. It details the different characteristics of the available ions as well as their physical advantages and drawbacks using the latest state-of-the-art active beam delivery system.

- Chapter 4 deals with modelling of helium ion beams with the Monte Carlo code FLUKA (Ferrari et al 2005, Böhlen et al 2013, Battistoni et al 2016) and a thorough comparison to measurements, allowing for validation of Monte Carlo predictions for further evaluation of both Monte Carlo-based and analytical treatment planning systems, the latter using Monte Carlo generated database.

- Chapter 5 presents an improved framework for patient-specific simulations at HIT based on the latest version of FLUKA, with new features such as the optional use of input phase space files and the rotation of voxelized patient geometries. It covers a comprehensive validation of the phase space approach for protons and carbon ions against simulations using the detailed HIT beamline, as well as experimental measurements.

- Chapter 6 introduces a prototype Monte Carlo treatment planning system (MCTP, Böhlen et al 2014, Mairani et al 2013) used to optimize spread-out Bragg peaks at several depths in water, with two different sizes and the four HIT ions. The validation of several dosimetric parameters against measurements ensures the reliability of this tool for absorbed dose calculations to be used in further planning comparisons with patient data. The possibility to link the MC tool to sound biological models is also presented.

- Chapter 7 compares meningioma treatment plans biologically optimized for protons and helium ions. Additionally, the effect of various planning parameters such as fraction dose size or the use of the ripple filter (RiFi, Weber and Kraft 1999), as well as the impact of a different tumor tissue type, were investigated using the same patient cases.

- Chapter 8 concludes this work and provides a future perspective of the clinical implementation of helium ions at HIT. It also presents work in progress related to both radiobiology and Monte Carlo modelling.

- Appendices A-D present supplementary material not included in the main chapters as well as side works related to the thesis.

Chapter 2. Ion Beam Therapy

In this Chapter, a general introduction to particle therapy concepts will be summarized, followed by a description of the Heidelberg ion-beam therapy center and Monte Carlo code used in this thesis.

2.1. Radiotherapy

The main goal of radiotherapy is the treatment of patient tumors through a lethal deposition of energy to the cancerous cells while minimizing damage to the surrounding healthy tissues and organs at risk (OAR). The amount of energy deposited by ionizing radiation to matter in a finite volume is defined as the absorbed dose (ICRU 1993):

$$D = \frac{\mathrm{d}\bar{\varepsilon}}{\mathrm{d}m}, \tag{2.1}$$

with *D*, the absorbed dose (J/kg), for a mean energy $\bar{\varepsilon}$ deposited inside a finite volume *V* of mass *m*. The absorbed dose unit name is the Gray (Gy).

Following equation 2.1, the dose *D*, deposited in a thin slice of absorber material with density ρ (g.cm^{-3}) by a monoenergetic beam of charged particles (e.g., ion beam or secondary electrons from photons interactions under the assumption of charged particle equilibrium) can be calculated as follows (Podgorsak 2005):

$$D = \Phi \times \frac{S}{\rho}, \tag{2.2}$$

with *S*, the stopping power of the charged particle in the considered material, and *Φ,* the particle fluence (cm^{-2}). Subsequently, the dose *D* can be obtained as reported in Schardt *et al* (2010):

$$D = 1.6 \cdot 10^{-9} \times \Phi \times \frac{\mathrm{d}E}{\mathrm{d}x} \times \frac{1}{\rho}, \tag{2.3}$$

with $\frac{\mathrm{d}E}{\mathrm{d}x}$, in units of keV.µm^{-1}, the stopping power linked to the energy loss of the charged particles per unit path length. This quantity is related to the linear energy transfer (LET), the energy deposited locally per unit path length, by a particle in a stopping material.

In the biological setting, radiation induces both direct and indirect damages to the cell's vital constituents: the DNA molecules (figure 2.1). Charged particles (from primary or secondary radiations) cause ionization of molecules undergoing rapid chemical changes with the possibility of breaking intra-molecular bonds (physical and chemical phase, Boag 1975). Such effects include single strand DNA helix breaks (SSB), double strand DNA helix breaks (DSB) or a more complex clustered strand breaks. If not repaired properly or in time, the damage may lead to the cell death (Goodhead 1994, Goodhead 2006). Irradiation, through the tumorous cell death, will provoke shrinkage or total sterilization of the patient cancer (early reactions on biological phase). However, such treatment methods can adversely affect normal, healthy tissues of a patient. Unwanted energy deposition in the normal cells causing their death or mutation could lead to radiation induced secondary cancer years after treatment (late reactions on biological phase). Thus, a highly conformal dose delivery to the tumor is desirable.

Several irradiation techniques are possible depending on the tumor localization, with two main categories of radiotherapy procedures: brachytherapy and external beam radiotherapy (Podgorsak 2005). While the radiation source (^{192}Ir, ^{125}I) in brachytherapy is placed directly in the proximity of the target (intracavitary, interstitial, surface or intraoperative brachytherapy), in external beam therapy the source is positioned at a specified distance away from the patient. External beam therapy is achieved mainly with photon (from a linear accelerator of electron beams or a ^{60}Co teletherapy unit) and electron beams, as well as, with less availability, protons, ions or neutrons.

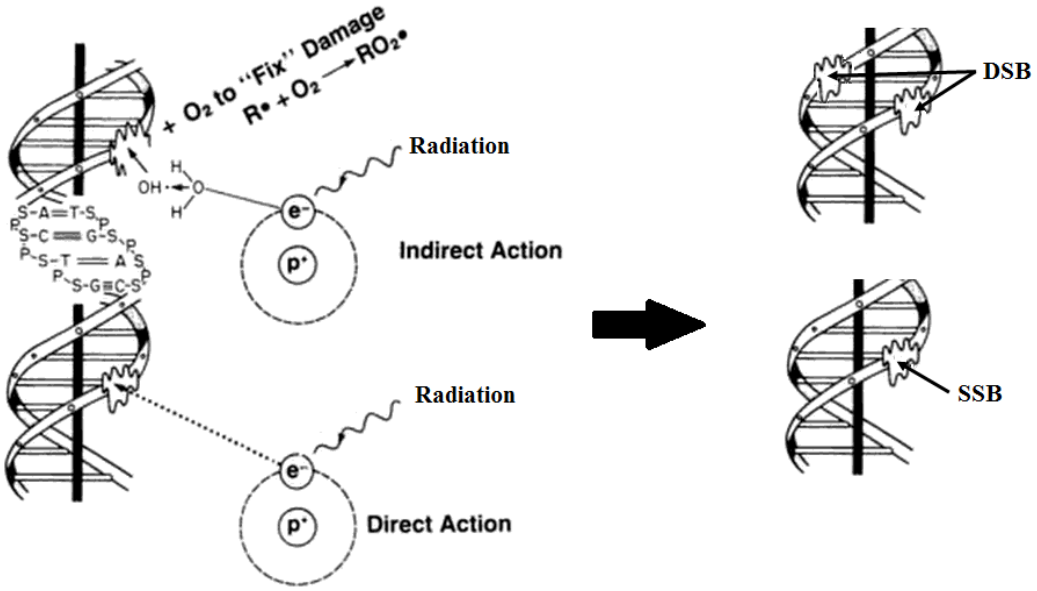

Figure 2.1: Simplified charts of the different pathways for radiation-induced DNA damage. On the left, interaction through direct and indirect damage due to an ionization event or the creation of free radicals, respectively. The right panel depicts the two types of damage on DNA, SSB and DSB (adapted from Hall 2012).

Since the first applications of radiotherapy at the end of the 19th century after the discovery of X-rays by Wilhelm Roentgen in 1895, major technological and computational advancements were made from conventional radiotherapy with simple beam ballistics to complex and conformal treatment delivery. Modern-day photon radiation delivery is performed via intensity modulated radiation therapy (Webb 2003) or volumetric intensity modulated arc therapy (Rao *et al* 2010) techniques, to achieve better coverage of the tumor target while sparing the surrounding healthy tissues. Wilson (1946) was the first to propose the use of fast ions for radiation therapy as an alternative to photon radiation. The main advantage of ions over photons, illustrated in figure 2.2, is their inverted depth dose distribution. Photons have a maximum dose deposition at a shallow depth, which then decreases with the attenuation of photons in matters at greater depths. On the other hand, ions lose their energy (and thus velocity) as they traverse a medium, leading to an enhanced dose deposition at the end of the path, in the so-called Bragg peak (Bragg (1905)), while having low dose in the entrance in comparison to photons, and no dose due to the primary particles after the peak.

The superimposition of multiple pristine Bragg peaks affords target coverage in a spread-out Bragg peak (SOBP), as illustrated in figure 2.2. In the case of ions heavier than protons, low dose after the peak can be observed due to fragmentation processes of the primary beam. Furthermore, these heavy-ions exhibit optimal dosimetric characteristics such as a reduced lateral spread and a sharper Bragg peak, potentially leading to a reduction in dose delivery to the surrounding healthy tissues. In addition to the physical advantages, ions possess enhanced biological effectiveness, due to the higher ionization density compared to photon beams, particularly in the Bragg peak region and in the case of heavy ions (Kraft 2000). These various aspects will be addressed in the following sections.

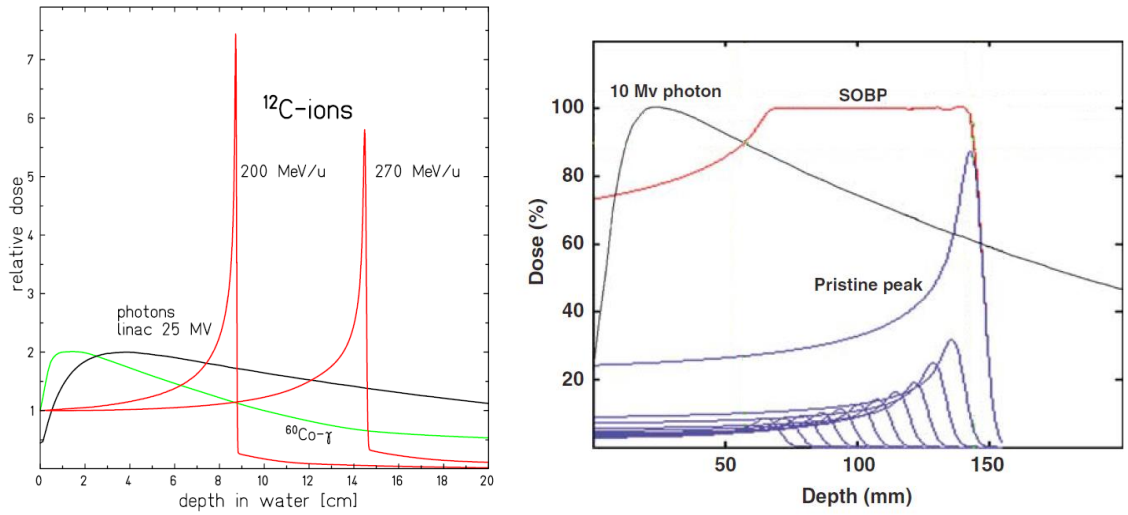

Figure 2.2: *Left:* Depth dose profiles for ^{60}Co, 25MV photons, and ^{12}C ions (200 and 270 MeV/u) in water (Schardt *et al* 2010); *Right:* Depth dose distributions of 10 MV photons and superimposition of several pristine Bragg peaks creating a SOBP (adapted from Levin *et al* 2005).

Lawrence Berkeley Laboratory was the pioneering institution to lead the world's first clinical application of ion beams, beginning with protons in 1954 (Tobias *et al* 1958), then helium ions in 1957 (Lawrence *et al* 1964), followed by heavier ion treatments in 1975 (Castro *et al* 1980). Since then, the interest in particle therapy has grown with the new technological developments above sixty particle therapy facilities in operation and around forty under constructions, according to the November 2016 update of the Particle Therapy Co-Operative Group (PTCOG). The total number of patients treated with charged particles at the end of 2015 was 154203 (131240 with protons, 19376 with carbon ions, 2054 with helium ions and 1533 with other particles).

2.2. Ion beams physical properties

The physical advantages of ions are resulting from the interaction properties of ions in matter, especially the energy loss of ions as they lose velocity and the associated range straggling, the lateral spread of the beam and the nuclear reaction.

2.2.1. Energy loss, range and range straggling

The total energy loss of ions in matter $\left.\frac{\mathrm{d}E}{\mathrm{d}x}\right|_{tot}$ can be decomposed in three components:

$$\left.\frac{\mathrm{d}E}{\mathrm{d}x}\right|_{tot} = \left.\frac{\mathrm{d}E}{\mathrm{d}x}\right|_{el} + \left.\frac{\mathrm{d}E}{\mathrm{d}x}\right|_{nuc} + \left.\frac{\mathrm{d}E}{\mathrm{d}x}\right|_{rad} . \quad (2.4)$$

The first component $\left.\frac{\mathrm{d}E}{\mathrm{d}x}\right|_{el}$ is the energy loss related to the inelastic interactions with atomic electrons (electronic stopping power), $\left.\frac{\mathrm{d}E}{\mathrm{d}x}\right|_{nuc}$ corresponds to the energy loss due to elastic interaction with the target nuclei (nuclear stopping power) and $\left.\frac{\mathrm{d}E}{\mathrm{d}x}\right|_{rad}$ is the energy loss involving radiative processes. For the energy range used in ion beam therapy up to ~450 MeV/u (Bragg peak at ~34cm for carbon ions), corresponding to a velocity about 70% of the speed of light, the energy loss is dominated by the electronic stopping power. Thus, it can be described by the Bethe-Bloch (Bethe 1930, Bethe 1933, Fano 1963) formula:

$$-\frac{\mathrm{d}E}{\mathrm{d}x} = 2\pi r_e^2 m_e c^2 N_e \frac{Z_p^2}{\beta^2}\left[ln\left(\frac{2m_e c^2\beta^2(1/\sqrt{1-\beta^2})^2 T_{max}}{\langle I\rangle^2}\right) - 2\beta^2 - 2\frac{C}{Z_t} - \delta\right]. \quad (2.5)$$

The term C and δ describe the energy shell and density correction terms introduced in Fano (1963), while c corresponds to the speed of light and Z_t as well as Z_p represent the nuclear charge Z of the target and particle, respectively. β is the projectile velocity (scaled in term of c), N_e is the target electron density and $\langle I\rangle$ its mean ionization potential. r_e and m_e are the radius and rest mass of an electron, respectively. T_{max} is the maximum energy transferred in a single collision with a free electron. The formula indicates that as the particle will be slowed down, the energy loss will increase due to the dependency in $\frac{1}{\beta^2}$. This formula 2.5 is valid for describing stopping power for energy above ~ 1MeV/u. For lower energies, recombination processes lead to a decrease of the projectile effective charge and thus of the energy loss after

having reached a maximum (e.g. at about 350 keV/u in water for ^{12}C as seen in Figure 2.3), at the Bragg peak position. This decrease is taken into account by substituting the Z_{eff} term in equation 2.5 instead of Z_p, approximated as described by Barkas (1963):

$$Z_{eff} = Z_p \times \left[1 - e^{-\alpha\beta Z_p^{-2/3}}\right], \tag{2.5}$$

with α ~ 125.

An absorber material of particular interest in ion beam therapy is water. The mean ionization potential $\langle I \rangle$ was defined for protons at 75 eV (ICRU 1994), however new values from the literature suggest higher values for protons and heavier ions in a range from 75 to 80 eV, with an ICRU value at 78 eV (ICRU 2009, Bichsel *et al* 2000, Krämer *et al* 2000, Kumazaki *et al* 2007, Andreo *et al* 2013) and as investigated in Chapter 4. The evolution of the stopping power in water for protons and ^{12}C ion beams is illustrated in figure 2.3. As described in figure 2.3, the contribution of the nuclear stopping power is relevant only at extremely low residual range of the particles, in the last µm, and can be neglected for particle therapy application (Elsässer *et al* 2009). Radiative stopping power is mainly present in high relativistic regime and can be therefore neglected as well, since therapy is working mostly in the medium-relativistic regime.

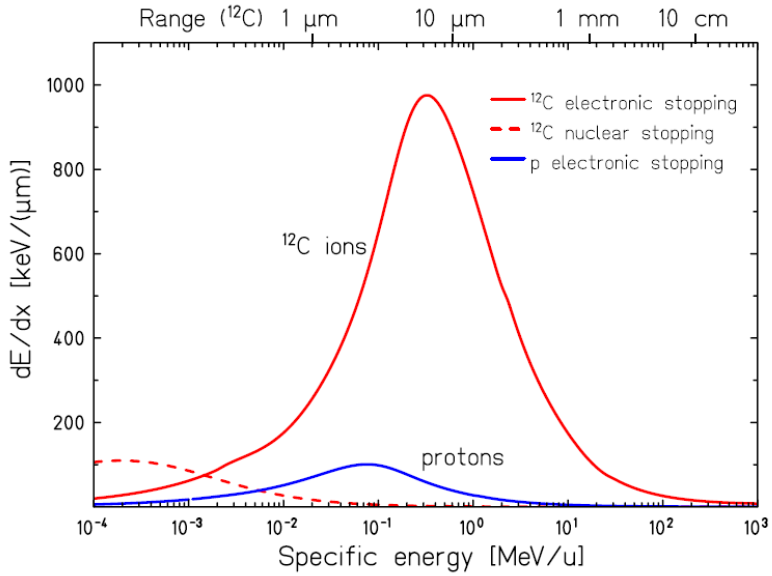

Figure 2.3: Specific energy loss $\frac{dE}{dx}$ in water for carbon ion and proton beams. (Schardt *et al* 2010)

The mean range of a particle, corresponding to the thickness of absorber medium traversed, is close, for ions, to the finite path length from the "continuous slowing down approximation", since heavy charged particles undergo little lateral scattering. Thus, the range of a particle with an initial energy *E* can be calculated as follows:

$$R(E) = \int_E^0 \left(\frac{\mathrm{d}E'}{\mathrm{d}x}\right)^{-1} dE' \,, \tag{2.6}$$

From equation 2.4 and 2.6, due to the dependency on Z_p^2 and $\frac{1}{\beta^2}$, it can be found that the range of different ions with a same velocity β can be scaled approximately with $\frac{A}{Z_p^2}$. The mean range of different ions in water is displayed in figure 2.4

However, equation 2.4 describes the mean stopping power for a single particle. Due to statistical fluctuation on the number of collisions for each particle, leading to energy loss straggling (Bohr 1913, Ahlen 1980) and thus a broader energy spectrum of the incident particles, the range will differ slightly for each particle, resulting into a broadened Bragg peak. This phenomenon is called range straggling. The straggling width can be approximated, as reported in Schardt *et al* (2010), for a particle with a mean range *R*, as:

$$\frac{\sigma_R}{R} = \frac{1}{\sqrt{M}} \times f\left(\frac{E}{Mc^2}\right), \tag{2.7}$$

with *f* a function with slow variation. Thus, heavier ions will undergo less range straggling, and thus have a sharper Bragg peak, as illustrated in figure 2.5. However, it can be beneficial for a treatment to have a broader Bragg peak. This can be achieved by artificially widening the initial energy spread of the accelerator with a passive energy degrader such as the ripple filter, leading to broadened initial energy spectra before the target.

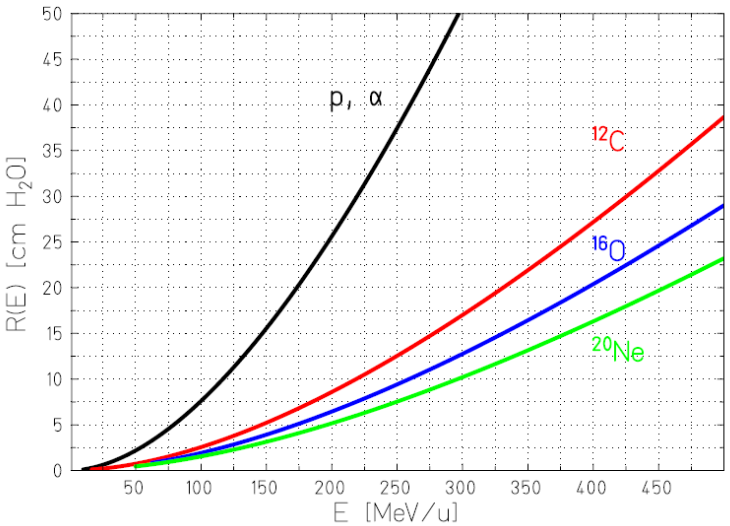

Figure 2.4: Mean range of different ions in water. (Schardt *et al* 2010)

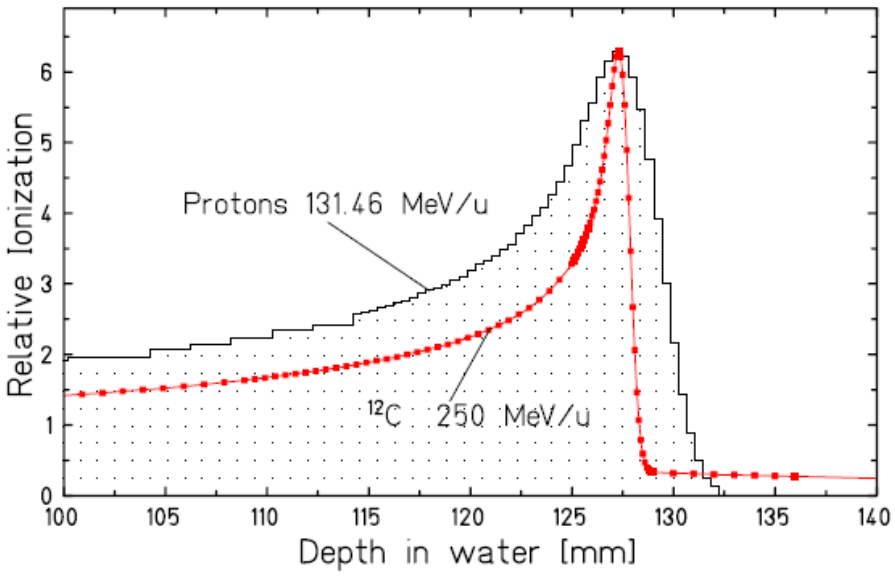

Figure 2.5: Bragg peak of protons and carbon ions, with the same mean range, measured in water. (Schardt *et al* 2010)

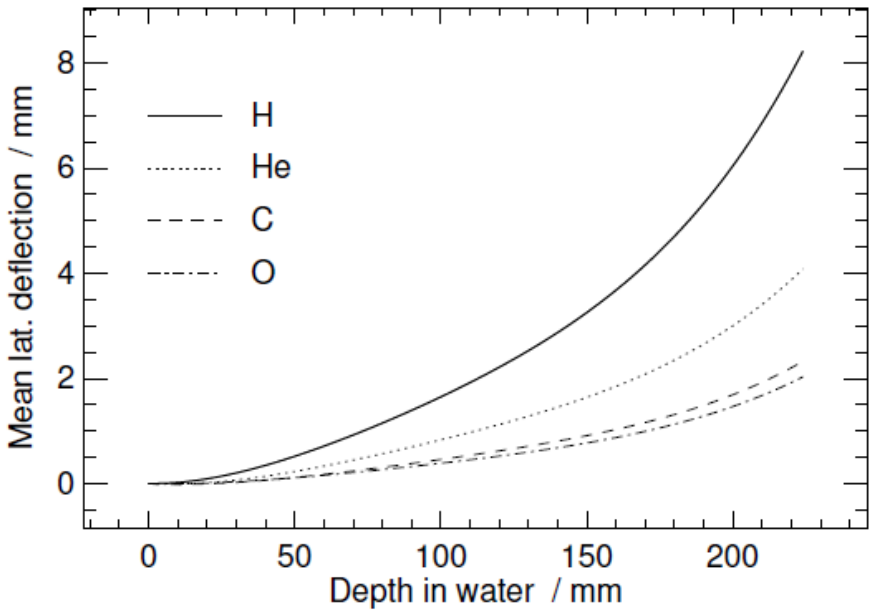

Figure 2.6: Lateral deflection of protons, helium, carbon and oxygen ion beams in water. (Parodi 2004)

2.2.2. Lateral scattering

The different interactions with the absorber will lead to small deflection of the incident beam, mainly dominated by multiple elastic Coulomb scattering. The Molière solution (1948) describes the angular distribution at a certain penetration depth, and was found in good agreement with measurements (Gottschalk *et al* 1993). An approximation for small angles was given by Highland (1975, 1979), described at a penetration depth by a Gaussian with a width σ_θ:

$$\sigma_\theta[rad] = \frac{14.1MeV}{\beta\rho c} \times Z_p \times \sqrt{\frac{d}{L_{rad}}} \times \left[1 + \frac{1}{9} log_{10}\left(\frac{d}{L_{rad}}\right)\right], \quad (2.8)$$

where d is the thickness of the traversed medium, L_{rad} the radiation length (with values available in Tsai (1974)) and p the particle momentum. Other quantities are already described in equation 2.5. Lateral straggling of different ions will be experimentally investigated in the Chapter 3. For similar penetration depth, the energy of lighter ions is lower than that of the heavier ions, manifested in the $\frac{1}{\beta\rho c}$ dependency to a larger lateral spread as seen in figure 2.6.

2.2.3. Nuclear interactions and fragmentation

Ions can undergo interactions with the medium via the strong nuclear force. Nuclear interactions will lead to a decrease of the initial primary beam fluence Φ_0, along the depth z, following:

$$\Phi(z) = \Phi_0 \times e^{-N\sigma_r z}\,, \quad (2.9)$$

with N the density of nuclei in the medium and σ_r the total reaction cross-section.

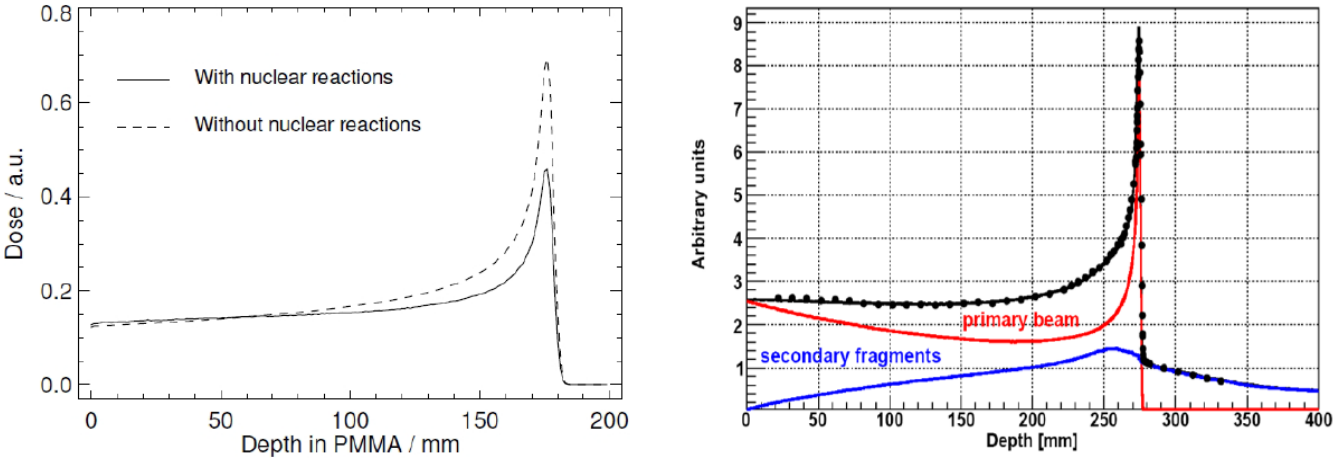

Figure 2.7: *Left:* Proton beam (175MeV) Monte Carlo predicted dose distribution in PMMA, with and without nuclear interactions (Parodi 2004). *Right:* Monte Carlo predicted dose deposition of carbon ion beams (400 MeV/u), separating the contribution of the primary beam and fragmentation products in water. (Mairani 2008)

In ion beam therapy, nuclear interactions will impact the dose distribution even if their cross-section is substantially smaller than that of Coulomb interactions. The effects of nuclear interactions have two main drawbacks as seen in figure 2.7, (1) the reduced entrance-to-peak ratio, due to the reduction of the primary beam fluence and (2), the rise of a dose fragmentation tail, due to the produced fragments with a lower Z, which will consequently undergo additional multiple Coulomb scattering events with greater lateral spreading than the initial beam. However, some fragments from the target or the projectile, such as ^{11}C or ^{15}O can be of interest for in-vivo range monitoring (review in Kraan 2015) with positron emission imaging (e.g. positron emission tomography, see section 2.8). The prompt gammas emitted as a result of nuclear interaction can also be used for range monitoring with prompt gamma imaging techniques (Min *et al* 2006, Hueso-Gonzalez *et al* 2016).

Protons are undergoing nucleon-nucleus reactions, leading as a final state to the production of target light fragments (e.g. from evaporation process), nucleons and de-excitation gamma-rays. For heavier ions, nucleus-nucleus interactions result in fragments from the particle and/or the medium. In the energy range of ion therapy, peripheral collisions are mostly dominant, mainly due to geometrical reasons. When these nuclear reactions occur, the beam particle and target can lose nucleons, described by the abrasion-ablation model (Serber 1947) as illustrated in figure 2.8. In the first step, nucleons are abraded from the overlapping zone ("fireball"), while outer nucleons are only slightly affected. In a second step, the target fragments and remaining projectile undergo de-excitation by evaporation of nucleons or clusters (ablation). The remaining projectile fragment keeps nearly the same velocity and direction as the initial projectile. Nuclear interactions and fragmentation processes have been investigated extensively as for example in Goldhaber and Heckman (1978), Hüfner (1985) or and Lynch (1987).

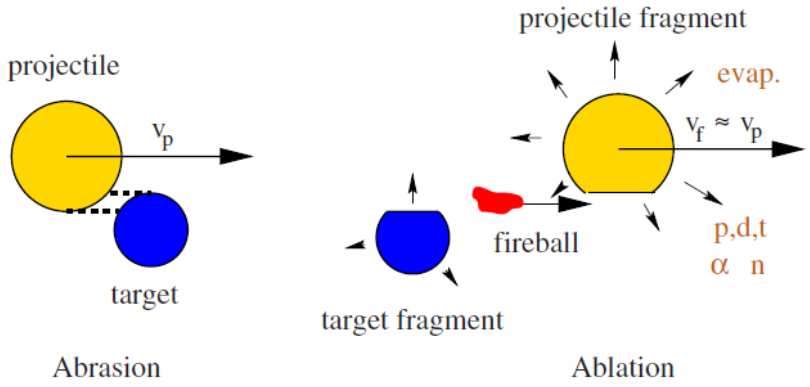

Figure 2.8: Illustrations of the abrasion-ablation model of peripheral collisions. (Schardt *et al* 2010)

2.3. Ion beam biological properties

In addition to physical advantages of ions over photons, enhancement of biological effectiveness and its dependency on dose, tissue type and LET are of interest. The two main phenomena are the relative biological effectiveness (RBE) and the oxygen enhancement ratio (OER). The RBE is defined as:

$$RBE = \left.\frac{D_{photon}}{D_{ion}}\right|_{isoeffect}. \tag{2.10}$$

It represents the ratio between the photon dose (D_{photon}) and the ion dose (D_{ion}) needed to achieve a same biological effect or endpoint. It can be illustrated as in figure 2.9 (left panel), with RBE for two different endpoints, either a cell survival of 10% (RBE_{10}) or 1% (RBE_1). It can be understood that due to the shape of the curves, the RBE will depend on the reference dose. Furthermore, the shape of the survival curves for photons will depend on the tissue type and can be described by the linear quadratic model (LQ, Fowler 1989):

$$S(D) = e^{-(\alpha D + \beta D^2)}, \tag{2.11}$$

with α and β, describing the linear and quadratic part of the curve respectively, with the ratio α/β being characteristic of the tissue type and the type of radiation. For photon radiation, a large α/β *(>5)* is characteristic of a cell type with small repair functions, and thus a large sensitivity to radiation (a common characteristic of tumorous tissues), while a relatively small α/β (<5) is attributed to normal tissues. In addition to its dependencies on the dose and the tissue type, RBE is also LET dependent, as seen in figure 2.9 (right panel) from Hall (2012). With higher LET, RBE decreases due to an "overkill" effect (Hall 2012), where energy is "wasted" due to the excess of ionizing events. RBE is assumed to be 1.1 for protons (ICRU 2007), however some studies are showing and modeling a variable RBE, as supported by in-vitro data (Polster *et al* 2015, Giovannini *et al* 2016, Mairani *et al* 2017a). Furthermore, a recent study shows a clinical evidence of variable RBE for pediatric cases (Peeler *et al* 2016). For heavier ions, different RBE models are proposed as for example the Local Effect Model (LEM, Elsässer *et al* 2010) or the Microdosimetric Kinetic Model (MKM, Inaniwa *et al* 2010) used clinically in Europe and Japan, respectively. In particle therapy, the effective dose (biological dose or equivalent dose), represents the absorbed dose multiplied by the RBE to achieve an isoeffect with photons, and is expressed in GyRBE (ICRU 2007).

The OER is defined as:

$$OER = \left.\frac{D_{hypoxia}}{D_{air}}\right|_{isoeffect}. \tag{2.12}$$

The OER is the ratio of doses without ($D_{hypoxia}$) and with oxygen (D_{air}) to produce the same biologic effect. As seen in figure 2.9 (right panel), OER decreases with the increasing LET. In other words, for a hypoxic tumor, with a low oxygenation level, lower LET particles will be less efficient than higher LET particles. And thus heavier particles could be more advantageous than protons in tumor control rate (Scifoni *et al* 2013).

Fractionation of the treatment plan (in typically 20-30 fractions), allows the exploitation of the differential effect on the survival between low and high α/β tissue types. The rationale behind fractionation can be explained by the concept of the classic 4R's: Repair (repair of damages by normal tissue cells), Redistribution (change in cells cycle between fractions), Reoxygenation (oxygenation of the tumor and thus higher efficiency) and Repopulation (increase in cell division). Radiosensitivity is now also considered as an important factor and the 5th R due to the intrinsic radiosensitivity/radioresistance of different cell types. Fractionation can also impact RBE by affecting the shoulder of the cell survival between photons and ions, progressively increasing RBE after the first few fractions, as seen in Hall (2012).

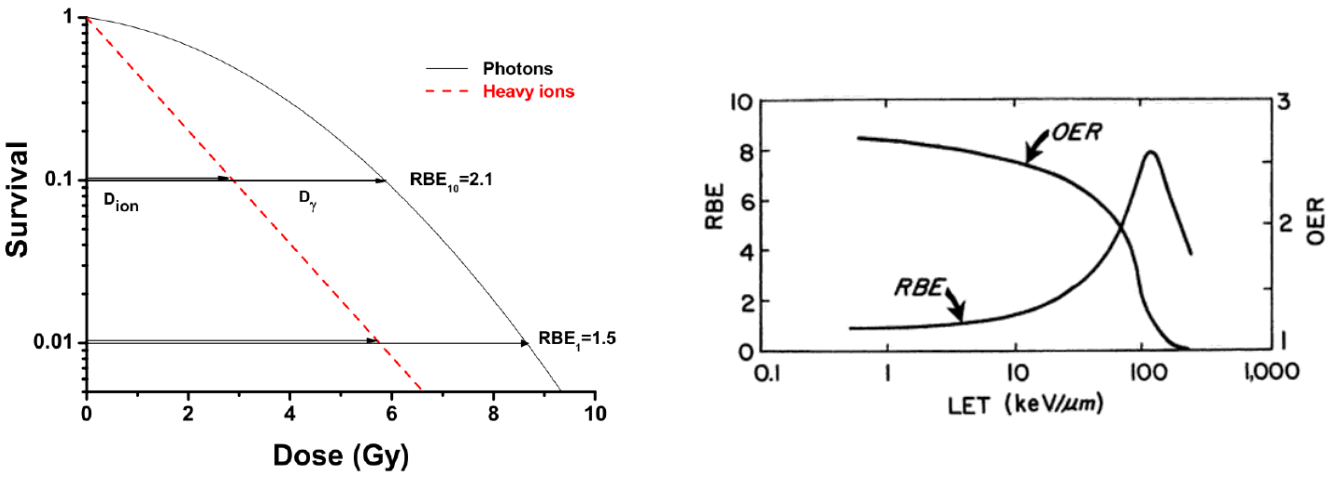

Figure 2.9: *Left*: Cell survivals for photons and heavy ions from Schardt *et al* (2010), and RBE at two different end points. *Right:* RBE and OER as function of LET from Hall (2012).

2.4. Accelerator and beam delivery

2.4.1. Accelerator types

Methods in ion acceleration and delivery have evolved over the last few decades (Owen *et al* 2016). Most particle therapy centers currently in operation are equipped with proton cyclotrons, with recent developments affording a compact design, with high intensity and stable delivery, such as the supra-conducting synchro-cyclotron. However, energy variation is made available by adding degraders, which deteriorate the beam quality and intensity. Some synchro-cyclotron models are foreseen to be used in conjunction with other ions, such as the planned C-400 (IBA), but a prototype has yet to be made available (Jongen *et al* 2010, Owen *et al* 2016). On the other hand, synchrotrons allow for active energy variation and are the only clinically viable method to deliver heavy ion beams at the moment.

Cyclotrons and particularly synchrotrons are expensive in comparison to conventional radiotherapy; however, technological developments as well as the increase in the number of centers will lead to more affordable market price with greater possibilities, such as one room solutions.

The development of novel beam production and delivery techniques is also underway, such as laser-based accelerator systems (Schwoerer *et al* 2006) and dielectric-wall accelerators (Poole *et al* 2007).

Regardless of the acceleration mechanism, the energetic ions are brought to the treatment room through a horizontal/vertical fixed beamline or gantry system, the latter providing greater geometric freedom for dose delivery. Compact gantry systems are available for protons and are becoming the gold-standard. The first worldwide heavy ion gantry was located at the Heidelberg Ion Beam Therapy center (see section 2.5) while underdevelopment at HIMAC facility (Iwata *et al* 2013, Noda 2016, Owen *et al* 2016).

2.4.2. Delivery techniques

After transport through the beamline, different beam delivery techniques are possible. Historically, the first techniques were “passive”, using passive elements with scattering system, energy degraders (modulating wheels / range shifters) and beam shapers (collimator, compensator), as seen in figure 2.10. The passive method provides a laterally broader beam from the initial pencil-like irradiation and then spreads the Bragg-peak longitudinally to adapt the distal edge of the dose distribution to the target position and size, while shaping the beam laterally accordingly. However, this technique can lead to unwanted dose in regions of normal tissue upstream from the tumor.

Another delivery techniques, so-called “active” beam shaping, such as raster scanning developed at GSI (Haberer *et al* 1993), affords target volume scanning with magnetic deflection of the beam (figure 2.11) for a fully active beam delivery. Scanning techniques were also introduced at the Paul Scherrer Institut (PSI) with spot scanning (Pedroni *et al* 1995), achieving longitudinal variation from the cyclotron beam with a passive range shifter. Scanning is performed for each energy slice, meaning that a certain depth has to be selected either by an active system (synchrotron for fully active beam delivery) or with degraders from an initial energy (cyclotron), providing conformal treatments with respect to tumor shape. Inverse treatment planning is implemented to design irradiations composed of several thousands of pencil beam scanning positions (called raster points in this work), as briefly described in section 2.6.

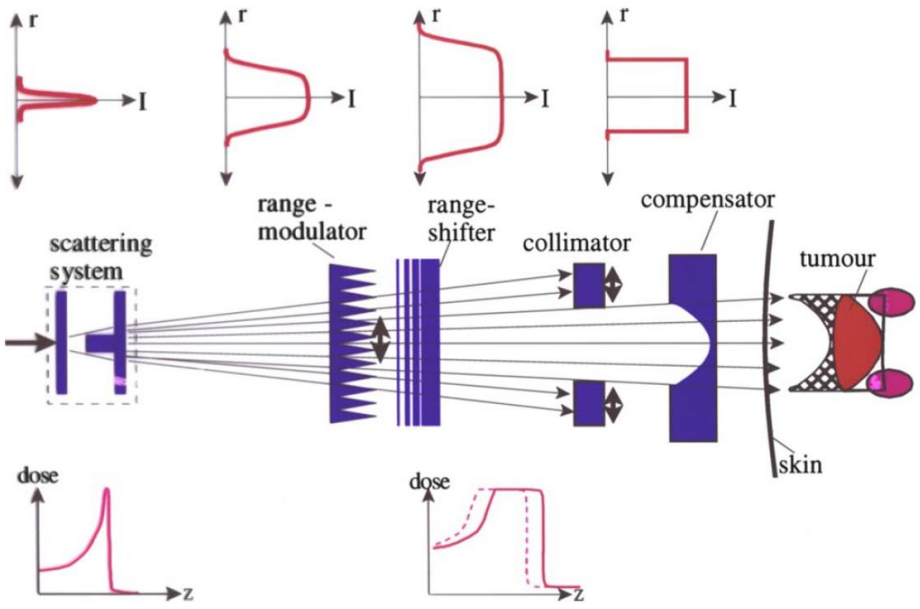

Figure 2.10: Schematic of a passive beam delivery from Schardt *et al* (2010), describing the evolution of the initial beam through the different passive elements to shape the beam to the tumour.

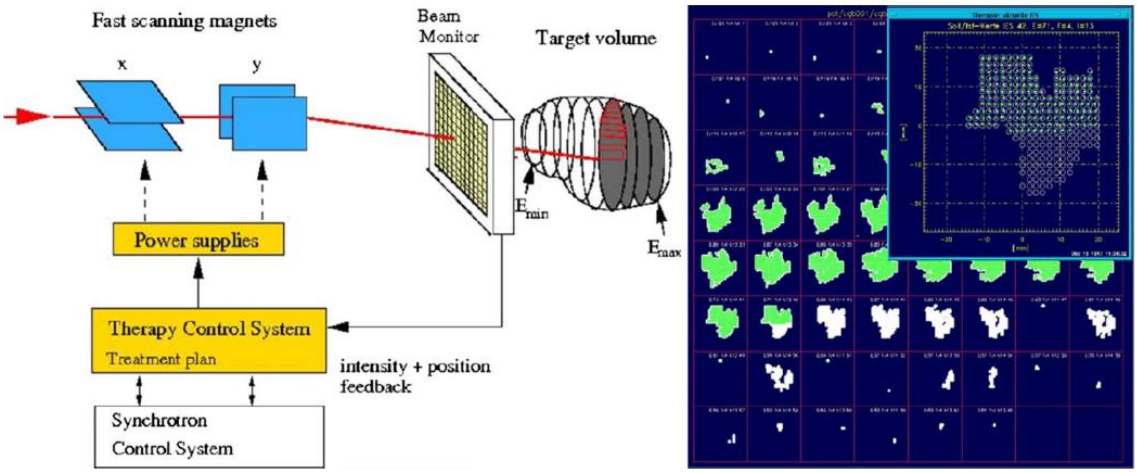

Figure 2.11: Workflow of an active beam scanning irradiation delivery from Schardt *et al* (2010), with an energy selection to reach a certain depth and a magnetic lateral scan to shape the delivery to the target volume.

2.5. The Heidelberg ion beam therapy center

The HIT center is a synchrotron based clinical facility with an active beam scanning delivery system similar to the prototype at GSI. In addition to two horizontal beam clinical treatment rooms, a third room is equipped with an isocentric gantry (figure 2.12). A third horizontal beam room is available for experiments. In addition to the clinically used protons (^{1}H) and carbon ions (^{12}C), two other ion species are available, ^{4}He and ^{16}O.

For each ion species, the synchrotron can accelerate 255 discrete energies (205 for oxygen) up to ~220MeV/u for protons and helium ions, and up to ~430 MeV/u for carbon and oxygen ions, each with ~32 cm range, except for ^{16}O with a range about 23 cm. A detailed description of the beams characteristics are presented in Chapter 3. The beam spot size (i.e., lateral size in air at isocenter) and intensity is adjustable for each energy from a library of 6 foci and 12 beam intensities. In clinical practice, 4 foci and 10 intensities are most commonly used (Parodi *et al* 2012). The so-called "Beam applications and monitoring system" (BAMS), situated at the end of the beamline, consists of three ionization chambers (IC) to monitor the fluence delivered per raster point and two multiple wires proportional chambers (MWPC) to verify and give feedback loop controls on the position of the beam and the its size during irradiation.

Treatment rooms are equipped with a 6 degrees of freedom robotic treatment table, granting sub-millimetric patient positioning before irradiation and verification with 2D-kV x-ray imaging systems.

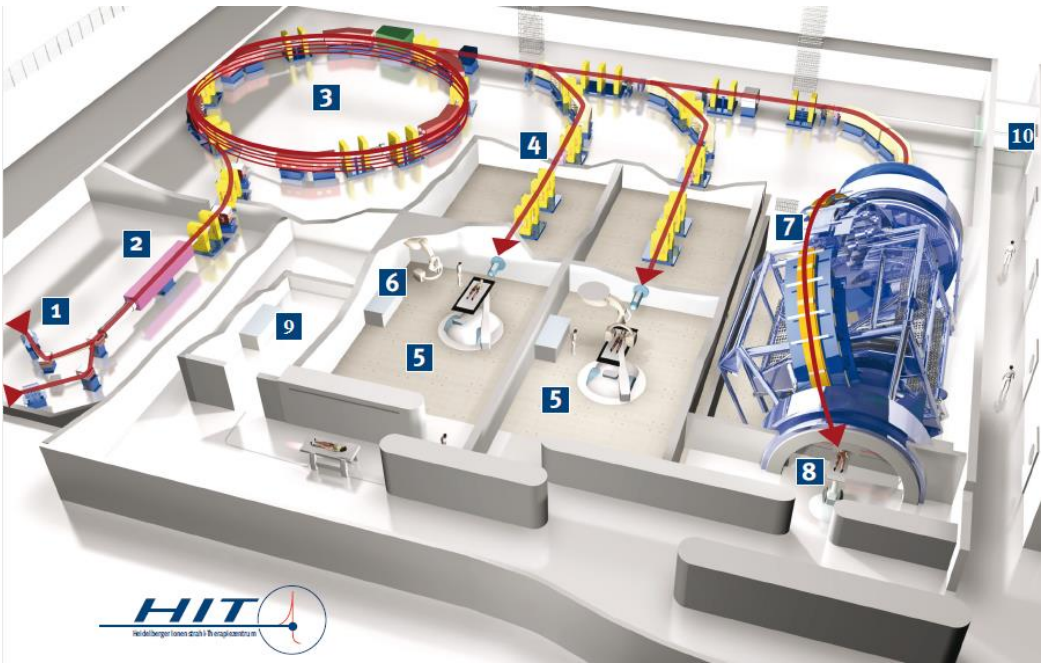

Figure 2.12: Layout of the HIT facility adapted from https://www.klinikum.uniheidelberg.de/, with (1) ion sources, (2) linear accelerator, (3) synchrotron, (4) high energy beam transfer line, (5) horizontal treatment rooms, (6) x-ray positioning control system, (7) gantry, (8) gantry treatment room, (9) PET-CT room and, (10) experimental room.

2.6. Treatment planning system and uncertainties

The treatment planning system (TPS) is used in modern conventional radiotherapy to create optimized radiation treatment plans from a complex patient geometry via an inverse planning algorithm. Such an approach is also needed for particle therapy, in the case of active beam delivery, to calculate particle fluence for thousands of raster points to reach specified dose levels. At HIT, the commercial TPS used (SyngoPT, Siemens), is based on TRiP98, the TPS developed at GSI for active beam scanning (Krämer 2009, Krämer *et al* 2000). It allows calculation of physical and biological dose distributions, the latest using the LEM model for RBE predictions. The TPS uses a physical database describing the laterally integrated depth dose distributions and lateral dose profiles (modelled with a double Gaussian parameterization), as obtained from experimentally validated Monte Carlo (MC) simulations (see section 2.7). Thus, the absorbed dose for a pencil beam can be calculated according to:

$$D_{PB}(x,y,z) = ddd(z) \times Lat(r,z) \times N_{PB}, \tag{2.13}$$

with $D_{PB}(x,y,z)$ beingthe dose due to a pencil beam, $ddd(z)$ the laterally integrated depth dose distribution for the corresponding energy, representing the dose deposition along the depth per particles, $Lat(r,z)$ the description of the lateral distribution, represented by a normalized double Gaussian at HIT, and N_{PB} the number of particles related to this pencil beam.

Subsequently the total dose for each voxel can be obtained by summing up the dose contribution of each pencil beam following:

$$D_{total}(x,y,z) = \sum_{PB} D_{PB}(x,y,z). \tag{2.14}$$

For biological calculation of heavy ions, spectra of the fragments along the depth is pre-calculated with MC (Parodi *et al* 2012) and coupled to the LEM for RBE predictions.

As in conventional radiotherapy, plans are based on computed tomography (CT) of the patient, which is typically used in combination with other modalities (e.g. magnetic resonance imaging (MRI), positron emission tomography (PET)) for delineation of the OAR and targets (planning target volume (PTV), clinical target volume (CTV), gross tumor volume (GTV)). For dosimetric calculations on the CT images, while in conventional radiotherapy a calibration is performed between Hounsfield unit (HU) and mass as well as electron density, in particle therapy the calibration is defined between HU and water equivalent path length or stopping power ratio. The ion beam range is then expressed in the patient geometry in terms of water equivalent thickness. The WEPL is linked to the ratio of the stopping power between the given material and water, which is correlated to the relative electron density of this material and thus to its HU on the CT. An example of HU-WEPL calibration curve is shown in figure 2.13. However, this conversion is one of the main sources of uncertainty in particle therapy estimated at about 1-3% (accounting for both HU values uncertainty and calibration curve uncertainty), thus meaning 1 to 3 mm range uncertainty for a 10 cm deep-seated tumor (Rietzel *et al* 2007). Several means to reduce these uncertainties involve the investigation of alternative calibration methods such as dual energy-CT (Yang *et al* 2010, Landry *et al* 2011, Hünemohr 2014) or ion-based radiography/tomography (Schneider *et al* 2005, Schulte *et al* 2008, Rinaldi *et al* 2013, Meyer *et al* 2017), in order to determine more precisely the stopping

power ratio of the material, thus decreasing the safety margins applied in clinical practice. Furthermore, other sources of uncertainty appear along the course of fractionated treatment, such as patient misalignment, as well as inter-fractional changes (anatomical changes) and intra-fractional patient motion (e.g. respiration, heart beat). For these sources of uncertainties, other dedicated techniques can try to reduce the uncertainties (e.g. cone beam CT imaging and re-planning (Landry *et al* 2015)), while other methods focus on their quantification, such as in-vivo monitoring with PET (see section 2.8, Parodi 2008, Bauer *et al* 2013a) or range verification with prompt gamma imaging (Min *et al* 2006, Richter et al 2016).

Newer versions of TPS incorporate more robust planning strategies (Fredriksson 2013) by including some of these uncertainties (e.g. HU-WEPL conversion, patient positioning) to more accurately predict the actual delivered dose to the target in the patient. 4D treatment planning is also employed (Richter *et al* 2013) to take into account motion, typically induced by respiration (e.g. on liver, lungs).

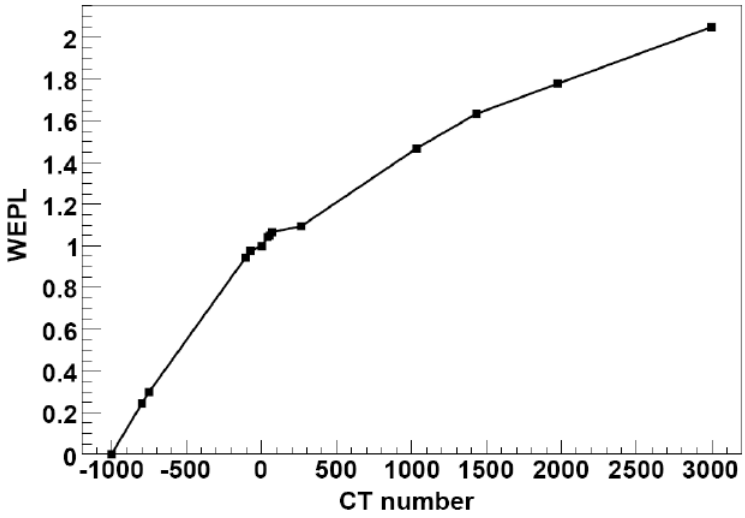

Figure 2.13: HU-WEPL calibration curve from measurements of tissue equivalent materials (Krämer *et al* 2000)

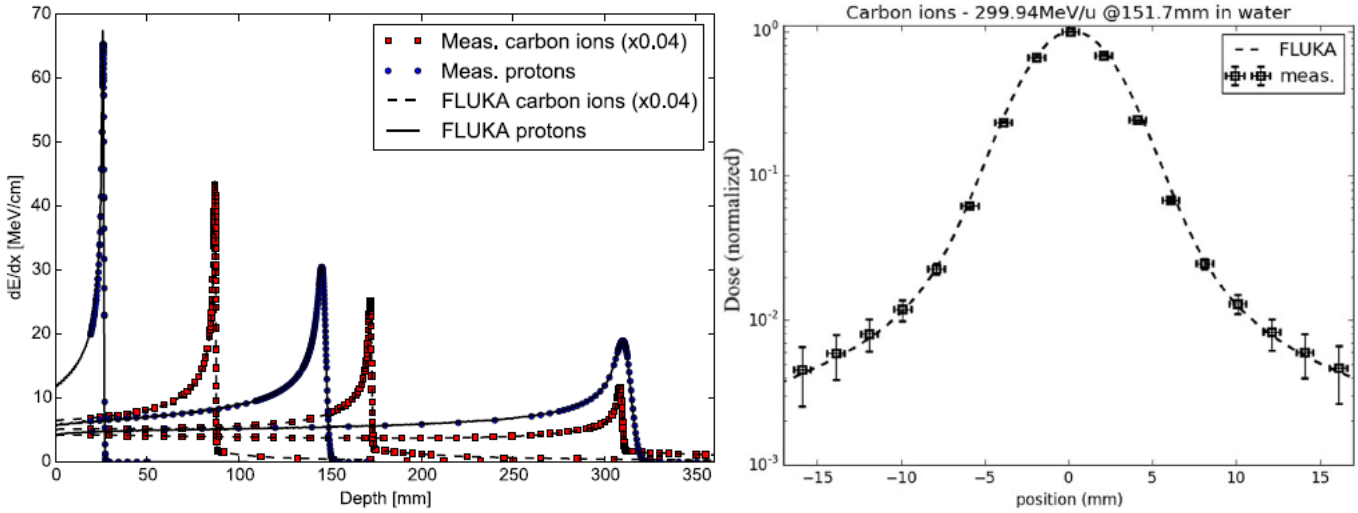

Figure 2.14: *Left*: Depth dose distributions comparison between FLUKA MC predictions and measurements for protons and carbon ions. *Right*: Lateral profiles comparisons between simulations and measurements for carbon ions. (Battistoni *et al* 2016)

2.7. FLUKA Monte Carlo code

MC codes are powerful tools in the field of particle physics and therapy. They provide the means to precisely describe the interactions of particles within matter, taking into account the particular geometry and medium composition traversed by the particles. Several codes are used in the field of ion beam therapy such as FLUKA (Ferrari *et al* 2005, Böhlen *et al* 2014), GEANT4 (Agostinelli *et al* 2003, Allison *et al* 2006), MCNPx (Hughes *et al* 1997), PHITS (Niita *et al* 2006) and SHIELD-HIT (Dementyev and Sobolevsky 1999, Gudowska *et al* 2004). Their predictions are particularly useful in describing the particle interaction and dose deposition inside voxelized patient geometry as in Bauer *et al* (2014), to support quality assurance and treatment verification (Molinelli *et al* 2013) or as support in developing new techniques (e.g. imaging, detectors applications). At HIT, the FLUKA MC code was chosen to generate the analytical TPS physics database (depth dose distribution, double Gaussian functions, secondary particles depth spectra for biological dose calculations of heavy ions(Parodi *et al* 2012, Parodi *et al* 2013, Mairani *et al* 2010)), as well as to support treatment verification with PET range verification analysis (see section 2.8, Bauer *et al* 2013a, as well as physical dose calculation and biological dose calculation for radiobiological experiments (Bauer *et al* 2014, Mairani *et al* 2016a, Mairani *et al* 2017a). Before its implementation, validation of FLUKA's dosimetric predictions was achieved for protons, carbon ions and oxygen ions (Parodi *et al* 2012, Parodi *et al* 2013, Kurz *et al* 2012) (figure 2.14).

The FLUKA code is a general purpose MC code simulating the interaction and transport of particles, developed in collaboration between the European Organization for Nuclear Research (CERN) and the Italian institute for nuclear physics (INFN). General information and descriptions can be found in Battistoni *et al* 2016 and *www.fluka.org*. The description of energy loss and fluctuation is based on an alternative approach to Landau and Vasilov distributions (Ferrari *et al* 1997) by simulating secondary electron production and transport down to 1keV (Battistoni *et al* 2016). Multiple Coulomb scattering is handled with an extended model based on Molière Theory, with the possibility of single Coulomb scattering. Nuclear processes (figure 2.14) are handled by the PEANUT (Pre-Equilibrium Approach to Nuclear Thermalization, Ferrari and Sala 1997) models for hadron-nucleus interactions for an

energy range from the MeV order up to 5GeV, describing the interactions along the steps of a generalized intranuclear cascade (GINC), followed by a pre-equilibrium particle emission and equilibrium phase. Based on a statistical approach, produced nuclei from the interaction can undergo evaporation. Nucleus-nucleus interactions are described by two distinct models in the therapeutic energy range, RQMD (relativistic quantum molecular dynamics, Sorge *et al* 1989) from 100 MeV/u to 5GeV/u, and the BME (Boltzmann master equation, Cavinato *et al* 1998) below 100 MeV/u, and can be interfaced with PEANUT (e.g. for further processing of fragments).

Biological modeling can be interfaced with the FLUKA code from an external database. At HIT, a re-implementation of the LEM was linked to FLUKA (Mairani *et al* 2010), predicting the RBE-weighted dose (D_{RBE}) for a mixed radiation field such as in the case of carbon ions. The dose-weighted average $\bar{\alpha}$ and $\bar{\beta}$ terms, from the LQ formalism, are computed online for each voxel $j(x,y,z)$ in the following approach:

$$\bar{\alpha}_j = \frac{\sum_i \Delta d_{i,j} \cdot \alpha_{i,j}}{\sum_i \Delta d_{i,j}} \quad \text{and} \quad \sqrt{\bar{\beta}_j} = \frac{\sum_i \Delta d_{i,j} \cdot \sqrt{\beta_{i,j}}}{\sum_i \Delta d_{i,j}} \,, \tag{2.15}$$

where $\Delta d_{i,j}$ is the dose from a particle i of the mixed radiation field in voxel j, associated to its corresponding α and β terms, and then summed over the i^{th} particles depositing dose inside the voxel j. The α and β terms are calculated on the run knowing the particles LET from the simulation and its corresponding α or β term from user external database (Battistoni *et al* 2016). Other biological models, phenomenological (Wedenberg *et al* 1993, Mairani *et al* 2016a) or biophysical (MKM), can also be interfaced by the user.

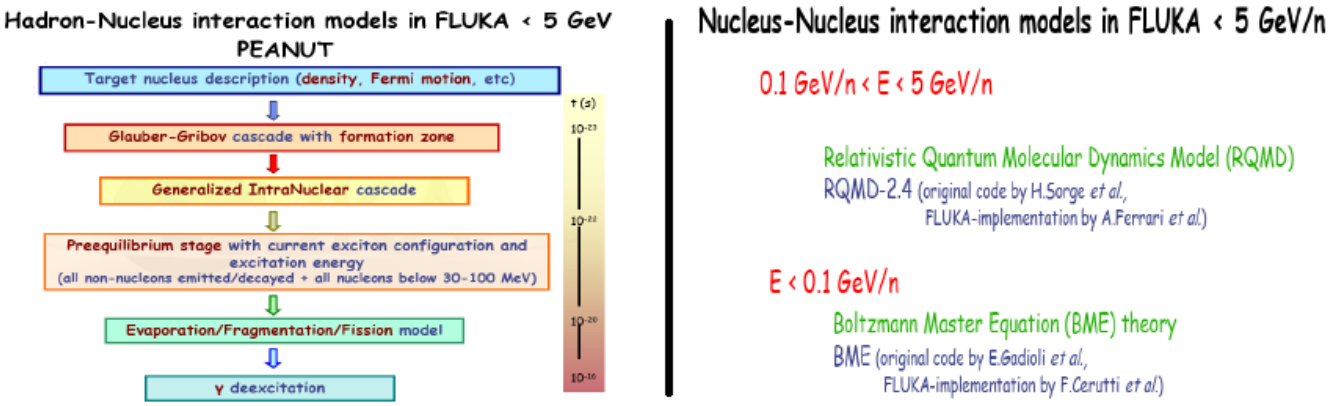

Figure 2.15: Diagram of the FLUKA nuclear interaction models for both hadron-nucleus and nucleus-nucleus interaction (from www.fluka.org , 18th FLUKA course).

2.8. Positron emission tomography

Nuclear processes described in section 2.2 can lead to the creation of β^+ emitters from either the fragmentation of the projectile or the target, as illustrated in figure 2.16 for protons (only from target fragments) and carbon ions (from both target fragments and projectiles, the latter stopping close to the Bragg peak position). As stated in section 2.2, these residuals of the nuclear interactions can provide useful information for monitoring the delivery "in-vivo", and indirectly inferring the ion beam range. However, PET information cannot provide absolute dose distributions and must be compared to a reference set of data, e.g. based on MC simulations or prior PET.

Several approaches have been investigated for PET monitoring, as reviewed in Kraan (2015), in-beam PET (e.g. during irradiations), in-room PET (after the irradiation but in the same room) or offline PET (after irradiation, with a PET/CT system in another room). From the pioneering work in GSI (in-beam PET, Enghardt *et al* 2004) and Massachusetts General Hospital (offline PET/CT system, Parodi *et al* 2007), the advantages of in-vivo PET range verification in the clinic has been demonstrated, as well as its limitation. At HIT, an offline approach was considered and used in clinical routine for in-vivo monitoring. Details about its workflow can be found in Bauer *et al* (2013a). In summary, after completing a fraction of radiation treatment, the patient is transported to the PET/CT room, immobilized in the same position as in the treatment room, where a 30 minute PET scan is acquired in list-mode. Compared to in-beam PET acquisition, many uncertainties are introduced due to the re-positioning of the patient, reduced radioactivity (due to the short lifetime positron emitters), the biological washout due to the patient physiology, and the loss of information if several beams are used, with imaging only of the integral beam delivery. Despite these drawbacks such methods can be readily integrated into the clinical workflow and show fairly good results (Shakirin et al 2011), compared to the more demanding implementation of in-beam PET or the suggested in-room PET, as evaluated in Shakirin et al (2011).

At HIT, PET acquisitions are compared to MC-based PET predictions simulated on the planning CT. Positron emitter 3D distributions are recorded for ^{11}C, ^{13}N, ^{15}O, ^{30}P, ^{38}K and post-processed to take into account physical decay from the irradiation to the acquisition time as well as tissue dependent biological washout (after HU-based segmentation, e.g. into fat, brain, soft bone, hard bone as in Parodi *et al* (2007)), and then convolved with a Gaussian kernel representing the response of the PET acquisition/reconstruction.

The range analysis is performed with an in-house-built graphical interface based on MeVisLab (www.mevislab.de) (Chen *et al* 2017), giving range shift estimations in beam-eye-view (BEV) using CT and PET information as seen in figure 2.17. In Handrack (2016), an assessment of the PET range verification performance with phantoms and patients was performed. Comparisons between PET simulation *vs.* PET simulation, PET measurement *vs.* PET measurement, PET simulation *vs.* PET measurement were achieved, reflecting different kinds of complexity and introduction of uncertainties. While phantom studies showed the potential of achieving range retrieval with errors below 1.5 mm, clinical studies indicated larger deviations due to the introduction of uncertainty in patient re-positioning and biological washout. Results suggest the use of a reference PET-CT acquisition for comparisons to further PET acquisitions to reduce the large uncertainty brought by the biological washout in MC simulations, as already suggested in Frey *et al* (2014).

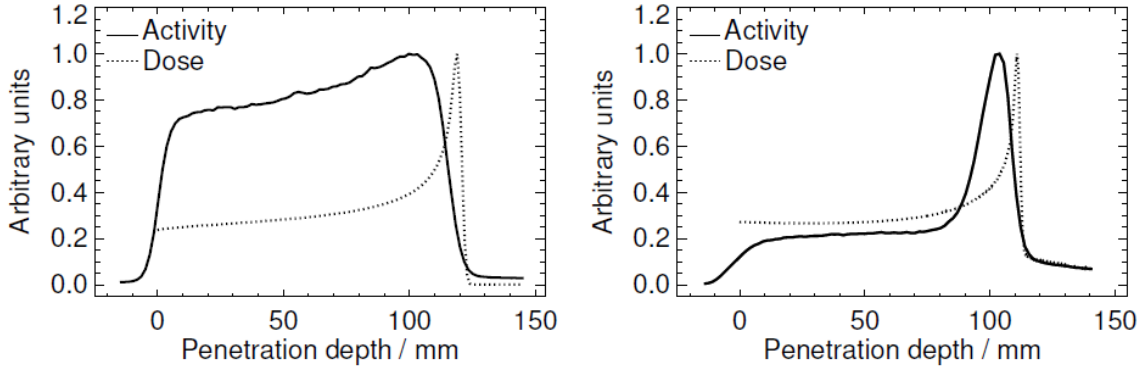

Figure 2.16: PET activity induced from a quasi-monoenergetic beam irradiation for protons (left) and carbon ions (right) (Parodi 2004)

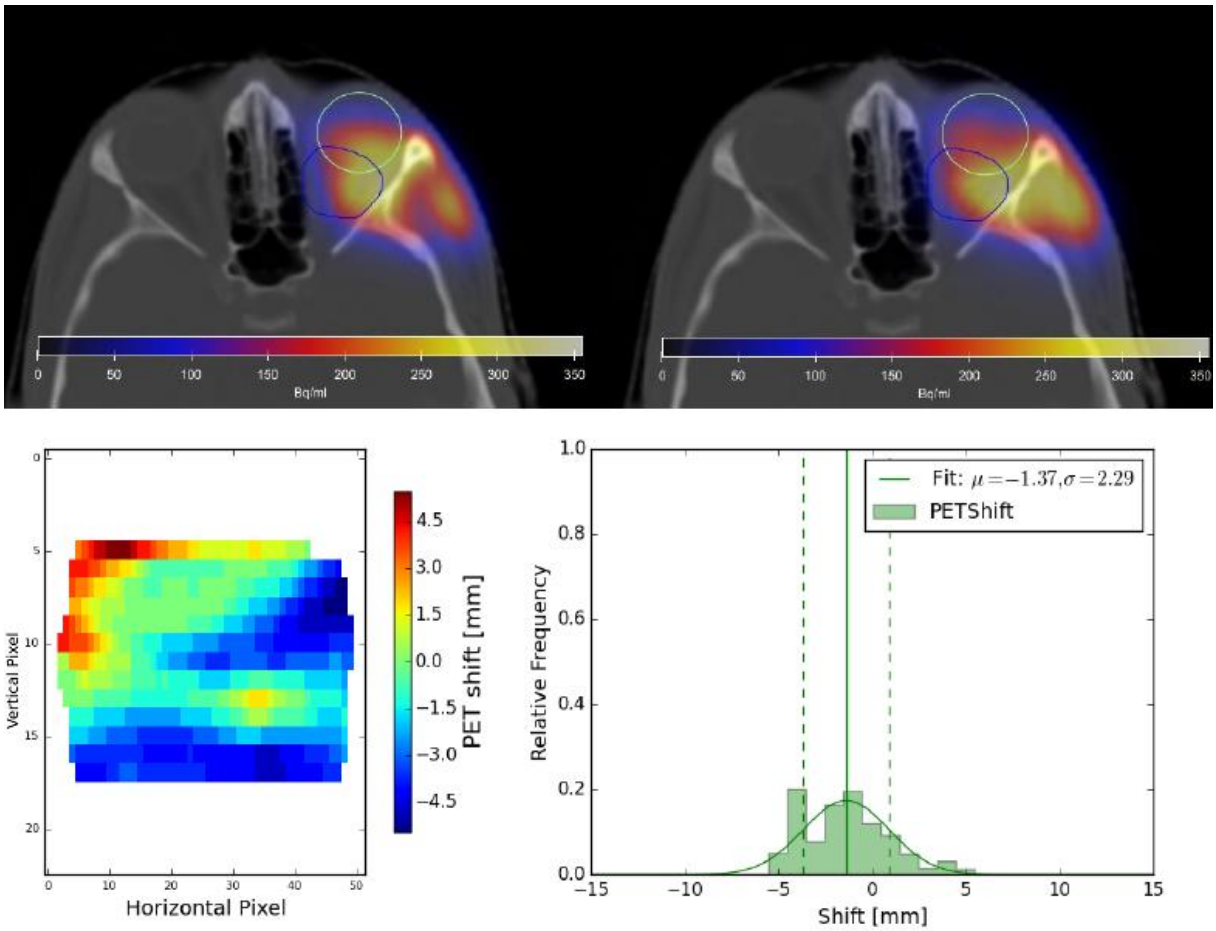

Figure 2.17: PET predictions from MC FLUKA on measured CT (from acquired PET/CT) (top panel left) and PET/CT measurement (top panel right) for a patient case, and corresponding analysis of the PET range difference through a BEV map (bottom left) and associated histogram (bottom right) (Handrack 2016).

2.9. Summary - towards “helium therapy”

This Chapter as introduced the physical and biological rationale for particle therapy as well as the description of the HIT facility, where the experimental work presented in the next chapters has been achieved. As previously stated in section 2.1, other ions than the clinically used protons and carbon ions have already been explored clinically back in the 50’s to 90’s at the Berkeley institute (Lawrence *et al* 1964, Kaplan *et al* 1994, Char *et al* 1998). However such treatments were not relying on the latest evolution of radiotherapy and particle therapy, featuring: (1) the introduction of the patient 3D geometry for radiotherapy treatment planning (Dobbs *et al* 1983), (2) the development of inverse planning algorithms (Brahme 1988, Bortfeld *et al* 1990) (3) the implementation of new delivery techniques in particle therapy (e.g. fully active delivery). The general characteristics of ions are known regarding the physical and biological concepts presented in section 2.2 and 2.3, respectively. However, in order to introduce in modern clinical routine ions such as ^{4}He, new experimental measurements with the latest delivery techniques are needed in order to:

(1) compare the physical features of these “new” ions with respect to the standard protons and carbon ions, with similar, state-of-the-art delivery techniques;

(2) thoroughly validate MC predictions used for planning/dose recalculation or for database creation as in Parodi *et al* (2012);

(3) evaluate the biological properties needed for radiobiological modeling;

(4) perform treatment planning comparisons between ions for different tumor entities.

For helium ions, step (1) will be described in Chapter 3 and continued in Chapter 6. The validation of MC FLUKA predictions, step (3), will be shown in Chapter 4, and in Chapter 6 for the deployment of a novel MC-based TPS. Biological validations of different radiobiological properties (step (3)) have been enabled by the work of this thesis and are still under investigations, but the resulting RBE model proposed for planning will be used for step (4) and presented in Chapter 7, using the improved simulation framework presented in Chapter 5. Chapter 8 will then conclude the thesis with an outlook to the next steps toward helium ion therapy including new biological experiments (cells, animals), the improvement of the computational tools (e.g. MC improvements, new analytical TPS) as well as the possibility of in-vivo range verification with PET.

Chapter 3. Experimental dosimetric comparison of ^{1}H, ^{4}He, ^{12}C and ^{16}O scanned ion beams at HIT

In this chapter, a thorough experimental comparison of the different ions available at HIT is performed, highlighting potential advantages of helium ions for therapy. The database obtained from all the reported measurements was a necessary step in order to perform the validation of the dose predictions from the Monte Carlo code FLUKA for helium ions, as presented in Chapter 4. The newly obtained dosimetric measurements were also used to refine the FLUKA simulations of the remaining different ions of HIT. The work presented in this chapter has been submitted for publication (Tessonnier *et al* 2017a).

3.1. Background

Since the first clinical applications of ion beams (mainly protons and helium ions) to radiation therapy half a century ago at Lawrence Berkeley Laboratory (LBL), the interest for particle therapy has grown considerably. Currently, there are roughly sixty facilities in operation (*www.ptcog.ch* 2016) using either carbon ions (10 centers) or protons (52 centers). The rationale for implementing particle therapy over conventional photon radiotherapy stems from the favorable physical and biological properties. The increased ionization density, especially enhanced at the end of the beam range in the so-called Bragg peak (BP), theoretically allows for a better dose conformation to the tumor, while optimally sparing surrounding healthy tissue (Schardt *et al* 2010). Moreover, the higher linear energy transfer (LET) of ions in comparison to photons offers radiobiological benefits, especially in terms of a selectively enhanced relative biological effectiveness (RBE) within the Bragg peak for ions heavier than protons.

At HIT, additionally to the clinically used protons and carbon ions beams, two others beam species are available for physical and biological research: ^{4}He and ^{16}O ions. Interest in using these particles for clinical purposes increased over the last decade, as reflected in the number of recent publications comparing physical and biological features. Most studies are based either on Monte Carlo simulations (Kempe *et al* 2007, Kantemiris *et al* 2011, Burigo *et al*

2015) or analytical models (Fuchs *et al* 2015, Krämer *et al* 2016), providing comparisons of the physical dosimetric characteristics or biological effects when coupled with biological models. Preclinical planning studies based on analytical dose calculation algorithms have also been recently published (Grün *et al* 2015, Knäusl *et al* 2016).

Helium ions, used successfully during the Berkeley trial for patient treatment (Castro *et al* 1997), possess properties in between proton and carbon ions. Compared to protons, they are expected to offer improved dose conformation to the target due to reduced lateral scattering and to exhibit a higher RBE. In comparison to carbon ions, helium ions afford increased sparing of the healthy tissue located behind the tumor, which can be mainly attributed to the reduced fragmentation tail. On the other hand, oxygen ions exhibit an even higher LET than carbon ions, thus enabling a lower oxygen enhancement ratio and a higher efficiency against hypoxic tumors (Scifoni *et al* 2013). Experimental dosimetric characteristics of proton beams for active and passive delivery can be found in the literature (Pedroni *et al* 2005, Parodi *et al* 2012, Würl *et al* 2016, Grassberger *et al* 2015) for depth and lateral dose distributions as well as for carbon ions (Schwaab *et al* 2011, Inaniwa *et al* 2014, Tessonnier *et al* 2016). However, compared to the relatively well-established proton and carbon ion therapy, only few dosimetric studies are available for helium (Lyman and Howard 1977, Krämer *et al* 2016) and oxygen ions (Kurz *et al* 2012) to validate the different proposed calculation models. The acquisition of new dosimetric data is thus essential to provide validated inputs for treatment planning systems in preparation for radiobiological experiments which aim to assess radiobiological properties and validate available biological models (Krämer *et al* 2016, Mairani *et al* 2016a, Dokic *et al* 2016). The combination of these dosimetric data with radiobiological information will enable experimentally validated treatment planning studies for clinical evaluation of the treatment of choice in different anatomical locations.

We present in this chapter quantitative comparisons of the dosimetric characteristics of protons, helium, carbon and oxygen ions from recently acquired data in a facility using an active beam delivery. The selected data, completing the description of all ion species available at HIT, feature depth dose distributions (*ddds*), lateral profiles and their single or double Gaussian parametrization, as well as dosimetric characteristics of spread-out Bragg peaks (SOBP). This study aims to provide a fundamental set of data for validation of dose calculation models.

3.2. Material and Methods

3.2.1. Pencil-Beam - Depth dose distributions

3.2.1.1. Reference measurements

Pencil-beam *ddds* were acquired in a clinical room of HIT. Measurements were performed with the PeakFinder (PKF) water column (PTW, Freiburg) equipped with two large parallel plane ionization chambers (ICs, radius 4.08 cm) at a reference voltage of 400V, allowing for acquisition of laterally integrated *ddd* with sub-millimetric precision (Karger *et al* 2010, Sanchez-Parcerisa *et al* 2012, Kurz *et al* 2012). For all acquired *ddds*, the step size in the BP region was set to 0.05 mm. The PKF was set right after the nozzle, as described in the work of Sanchez-Parcerisa *et al* (2012), and the absolute position in water was retrieved as if the beam was impinging on water from vacuum, i.e., by correcting for the energy loss in the vacuum window, beam monitor system and air gap of the HIT beamline. According to Sanchez-Parcerisa *et al* (2012), the achievable BP accuracy is estimated to be better than 0.05 mm, though estimated at 0.1 mm by manufacturer. Furthermore, the reproducibility was assessed by repeating a reference measurement for the highest carbon ion beam energy over the

measurement period of four non-consecutive days and in two clinical rooms. The reproducibility was found in the same range as the accuracy presented by Sanchez-Parcerisa *et al* 2012 with a value of about 0.05 mm.

The energy library of the HIT synchrotron foresees 255 discrete energies for protons, helium (^{4}He) and carbon ions (^{12}C), and 205 for oxygen ions (^{16}O), with energy range of [48.12-221.05 MeV/u], [50.57-220.51 MeV/u], [88.83-430.10 MeV/u] and [103.77-430.32 MeV/u], respectively. A total of 10 discrete energies for protons, helium and carbon ions, and 8 for oxygen ions, due to the restricted energy range, were chosen for this study. The datasets common to all ions shared a similar energy index from the energy tables, thus corresponding to similar range in water, with less than 2 mm difference in BP position. Details about the chosen energies are presented in table 3.1. The irradiation consisted in the delivery of quasi-monoenergetic beams along the central axis, with an initial energy corresponding to the selected index. Irradiations were performed with clinical-like lateral beam sizes (foci). For protons and helium ions, the smallest focus (focus index 1) was used, which exhibits a full-width at half-maximum (FWHM) size in air at isocenter without ripple filter (RiFi) of [32.4-8.1 mm] (Parodi *et al* 2012) and [18.6-4.9 mm], respectively, in the energy range above mentioned. For carbon and oxygen ions, focus index 3 was chosen, with FWHM values without RiFi of [12.1-7.8 mm] (Parodi *et al* 2012) and [13.1-10.1 mm], respectively, in the selected energy range. However, as evaluated in Kurz *et al* (2012), the focus size does not influence on the BP position. The beam intensity was set to $3.2 \cdot 10^{8}$, $8.0 \cdot 10^{7}$, $1.0 \cdot 10^{6}$ and $4.0 \cdot 10^{6}$ particles per second, respectively, for protons, helium, carbon and oxygen ions, corresponding to the same intensity index (intensity 4) in the HIT accelerator libraries. This intensity allowed staying in the same charge measurement range of the PKF electrometer for all ions and energies, preventing from charges overflow and ensuring a good signal quality. Measurements were performed with and without RiFi, from an absolute depth in water of 16 mm to at least 20 mm after the BP position.

The position of the BP was found by fitting the region of the *ddd* above 85% of the maximum dose with a 4th order polynomial. In a second step, as in Kempe *et al* (2007) and Bortfeld (1997), the distal range 80% (R_{80}), corresponding to the distal position of the *ddd* reaching 80% of the maximal dose was extracted from linear interpolation and evaluated as a function of the initial beam energy. The other parameters of interest for all *ddds* (with or without RiFi) were:

- the Peak-width 80% (PW), corresponding to the distance in mm between the proximal and the distal positions in water of the dose level 80%,
- the entrance-to-peak ratio (EPR), corresponding to the ratio of the peak dose relative to the entrance dose at 16 mm in water,
- the distal fall-off, corresponding to the distance in mm between the positions of the distal 80% and 20% dose fall-offs in water,
- the tail-to-peak ratio, corresponding to the ratio of the dose in water 10 mm after the BP position, relative to the peak dose.

These *ddd* parameters were evaluated as a function of their corresponding R_{80} for each ion/energy combination without RiFi. Furthermore the range shift and PW changes introduced by the RiFi were analyzed by comparing the corresponding parameters with and without RiFi.

Energy Index	Ion	Energy [MeV/u]	RiFi	Voltage [V]	Study
6	p	54.19	w / wo	400	*ddds*
	He	56.44			
	C	100.07			
	O	117.20			
30	p	78.30	w / wo	400	*ddds*
	He	79.78			
	C	145.47			
	O	171.03			
33	p	80.90	wo	100, 200, 300, 400, 500, 600	*CCE*
	He	82.33			
	C	150.42		50,100,150, 200,250, 300,350, 400, 500, 600	
	O	176.88		100, 200, 300, 400, 500, 600	
60	p	101.90	w / wo	400	*ddds*
	He	103.05			
	C	190.75			
	O	224.84			
90	p	121.95	w / wo	400	*ddds*
	He	122.93			
	C	229.76			
	O	271.59			
120	p	139.84	w / wo	400	*ddds*
	He	140.71			
	C	264.95			
	O	313.96			
150	p	156.35	w / wo	400	*ddds*
	He	157.03			
	C	297.79			
	O	353.56			
152	C	299.94	wo	50,100,150, 200,250, 300,350, 400, 500, 600	*CCE*
	O	356.20		100, 200, 300, 400, 500, 600	
180	p	172.11	w / wo	400	*ddds*
	He	172.28			
	C	329.44			
	O	391.82			
205	O	430.32	w / wo	400	*ddds*
210	p	191.18	w / wo	400	*ddds*
	He	190.85			
	C	368.21			
240	p	211.42	w / wo	400	*ddds*
	He	210.92			
	C	409.97			
255	p	221.05	w / wo	400	*ddds*
	He	220.51			
			wo	100, 200, 300, 400, 500, 600	*CCE*
	C	430.10	w / wo	400	*ddds*
			wo	50,100, 200, 300, 400, 500, 600	*CCE*

Table 3.1: Details of the depth dose distribution (*ddd*) measurements: irradiation parameters and PeakFinder settings. *CCE* stands for charge collection efficiency and *w/wo* for with/without. The energy represents the nominal energy from the HIT accelerator library. *p* stands for protons, He for helium ions, C for carbon ions and O for oxygen ions.

3.2.1.2. Charge Collection Efficiency

The charge collection efficiency (CCE) of the PKF was investigated as in Kurz *et al* (2012) for three energies within the therapeutic range of each ion. Two different power supplies were used: the dedicated power supply of the PKF (maximum 400V) and an external one (up to 600V). The combinations of voltage/ions used to investigate the CCE are shown in table 3.1. The saturation charge Q_{sat} used to estimate the CCE in the reference measurements (400V) is evaluated by fitting the inverse of the charge Q collected at a voltage V with either $1/V$ or $1/V^2$ (Podgorsak 2005), and extrapolating this relationship to zero. The uncertainty on the measured charge at 400V is evaluated from two measurements at 400V with the reference power supply and a third measurement with the secondary one. The CCE is defined as the ratio between the charge Q at 400V and the evaluated Q_{sat}. The analysis for each energy and ion was performed on different comparable subsets of the *ddd*: the plateau region, the peak region, or the entire *ddd*.

3.2.2. Pencil-Beam – Lateral dose profiles

The evaluation of the lateral dose profiles was performed in a water phantom (Karger *et al* 1999) for three energies in the therapeutic energy range: [80.90 - 157.43 - 221.06 MeV/u], [82.33 - 158.08 - 220.51 MeV/u], [150.42 - 299.94 - 430.10 MeV/u] and [176.88 - 356.20 - 430.32 MeV/u] for protons, helium, carbon and oxygen ions, respectively. For each ion, these energies have a comparable range in water (except for the highest energy of oxygen ions). As described in Schwaab et al (2011) and as it will be described in detail in Chapter 5, lateral profiles were measured horizontally, perpendicular to a vertical scanned line irradiation. Each irradiation plan was composed of 101 pencil beams centered horizontally at the isocenter, and ranging from -50 to +50 mm vertically with a step size of 1 mm. The irradiation of these vertical lines was performed in the HIT experimental room, using the HIT raster scanning system (Haberer *et al* 1993). The smallest foci for every ions were used, corresponding to a FWHM in air at isocenter of [19.6 - 10.7 - 8.1 mm], [11.3 - 6.3 - 4.9 mm], [6.5 - 3.9 - 3.4 mm] and [5.4 - 3.1 - 2.7 mm] for protons, helium, carbon and oxygen ions respectively, at the above given initial beam energies. The water phantom was positioned with its entrance window at the isocenter. The 24 motorized pinpoint ICs (PTW, 0.030cm^3) are arranged in a block of 6 rows in depth, separated by 10 mm one from each other. In each row, 4 ICs are aligned horizontally, with a distance of 12 mm between the ICs. From one row to another, the ICs are shifted horizontally by 6mm, to avoid shadowing. The first two rows are separated vertically by 7 mm from the next two rows, the latter being separated also by 7 mm from the last two rows. This geometric arrangement allows to record data for each irradiation at 4 different lateral points for 6 different positions in depth. After each line scan, in order to complete the profile, the block was moved 2 mm horizontally. After 6 irradiations, profiles were completed for a lateral extension of 46 mm, either from -15 mm to 31 mm or -21 to 25 mm, depending on the row. The block was then moved further in depth and the same procedure was repeated. For each energy and ion, profiles were acquired in depth from about 16 mm in water to positions 30 mm after the BP. The number of particles was adapted for every plan in order to acquire one full measurement in one synchrotron extraction cycle, leading to doses in the high dose region of about 1-2 Gy.

As described in Schwaab *et al* (2011) and Parodi *et al* (2013), a lateral distribution can be as approximated by a double Gaussian distribution (Pedroni *et al* 2005) with the narrow Gaussian representing the primary core and the broad Gaussian the secondary halo:

$$d(x,y) = n \times \left[\frac{1-w}{2\pi {\sigma_1}^2} \times e^{-\frac{(x-sh)^2}{2{\sigma_1}^2}} + \frac{w}{2\pi {\sigma_2}^2} \times e^{-\frac{(x-sh)^2}{2{\sigma_2}^2}} \right], \quad (3.1)$$

assuming a y value at 0 for the line irradiation, with *d* being the relative dose, *x* the position of the lateral profile, σ_1 and σ_2 the widths of the narrow and broad Gaussians respectively. *w* stands for the relative weight of the two Gaussians, *n* is a normalization factor and *sh* is a potential shift to the central position due to position uncertainties of the IC block, the water tank or the beam position. This kind of double Gaussian parameterization of the ions lateral dose profiles is implemented in the clinical treatment planning system (TPS) of HIT, based on single spot Monte-Carlo simulations for protons and carbon ions (Parodi *et al* 2013), with the Monte-Carlo code validated beforehand against line profile measurements to remove positional uncertainties of single spot measurements.

Every profile was processed with ROOT (root.cern.ch), using the MINUIT minimization package with a least square optimization. The fitting weights, as described in Schwaab *et al* (2011), were defined as $1/(\sqrt{d}/100)^2$, with *d* the measured dose. A first optimization was performed to retrieve the shift for every profile. This procedure allows restricting the profile values to lateral positions within +/-25 mm, ensuring similar lateral range for every profile and subsequently less variation in the retrieval of the double Gaussian parameters. During the second optimization pass, dose profile points with less than 0.1% of the maximum dose of the Bragg curve (1-2 Gy) were discarded, avoiding low dose noisy data and ensuring a correct convergence of the optimizer. As starting values before the second optimization for the first depth, σ_1 was initialized as the width at isocenter expected from the accelerator library, σ_2 was set to 0 with a weight *w* equal to 0. For all the next depths the initialization values were taken from the values obtained in the previous depth. As described in Parodi *et al* (2013), for light ions, σ_1 was kept constant after 35% of the distal dose fall-off, determined from the *ddd* measurements. In order to have a fair comparison between the evolution of the double Gaussian parameters along the depth in water for the different ions, the extracted σ values were corrected for the initial beam size which changes from ion to ion. To this purpose, the σ_1 value at 0 cm depth, $\sigma_{1\text{-}0cm}$ was estimated with a linear fit from the first measurement points, and then quadratically subtracted from the fitted σ_1 and σ_2 values.

$$\sigma_{corr}(z) = \sqrt{\sigma(z)^2 - {\sigma_{0cm}}^2}, \quad (3.2)$$

This approach yields σ_{corr}, the Gaussian width (σ_1 or σ_2) corrected for the beam width at isocenter, and can be interpreted as the evolution along the depth *z* of an infinitely narrow beam impinging on the water tank.

A simpler description may be obtained with a single Gaussian parametrization instead of the double Gaussian function. After normalization to their local maximum, only the profile data values exceeding 20% of the local maximum are kept, in order to properly describe the main Gaussian core:

$$d(x,y) = n \times \frac{1}{2\pi {\sigma_0}^2} \times e^{-\frac{(x-sh)^2}{2{\sigma_0}^2}}, \quad (3.3)$$

assuming a y value at 0 for the line irradiation, with *d* being the relative dose, *x* the position on the lateral profile σ_o the width of the Gaussian, *n* a normalization factor and *sh* the shift to the central position. As described previously, $\sigma_{0\text{-}0cm}$ is estimated and subtracted quadratically to σ_0 to ensure a fair comparison between the ions.

3.2.3. Spread-Out-Bragg-Peak

To evaluate the impact of the ion properties on a higher level of complexity compared to pencil-beam situations, SOBP plans were created. The analytical TPS TRiP98 (Krämer et al 2000, Krämer and Scholz 2000) was used to create these plans. The clinical database for protons and carbon ions is relying on previous works (Parodi *et al* 2012, Parodi *et al* 2013), while for oxygen ions the pre-clinical database is based on the work described in Kurz *et al* (2012). For helium ions, a pre-clinical database was created in this work from MC simulations based on the code FLUKA, for single spot irradiation, after an extensive validation against *ddds* similar to the approach described in Kurz *et al* (2012), as it will be described in detail in Chapter 4. The SOBP in water was prescribed to have a size of 140 mm × 140 mm × 140 mm, centered at 80 mm depth, for a planned physical dose of 1 Gy. A RiFi was used for carbon and oxygen ions. The optimization was performed only in depth. To obtain the planned SOBP lateral size, from this one-dimensionally optimized plan, a simple lateral expansion was made. Thus, within the same energy slice, every created pencil beam is delivering the same number of particles. The lateral step size between two pencil beams within one energy slice was set to 2 mm, inferior to 1/3 of the FWHM at isocenter in air for all ions/energies. The number of energy slices was 38 for protons (from 89.91 to 116.85 MeV/u), 39 for helium ions (from 89.64 to 116.58 MeV/u), and 20 for carbon (from 173.63 to 223.56 MeV/u) and oxygen ions (from 204.44 to 264.16 MeV/u). The irradiation was performed in the experimental room of HIT with an active beam delivery system.

The dosimetric characterization was performed in the water tank described above (cf section 3.2.2), positioned with its entrance window at the isocenter. Measurements were carried out both in depth and laterally. In the distal fall-off region the step size in depth for each measurement was about 1 mm. For the lateral measurement, 11 lateral profiles were acquired with at a distance of 10 mm in depth. In the lateral fall-off region the lateral step size was about 1 mm.

In the depth dose measurements several parameters were analyzed: the entrance-to-plateau ratio (with the entrance dose taken at 16.7mm depth), the SOBP size (between the position of the proximal and distal 90% dose), the distal fall-off (R_{20}-R_{80}) and the tail-to-peak ratio (with the tail defined at 10 mm after R_{90}). Some other dosimetric properties were investigated to verify the quality of the irradiation with measurements done inside the SOBP, such as the homogeneity (ratio between the minimum and maximum dose in the SOBP), the mean dose and its standard deviation. The lateral fall-off, defined as the distance between the 20% and 80% doses of the normalized lateral profile, was investigated as a function of the depth in water. In the SOBP, the lateral sizes of the treated- (receiving at least 90% of the prescribed dose) and irradiated- (receiving at least 50% of the prescribed dose) volume were compared.

3.3. Results

3.3.1. Pencil-Beam - Depth dose distributions

3.3.1.1. Charge collection efficiency

Prior to analyzing the results and comparing the *ddd* characteristics, the CCE of the PKF chambers for the different ions were evaluated. The dependencies on *1/V* and *1/V²* as a function of *1/Q* were investigated thoroughly for carbon ions, as in Kurz *et al* (2012) for oxygen ions. Figure 3.1 presents the inverse of the collected charge *Q*, in the peak region, for low energy carbon ions (150.42 MeV/u) as a function of *1/V* (left panel) or *1/V²* (right panel) together with the linear fit for *V* values above 150V (in the near saturation region with CCE>0.97) or for the entire voltage range. In the lower panel the CCE is displayed as a function of *V*. The adjusted R² was evaluated for the data in the near-saturation or the entire voltage range. The adjusted R² is defined as:

$$R_{adj}{}^2 = 1 - \frac{SS_{res}/(n-p-1)}{SS_{tot}/(n-1)}, \tag{3.4}$$

$$SS_{tot} = \sum_i (y_i - \bar{y})^2, \tag{3.5}$$

$$SS_{res} = \sum_i (y_i - f_i)^2, \tag{3.6}$$

with R^2_{adj}, the adjusted R², *n* the number of collected data, *p* the number of variable of the fit. SS_{tot} is the total sum of squares (linked to the data variance) with y_i the charge *Q* at either *1/V* or *1/V²* and $\bar{y}$ the mean of the charge on the *n* data. SS_{tot} is the residual sum of squares with f_i the predicted charge by the model at either *1/V* or *1/V²*.

Fitting on the entire *V* range [50V-600V] was giving low agreements with the data on the near saturation region, with an adjusted R² between [0.17-0.92] for the *1/V* and *1/V²* dependencies. While fitting only in the near saturation region, adjusted R² showed better results with values between [0.96-0.99]. The linear fit on *1/V²* showed the best agreement (R²>0.98) and was kept for the complete analysis of the CCE. As mentioned by Kurz *et al* (2012), the dependencies on *1/V* and *1/V²* are not purely linear, with a probable contribution of initial and general recombination (Palmans *et al* 2006). The results of the analysis are presented in table 3.2. All CCE are above 0.99. The uncertainty on the CCE was evaluated to be at maximum 0.4%. This finding ensures fair comparisons of the dosimetric properties of the ions while using the PKF as detector, as reported in the following sections. In the peak regions, the CCE is found lower for heavier ions due to reduced lateral and longitudinal straggling and superior ionization density. For low energy ions, reduced longitudinal straggling is expected, and consequently, a higher ionization density, leading to lower CCE. This result was anticipated considering the relatively lower range of low energy ions in water. This is particularly true for high-LET particles such as carbon and oxygen ions. As the CCE for protons was found higher than 0.999 in the peak region for the lowest energy investigated, no measurements were performed at higher energies. Compared to the peak region, the lower LET in the plateau region gave values of CCE even closer to unity. The data presented in Kurz *et al* (2012) were evaluated in the near-saturation region and were in good agreement with these findings, with CCE higher than 0.99.

Ion	Energy index	*ddd* region	CCE	Ion	Energy index	*ddd* region	CCE
p	33	plateau	1.000	C	33	plateau	0.999
		peak	0.999			peak	0.993
		ddd	1.000			ddd	0.998
He	33	plateau	0.999		152	plateau	1.000
		peak	0.998			peak	0.996
		ddd	0.999			ddd	0.999
	255	plateau	0.999		255	plateau	0.999
		peak	0.998			peak	0.997
		ddd	0.999			ddd	0.999
O	33	plateau	0.998	O	152	plateau	1.000
		peak	0.991			peak	0.993
		ddd	0.997			ddd	0.999

Table 3.2: Charge Collection Efficiency: Results for the different ions, energy and Bragg curve regions investigated. The uncertainty (1 σ) on the CCE was estimated to be at maximum 0.4%

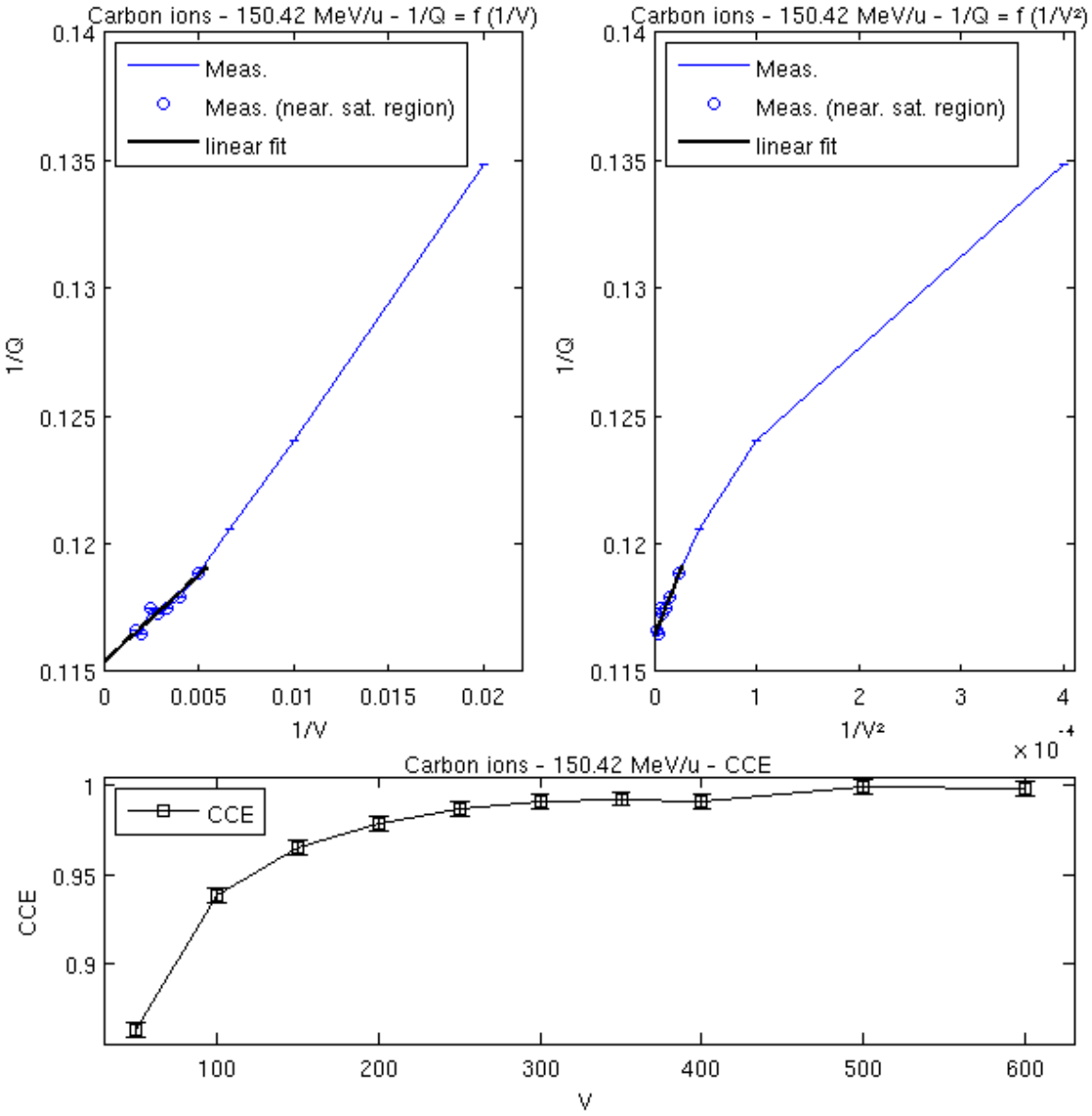

Figure 3.1: Charge Collection Efficiency for carbon ions at 80.90 MeV/u: Relation between *1/Q* as a function of *1/V* (left panel) or *1/V²* (middle panel). In the right panel, the CCE is expressed as a function of *V*. "Meas." stands for measurements, "Meas. near sat. region" stands for measurements in the near saturation region.

3.3.1.2. Distal range 80%

Figure 3.2 displays the acquired *ddds* without RiFi (left panels), together with the relationship between the distal range 80% (R_{80}) and the ion energies (right panels), for protons, helium, carbon and oxygen ions. In appendix A are presented the *ddds* with RiFi (figure A.1). The dosimetric properties of the ions are displayed as a function of R_{80} without RiFi in the following figures. The difference in R_{80} between curves with or without RiFi was consistent for every ion, with a mean value of 1.91 mm (σ = +/- 0.08 mm). At small energy a dependence was observed, with values ranging from about 1.94 mm for low beam energies (R_{80} ~ 26 mm) to 1.89 mm for higher beam energies (R_{80} ~ 312 mm).

3.3.1.3. Peak-width

The peak-widths of the depth dose distributions are shown in figure 3.3 (top right left) for every ion with or without RiFi as function of R_{80}. Without RiFi, a linear trend can be observed for all ions with a steeper slope for lighter ions. The range of observed PW is between [0.9-8.0 mm] for protons, [0.7-4.4mm] for helium ions and [0.6-2.7 mm] for heavier ones. The enlargement of the PW with increasing energy is mainly related to the range straggling effect along the path of the ions in addition to multiple coulomb scattering, leading to broader peaks at large depths. At higher energies with R_{80}>120 mm, protons and helium ions exhibit a PW/R_{80} ratio 3.5 and 1.9 times larger than oxygen ions, respectively, while carbon ions exhibit a PW/R_{80} ratio 1.1 times larger than oxygen, as seen in Appendix A (figure A.2). As a function of particle mass *M*, the PW/R_{80} results, relative to oxygen ions, suggest a relationship for protons, helium and carbon ions respectively of about $0.85 \times (\sqrt{M_O}/\sqrt{M_p})$, $0.93 \times (\sqrt{M_O}/\sqrt{M_{He}})$ and $0.97 \times (\sqrt{M_O}/\sqrt{M_C})$. These results are close, but slightly inferior, to the dependency of $1/\sqrt{M}$, with *M* the particle mass, of the range straggling width over range (Schardt *et al* 2010) dependency expected without consideration of other effects (e.g. density inhomogeneities or initial energy spread). The presence of the RiFi increases the PW due to the introduction of an additional range spread resulting from its shape. For heavy ions, the PW increases from 1.7 mm for low energy to about 1.1 mm at higher energy for carbon ions and 1.6 mm for oxygen ions. For protons and helium ions, the increase at low energy is similar to heavier ions, about 1.5 mm and 1.6 mm respectively, but decreasing to 0.2 mm and 0.6 mm at higher energies. For lighter ions, when the energy and thus the position of the BP in water increase, the effect of the initial energy spread due to the RiFi becomes less important regarding the effects of range straggling.

3.3.1.4. Entrance-to-peak ratio

The EPR, is shown in figure 3.3 (top left) for the different ion species (with or without RiFi) as a function of R_{80}. For R_{80} smaller than 52 mm and 80 mm for both measurements with and without RiFi, respectively, EPRs are discarded from the analysis, since the entrance dose value at 16 mm in water is already on the ascendant part of the BP. Without RiFi for low beam energies (R_{80} < 140 mm), the heavier ions have an advantageous EPR [16-19%] compared to protons [20-21%] and helium ions [17-19%], due to a smaller longitudinal straggling leading to a narrower PW and thus a higher BP. For energies with R_{80} >140 mm, the advantage of the heavy ions in EPR is lost due to an increase of nuclear interactions, reducing the peak height and producing buildup in the plateau, resulting in an increased EPR up to 36% for carbon ions (29% for oxygen ions at the highest energy available). The fragmentation of helium ions, associated to the enlargement of the PW, yields EPR values from 19% to 28%. Protons EPR rises from 21% to 25% at high energy. The introduction of

the RiFi, leading to a broader PW as seen previously, changes the ratio between the entrance and the peak dose. The heavier the particle, the larger is the impact on the PW, as seen previously. This yields an absolute increase in EPR values of 8% to 6% for oxygen ions at larger depth, 7% to 4% for carbon ions, 5% to 1% for helium ions and 3% to below 0.5% for protons.

3.3.1.5. Distal fall-off

The distal fall-off expressed as a function of $R_{80,}$ is shown in figure 3.3 (bottom left) for the different ions with and without RiFi. Without RiFi, the evolution of the distal fall-off shows a linear trend for every ion species from [0.5-4.3 mm], [0.3-2.4 mm], [0.2-1.7 mm] for protons, helium and heavier ions respectively. For lighter ions, due to the range straggling along the path, the distal fall-off is larger than for heavier ones. With the introduction of the additional range spread due to the RiFi, the distal fall-off increases particularly for heavier ions, where the RiFi impact is larger than the one introduced either by range straggling or multiple coulomb scattering. This increase was about [1.1-0.7 mm] for heavy ions, [0.9-0.3 mm] for helium ions and [0.8-0.2 mm] for protons, for the whole energy range. At low energies and thus shallow BP depths the impact on the distal fall-off is higher than at larger energies/depths, due to the importance of the energy spread introduced by the RiFi, compared to the one introduced by range or lateral straggling.

3.3.1.6. Tail-to-peak ratio

The tail-to-peak ratio is shown as a function of R_{80} in figure 3.3 (bottom right), for each ion species with or without RiFi. Without RiFi, the evolution of this relative dose follows a linear trend for ions with charge Z>1, due to the fragmentation of the primary beam into lighter fragments. The relative tail contribution to the dose, within the available R_{80} range, was about [1-16%] for oxygen ions, [1-14%] for carbon ions and [<0.5-4%] for helium ions. For protons, although there is no fragmentation tail due to the primary beam, the tail-to-peak ratio was nonzero for R_{80} superior to 200 mm, due to the large distal fall-off at these energies, and up to 4% for high initial beam energies. By introducing the RiFi, a maximal tail-to-peak ratio dose enhancement of 3%, 2% and <0.5% was observed for oxygen, carbon ions and the lighter ions, respectively. The main reason behind this rise is the normalization with respect to the dose in the BP, which is getting broader and smaller, as seen before for the EPR. Thus, when normalizing the tail dose to the entrance, no relevant difference was observed between the tail-to-entrance curves with or without RiFi.

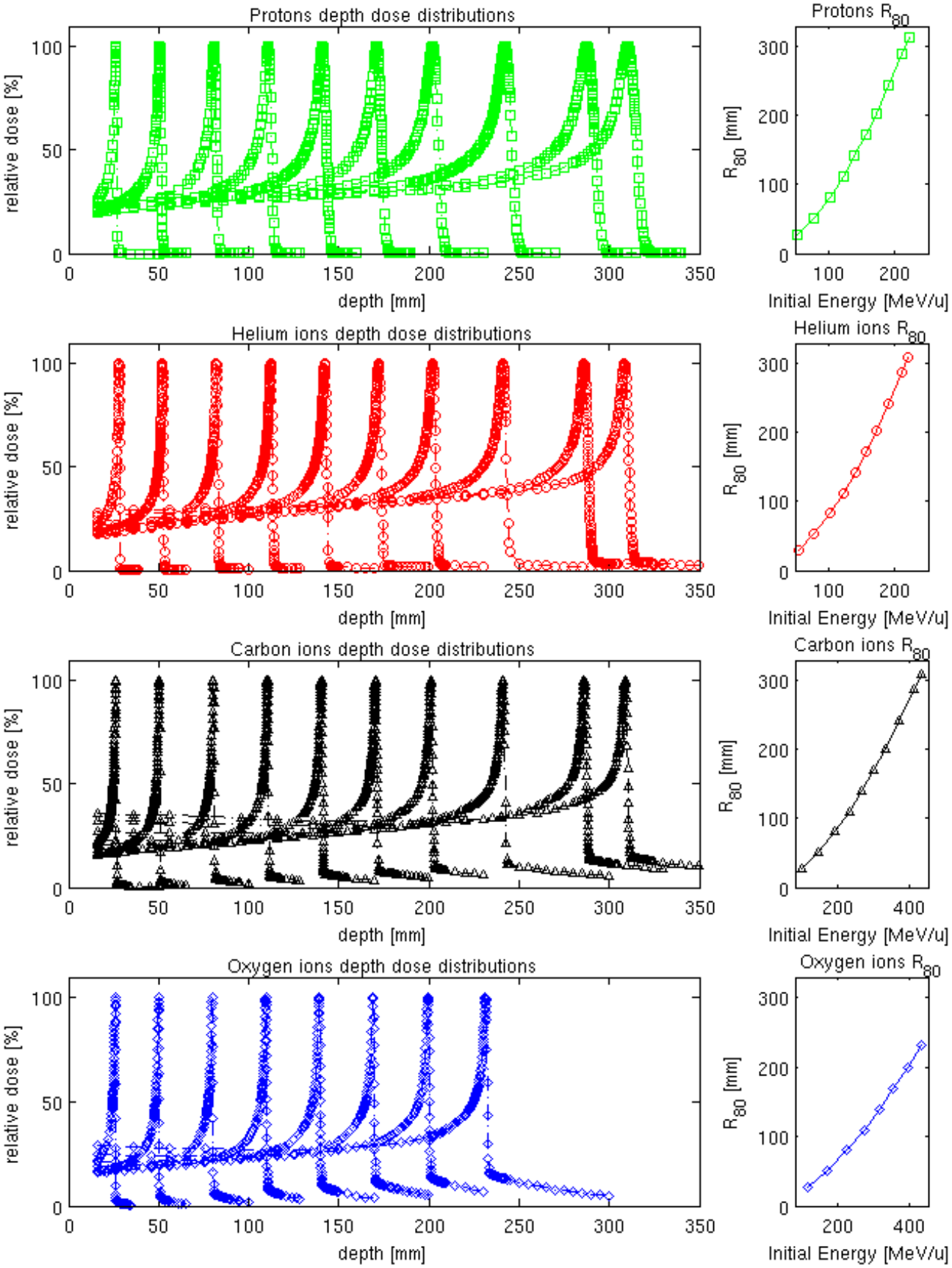

Figure 3.2: Depth dose distributions results for protons, helium, carbon and oxygen ions, respectively, from the top to the bottom panels. In the left panels the *ddds* of the ions in water, in the right panels, the dependence of R_{80} as a function of the ion energy.

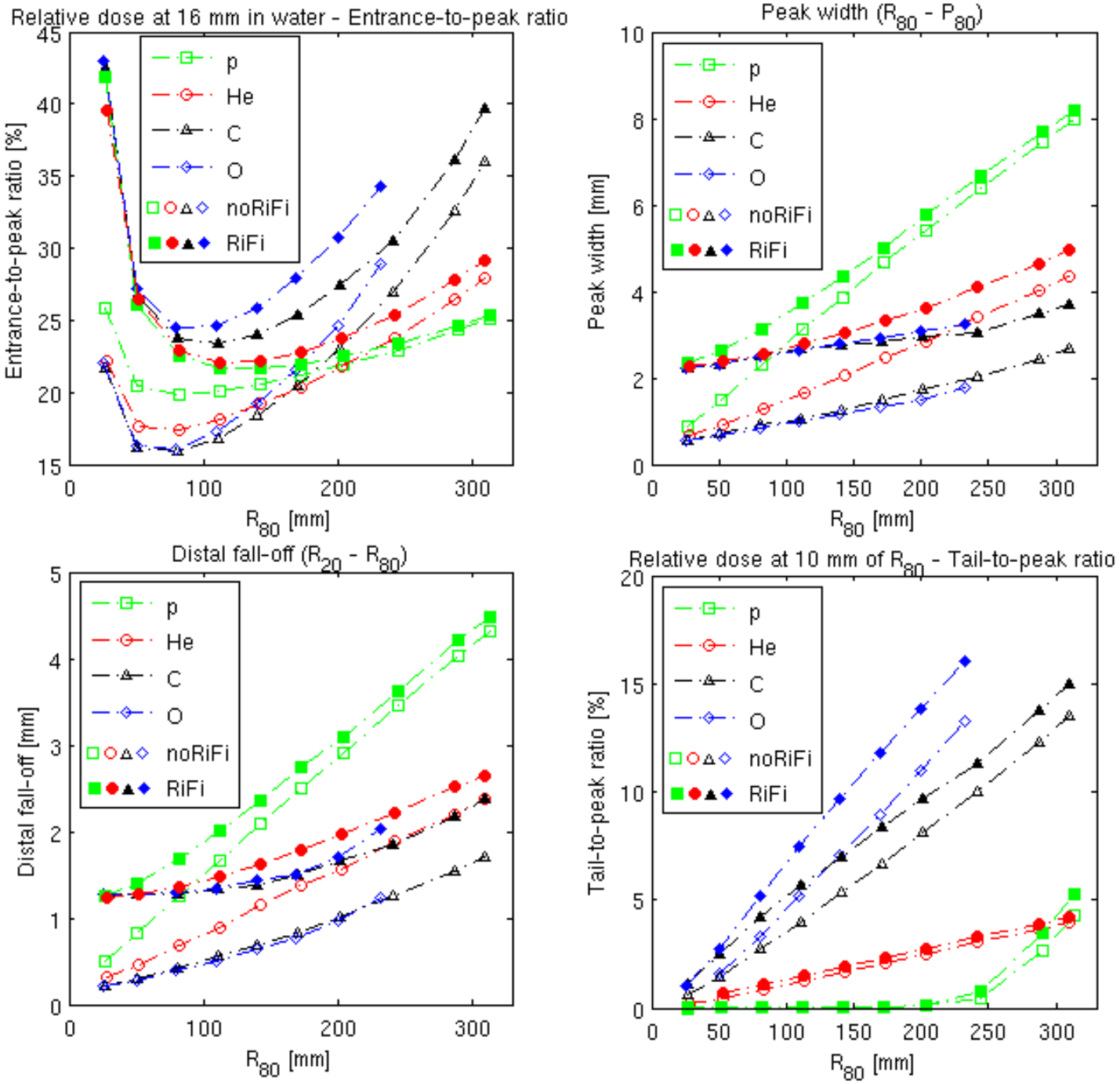

Figure 3.3: Parameters inferred from the depth dose distributions: PW (top left panel), EPR (top right panel), distal fall-off (bottom left panel) and tail-to-peak ration as a function of R_{80}. Protons are represented with squares, helium ions with circles, carbon ions with triangles and oxygen ions with diamonds. Parameters with the RiFi are shown with filled symbols, while without RiFi are not.

3.3.2. Pencil-Beam – Lateral dose profiles

Profiles measured at the entrance or near the BP position in the water tank are shown in figure 3.4 for the three energies (low, medium and high) and four ion species investigated without RiFi, together with simple and double Gaussian fits. As described in Weber and Kraft (1999), RiFi for carbon ions has only a minor influence on the lateral profiles, leading to an increase of the FWHM at isocenter for focus 1of about 1.9 and 0.3 mm for low and high energy beams, respectively. While the simple Gaussian fit allows to describe the central core of the Gaussian and the evolution of σ in depth, the double Gaussian, introduced by Pedroni *et al* (2005) and used in Schwaab *et al* (2011) for HIT data, describes these profiles more precisely. Other parametrizations reviewed in Bellinzona *et al* (2015), such as a triple Gaussian parametrization (Inaniwa *et al* 2014), could help describing the behavior of the profiles more precisely, particularly for the entrance regions and for ions with charge Z>1. In fact, the first Gaussian provides a good description of the central core dominated by multiple Coulomb scattering with small angles. The second Gaussian gives a good approximation of non-elastic interactions in water as well as elastic large-angle single scatters (defines as "halo" in Gottschalk *et al* (2015)). However, with only two Gaussians, the parametrization fails to reproduce the "spray" (Gottschalk *et al* 2015) stemming from large angle scatters from elastic interactions in the beamline and air, with an effect more pronounced for protons as it can be observed for the entrance profile at high energy (figure 3.4). Nevertheless, at larger depth, the contribution of the spray is smeared out by the importance of interaction in water (elastic/non elastic) in the lateral field extension relevant for this study.

In order to compare the evolution of the single or double Gaussian parametrization for the different ions, the width of the beam at isocenter was extracted to obtain by a subsequent quadratic subtraction the different σ_{corr} as described in 2.2. For the simple and double Gaussian parametrization, the extracted $\sigma_{0\text{-}0cm}$ / $\sigma_{1\text{-}0cm}$ and thus the corresponding $FWHM_{0\text{-}0cm}$ /$FWHM_{1\text{-}0cm}$ are compared to the nominal foci values at isocenter from the HIT accelerator library and to the values measured by the beam monitors chambers (BAMS, Beam Application and Monitoring System), subsequently converted to FWHM at isocenter. In figure 3.5 (top panels), it can be seen that for protons, helium and carbon ions, the extrapolated FWHM values from the simple and double Gaussian parametrization are similar, with the largest difference for low energies where the contribution of the second Gaussian leads to a smaller central core for $\sigma_{1\text{-}0cm}$ compared to $\sigma_{0\text{-}0cm}$. Our measurements and the ones from the BAMS are inside the tolerance of +25%/-15% accepted at HIT. The maximum deviation between upstream BAMS measurements converted to the isocenter and our data acquired in the water phantom was +10%, while the maximum difference between nominal value and measurement in the phantom was +7%. However, for oxygen ions, the values measured in this study were out of tolerance, due to the fact that the beam foci were not yet fully optimized by the accelerator team at the time of our measurement, and no information on the irradiation characteristics from the monitoring system was recorded for the highest energy. The varying absolute values of FWHM of the ions at the isocenter (e.g. 19.6 mm for protons, 5.4 mm for oxygen ions for the lowest energy), due to the different impact of scattering in the beamline, justify the need of a correction for this offset to compare the evolution of the width distributions parameters.

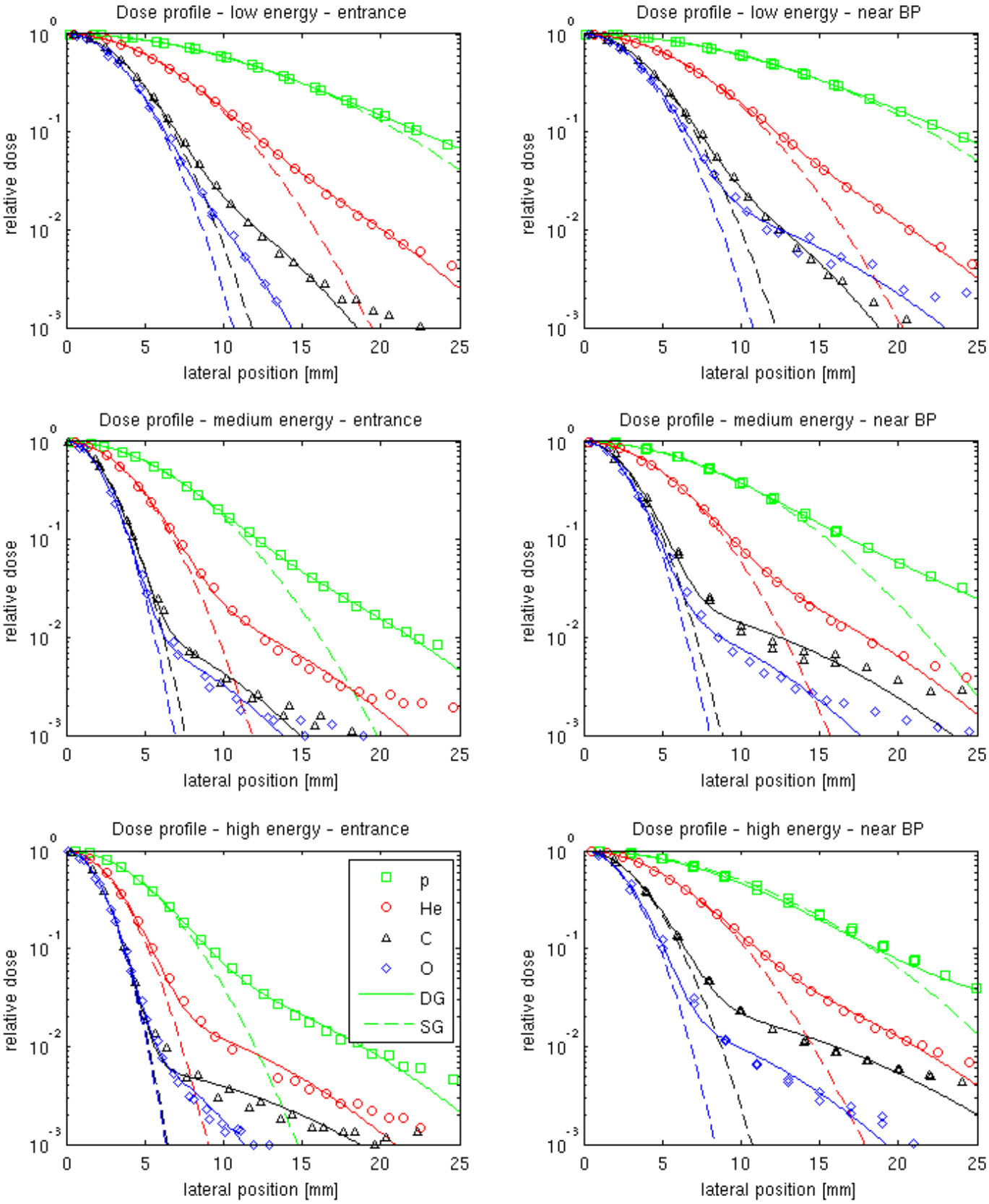

Figure 3.4: Lateral dose distribution: Protons are represented with squares, helium ions with circles, carbon ions with triangles and oxygen ions with diamonds. In solid line, the double Gaussian (DG) fits are shown, and in dashed line the simple Gaussian (SG) fits.

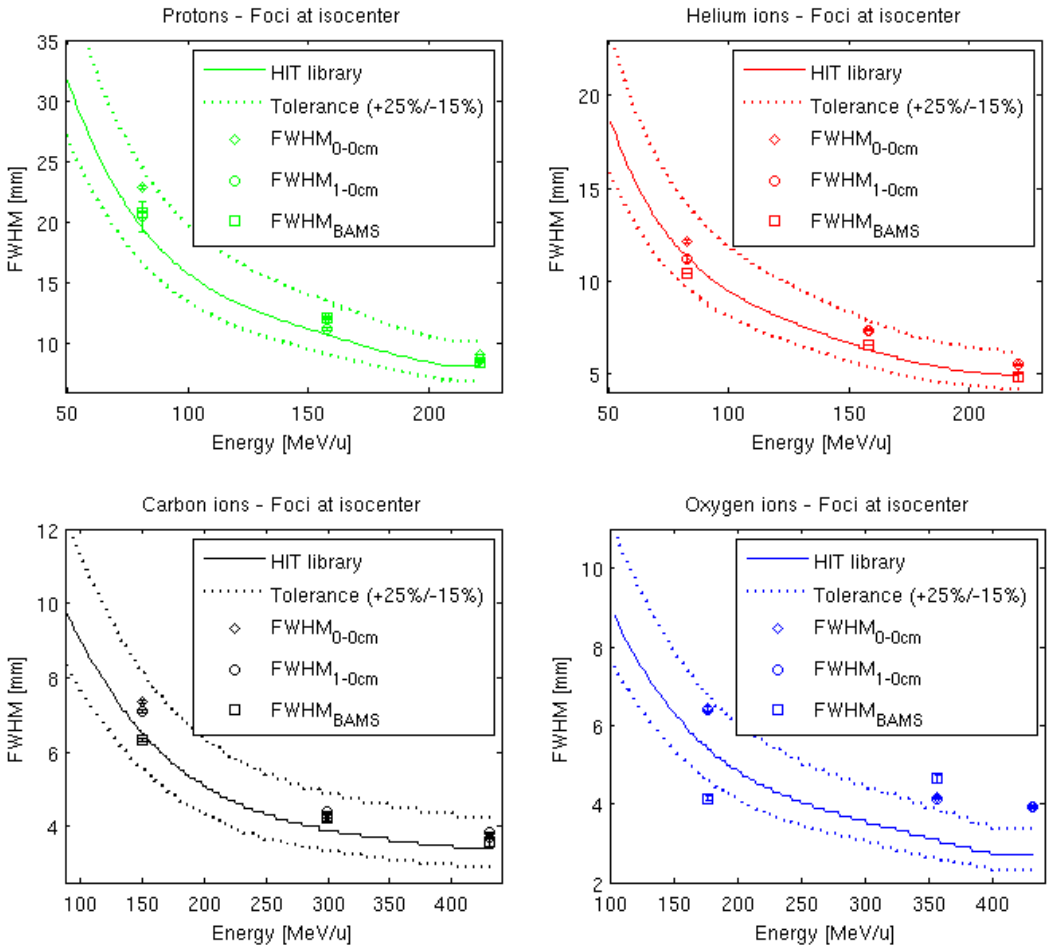

Figure 3.5: FWHM of the extracted $\sigma_{1\text{-}0cm}$ (circles), compared to the extrapolated measurements of the BAMS (squares) and the HIT foci library (solid lines, with acceptance limits as dashed lines), for protons, helium, carbon and oxygen ions, respectively from left to right.

For the single Gaussian parametrization, the evolution of σ_{0corr} is shown in figure 3.6 (left panels) for all ions, at the three investigated energies, as function of the relative depth (depth normalized to the BP position). For the medium energy, compared to the width of the clinically used carbon ions, protons and helium ions exhibit a width 3.2 and 1.7 times larger, while oxygen ions exhibit a width 1.1 times smaller, as seen in Appendix A (figure A.3). As a function of particle mass *M*, the width relative to carbon ions can be described by the following relations for protons, helium and oxygen ions respectively: $0.9 \times (\sqrt{M_c}/\sqrt{M_p})$, $\sqrt{M_C}/\sqrt{M_{He}}$, and $1.05 \times (\sqrt{M_C}/\sqrt{M_O})$. As expected, the heavier the ion, the smaller is the width of the beam, with a relation close to $1/\sqrt{M}$. After the BP, the single Gaussian describes the behavior of the secondary particles produced upstream, for ions with Z>1. For helium ions, the beam width distribution of the secondary particles was found to be larger than for carbon and oxygen ions, with a steeper increase of the Gaussian width with depth. These effects are related to the lighter fragments originating from the fragmentation of helium ions compared to heavier primary ions, and the fact that light ions produced by heavier ions are more focused in forward direction. A particular behavior of the width evolution was observed just after the BP, with a drop of σ_{0corr} that can be interpreted by the fact that only the primaries which underwent small straggling (range or lateral) remain there and lead to a smaller beam width compared to the upstream depths. Compared to σ_{0corr} values for carbon ions at the BP position (relative depth ~1), σ_{0corr} values were found to be larger for protons and helium ions by roughly [2.3, 3.4, 5.1 mm] and [0.8, 1.3, 1.8 mm], for the low, medium and high energy, respectively The width difference was below 0.3 mm between oxygen and carbon ions, except for the highest initial beam energy, where the energies were not comparable, as oxygen ions have a range of 231 mm compared to the 308 mm of carbon ions.

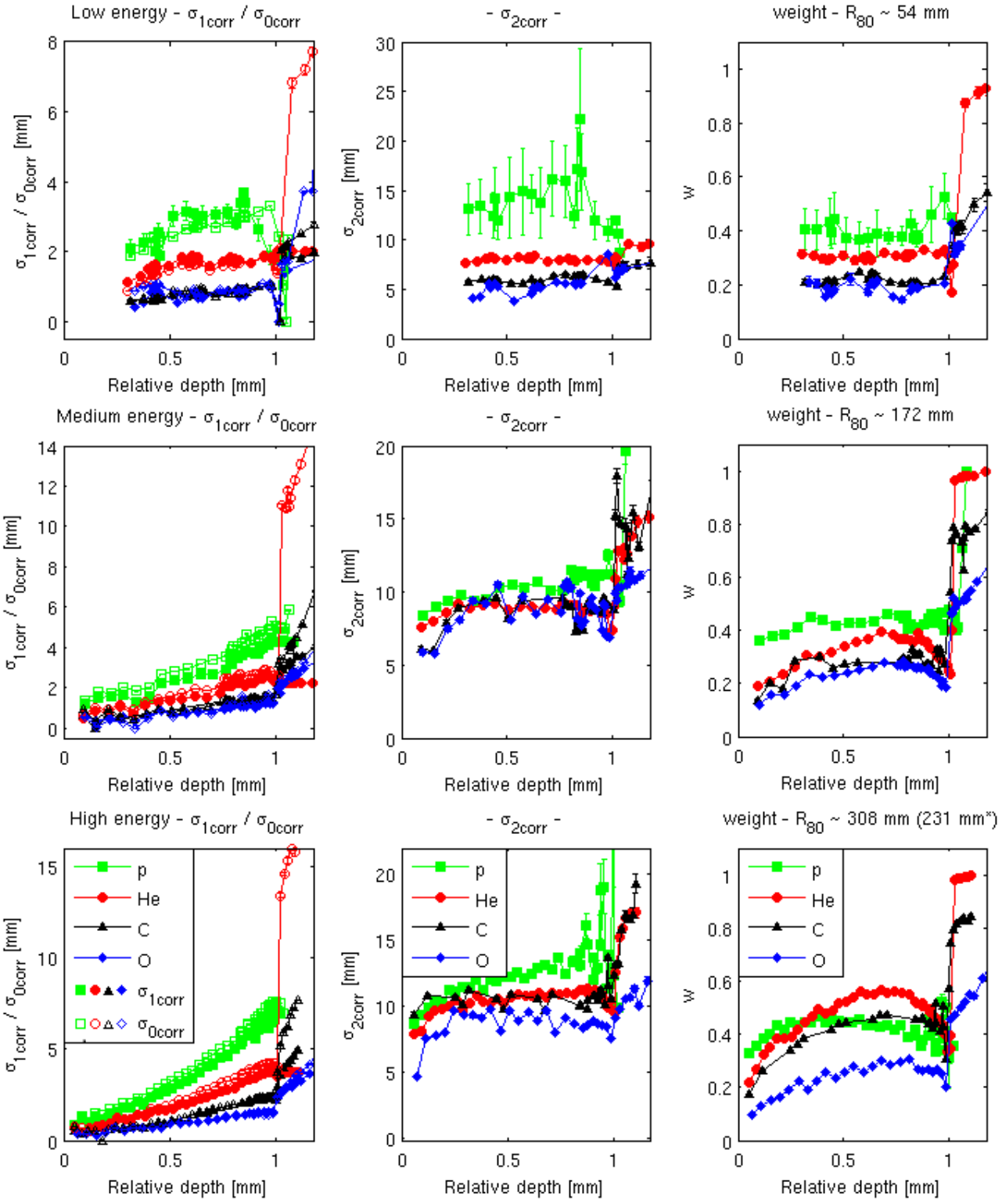

Figure 3.6: Fitted single and double Gaussian parameters: the left panels show the evolution in water of σ_{0corr} (empty symbols) and σ_{1corr} (filled symbols), the middle panels depict the evolution of σ_{2corr} and the right panel displays w for the different ions (protons with squares, helium ions with circles, carbon ions with triangles and oxygen ions with diamonds), for low, medium and high energy (top to bottom panels). The depth is normalized to the BP position. The approximate range of the ions is presented (* stands for the range of the highest oxygen energy).

Figure 3.6 presents the evolutions of the parameters of the double Gaussian parametrization for the different ions and energies investigated. The evolution of σ_{1corr} (figure 3.6 left panels) is close to σ_{0corr} before the BP. Due to the contribution of the particles contained in the second Gaussian, σ_{1corr} is slightly smaller than σ_{0corr} (maximum difference of 1 mm for high energy protons and less than 0.5 mm for all other cases). The value of σ_{2corr} (figure 3.6 middle panels) is not starting at zero, regardless of the ion, showing the impact of scattering upstream of the phantom entrance window, with higher width values for low energy and light ions. For medium and high energies, after an initial build-up (which is not visible for low energies), the values of σ_{2corr} remain stable (within the error bar), as already observed for low energies. The build-up region can be seen as the propagation of the high energy fragments produced in the entrance of the water phantom and in the upstream beamline. The plateau regions of σ_{2corr} can be interpreted as the fact that the angular distribution of secondary particles is not changing much with depth, as seen in Haettner *et al* (2013) for carbon ions. Thus, in the plateau region in the lateral field investigated and within the dose threshold set, there is an equilibrium between the contribution of secondary particles which are already spread from the entrance region and the contribution of the newly produced particles (with lower energies and a slightly broader angular distribution). The $1/\sqrt{M}$ dependency of the secondary Gaussian width is no longer valid, as it was for the primary Gaussian, due to the mixed radiation field. As seen in Haetnner *et al* (2013) and Krämer *et al* (2016), the contribution of the secondary particles is mainly due to protons and helium ions. Furthermore, the light swift ions, such as protons, from fragmentation processes of primary carbon or oxygen ions are produced with smaller angles compared to the one stemming from primary protons or helium ions. As a result, the second Gaussian component was found to be broader for protons, followed by helium ions and the heavier ions. The evolution of the weight, *w* (figure 3.6 right panels), was stable of around 40% for protons before the BP (from 35% up to a maximum of 45% at high energy), regardless of the energy, while for heavier ions *w* is increasing due to the attenuation of the primary beam and the production of secondary particles, particularly at high initial beam energies. For oxygen ions, *w* was about 11% at the entrance, rising up to 25% for low energy and up to 30% for high initial energy beams. For carbon ions, *w* was about 15% close to the entrance and up to 25% for low energy and 45% for high energy beams. For helium ions, *w* was about 27% at the entrance, rising up to 30% for low initial beam energy and 56% at high energies. The contribution of the secondary particles to the dose halo, stemming from helium ions, exceeds the one from protons at high initial beam energies, due to the increased productions of secondary protons. Finally, the contribution of the second Gaussian is not negligible for heavier ions particularly at high initial beam energies, mainly due to the production of secondary particles at large angle and their propagations in water.

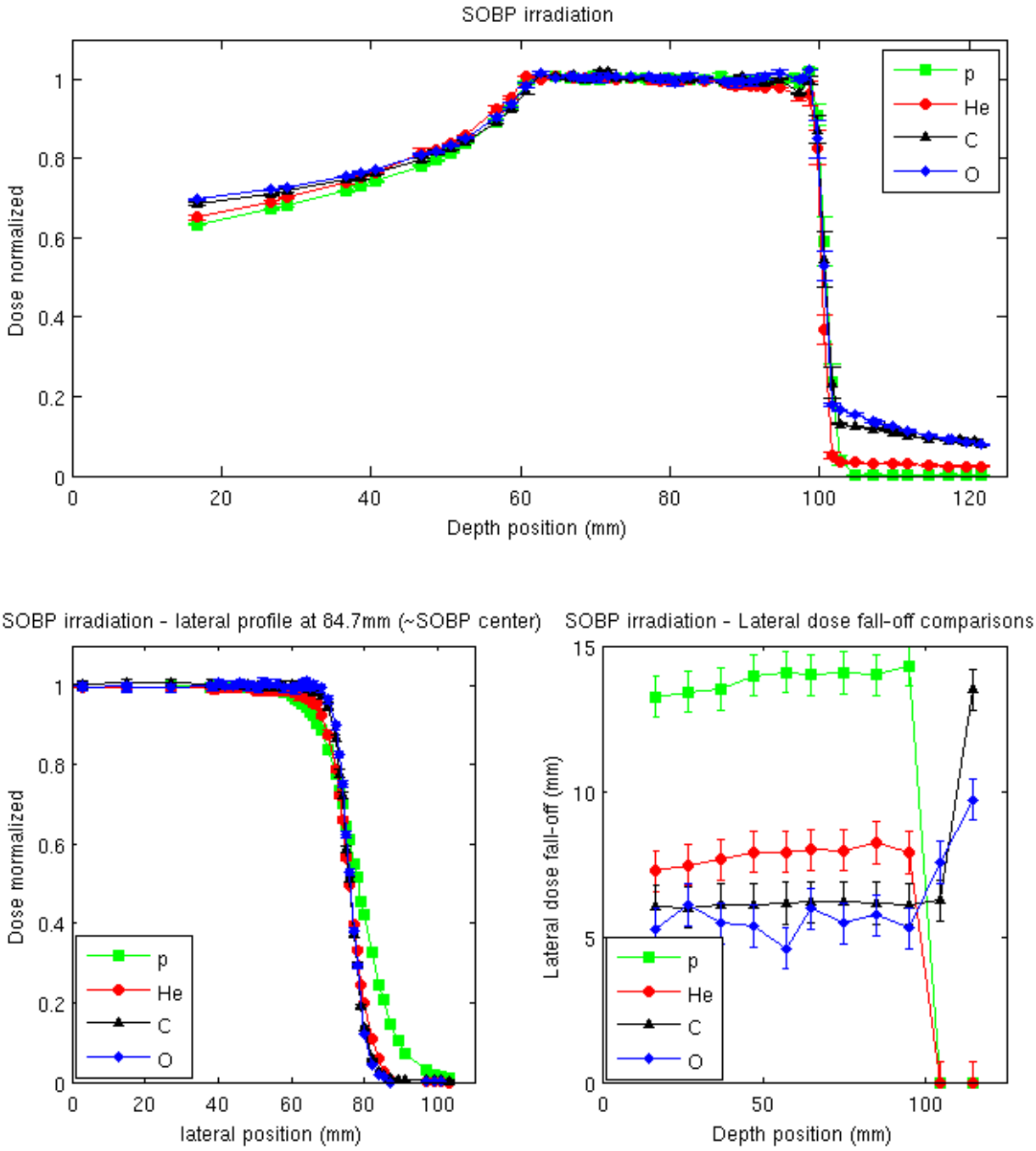

Figure 3.7: Spread-out Bragg peak: depth dose distributions (left panel), lateral dose distributions at the SOBP center (middle panel) and evolution of the lateral dose fall-off in water (right panel). Protons are displayed with squares, helium ions circles, carbon ions with triangles and oxygen ions with diamonds.

3.3.3. Spread-Out-Bragg-Peak

The mean dose measured in the SOBP region by the ICs, compared to the planned dose value of 1Gy, was -1.5% lower for protons, -1.8% for carbon ions, +4.6% for helium ions and +5.5% for oxygen ions. The reason for the larger discrepancy for helium and oxygen ions is stemming from the fact that the beam monitor calibration for these two ions was not yet completed at the time of this study. Hence, to ensure fair comparisons between the different distributions, a normalization of the data was performed, using these deviations as normalization factors. The depth and lateral dose profiles (at the entrance and center of the SOBP), together with the evolution of the lateral dose fall-offs, are shown in figure 3.7.

In table 3.3, the entrance-to-plateau ratio, the size in depth of the SOBP, the distal fall-off and the dose 10 mm after the distal range (defined as the 90% dose fall-off), the homogeneity and the standard deviation of the mean dose value inside the SOBP are shown, together with the size of the laterally treated and irradiated volume sizes.

Protons and helium ions showed favorable entrance doses compared to oxygen and carbon ions, which were about 5% higher. These results are consistent with the finding in section 3.1.4 for the EPR of heavy ions with RiFi compared the light ions without. The distal fall-offs of helium ions were found to be smaller than for the other ions, but the distal fall-off values of the different ions were rather close to each other, which is consistent with the results found in section 3.1.5. However, the results are not as separated as the ones from the water column measurements, since the measurement step size in depth here was only about 1 mm (compared to 0.05 mm of the PKF), and the sensitive volume of the pinpoint IC (chamber radius of 1.45mm) is non-negligible compared to the fall-off values. Furthermore according to Karger *et al* (1999), the uncertainty in the IC measurement position is about 0.5 mm, accounting for the step motor and effective point of measurement errors as well as the IC position in the water tank. The dose 10 mm after the SOBP was higher for heavy ions compared to light ions, with larger values than in the water column results for pencil beam-like irradiation, due to the summation of the tails of the individual peaks making up the SOBP. The size of the SOBPs were similar for the different ions, with a homogeneity <5% and a deviation to the mean dose <1%. Regardless of the calibration of the beam monitor, the helium and oxygen ions show dosimetric beam qualities comparable to the clinically used protons and carbon ions.

The lateral fall-off for protons was clearly larger than for helium ions by about 6 mm, and 8 – 8.5 mm compared to carbon and oxygen ions. While the lateral fall-off was slowly increasing with depth for protons (from 13.3 to 14.3 mm) and for helium ions (from 7.3 to 8.1 mm), the lateral fall-off was found to be between 6.1 and 6.2 mm for carbon ions and around 5.5mm for oxygen ions, due to the observed slow evolution of the primary Gaussian core (see section 3.2). In the SOBP region the difference between the treated and irradiated volume is found up to 11.0 mm for protons, 6.7 mm for helium ions, 5.0 mm for carbon ions and 4.4 mm for oxygen ions. The uncertainty of the lateral/distal fall-off, SOBP depth size is about 0.8 mm. These results are consistent with the trend found for the pencil-beam lateral fall-off results. However, it should be noted that SOBP optimization was performed in one dimension (in-depth), without intensity modulation within the same energy slice. Hence, one can expect better results in term of lateral fall-off and conformity to the initial planned lateral size with a 3D optimization, particularly for protons (Scheib and Pedroni 1992).

	Depth dose distributions						Lateral dose distributions in SOBP	
Ion	Rel. entr. dose	Size	Distal fall-off	Rel. tail dose	Homogeneity	σ	Treat. lat. size	Irr. lat. Size
p	63.4% (+/- 0.3%)	42.5 mm	1.7 mm	0% (+/- 0.03%)	3.3% (+/-1.4)	0.6%	134.6 mm +/- 1.0 mm	156.7 mm +/-0.7 mm
He	65.2% (+/- 0.9 %)	42.7 mm	1.3 mm	3.1% (+/- 0.4%)	4.7% (+/-1.4%)	0.9%	138.9 mm +/- 0.9 mm	152.3 mm +/-0.9 mm
C	68.6% (+/- 0.6%)	42.0 mm	1.5 mm	10.7% (+/- 0.2%)	3.9% (+/-1.4%)	0.8%	142.4 mm +/- 0.9 mm	152.3 mm +/-0.8 mm
O	69.6% (+/- 0.4)	42.7 mm	2.0 mm	12.4% (+/- 0.6%)	4.9% (+/-1.4%)	0.9%	143.8 mm +/-1.1 mm	156.7 mm +/-0.7 mm

Table 3.3: Spread-out Bragg peak results: For the depth dose distribution analysis: relative entrance dose (Rel. ent. dose), SOBP depth size, distal fall-off and relative dose 10 mm after the SOBP (Rel. tail dose), homogeneity between minimal and maximal dose and standard deviation in the SOBP. For the lateral dose distributions analysis inside the SOBP region: Treated and irradiated lateral size. The uncertainty on the distal fall-off, SOBP depth size is estimated at 0.7 mm.

3.4. Discussion

The results shown in this chapter (and Appendix A) give an overview over the dosimetric characteristics of all ions available at HIT, complementing previous studies (Schwaab *et al* 2011, Parodi *et al* 2012, Kurz *et al* 2012). Even if the behavior of the different ions is expected from literature (previous experiments or simulations), experimental depth dose and lateral distributions are fundamental quantities for validation of Monte Carlo codes (Parodi *et al* 2012, Parodi *et al* 2013) and analytical engines (Krämer *et al* 2000, Krämer *et al* 2016), or even for beam parametrization (Grassberger *et al* 2015, Bellinzona *et al* 2015). Compared to Kurz *et al* (2012), the CCE for all ions was found to be superior to 99% due to an improved number of data points included in this study and an evaluation only in the near-saturation region. In the near saturation region, linear fits on $1/V^2$ (continuous beam, general recombination) were showing better agreement than for $1/V$ (initial recombination for pulsed/continuous beam, general recombination for pulsed radiation). Even if a mixture of these effects due to the synchrotron beam structure is present in the measurements, as postulated by Kurz *et al* (2012), general recombination from the continuous-like spill structure seems to be dominant in the presented PKF measurements. A study from Rossomme *et al* (2016) on ion recombination strongly recommends from their results the use of corrections for *ddd* acquisition. However due to the different operating voltage of the PKF (400V) compared to the one from their study (-100V), the CCE is found high enough even in high dose region, to neglect recombination corrections. The newly measured *ddds* and lateral profiles were used to adjust the modeling of the HIT beamline and the input parameters of FLUKA simulations for phase space files generation (Chapter 5), biological dose calculations (Mairani *et al* 2016a), and creation of an experimentally validated physical database input for the analytical research TPS used for biological experiments (Dokic *et al* (2016)) with all available ions.

Compared to Schwaab *et al* (2011), the results are similar for the extracted $\sigma_{1\text{-}0cm}$ for protons, even with a different fitting software package. Carbon ions $\sigma_{1\text{-}0cm}$ are not comparable as only data with RiFi are presented in Schwaab *et al* (2011). However, less spread in the σ_2 values was observed due to the restriction in the lateral field of the values < |25|mm, leading also to lower values in this study for σ_2. The $\sigma_{0\text{-}0cm}$ values, and corresponding $FWHM_{0\text{-}0cm}$, are for protons, carbon ions and helium ions higher than the values at isocenter expected from the HIT pencil beam library. In addition to a possible daily variation of the beam spot size, this finding can be attributed to the use of a vertically scanned line instead of a single spot. While using a line, each single spot contributes to the measured profiles as it is integrated vertically. It was already noticed in Tessonnier *et al* (2016) that profiles integrated vertically are larger than profiles sampled at the middle of a single spot due to the non-single Gaussian shape of the beam at isocenter, leading to an enlargement between 0.1-0.4 mm for carbon ions and 0.5-2.5 mm for protons, as it will be also described in Chapter 5.

Measured *ddds* for protons, carbon and oxygen ions were consistent (within 0.3 mm range agreement) with the ones reported in previous studies at HIT (Parodi *et al* 2012, Kurz *et al* 2012). First *ddds* for helium ions were characterized by Lawrence *et al* (1977) at the Lawrence Berkeley Laboratory (LBL). The main features reported for 150 and 225 MeV/u ion beams, such as R_{80} and EPR, were found in good agreement with the findings of this study: R_{80} values of [150 mm – 312 mm] and EPR values of [18% - 30%] at LBL, while R_{80} [159 mm – 321 mm] and EPR [18% - 29%] for the HIT beamline energy (with extrapolation of the values for the 225 MeV/u). As found in Krämer *et al* (2016), a constant shift of about 9 mm is to be applied to match the LBL data, probably due to the Berkeley beamline and the water equivalent thickness of the detector setup not corrected for their reported range.

In terms of absolute dosimetry for SOBP scanned beam delivery, the beam monitor calibration used at HIT has recently been upgraded after completion of this study, allowing dose deviation below 3.5% for all ions and for SOBPs at different depths in water, and will be discussed in Chapter 6. Nevertheless, this does not affect the main findings of this study regarding the difference in SOBP characteristics for different ions, which seemed to be consistent with the observations from the *ddds* and the lateral dose distributions. However, it should be noted that the lateral dose fall-offs and the differences between treated and irradiated volumes could be further reduced in theory with 3D intensity modulated optimizations, allowing steeper lateral dose gradients. Such a refined approach would decrease the differences between light and heavy ions for these parameters. Nevertheless, the presented approach allows a more physical comparison of the SOBPs of the different ions, without influence of the characteristics and performances of a more complex optimizer. The dose at the entrance is particularly interesting for light ions in the case of a physically optimized SOBP, however in case of biologically optimized SOBP the physical dose in the entrance could drop further due to the higher RBE of heavy ions, thus becoming more favorable for heavy ions.

Regarding the *ddds* and lateral distribution parameters, for deep seated SOBP, helium ions could be advantageous over protons for better distal and lateral fall-off, leading to a better conformity while sparing the surrounding healthy tissues. The main drawback of helium ions compared to protons in this SOBP study is the dose due to the fragmentation tail, that can be a disadvantage for opposite fields irradiation as investigated in Kantemiris *et al* (2011).

Compared to heavier ions, helium ions are providing interesting features such as a lower fragmentation tail and an advantageous entrance dose, while similar lateral and distal fall-off properties. Nevertheless biologically optimized SOBPs might offer smaller fragmentation tails and a lower entrance doses for the different ions compared to the results suggested by this study using physically optimized SOBPs. While for carbon and oxygen ions the need of

the RiFi is commonly accepted, for helium ions it appears that the RiFi could be necessary for certain tumor depths to reduce the number of energy slices needed to achieve a homogeneous distribution, due to the small peak width for R_{80} below 170 mm. Some studies, such as Furusawa *et al* (2000), found a shift of the high RBE values toward the low-LET region for light ions such as helium ions compared to heavier ones. However, due to the difference in achievable LET values, heavier ions remain of clinical interest for certain kinds of tumors such as hypoxic tumors.

The physical characterization reported here and in recent reviews of biological investigations (Held *et al* 2016) suggest that helium ions could regain interest for future therapeutic applications, thanks to their overall physical and biological properties. However, as shown in Grün *et al* (2015), the choice of an ion is not straightforward and depends on several criteria such as the tumor and healthy tissues types, target localization and the associated beam ballistics (number of fields, angles). Thus, more treatment planning comparisons with experimentally validated physical and biological model are needed, and this experimental might be considered as a reference for dosimetric validation of the employed computational models, paving the way to such studies.

3.5. Summary

This chapter presents a detailed analysis of the dosimetric characteristics of the proton, helium, carbon and oxygen ion beams available at HIT. Although the therapeutic use of helium ions had been discontinued after the end of the clinical experience at the Berkeley National Laboratory in 1992, our experimental results indicate that helium ions could be a good candidate for further improvements in particle therapy, with intermediate properties between the clinically used proton and carbon ions. The main features are especially a smaller lateral scattering compared to protons and a very low tail-to-peak ratio compared to carbon or oxygen ions. These experimental results can be exploited for validation of physical models for further patient planning studies. Moreover, this study was used to create the first helium ions physical database at HIT, enabling accurate design of ongoing biological experiments which will ensure proper treatment planning and future fair comparisons between planning studies with different ions.

Chapter 4. Helium ions at HIT: Comparisons between FLUKA code predictions and measurements

We present in this chapter the comparisons and validations of the Monte Carlo FLUKA code against in-depth dosimetric measurements acquired at the Heidelberg Ion Beam Therapy Center. Future chapters building upon this section will include treatment plan comparisons (Chapter 7), using validated biological models (Appendix C), between proton and helium ions with a validated Monte Carlo treatment planning engine (Chapter 6) based on the same code FLUKA. The work presented in this chapter has been submitted for publication (Tessonnier *et al 2017b*).

4.1. Background

After the end of the clinical experience with helium ions at the Lawrence Berkeley National Laboratory (LBL) in 1992, a particular renewed interest for helium emerged as explained in Chapter 2. Most of the publications, either based on Monte Carlo (MC) simulations (Kempe *et al* 2007, Kantemiris *et al* 2011, Burigo *et al* 2015) or analytical models (Fuchs *et al* 2015, Krämer *et al* 2016, Grün *et al* 2015, Knäusl *et al* 2016), are not relying on detailed dosimetric data for models validation. Hence, we present in this chapter a comprehensive validation of MC simulations based on the FLUKA code (Ferrari *et al* 2005, Bohlen *et al* 2014, Battistoni *et al* 2016) against dosimetric measurements in water with ^{4}He ions, based on the data presented in the previous chapter. Experimental laterally integrated depth dose distributions (*ddds*), with or without ripple filter (RiFi), lateral dose profiles and their parameterization along the depth, as well as a spread-out Bragg peak (SOBP) are compared to MC simulations. Through this work, we could provide a thoroughly validated database for input to the analytical research treatment planning system (TPS, Krämer *et al* 2000, Krämer and Scholz 2000) currently used at HIT for planning radiobiological investigations at HIT, as previously

done in Kurz *et al* (2012) for oxygen ions and Parodi *et al* (2012, 2013) for protons and carbon ions. Furthermore, this work builds the basis for future treatment planning studies based on validated physical and biological models (Mairani *et al* 2016a, Mairani *et al* 2016b) for helium ions, which will be presented in Chapters 7.

4.2. Materials and Methods

4.2.1. The FLUKA Monte Carlo code

All simulations presented in this chapter are based on the MC code FLUKA (development version July 2015) and the following simulation parameters were kept consistent throughout the study. In the entire particle therapy energy range (~50-220 MeV/u for ^{4}He ion beams), the two models handling nucleus-nucleus interactions are RQMD (Relativistic Quantum Molecular Dynamics, Sorge *et al* 1989) for particles below 5GeV/u and BME (Boltzmann Master Equation, Cavinato *et al* 1998) below 120MeV/u (cf. Chapter 2). The defaults setting HADROTHErapy was selected, including an accurate modeling of charged particles multiple Coulomb scattering, with a particle transport and delta ray production threshold set to 100 keV. The production of energetic heavy fragments via the coalescence mechanism (Battistoni *et al* 2016) and the evaporation of heavy fragments have been activated through the COALESCE and EVAPORATION cards, respectively.

Regarding the standard geometry of all simulations, a detailed model of the HIT beamline was implemented (Parodi *et al* 2013, Tessonnier *et al* 2016), describing the vacuum window, the beam applications and monitoring systems (BAMS) consisting of three parallel plane ionization chambers and two multiple wires proportional chambers, as will be described more in detail in Chapter 5. The RiFi model, used in previous work for generation of the carbon ions database (Parodi *et al* 2012, Mairani *et al* 2010), was added to the simulation geometry, if needed.

To replicate the experimental setup, either a semi-infinite water slab (for *ddds)* or a water tank (with a 5 mm PMMA entrance window for lateral profiles and SOBP) were placed at the isocenter as depicted in figure 4.1.

4.2.2. Depth dose distributions

Measurements of the pencil-beam *ddds* were performed in a treatment room at HIT with the PeakFinder (PKF) water column in a similar fashion as in previous works for protons, carbon and oxygen ions (Parodi *et al* 2012, Kurz *et al* 2012) and described in Chapter 3. The ten energies presented in Chapter 3, selected from the 255 discrete energies available at HIT, are summarized in table 4.1 and will be compared to MC predictions in this Chapter. As described in Chapter 3, quasi-monoenergetic beams along the central axis were delivered with or without RiFi and clinical-like beam spot sizes (foci). The measurements were ranging from depths in water of 16 mm up to at least 20 mm after the BP position. The charge collection efficiency over the whole Bragg curve for low (82.33 MeV/u) and high (220.51 MeV/u) energies was studied in the previous Chapter 3 and was found higher than 0.998 +/- 0.4%.

Initial Energy (MeV/u)	56.4	79.8	103.1	122.9	140.7	157.0	172.3	190.9	210.9	220.5
Focus size (mm)	16.7	11.6	9.2	7.9	7.1	6.3	5.8	5.3	5.0	4.9
Intensity (ions/s)	8.0×10^7									
IC Voltage (V)	400									
RiFi	with / without									

Table 4.1: Depth dose irradiation parameters: Initial energy of the beam, beam spot size without RiFi (FWHM) and intensity used for the different acquisitions (with and without RiFi). Voltage used by the ICs of the PKF.

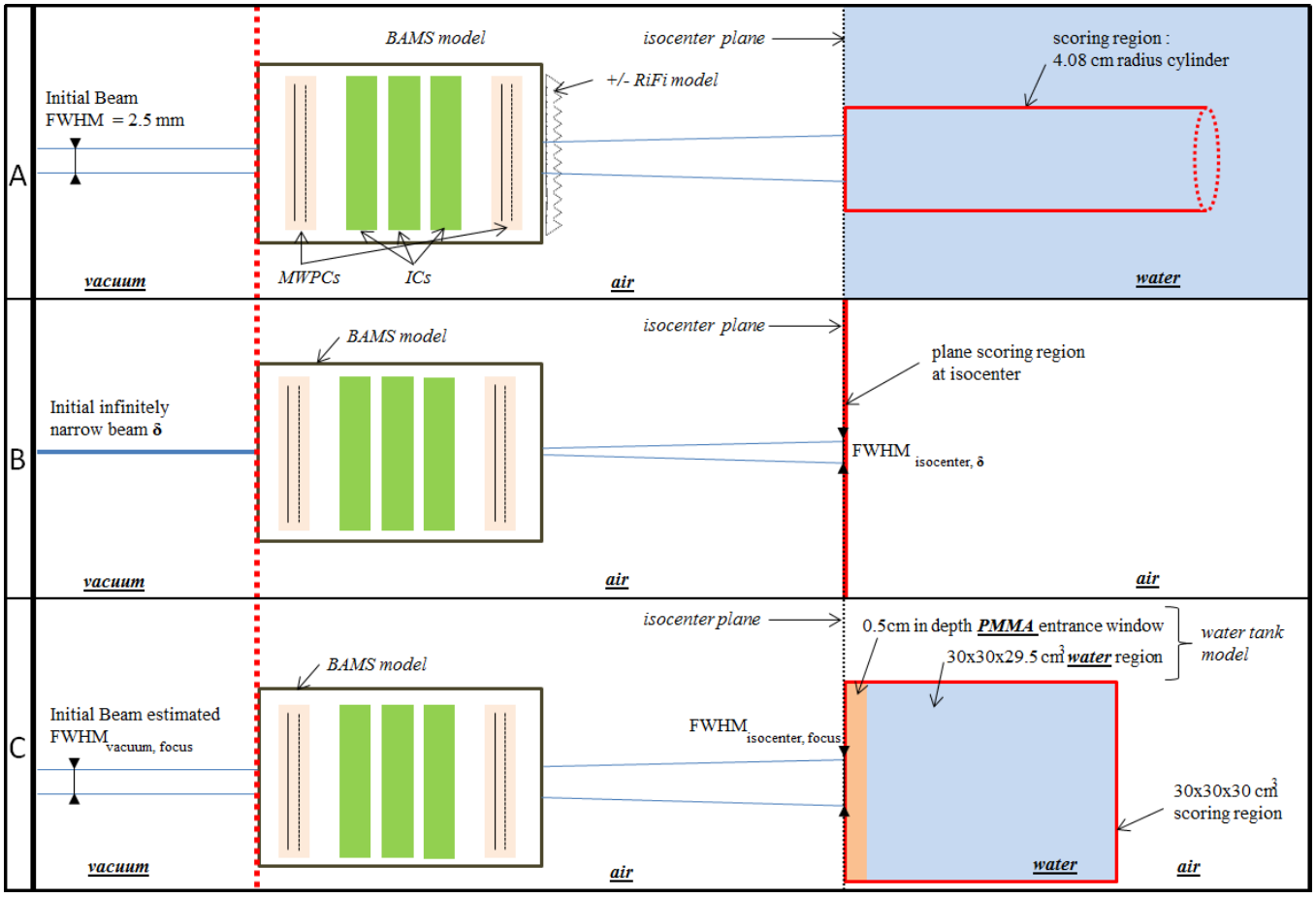

Figure 4.1: Different setups used in the simulations: the top panel shows the geometry used for the depth dose distribution simulations (A) with the scoring region of 4.08cm radius inside a water slab, with or without RiFi. The middle panel (B) depicts the setup used to extract the FWHM of the primary particles fluence at isocenter without RiFi for an initial infinitely narrow beam impinging on the BAMS. The bottom panels (C) illustrates the setup used with the water tank, for both lateral profiles and SOBP simulations.

For reproducing the experimental setup in the simulations, a water region is added at isocenter (112.6 cm downstream from the last elements of the BAMS) to the standard geometry of the simulation described in section 3.2.1, as seen in figure 4.1. The beam Gaussian size in vacuum was defined as 2.5 mm, as used in Parodi *et al* (2012) for the smallest spot size of protons and carbon ions. However, as evaluated in Kurz *et al* (2012) with measurements, spot sizes do not have influence on the recorded *ddds.* Scoring bin size was set to 25µm in depth while integrating the dose on a radius of 4.08 cm laterally, consistently with the ICs in the PKF. The number of primary particle histories was set to 1×10^6. The water density value used for the simulations was set to 0.998g.cm^{-3}, in order to reproduce more accurately the experimental temperature conditions (~20°C). To determine the optimal configuration of the simulation (e.g. water ionization potential (*Ipot*) and relative initial beam momentum spread (*dp/p*) values), an iterative process of trial-and-errors was applied for simulations without RiFi. The *Ipot* value was kept fixed for all energies, while the *dp/p* values were tuned individually. First the *Ipot* value was adjusted in order to reduce the shift between measured and simulated Bragg curves over the entire therapeutic interval. The BP position was determined from a 5th polynomial order function fit to the Bragg curves above 80% of the maximum values (BP). Both the distal range at 80% (R_{80}) of the maximum dose and the BP position were evaluated as a function of *Ipot*. The advantage of R80 over the BP position is a lower sensitivity to momentum spread variations, as described in Bortfeld (1997) and therefore already used in Kempe et al (2007) with MC simulations, as well as in the previous Chapter 3. After the determination of the optimal Ipot value, the simulated curves were aligned to the measurement curves, using the newly calculated shifts between their respective R_{80}, for further comparisons. Then, both measured and simulated *ddds* were normalized by their area. For the investigated energies, the *dp/p* tuning was performed by minimizing an objective function χ^2 (Kurz *et al* 2012), defined as:

$$\chi^2 = \sum_i \left[\Delta_{meas}^{sim}(z_i)^2 \Big/ d_i \right] \times \Delta z_i^{i+1} \ , \tag{4.1}$$

where Δ_{meas}^{sim} is the difference between the simulated and measured *ddds* at the depth z_i. The $1/d_i$ and Δz_i^{i+1} are weighting factors accounting for both the increased absolute error at higher dose levels and the varying spacing of the measurement positions, along the Bragg curves.

From this set of parameters, final *ddds*, with and without RiFi, were simulated for comparison with measurements. Several parameters were extracted:

- The R80 and BP position as described previously,
- The entrance dose difference at 16 mm between measurement and simulation, relative to the maximum measured dose for the normalized ddds,
- the highest dose difference in the BP region (i.e., above 90% of the maximum dose) between normalized ddds,
- the entrance-to-peak ratio (EPR), defined as the ratio between the entrance dose to the dose at the BP position,
- the tail-to-peak ratio (TPR), defined as the ratio between the dose found 10 mm after the BP position relative to the BP dose,

- the peak-width (PW) at 80%, defined as the distance in mm between the proximal and distal position at 80% of the BP,
- the distal fall-off (FO), defined as the distance in mm between the 80% and 20% distal dose position,
- The dose-weighted average dose-difference $\overline{\Delta D/D}$ (Battistoni et al 2016), defined as:

$$\overline{\Delta D/D} = 100 \times \frac{\sum_i D_i^{meas} \times \Delta z_{i-1}^{i+1} \times |(D_i^{meas} - D_i^{sim})/D_i^{meas}|}{\sum_i D_i^{meas} \times \Delta z_{i-1}^{i+1}}, \quad (4.2)$$

with D_i being the normalized dose at the depth z_i from simulation or measurements and Δz the mean step size between the z_{i+1} and z_{i-1} depth, giving an index of the overall agreement between simulated and measured Bragg curves.

While the entrance dose difference and the highest dose difference give information about discrepancies between normalized *ddds*, EPR, TPR, PW and FO are representative of relative dose comparisons.

4.2.3. Lateral dose profiles

4.2.3.1. Beam size in vacuum

The beam size in vacuum for the different foci available was determined for helium ions using a narrow beam approach as defined in Tessonnier *et al* (2016) for protons, as it will be explained in detail in Chapter 5. For all energies, the primary particle fluence at the isocenter was recorded for an infinitely narrow initial beam. Subsequently, the FWHM of the primary particles fluence distribution was extracted and the FWHM of the beam in vacuum for each focus was estimated using the following equation:

$$FWHM_{vacuum,focus} = \sqrt{FWHM_{isocenter,focus}{}^2 - FWHM_{isocenter,\delta}{}^2}, \quad (4.3)$$

with *FWHM* being the full-width half maximum of the particles distributions either at the *isocenter* or before the BAMS in *vacuum*, for an infinitely narrow beam δ or a selected *focus* spot size. $FWHM_{isocenter,\delta}$ is extracted from the simulation, while $FWHM_{isocenter,focus}$ is known from the HIT accelerator library.

The energies investigated were [50.57, 55.30, 60.80, 79.78, 103.05, 122.93, 140.71, 157.03, 172.28, 190.85, 210.92, 220.51 MeV/u] for 1×10^6 primary histories per run. Using the estimated $FWHM_{vacuum,focus}$, new simulations for focus index 1 were performed and the primary fluences FWHMs at isocenter were compared to the values of the HIT library for the same energies.

4.2.3.2. Comparison of measurements and simulations

Lateral dose profile measurements of vertically scanned line irradiations were performed in a water tank at the HIT experimental room, as described in Chapter 3. Details on the setup and energy used can be found in Chapter 3, section 3.2.2. The range R_{80} for the low, medium and high energies is about 54, 172 and 308 mm, respectively. Simulations were performed for the

same irradiation configuration described above. The geometry of the water tank, featuring a 5 mm PMMA entrance window placed at the isocenter before a 30 cm × 30 cm × 29.5 cm water cube, was exactly modelled (see figure 4.1). The optimal input parameters described in the previous sections were used (*Ipot*, *dp/p*, beam size in vacuum). Dose depositions were scored using FLUKA built-in scoring capabilities in Cartesian voxels of 1 mm × 1 mm × 1 mm size for 200 independent runs of 1×10^6 primary histories each.

Qualitative comparisons between measurements and simulations were realized through visual inspection of the data, with normalization to the maximum of each profile. Quantitative assessments were achieved through lateral Gaussian parameterizations (single and triple (Inaniwa *et al* 2014)) along the depth. To extract the parameters, lateral profiles were processed with the MINUIT minimization package (James and Roos 1975) of ROOT (root.cern.ch, Brun and Rademakers 1997) using least square optimization. The fitting weights were defined as $1/(\sqrt{D_i}/100)^2$ as in Schwaab *et al* (2011) and Chapter 3.

The simple single Gaussian (SG) describes the central core of the profiles, restricted to values (simulated or measured) above 20% of the profiles normalized to their local maximum (for each depth), and is defined as:

$$d(x,y) = n \times \frac{1}{2\pi{\sigma_{SG}}^2} \times e^{-\frac{(x-sh)^2}{2{\sigma_{SG}}^2}}. \quad (4.4)$$

For line irradiation, *y* is assumed to have a constant value of *y*=0, while *d* stands for the relative dose, *x* denotes the position on the lateral profile, σ_{SG} is the width (standard deviation) of the Gaussian, *n* is a normalization factor and *sh* indicates the shift to the central position, either due to uncertainties in the IC block or beam position as well as the water tank alignment for the measurements.

In the triple Gaussian (TG) parametrization, the same lateral extension was selected keeping only the measurements/simulations with a lateral position |x| < 25 mm with respect to the maximum IC position from all chambers. Measured/simulated points with a relative dose contribution to the profile maximum below 0.5% were excluded to avoid noisy data. The triple Gaussian is defined as:

$$d(x,y) = n \times \left[\frac{w_1}{2\pi{\sigma_1}^2} \times e^{-\frac{(x-sh)^2}{2{\sigma_1}^2}} + \frac{w_2}{2\pi{\sigma_2}^2} \times e^{-\frac{(x-sh)^2}{2{\sigma_2}^2}} + \frac{w_3}{2\pi{\sigma_3}^2} \times e^{-\frac{(x-sh)^2}{2{\sigma_3}^2}}\right], \quad (4.5)$$

$$w_1 = 1 - w_2 - w_3, \quad (4.6)$$

with *d* being the relative dose, *x* the position of the lateral profile, σ_x the widths of the narrow (σ_1) and broader Gaussians (σ_2 and σ_3). Moreover, w_x stands for the relative weight of the different Gaussians, *n* is a normalization factor and *sh* is the shift to the central position (as introduced for the single Gaussian). As described previously, *y* is assumed to be equal at 0.

As described in Chapter 3, a fair comparison of the evolutions of the different σ, regardless of possible uncertainties of the initial beam spot size, is allowed by quadratically subtracting from the depth-dependent $\sigma(z)$ the width at the phantom entrance window placed at isocenter, σ_{0cm}, which is extrapolated for the smallest Gaussian (σ_{SG} or σ_1):

$$\sigma_{corr}(z) = \sqrt{\sigma(z)^2 - \sigma_{0cm}{}^2}, \quad (4.7)$$

This approach yields σcorr, i.e., the Gaussian widths (σ_{SG}, σ_1, σ_2 or σ_3) corrected by the initial beam width at isocenter, which can be interpreted as the evolution along the depth z of an infinitely narrow beam impinging on the water tank. The single Gaussian through the evaluation of σ_{SGcorr} allows following the main evolution of the beam width in depth. The analysis of the triple Gaussian with its parameters enables disentangling the dose contributions to the lateral profile from the primary beam and its small and large angle emission/scattering secondary particles, and their evolution along the depth in water.

4.2.4. Spread-out Bragg peak

As example of a more complex geometry, a laterally and longitudinally extended SOBP was also studied. The SOBP was planned to deliver 1 Gy absorbed dose to a 140 mm × 140 mm × 140 mm target centered at 80mm depth in water, as in Chapter 3. The optimization was performed using a pre-clinical database generated from section 4.2.2, and the SOBP was optimized only in depth without RiFi. The experimental setup is described in detail in Chapter 3, section 3.2.3.

Simulations were performed using the same setup described previously (cf. section 4.2.2), scoring the dose in 1 mm × 1 mm × 1 mm voxels in the transport of 2×10^8 primary histories. The ICs finite sensitive volume was taken into account in the data analysis.

Besides the dose comparison between simulations and measurements, assessment of different lateral field parameters and their evolutions along the depth in water was carried out, such as the evolution of the local 90% SOBP size (defined as the distance between the lateral positions where the dose reaches 90% of the SOBP mean dose within the investigated profile), the lateral FO (defined as the 80%-20% distance) or the evolution of the irradiated lateral size (identified by the 50% isodose, in this study 0.5 Gy).

4.3. Results

4.3.1. Depth dose distributions

A value of 76.8 eV for the first simulation parameter investigated, *Ipot*, was found to minimize the range shift for all energies below +/- 0.1mm. The optimal relative momentum spread *dp/p* values, giving the lowest χ^2 scores, were extracted individually for the ten investigated energies, as seen in Appendix B (figure B.1), and then interpolated to the whole energy range as seen in figure 4.2 (left panel). All simulations presented in the next part of this chapter were performed with these parameters.

The simulated Bragg curves plotted against the measured data are shown in figure 4.3 (top panel) without RiFi and figure 4.4 with RiFi (top panel), normalized to their area. The range differences (from either BP position or R_{80}) between MC predictions and measurements are below 0.1mm for both investigated cases with and without RiFi (figure 4.2, right panel), centered around 0 mm with no evident trends. For the data without RiFi, the EPR is shown in figure 4.3 (middle left panel), indicating a good agreement between MC and measurements up to an energy corresponding to a R_{80} of 120mm, while differences get as large as 1.9% at higher depths. Regarding the PW (figure 4.3, middle central panel) and the distal FO (figure 4.3, middle right panel), measurements and simulations show good agreement with

differences below the measurement uncertainties. The TPR (figure 4.3, bottom left panel) shows discrepancies from less than 0.2% at R_{80} around 120mm up to 0.7% for the highest energies. The $\overline{\Delta D/D}$, shown in figure 4.3 (bottom center panel), indicates that the overall agreement between the measured and simulated data is deteriorated, mainly at higher energies, with a trend from 0.6% at low energy up to 2.3% differences at higher energy. When normalizing the Bragg curves to their area, the entrance dose differences are below 0.5% for all investigated energies, while in the high dose regions dose differences up to 5.5% can be encountered for high energies as shown in figure 4.3 (bottom right panel). In the comparisons of the Bragg curves with RiFi, the same trends were observed, starting with an EPR in good agreements up to a R_{80} of 120mm, but then reaching differences of about 2.2% at high energies (figure 4.4, middle left panel). Differences in TPR (figure 4.4, bottom left panel) were evolving in a similar way as well, from 0.3% at R_{80}≈120mm up to 0.9% at high energies. PW (figure 4.4 middle center panel) and FO (figure 4.4 middle left panel) evolutions as a function of energy show good agreement within 0.1mm between simulations and measurements. The $\overline{\Delta D/D}$ evolution with RiFi, shown in figure 4.4 (bottom center panel), indicates a better agreement at low energies than at higher ones, with differences rising up to 2.3%. Regarding the comparisons of the curves normalized to their area, dose differences in the entrance region were below 0.5%, while in the high dose region differences below 0.6% were observed for low energies, rising up to 5.9% at high energies (figure 4.4, bottom right panel).

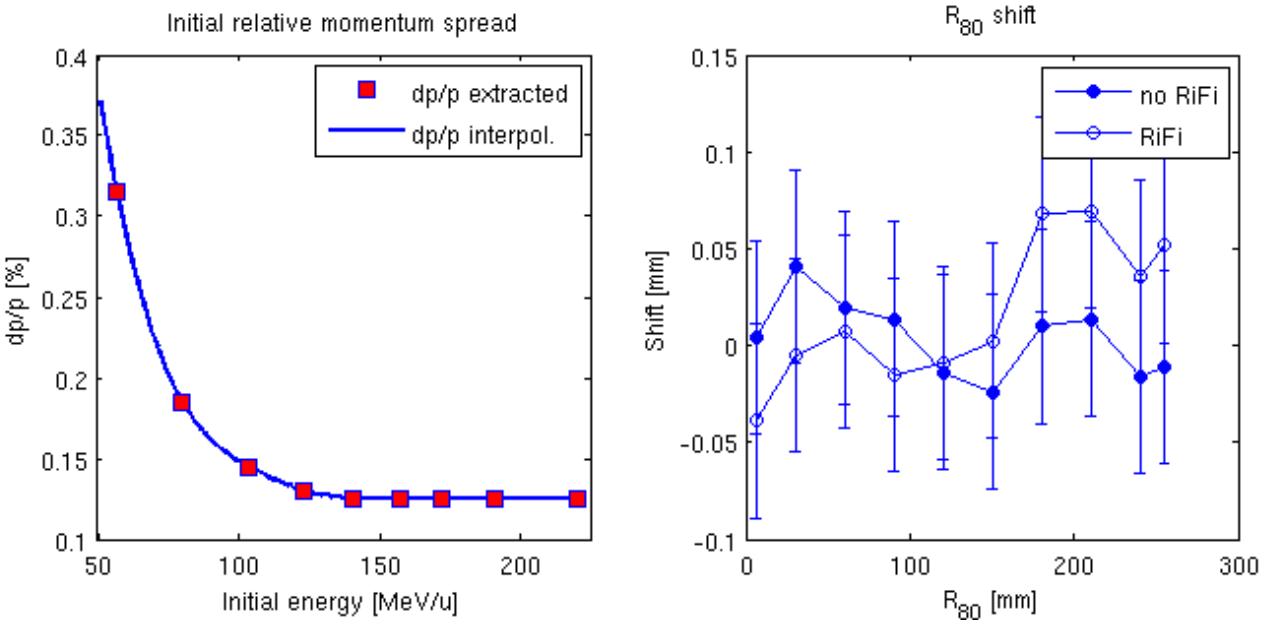

Figure 4.2: Left panel: initial relative momentum spread found during the error-and-trial process (square) for the ten investigated energies (without RiFi), then interpolated (line) to the entire energy range. Right panel: range (R_{80}) shift differences between simulations and measurements, as a function of R_{80} of the measured energies, with and without RiFi.

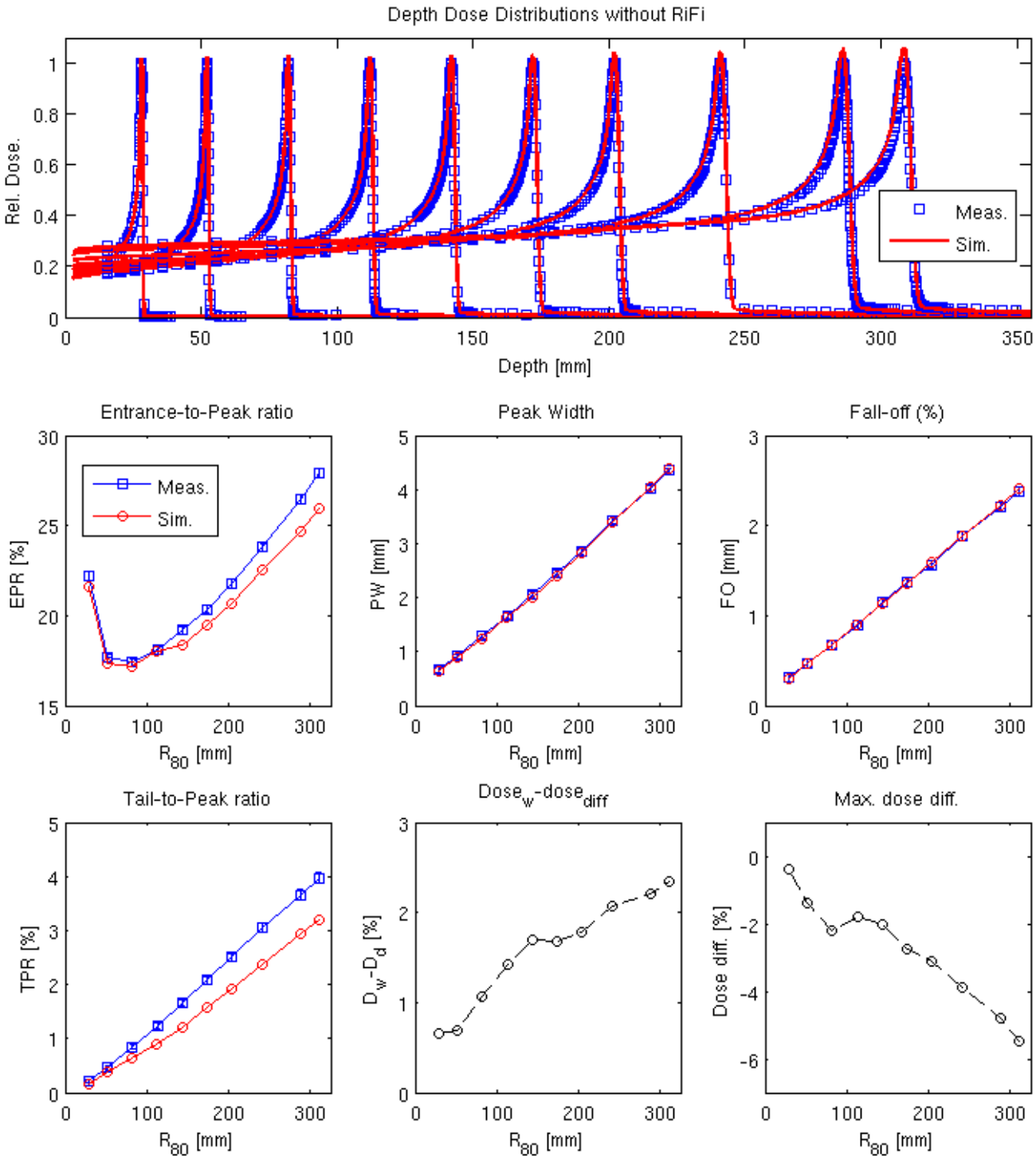

Figure 4.3: Measured/simulated depth dose distributions and extracted parameters comparisons without RiFi. In the top panel, measured (squares) depth dose distributions and simulated (lines) are shown after shift and normalization to the area (cf. section 2.1), and then normalized to the maximum of the measured curve for display purpose only. The middle left panel depicts the EPR as a function of R_{80}, the middle central panel shows the PW as a function of R_{80} and the middle right panel illustrates the FO as a function of R_{80}. The bottom left panel shows the TPR, the bottom central panel the $\overline{\Delta D/D}$ and the bottom right panel the maximum dose difference of the normalized curve as a function of $R_{80.}$ Parameters derived from measurements appear with squares, while circles refer to simulations.

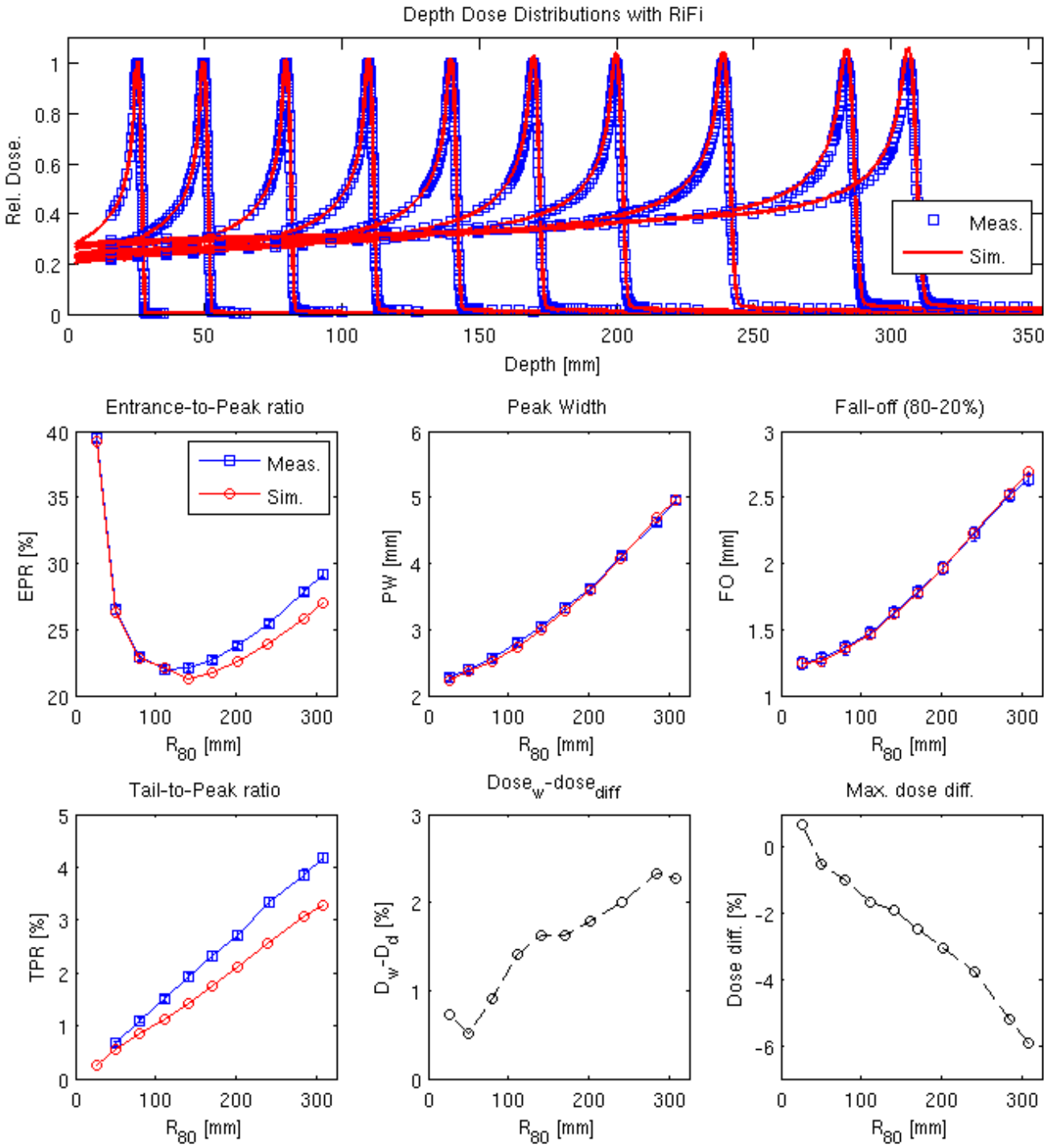

Figure 4.4: Comparisons of measured/simulated depth dose distributions and related extracted parameters with RiFi, as described in Figure 4.3 for a delivery without RiFi. Parameters derived from measurements appear with squares, while circles for simulations.

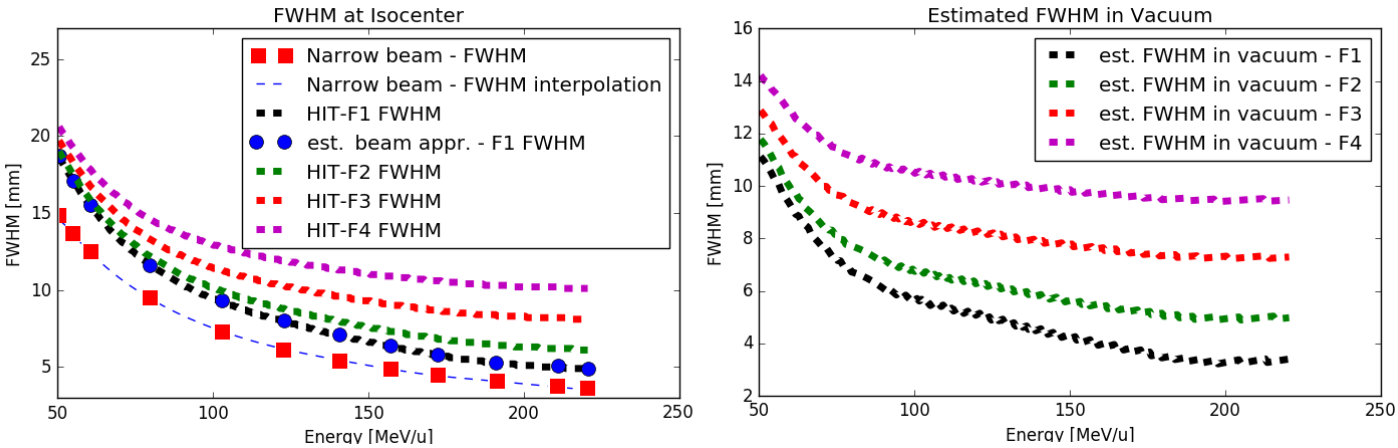

Figure 4.5: In the left panel, different FWHM at isocenter are compared. HIT-Fx stands for the beam spot size at isocenter (index 1 to 4) from the HIT accelerator library. "Narrow beam – FWHM" (red square) is the simulated FWHM of the primary particles fluence starting from an infinitely narrow beam before the BAMS. "Est. beam appr. –F1 FWHM" (blue circle) stands for the FWHM from the estimated beam approach for the smallest focus (focus 1). It represents the FWHM obtained from simulations using the estimated beam FWHM in vacuum for focus 1 (right panel). In the right panel are presented the FWHM values in vacuum for the four first HIT focus indices estimated from the infinitely narrow beam approach simulation and the HIT accelerator library.

4.3.2. Lateral dose profiles

The results of the Gaussian beam width parameters extracted from data and simulations in vacuum and its verification are shown in figure 4.5. The FWHM of the primary particles fluence at isocenter for a simulated infinitely narrow beam was extracted for the investigated beam energies (figure 4.5 - left panel with squares), then interpolated. Subsequently, the size of the beam in vacuum, for the different helium ion spot sizes, was estimated (figure 4.5 – right panel). New simulations using these estimated values were finally performed for the smallest HIT focus size. The FWHM of the primary particle fluences for the ten energies investigated was found in excellent agreement with the expected values from the HIT library, with differences below 0.2 mm (figure 4.5 - left panel with circles).

Lateral dose profile measurements overlaid with simulation results are shown in figure 4.6, for the three different investigated energies and two positions in depth, at the entrance of the water phantom and near the Bragg peak position. The profiles are normalized to their local maximum. The absolute water-equivalent thickness of the measurement position is about 19 mm at the entrance of the phantom, and about 53 mm, 169 mm and 300 mm (near the BP) for the low, medium and high energy, respectively. For all investigated energies the entrance profiles, restricted to values above the 1% dose level with respect to the profile maximum, are found in good agreements between simulations and measurements. Thus, knowing that the EPR is about 20-25%, these agreements are found for dose levels above 0.3% of the maximum dose delivered to the BP. However, when looking at differences for lower dose levels in the entrance, it can be noticed that for the higher beam energies, larger discrepancies can be found in the halo comparing the local value between simulation and measurement, with local deviation up to 45% (for a relative dose level of 0.2% with respect to the profile maximum) for the highest energy, up to 42% (0.2%) for the mid-range energies, and 14% (0.4%) for the lowest energy.

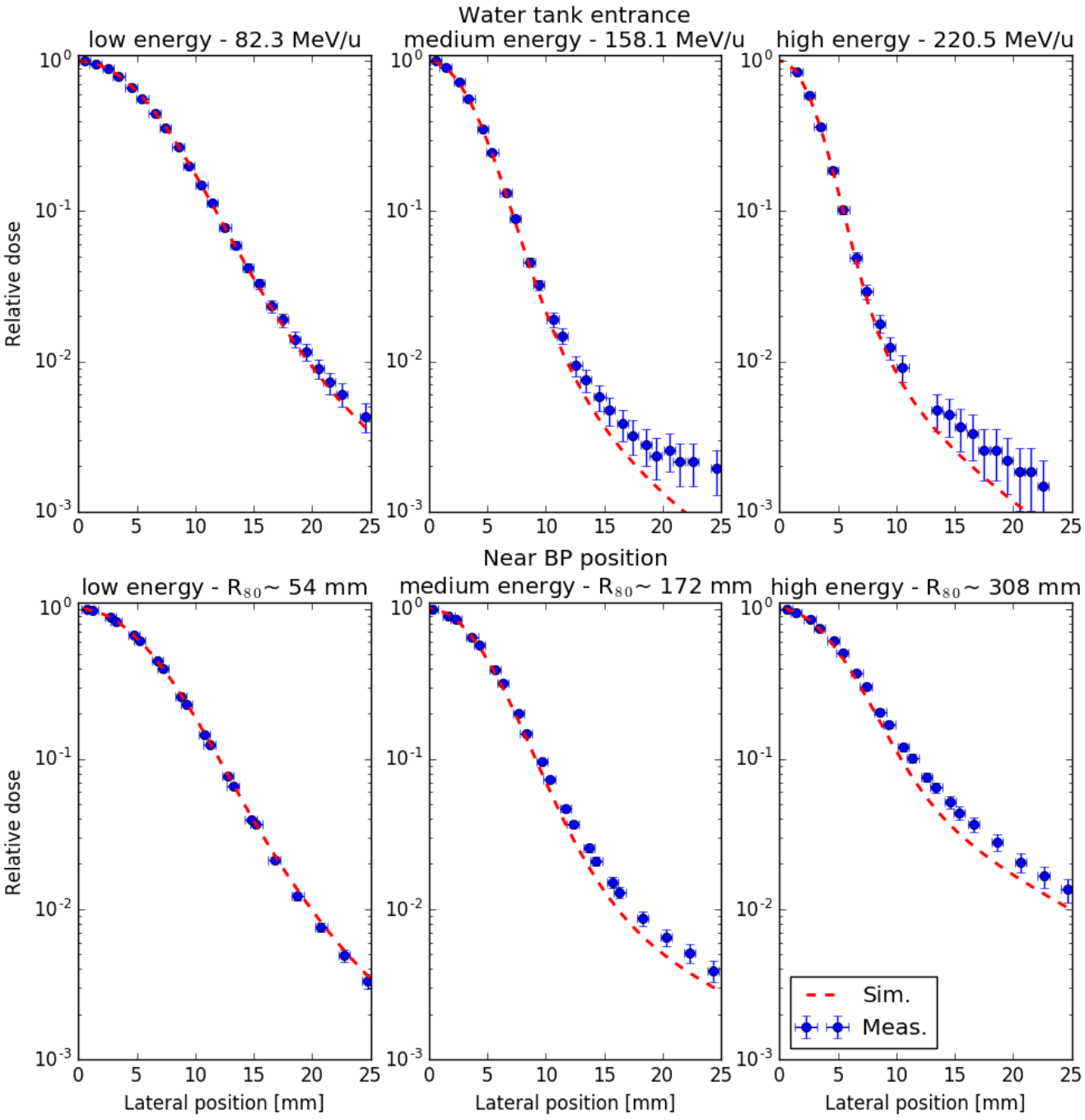

Figure 4.6: Lateral profiles for the three investigated energies, namely low, medium and high from left to right, sampled both at the entrance of the phantom (top) or near the BP (bottom). Profiles are normalized to the local maximum and depicted in semi-logarithmic scale. Simulations are displayed with lines, while the measurements with circles.

Near the BP position, the underestimation of the halo dose in the FLUKA simulations increases, with discrepancies up to 26% (1.3%) for the highest energy and 23% (0.4%) for the intermediate one. For the lowest energy, a good agreement is kept with differences up to 9% (0.3%). In the high dose regions, all points agree within the experimental uncertainty either due to the positioning of the IC or beam as well as the dose measurement. The statistical uncertainties on the simulation are below 0.1% in the high dose region and about 1% at the extreme positions of the investigated profiles, for all energies and depths investigated.

The SG parametrization for the three energies is shown in figure 4.7 for σ_{SGcorr} as a function of the relative depth in water (normalized to the BP position) and corrected by the σ_{SG} value extrapolated at 0cm. Error bars for measurements are taking into account the uncertainty on σ_{SGcorr} due to the retrieval process and the positioning uncertainty during the measurements, while for simulation only uncertainties related to the fitting procedure are shown. The values of $\sigma_{SGcorr\text{-}0cm}$ are about 5.19 (+/- 0.72) mm, 3.16 (+/- 0.71) mm, 2.31 (+/- 0.71) mm for measurements and about 5.21 (+/- 0.04) mm, 3.13 (+/- 0.02) mm, 2.39 (+/- 0.03) mm for simulations, respectively, for low, medium and low energies. The agreement between these values is good, below 3.1% (0.07 mm) difference, and below 16.9% (0.45 mm) in comparison to the HIT spot size library. The evolution of σ_{SGcorr} along depth in water is similar for both measurements and simulations, with differences below 0.2 mm in average for low energy, 0.2 mm for medium energy, and 0.3 mm for the highest energy.

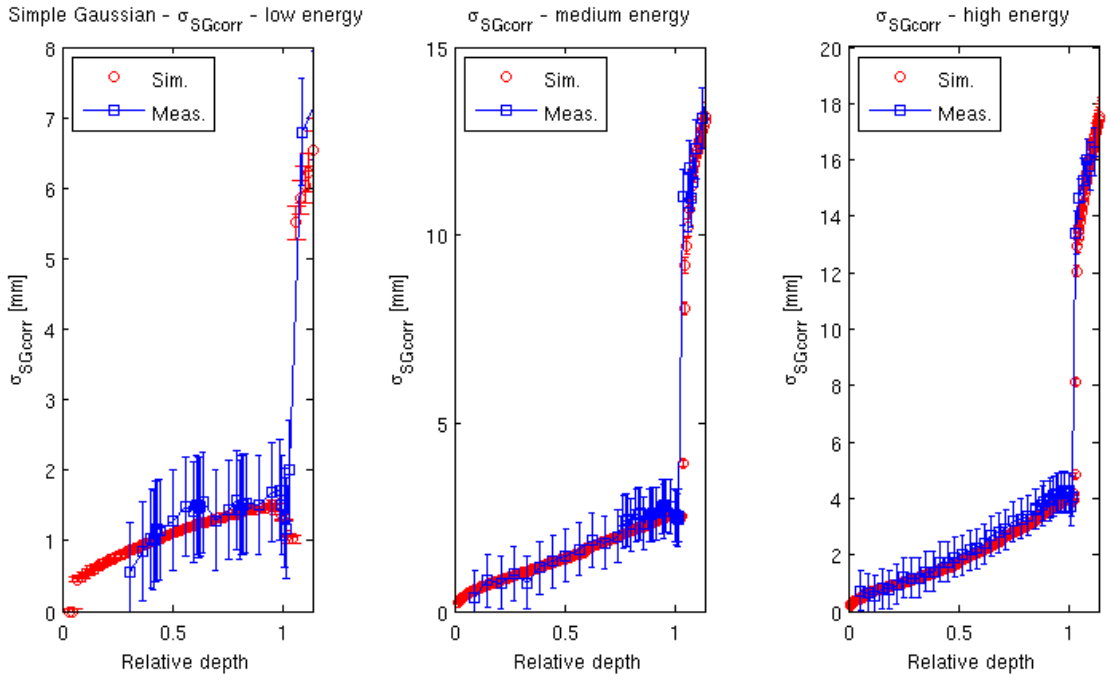

Figure 4.7: Single Gaussian parametrization of beam width evolution with depth in water (relative to the BP position) for the three investigated energies (low, medium and high from left to right). Simulations are displayed with circles and measurements with squares.

The TG parametrizations was performed for the three energies and the results for the highest energies are shown in figure 4.8 or in Appendix B (figure B.2 and figure B.3). Error bars are displayed in a similar way as for the SG. Regarding the first Gaussian width extrapolated at 0 cm, $\sigma_{1\text{-}0cm}$, for the different energies, it was found to be 4.44 (+/- 0.86) mm, 2.90 (+/- 0.71) mm and 2.13 (+/- 0.70) mm for measurements and 4.74 (+/- 0.31) mm, 2.91 (+/- 0.21) mm and 2.27 (+/- 0.13) mm for simulations, thus showing an agreement within 0.3 mm. The evolution of the different Gaussian widths in water depicted in figure 4.8 is corrected by these values. For low energies, the three corrected Gaussian widths are in good agreement within the error bars, with less than 0.02 (+/- 0.94) mm difference on average for σ_{1corr}. The same behavior is found for the highest energies as well, with differences in σ_{1corr} values below 0.08 (+/- 0.18) mm for medium energies and 0.02 (+/- 0.13) mm on average for the highest energy. For σ_{2corr} and σ_{3corr} no direct comparisons can be performed due to the larger fluctuations of the results, as can be seen for the highest energy in figure 4.8. Nevertheless, the comparisons between simulation and measurements follow the same trends with similar values within the error bars, and this is true for all investigated energies. Regarding the weight of the different Gaussians, for the lowest energy investigated no particular differences between measurements and simulations were found. However, for medium and high energies, larger discrepancies were found as seen in figure 4.8. The weight of the 1st Gaussian is overestimated in FLUKA simulations by about 6% - 11%, while the 2nd Gaussian is underestimated by about 2 – 4%, and the 3rd Gaussian by about 4% - 7% for medium and high energy, respectively.

4.3.1. Spread-Out Bragg Peaks

The results of the dose measurements, corrected for the beam monitor calibration deviation of 4.6% (cf. Chapter 3), and FLUKA simulations of the SOBP are shown in figure 4.9. For the depth dose distribution (figure 4.9 top right panel), the dose differences in the SOBP regions are below 1% and in the entrance region below 2% compared to the maximum. The range difference is below the positioning uncertainty of the IC chambers of 0.5 mm. In the lateral dose profiles, an overall good agreement is observed as seen in figure 4.9 (top right panel) at the middle of the SOBP. The dose deviations are below 1% in the plateau region and below 3% in the high dose gradient regions. The extracted local SOBP size (90% of the local maximum profile dose) shows a similar trend along depth in water, with maximal difference of 0.9 mm. In the lateral FO evolution a similar behavior is observed between simulations and measurements, with an underestimation of the simulated values of about 0.3 mm, however being still within the measurements error bars. The evolution of the SOBP irradiated size (isodose 50%, i.e., 0.5 Gy in the presented case) is consistent between measurements and simulations, with a maximum difference of 0.6 mm in the SOBP region and of 0.3 mm in the entrance.

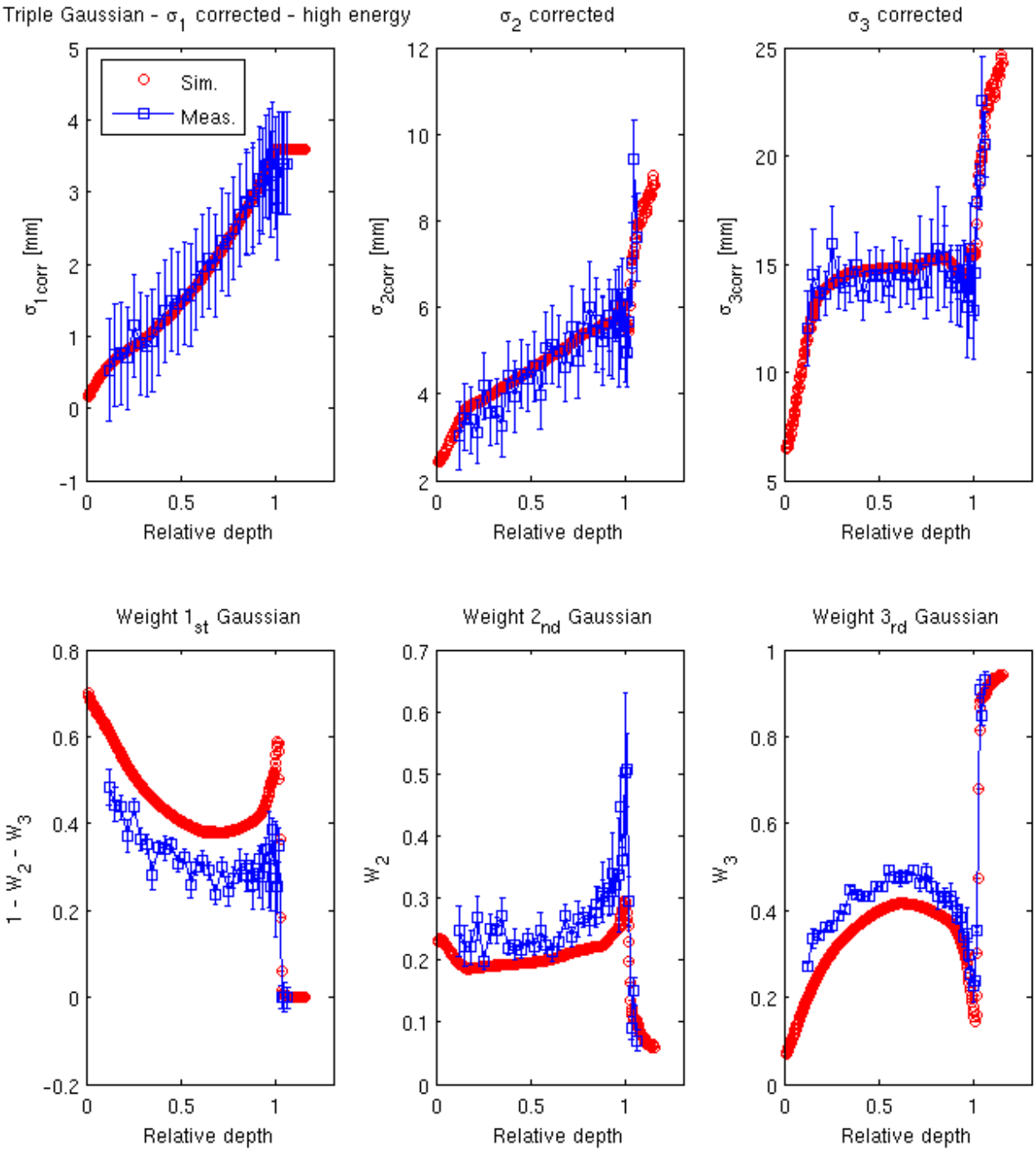

Figure 4.8: Triple Gaussian parametrization for the highest beam energy. Simulations are displayed with circles and measurements with squares. The top panels depict the Gaussian widths evolution in water (relative to the BP position), from the smallest Gaussian to the broader one from left to right. The bottom panel shows the corresponding weights.

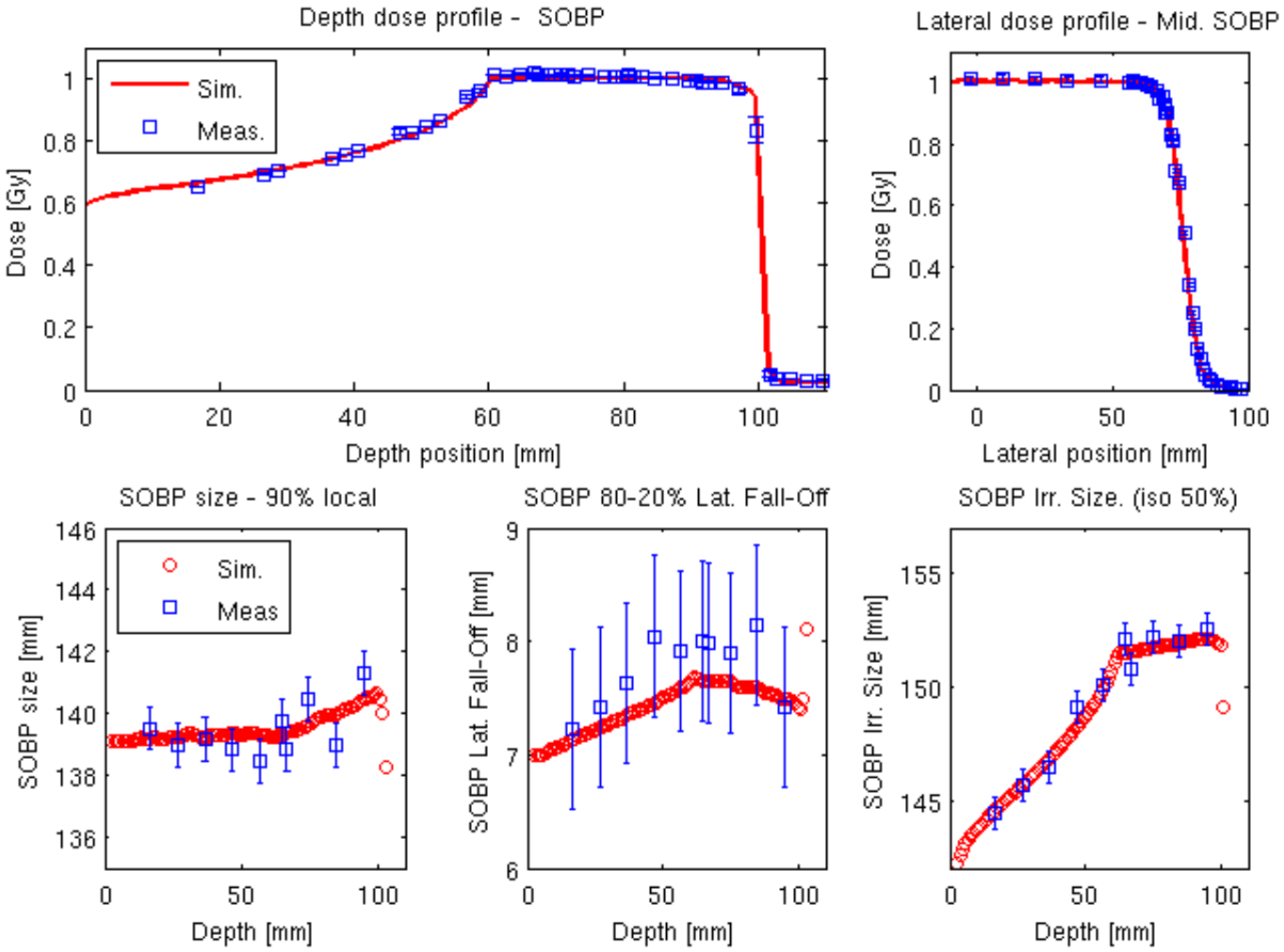

Figure 4.9: Spread-out Bragg-peak results: the top panels depict the depth (left) and lateral (right) dose distributions (simulations displayed with continuous line, measurements with squares). In the bottom panels, the SOBP size (between the local 90% dose) is shown on the left, the FO in the center and the SOBP irradiated dose (isodose 50%) in the right panel. Simulations are displayed with circles, measurements with squares.

4.4. Discussions

In terms of the modelling parameters, the initial beam momentum spread is consistent with *dp/p* values obtained for the HIT synchrotron in prior works for carbon ions and protons, which were ranging in the same order of magnitude from approximately 0.3% at low energies up to 0.1% at high energies (Parodi *et al* 2012, Kurz *et al* 2012). The value of *Ipot* of 76.8 eV is different from the values reported in those two studies. However, those works were assuming a water density of 1.0 g.cm^{-3} and performed with a previous version of FLUKA. New simulations using the detailed model of the beamline and a density of 0.998 g.cm^{-3} were compared to the experimental measurements presented in those works, and were found in excellent agreement for an *Ipot* value of 76.8 eV for carbon and oxygen ions, and 77.3 eV for protons. Thus, the water *Ipot* values needed by FLUKA for simulation of HIT *ddds* for different ions can be brought closer to each other, close to the most recent ICRU recommendation (78 eV ICRU 2009, Andreo et al 2013) and similar to the value of 77.0 eV suggested by Krämer *et al* (2000). The estimated beam size in vacuum is experimentally validated regarding the small differences found between the extracted $\sigma_{SG\text{-}0cm}$ from simulations which are close (within 0.1 mm) to the $\sigma_{SG\text{-}0cm}$ of measurements. The differences from these values to the HIT library ones are due to the way of performing the irradiation. As the delivery is made as a line scan and not as a single spot, the contributions of the different spots lead to a larger value of σ_{SG} at isocenter, as already observed in Tessonnier *et al* (2016).

The depth dose distributions of individual pencil beams are showing an overall good agreement between simulations and measurements, however the differences are increasing for higher initial beam energies of the particles. Both the relative value to the maximum (EPR, TPR, $\overline{\Delta D/D}$) and the maximum difference while normalizing to the area are increasing as a function of the beam energy. This could hint at a possible underestimation of the secondary particle production or secondary particle angular distribution at large angles from the FLUKA code. However, the excellent agreement of the range, PW and distal FO, mainly linked to the dose contribution of the primary helium ions, shows that the FLUKA code is able to accurately reproducing energy loss and range straggling of ^{4}He ions. In order to better understand the dose underestimation problem observed at high energies, the attenuation of the primary beam was also investigated, by reproducing the same experimental setup presented in Krämer *et al* (2016) and Rovituso *et* al (2017) for a 200MeV/u helium ions beam. The simulated attenuation results shown in the Appendix B (figure B.6) were found to be consistent with the experimental findings for ^{4}He attenuation. Thus, the dose differences could be ascribed to the secondary particles (^{3}He, ^{3}H, ^{2}H or ^{1}H) behaviors, such as their angular distributions or nuclear interactions, rather than a deficit of nuclear interactions and fragmentation of ^{4}He. Investigations on the angular distribution of 120 and 200MeV/u helium ions and secondary particles in the FLUKA MC code are presented in Appendix B (figure B.7), compared to experimental data from Rovituso *et al* (2017). The lateral dose profiles are showing similar trends for higher energies at the entrance, with discrepancies on the halo dose indicating an underestimation of the FLUKA simulations compared to the measurements, and even higher differences at larger depths at the BP position. However, even if local deviations can show differences up to 26% at a dose level of 1.6% for the highest energy investigated, it should be noticed that all the discrepancies are below 1% with respect to the profile maximum (global deviation). The evolutions of the σ_{SGcorr} shows good agreement between simulations and measurements for the three investigated energies, and are a direct indicator of the evolution of the core beam along the depth. In fact, the primary beam is the main contributor to the central Gaussian core and leads to the observed good agreement on the FWHM broadening in depth, which is mainly due to multiple Coulomb scattering processes. For the highest energy at large depths before the BP, a slight difference of 0.7 mm appears which is

due to the enhanced contribution of the secondary particles at such depths. When using the TG parametrization at this energy, the σ_{1corr} is not showing anymore these discrepancies, as it is removing the dose contribution of fragments to the central core. The TG parametrization is thus leading to good agreement on the Gaussian widths evolution between measurement and simulations within the uncertainties of both measurements and parametrization processes. However, FLUKA simulations for medium and high energies are underestimating the weight of the second and third Gaussians, thus again suggesting a possible lack of secondary emissions at large angles or scattered particles. For the highest energy, the possibility of a non-single-Gaussian beam in vacuum was investigated for different double-Gaussian shapes in vacuum as explained in Appendix B (figure B.4). The main Gaussian width corresponds to the width extracted in section 4.3.2, while the second one is related to the range of widths of the second and third Gaussian. It allowed forcing the MC and measurements lateral profiles to match at the phantom entrance, however the dose underestimation with MC predictions at larger depths compared to measurements could not be eliminated, thus still hinting on a possible room of improvement for the models of the MC code FLUKA. Additional investigations were performed in Appendix B, weighting the dose contributions of the secondary particles in order to retrieve better *ddds* or lateral profiles.

The results of the SOBP are overall encouraging, with good agreement between corrected measurement and simulations even in the high dose gradient regions. Furthermore, more recent measurements for SOBPs at different depths with an updated dose calibration have shown differences between measurements and simulations below 1% in the SOBP region without any dose corrections in the analysis (data not shown). The reported differences on the lateral FO and irradiated size could originate from the halo dose contributions of the large number of spots used to build the SOBP lateral extension, as well as from IC and/or beam positioning uncertainties. The better agreement found for the SOBP lateral dose compared to previously presented lateral dose profiles is linked to the fact that the investigated SOBP is not as deep seated as the medium and high energies investigated. This implies that for greater depths a larger disagreement in the investigated parameters of lateral FO and irradiated size are to be expected. In addition to the dosimetric validation of the FLUKA MC code for modeling helium irradiation, the possibility to link the simulations to validated biological models as presented in Mairani *et al* (2016a, 2016b) will allow MC treatment planning optimization (Mairani *et al* 2013, Böhlen *et al* 2013) and comparison between different ions, as will be shown in Chapters 6 and 7. Furthermore, this work enabled the creation of a validated physical database of helium ion *ddds* for input into the analytical research TPS at HIT, which is regularly used for planning biological studies (Dokic *et al* 2016), as well as the creation of phase space files as in Tessonnier *et al* (2016) for external user applications, in an identical way that what will be presented for protons and carbon ions in the next Chapter 5.

4.5. Summary

We presented in this chapter an in-depth validation of the FLUKA MC code against dosimetric measurements of ^{4}He ion beams. The results are overall satisfactory even in the case of a 3D SOBP, which is a more complex scenario than *ddds* and line irradiations. Differences in the high dose region were below 1% and below 3% for the entire dose distribution, which demonstrate that the FLUKA code is reliable enough for future clinical use and further studies. Despite the overall very promising agreement, some model improvements could be foreseen to reduce the discrepancies observed in the contribution at large angles of the secondary particles, impacting both *ddds* and lateral profiles, particularly at large energies. By using the experimentally validated MC code in conjunction with validated biological models, it is now feasible to conduct reliable treatment plan comparisons between helium ions and protons (or heavier ions) to investigate the possibility of improving dose distributions and thus patient treatment outcome, in view of the foreseen clinical deployment of helium ion therapy at HIT. A research MC-based treatment planning system and related plan comparisons will be presented in Chapters 6 and 7.

Chapter 5. Phase space generation for proton and carbon ion beams for external users' applications and in-house simulation framework implementation

This chapter deals with the generation of phase-space files created using the beamline model previously presented in Chapter 4, and their implementations within the Monte Carlo framework presented in Bauer *et al* (2014). After describing the theory behind the proposed approach to generating phase-space files for protons and carbon ions and validating against measurements and simulations with the beamline, an example of the application within the framework is shown. The method of phase-space files generation was then extended to helium and oxygen ions, completing the characterization of all available ions at HIT. Further applications of this work are presented in the next chapters. A part of this work was published in (Tessonnier *et al* 2016).

5.1. Background

In the particle therapy field, MC codes provide a powerful tool to perform accurate calculations, with a precise description of the transport and interactions of the beam with the traversed materials, compared to the current treatment planning systems (TPS) as the one used at HIT (Syngo RT Planning TPS, Siemens AG Healthcare), which is based on analytical algorithms using fast pencil-beam dose calculation algorithms (Krämer *et al* 2000). At HIT, the FLUKA MC code was chosen to support the creation of the TPS basic input data (Parodi *et al* 2012), as exlpained in Chapter 2, section 2.7 and performed for helium ions based on the work presented in Chapter 4. The beamline has been modeled in great details, particularly the vacuum window and the Beam and Application Monitoring System (BAMS), composed of

two multiwire proportional chambers and three ionization chambers which are monitoring the beam, providing accurate data for the parametrization of the lateral dose spread for additional input to the analytical clinical TPS (Parodi *et al* 2013, Chapter 4). A MC framework, without using the beamline model but a beamline approximation closely resembling the TPS approach, has been also developed and is used to perform both dose forward calculation and range verification (Bauer *et al* 2013a, 2013b, 2014), providing a powerful computational tool to complement the clinical TPS.

The use of modeled beamlines in MC applications has been described in many works for beam delivery with active energy selection (Parodi *et al* 2013, Molinelli *et al* 2013, Mairani *et al* 2013, Magro *et al* 2015), for passive energy selection with pencil-beam scanning (Grassberger *et al* 2015, Paganetti *et al* 2008), or for passive scattering (Paganetti *et al* 2004, Stankovskiy *et al* 2009). In our case, due to confidential issues with the beamline geometry, the model is not available for external users in need of precise simulation, neither for data analysis comparisons after irradiation at HIT nor for simulation-related researches.

This chapter proposes a solution to this problem with the creation of phase space (PS) files containing the characteristics (charge, mass, energy, coordinates and direction cosines, history number) of all particles (primary protons and carbon ions as well as secondaries) at the end of the beamline, for each of the 255 available initial beam energies. Furthermore, the adaptation to the delivery pattern from the raster scanning system has to be possible with these PS, as well as the accommodation of the 4 different foci used clinically at HIT, i.e. the FWHM of the lateral beam sizes in air at isocenter according to the accelerator database (LIBC, as seen in Chapter 3). PS files created from beamline geometries, in the particle therapy field, have already been investigated for proton beam applications with passive beam delivery or scanned beams of fixed lateral size (Paganetti *et al* 2008, Stankovskiy *et al* 2009, Ramos-Méndez *et al* 2015, Schümann *et al* 2012, Parodi *et al* 2007). The approach presented in this chapter proposes a novel narrow beam approximation to generate PS which can be accurately adapted to reproduce all the foci available at HIT and scanning pattern of irradiation plans for both protons and carbon ions. Several validation steps against simulation with the full beamline geometry will be presented. Simulations using the PS approach will be compared to measurements in a water phantom. After implementation of the PS within the in-house simulation framework, an application of the proposed approach to a small target patient plan will be shown and compared to the results of the simplified MC framework. For this plan, the two approaches will be evaluated against measurements in a water phantom.

5.2. Materials and Methods

5.2.1. Phase space generation

5.2.1.1. Monte-Carlo code and modeling approaches of the HIT beamline

Different approaches have been used concerning the modeling of the beamline for MC simulation at HIT. The detailed geometrical model (Parodi *et al* 2013) allows simulating transport and interactions occurring in the beamline more precisely, particularly inside the BAMS, for accurate prediction of lateral beam scattering (figure 5.1). The different foci are representative of the spread of an initially small (millimeteric) beam in vacuum into the beamline and air. In the simplified MC framework the beamline is approximated by an energy reduction before the propagation of the particles in vacuum, according to the water equivalent thickness of the beamline and air distance to the isocenter. The focus is then adapted geometrically to its nominal value at the isocenter (Parodi *et al* 2012, Bauer *et al* 2014),

similar to the TPS approach dealing with a beam impinging on the target in vacuum. With this simplified approach, forward recalculation of planned treatments could well predict dosimetric measurements in most of the cases, with differences below 3% (Bauer *et al* 2014). However, the approximations made in such MC framework (so called TPS-like approach (Bauer *et al* 2014)) could have limitation for extreme cases e.g. small fields, due to an underestimation of large angle lateral scattering in the elements before the target. Furthermore, with the explicit modeling of the beamline geometry, information on the primary and secondary particles exiting the BAMS could be tracked, as well as their impacts. Hence, in order to give the possibility to external users to perform precise simulations using the detailed geometrical modeling of the beamline, without disclosing its confidential components, we developed an original PS approach (see next section).

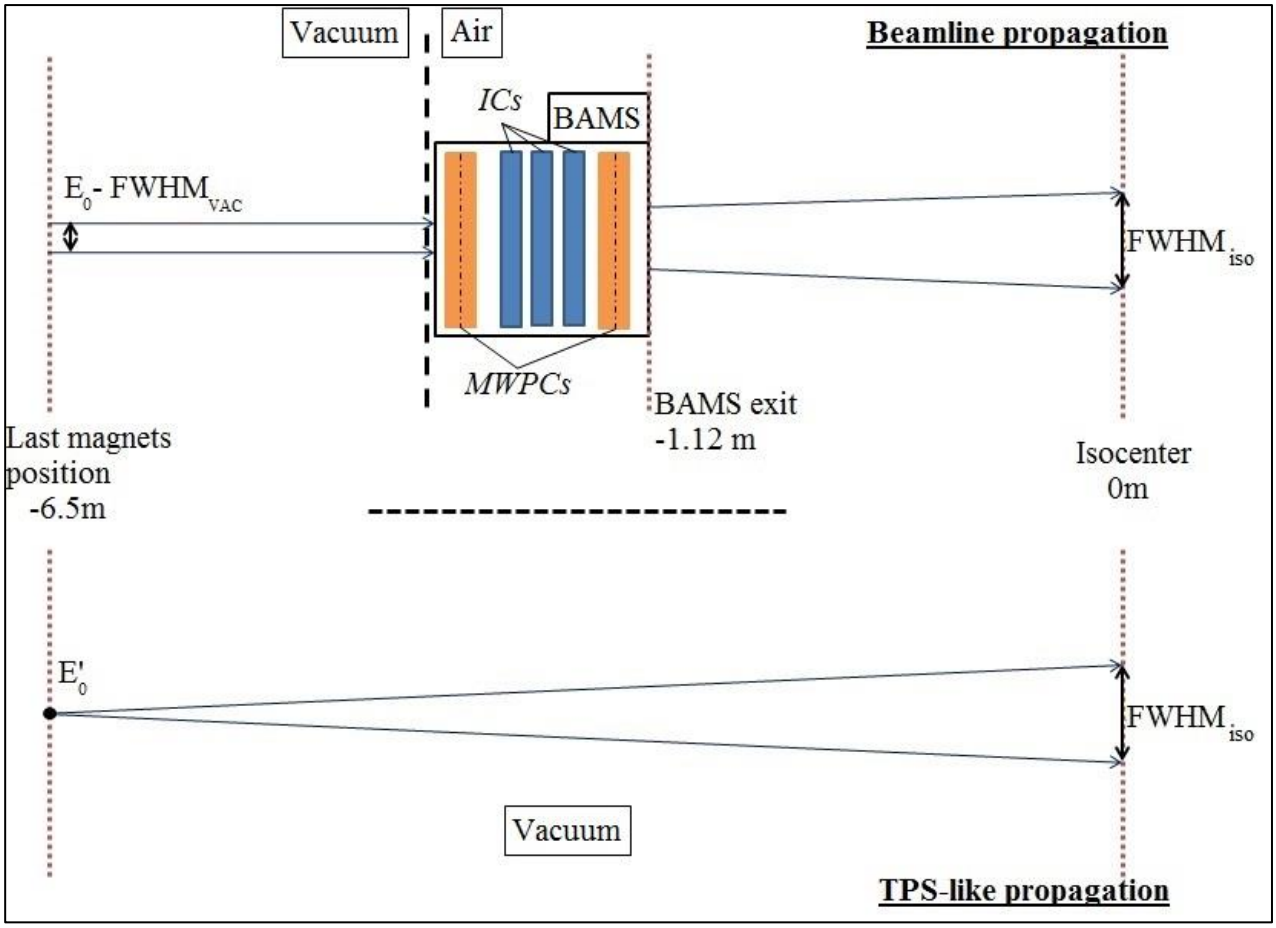

Figure 5.1: Schematics of different MC approaches for simulation transport: on the upper panel, the detailed beamline allowing precise description of the particle interactions, from a proton beam with an initial energy E_0 and an initial focus $FWHM_{vac}$; on the bottom panel the simplified TPS-like approach propagating the particle in vacuum to the isocenter, with an initial energy E'_0 taking in account the energy reduction of E_0 due to the BAMS water equivalent thickness and adapted geometrically to the same $FWHM_{iso}$ used by the TPS at isocenter.

The FLUKA version used in this chapter was the 2011.2c. The version used in the other chapters is the development version to include the latest physics related to helium ions. However, between these two versions, no particular differences were found for protons and carbon ions due to the changes in models, as verified on test cases such as depth dose distributions, as presented in the following. In order to reproduce the HIT reference Bragg curves presented in Chapter 3 and with a similar process as that presented in Chapter 4 for helium ions, several optimizations have been made on the initial beam momentum spread for every energy as well as the ionization potential in water, analogue to prior studies using older FLUKA versions (Parodi *et al* 2012, Kurz *et al* 2012). The optimal ionization potential value in water was found at 77.3 eV for protons and 76.8 eV for carbon ions, as previouly mentioned in Chapter 4. The "HADROTHErapy" settings with the "EVAPORation" physics model were used for both phase space generation and dosimetric verification. These two settings were described in detail in Chapter 4. In consideration of time and data storage efficiency during PS file generation, photons and electrons were not transported, thus depositing their energy at the production point.

5.2.1.2. Phase space requirements

The PS files characterize the beam on a plane perpendicular to its propagation at a defined position along the beam path, by describing the properties of every crossing particle (charge, mass, energy, coordinates and direction cosines, history number).

Several goals were defined prior to the generation of the PS: (1) for every initial beam energy of proton and carbon ions, a unique PS should be generated and adapted to all the possible foci available at HIT, (2) the FWHM in air at isocenter obtained with the PS should not be different from the reference foci values of the TPS basic data or LIBC (i.e., FWHM in air at isocenter) within the tolerances defined internally at HIT to account for possible daily variations of the beam shape ([-15 , 25] % of the reference). The same tolerances are defined for comparing the simulations using the new PS approach to measurements of FWHM in water at different depths. For the comparisons between the full beamline geometry (BL approach) and the PS approach, we decided that the differences in FHWM at isocenter in air should be inferior to 3%. (3) Additional requirements included a consistent propagation of the primary and secondary particles, meaning that particles generated from the same primary history must be transported together. Also, the PS approach should lend itself to beam propagation according to the raster scanning pattern of the treatment plan. (4) A reasonable compromise between the size of the PS files and the number of simulated particles has to be found, in order to have enough available statistics per energy and also saving all the needed information.

5.2.1.3. Phase space narrow beam approach

In order to respect the requirements on the adaptability of a unique PS to different foci we develop an original narrow beam approach for PS files generation. It can be explained by analogy with a homogeneous analytical system, whose response R_δ to a Dirac signal δ is its impulse response S. In addition, the response R_G of this system to a Gaussian signal G will be the convolution between the signal G and the impulse response S.

$$R_\delta = S * \delta = S, \tag{5.1}$$
$$R_G = S * G, \tag{5.2}$$

In this way, when using an infinitely narrow ("zero-width") beam propagated in the beamline (by analogy δ), the PS scored at the end of the BAMS of the beamline (by analogy the system), specifically the information on the particles position, represents the impulse response *S* of this system.

Therefore, an adaptation to every focus is possible by convoluting the PS with the information on the particle position, using a Gaussian distribution *G* to represent the beam in vacuum before entering the beamline. It is known that the result of the convolution between two Gaussian functions is still a Gaussian, with a width (standard deviation) σ(G1*G2) corresponds to the quadratic addition of the widths of the two Gaussians G1 and G2, σ(G1) and σ(G2). Assuming that the fluence distribution of this PS is Gaussian-like, this approach is consistent with the quadratic addition as in Parodi *et al* (2013), with σ the beam focus at isocenter, σ_0 the beam broadening at isocenter due to a 'zero-width' beam and σ_{ini} the estimated initial beam in vacuum:

$$\sigma(G1 * G2)^2 = \sigma(G1)^2 + \sigma(G2)^2, \quad (5.3)$$

$$\sigma^2 = {\sigma_0}^2 + {\sigma_{ini}}^2, \quad (5.4)$$

For every focus a different value of the beam initial size in vacuum is needed and has to be estimated. The theoretical Gaussian FWHM of the beam in vacuum (before the beamline) is investigated as a function of the energy using this narrow beam approach. By scoring the position of the primary particles at the isocenter, for several energies in the therapeutic range, and evaluating the FWHM of their distributions at the center of the beam spot along the horizontal axis, the FWHM of the vacuum Gaussian beam $FWHM_{Vacuum}(focus)$ can be retrieved using the following equation for every focus:

$$FWHM_{Vacuum}(focus)^2 = FWHM_{Isocenter}(focus)^2 - FWHM_{Isocenter}(\delta)^2, \quad (5.5)$$

where $FWHM_{Isocenter}(focus)$ is the FWHM size at isocenter in air for one focus extracted from the HIT LIBC database, $FWHM_{Isocenter}(\delta)$ is the FWHM size in air at isocenter after the propagation of an infinitely narrow beam. The energies investigated are {48.12, 54.19, 80.90, 106.82, 132.30, 157.43, 182.66, 221.05} MeV/u for protons and {88.83, 100.07, 150.42, 200.28, 250.08, 299.94, 350.84, 430.10} MeV/u for carbon ions.

Calculated $FWHM_{Vacuum}(focus)$ are compared to the expected values from previous work (Parodi *et al* 2012) and are used for the final validation of the PS approach, as well as for the rest of the study. A total of 1×10^7 primary histories are simulated for each run.

With the beam records of the irradiation, where the information about the size of the focus at the isocenter are recorded, a new estimated focus size in vacuum could be calculated by replacing the nominal $FWHM_{Isocenter}(focus)$ with the value extrapolated from the upstream measurement of the BAMS.

5.2.1.4. Phase space scoring

PS files are generated for protons and carbon ions at every energy in the HIT accelerator library, using an optimized beam momentum spread, transporting 1×10^7 primary histories in total, resulting in files with a total size of about 500Mb each. The initial lateral size of the beam is set to a zero-width distribution (see section 5.2.1.3). The scoring is done on a 4m²

square plane perpendicular to the beam direction at the end of the BAMS, just after the last element of the beamline, i.e., the second multiwire proportional chamber, at about 112 cm before the isocenter.

Two files are created. The first file corresponds to the scoring of the primary beam with the information about the energy, the position in the plane (X,Y position) and the direction cosines (d_X, d_Y direction cosines). The second file contains the information about the secondary particles (except photons and electrons) in terms of energy, position, direction cosines, charge and mass information of every particle. Last information to be saved in both files is the generation number of the primary, which allows linking primary to secondary particles during the propagation process. To ensure that the PS is representative of the different interactions occurring in the beamline, the starting positions of the narrow beam are randomly selected in a 5mm x 5mm square around the central axis. Information on these starting positions is kept during the beam propagation in the beamline to the scoring position, and then subtracted to the scored position of every particle in the PS files.

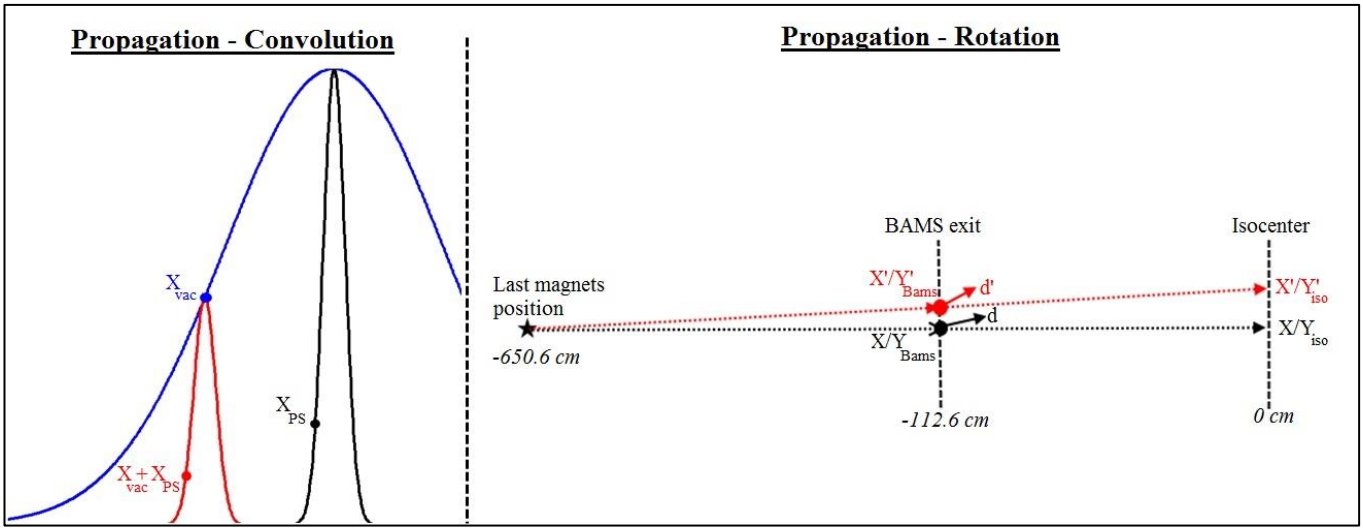

Figure 5.2**:** PS propagation process: on the left panel, convolution results (red) between the PS from the narrow beam (black) and the Gaussian in vacuum (blue): new position (X_{vac}+X_{PS}) obtained from the original position on the phase space (X_{PS}) and the selected position on the Gaussian in vacuum (X_{vac}); on the right panel, rotation of the beam to the expected position: transformation from the X/Y position at the BAMS with a direction cosine d to the new X'_{Bams}/Y'_{Bams} position at the BAMS with the direction cosines d' in order to reach the X'_{iso}/Y'_{iso} position at isocenter.

5.2.1.5. Phase space propagation for scanned beam delivery

While performing a treatment plan simulation using the PS, so called PS approach, the propagation process is divided in 5 steps:

- Reading the plan used for irradiation and segmenting the requested number of primary histories for the simulation run among the different energy slices according to the weight of the number of particles per slice compared to the total number of particles of the plan. This is the only step of the process which is not random in order to read the PS files only one by one, not to overload the computer memory.
- Reading the PS file of the current energy slice and linking primary and secondary particles.
- Selecting randomly a generation number among the 10 million possible, to be handled as the next primary history. Then loading all the particles related to this primary history into the stack of particles to be propagated. Every possibility can be handled (a primary with no secondaries, only secondaries, primary and secondaries, no particles scored in the PS).
- The convolution process at the single particle level is performed by adding the position information (X_{PS}, Y_{PS}) of each particle of the stack (loaded from the PS) to respectively 2 distinct random positions (X_{Vac}, Y_{Vac}) selected from a Gaussian distribution with a FWHM size corresponding to the expected Gaussian size of the beam in vacuum for the selected focus (see figure 5.2 and section 5.2.1.3). This initial Gaussian distribution in vacuum is assumed to have the same FWHM in X and Y. The final position of the particle to be transported is then $X_{PS} + X_{Vac}$, $Y_{PS} + Y_{Vac}$.
- Selecting randomly one of the planned positions at isocenter (X'iso,Y'iso) in the current energy slice, with probability weighted by the number of particles to be delivered to this spot compared to the total one of the energy slice. In order to reach this position the PS have to be rotated from the original position (X_{iso} ,Y_{iso}, corresponding to the position of the central beam axis at isocenter) to the selected coordinate (X'_{iso},Y'_{iso}). This means finding a new position on the PS plane (X'_{Bams},Y'_{Bams}) with respect to the original one along the central axis (X_{Bams},Y_{Bams}) and adapting the new direction cosines (d') from the original one of the selected particles (d) in order to target the selected isocenter position after propagation (figure 5.2).

This method holds the advantage that even with only 10 million particles in the PS, the convolution with random positions of the beam Gaussian shape in vacuum increases the number of combinations of position and energy, thus decreasing the probability to have the same event repeated twice.

5.2.2. Validation and comparisons

5.2.2.1. Validations of the PS approach

Validations of the PS approach are performed against the BL approach, i.e., propagation with the beamline geometry, for different cases. The first pencil-beam validation step is focused on the differences between the two approaches in terms of fluence distributions and particle spectra for a central beam delivery without scanning. For the additional validation steps with scanned beam delivery featuring line scans and spread out Bragg-peak (SOBP) distributions, the comparisons are made on the dose results.

5.2.2.1.1. Pencil-Beam validation

For both protons and carbon ions, two energies have been investigated, namely the lowest (respectively 48.12 and 88.83 MeV/u) and the highest (respectively 221.06 and 430.10 MeV/u), for the largest and smallest foci (i.e., focus index 1 and 4) used in clinical routine. Different PS files were generated at different positions along the beam path in order to investigate the beam propagation in air for a fixed central pencil beam: PS_{BAMS} is recorded on a 4m² plane at the BAMS exit at the same position as the one generated with the narrow beam approach, while PS_{iso} is recorded on a 4m² plane at the isocenter. Three scenarios are compared for the different energies:

- Simulations with BL approach with different focus sizes: $PS_{BAMS,BL(focus)}$ and $PS_{iso,BL(focus)}$, starting from a beam in vacuum with the estimated beam size in vacuum before the beamline
- Simulations with BL approach for the narrow beam propagation: $PS_{BAMS,BL(\delta)}$ and $PS_{iso,BL(\delta)}$, starting from an infinitely narrow beam in vacuum before the beamline, as in the PS generation process
- Simulations with the PS approach for different focus sizes: $PS_{iso,PS(focus)}$, starting from the PS in air at the BAMS exit position (where the PS have been generated)

The fluence and energy distributions are investigated for both primary and secondary particles.

On the planes perpendicular to the beam propagation, at the BAMS exit position and the isocenter, the FWHM of the fluence distributions at the center of the pencil-beam spot along the horizontal axis are reported, as well as the FWHM of the vertically integrated profiles.

For the vertically integrated profiles at the isocenter, the absolute global differences are also analyzed. It corresponds to:

$$Difference_{global}(x) = 100 \times \frac{|Fluence_{PS}(x) - Fluence_{BL}(x)|}{\max(Fluence_{BL})}, \quad (5.6)$$

with *Fluence(x)* the fluence on the profile at the position x (for both approaches), and $max(Fluence_{BL})$ the maximum fluence along the profile. The mean, standard deviation and maximal deviation of these differences are reported. These values are calculated in a region of the profiles where the fluence is superior to 0.1% of the maximal fluence. The bin size of the profile is 0.2 mm.

For the energy spectrum, the same analysis is performed on the different PS files acquired at the isocenter, however the *x* variable corresponds to an energy bin in the energy distribution. The bin size is 0.04 MeV/u. The energy spectrum of the secondaries is qualitatively analyzed as their proportion compared to the primaries is low (maximum probability for an energy bin around 0.05% per primaries), hence only the trend and similarities of the spectrum are compared.

For the BL and the PS approach scenarios 1×10^7 and 5×10^6 primary histories are simulated respectively. For quantitative purposes, only 5×10^6 primary histories are used for the analysis, for both approaches, in order to have a fair comparison.

5.2.2.1.2. Line scan validation

For both protons and carbon ions we designed plans corresponding to a vertical line scan, extending from -5 cm to +5 cm with a 1mm step and centered horizontally (i.e., at 0 cm), in a similar way as presented in Chapter 3 and Chapter 4. Three initial beam energies within the therapeutic range are investigated, a low energy (80.90 and 150.42 MeV/u for protons and carbon ions, respectively), a middle energy (157.43 and 299.94 MeV/u, respectively) and the highest energy (221.06 and 430. MeV/u), in combination with each of the four foci used in clinical routine, thus resulting in a total of 24 line scans. The geometry of the simulated target represents the water phantom used for plan verification measurements, positioned at the treatment isocenter, with a 5 mm PMMA entrance window, as presented in Chapter 4, section 4.2.3.2 . The bin size of the dose scoring grid is set to 0.5 mm x 0.5 mm x 0.5 mm. To ensure enough statistics, 1×10^8 primary histories were simulated for both approaches in 100 statistically independent runs. Both laterally integrated depth dose profiles, scored along the beam penetration in water, and lateral dose profiles, sampled at the entrance of the target, are compared between the BL and PS approach. For every dose profile, we investigate both the absolute local dose relative difference:

$$Difference_{local}(x) = 100 \times \frac{|Dose_{PS}(x) - Dose_{BL}(x)|}{Dose_{BL}(x)}, \quad (5.7)$$

and the absolute global dose relative difference:

$$Difference_{global}(x) = 100 \times \frac{|Dose_{PS}(x) - Dose_{BL}(x)|}{\max(Dose_{BL})}, \quad (5.8)$$

with *Dose(x)* being the dose of the profile at the position *x* (for both approaches), and *max(Dose$_{BL}$)* being the maximum dose along the profile.

5.2.2.1.3. SOBP validation

SOBP plans have been simulated with both the PS and the BL approaches for protons and carbon ions, in the latter case using the ripple filter geometry (RiFi, as seen in Chapter 4). SOBP plans are designed to deliver 1 Gy to a 5 cm x 5 cm x 3 cm target, centered at 10cm depth in water. The same MC geometry with the water phantom is used, as described in section 5.2.2.1.2. The dose scoring grid is set to a bin size of 1 mm x 1 mm x 1 mm. A total of 1×10^8 primary histories are used to simulate these plans. In this more clinical-like scenario only the absolute global differences of the doses between the BL and PS approaches are investigated along the central depth dose profile and for the lateral dose profiles sampled at the entrance of the target and in the middle of the SOBP.

5.2.2.2. Comparisons of the PS approach with measurements

The line scan plans, presented in section 5.2.2.1.2, have also been irradiated in the experimental room at HIT. The measurements were performed in the water phantom equipped with 24 motorized pinpoint ionization chambers, previously described in Chapter 3. For each block position in depth, six measurements were performed with a 2 mm horizontal shift perpendicular to the beam direction to complete the lateral profiles. The lateral extension of each profile is 46 mm. The block was put at three positions along the beam path in order to

sample lateral profiles at the entrance of the phantom, in the plateau of the Bragg peak and near the Bragg peak. The measurements were acquired for every combination of particle type / energy / focus presented previously in section 5.2.2.1.2.

For this comparison, the MC simulations using the PS approach are the same as the one presented previously. However, in order to have a fair comparison between the PS approach and the measurements, the sensitive volume of the ionization chamber has been taken into account in the MC dose results, by averaging the dose value of the voxel of interest with the surrounding ones to obtain a resulting integration volume close to the one of the ionization chamber.

The lateral profiles are analyzed quantitatively at three different depths, for each energy and focus, and the FWHM of both measurements and simulation are compared. For the lowest energy, with a range of around 53 mm, the depths analyzed are 15.7 mm, 30.7 mm and 45.7 mm. For the middle energy, with a range around 172 mm, the depths analyzed are 15.7 mm, 85.7 mm and 151.7 mm. For the highest energy, with a range around 308 mm, the depths analyzed are 15.7mm, 195.7mm and 267.7mm. The mean and the standard deviation of the absolute differences are reported for protons and carbon ions.

5.2.3. Implementation of the PS in the MC framework

In order to take advantage of the beamline model in the in-house MC framework, PS files were implemented in the simulations. Several changes regarding the original framework using the PS approach were made, also taking advantage of new capabilities of FLUKA, and are schematized in figure 5.3:

- The direction of the beam is fixed in contrast to the original simulations, where the beam was rotated around the patient as a function of the beam angle and the couch position (rotation, pitch and roll).
- The patient CT voxelized geometry is moved (via rotations) to adapt to the movement of both the gantry (beam angle) and the couch position, while it was fixed in the previous version for both parameters.
- More precise description of the interactions in the beamline, as seen in figure 5.2, with air instead of vacuum between the PS plane (end of BAMS) and the patient.

Several tests were designed with different levels of complexity and compared to the TPS as gold standard. These tests need to describe all the possibilities allowed by the use of a gantry (rotation around the table with respect to a horitontal axis centered on the isocenter), the rotation of the treatment table (rotation of the couch in the horizontal plane around a vertical axis at isocenter, and pitch and roll rotation around an axis centered at isocenter and oriented along either the lateral or longitudinal axis of the treatement table). The plans included the following:

- one to several beams,
- fix table with different beam angles,
- fix beam angle with rotation of the couch,
- the previous case with pitch and/or roll,
  a combination of the different precedent possibilities.

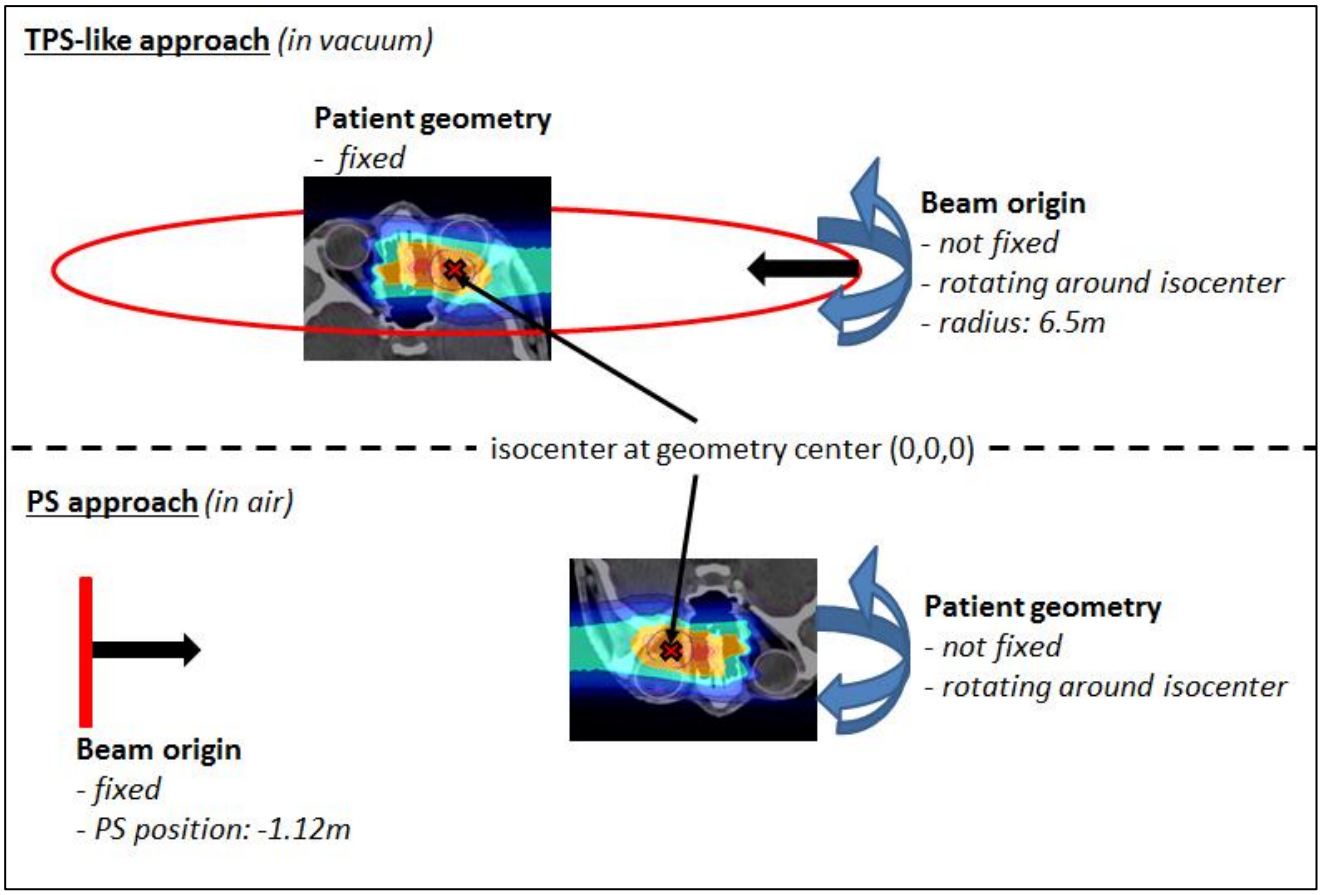

Figure 5.3**:** Schematic of different framework approaches for simulation: on the upper panel, the TPS-like approach with a fixed patient geometry and a rotating beam as a function of the plan parameters. In the lower panel the PS implementation approach with a fixed origin at the PS plane and a rotating voxelized patient geometry as a function of the beam plan parameters.

5.2.3.1. Application to a small target clinical case

A challenging clinical case has been selected for testing the PS application: an arterio-venous malformation (AVM). AVM are congenital malformation assumed to not undergo modification in time (implying then low α_x/β_x from LQ model as explained in Chapter 2, section 2.3), which are mostly treated following hypofractionation scheme. Some studies demonstrate that AVM yield a high α_x/β_x which should support hyperfractionation (Vernimmen et al 2010), however α_x/β_x are elusive for smaller target. At HIT, the selected AVM are a small targets, inferior to 20 ml in most of the cases and below 3 ml in our study, treated at HIT with protons in one fraction of 18 Gy RBE at the isodose 80%. Magro *et al* (2015) found for small targets at shallow depth discrepancies between TPS and measurements in water up to ~19%.

Among the four beams of the plan, we selected the plan delivering the highest dose. Dosimetric measurements for this beam were performed in the same water phantom described in section 5.2.2.2, and compared to the dose calculations resulting from the PS approach and

the simplified MC framework using the TPS-like approach. Several lateral profiles in the horizontal direction, with a 1mm lateral step, are acquired at different depths of 19.7mm, 29.7mm 39.7mm and 49.7mm.

Furthermore, using the information from the irradiation beam records registered by the BAMS, it was found that all foci were on average 1mm larger than the values of the TPS database, used in both the PS (in terms of the beam vacuum size added to the narrow beam approach) and TPS-like simulations. Hence, new expected Gaussian sizes of the beam in vacuum were generated and an additional simulation was performed for the PS approach with these new parameters for comparison to the measurements and the previous simulations.

The geometry for the MC simulations is using the same water phantom target as for the SOBP simulations. The dose scoring grid is with a bin size of 1mm x 1mm x 1mm and the number of primary histories is set to 5% of the beam total number of particles, which is five time higher than the recommend statistics according to Bauer *et al* (2014).

In a second step, forward dose calculations of the whole plan in the patient CT geometry have been performed for both the TPS-like and PS approach, using the reference LIBC foci value at isocenter. The results are compared in term of dose profiles sampled within the target region (planning target volume, PTV) region and PTV dose volume histograms.

5.3. Results

5.3.1. Validation of the PS approach

5.3.1.1. Gaussian shape in Vacuum

For Carbon ions, the calculated FWHM values of the Gaussian lateral beam distribution in vacuum are within 0.2 mm to the ones expected: 2.5 mm, 5 mm, 7.5 mm, and 9.5 mm for the foci from 1 to 4. For focus 1, the mean calculated FWHM (μ) is 2.46 mm with a standard deviation σ of 0.15 mm, μ=5.02 +/- 0.09 mm, μ=7.47 +/- 0.07 mm and μ=9.49 +/- 0.06 mm for focus 2, 3 and 4 respectively. As the focus increases, the σ decreases due to an easiest FWHM evaluation in regards to the bin size. Considering the bin size of 0.2 mm and the small difference to the expected value, the nominal values are kept for the whole work.

In constrast, the calculated FWHM for protons are far different from the initial values of {2.5, 6, 8 and 10} mm assumed in a previous work, which involved only using a simplified beamline modeling to guide the LIBC generation at a time when beamline details had not been yet disclosed by the vendor (Parodi *et al* 2012). It should also be noted that for foci higher than focus 1, the FWHM foci values for the low energy region (<100 MeV/u) do not correspond to the cited values, due to an asymptotical convergence used to avoid too large beam width at the isocenter (Parodi *et al* 2012). From the simulated eight energies in the therapeutic range, an interpolation is done (figure 5.4). For focus 1, we found μ=6.46 +/- 2.05 mm on the whole energy range. For energies above 100 MeV/u, for focus 2 we obtained μ=7.69 +/- 0.37 mm, for focus 3 μ=9.40 +/- 0.30 mm, for focus 4 μ=11.16 +/- 0.26 mm. These new values are used for the whole study in order to reach with the PS simulation a good agreement to the LIBC foci values at isocenter, which are also used by the TPS.

5.3.1.2. Pencil-Beam validation

5.3.1.2.1. Fluence distributions

For the two extreme foci analyzed, the lateral profiles obtained at isocenter with the PS and BL approaches are similar, regardless of the considered energy and ion species (figure 5.5). The absolute global differences between the two approaches are under 2.5% for protons and under 1.3% for carbon ions (Table 5.1). The FWHM values of the lateral profiles, for the

profiles in the center of the pencil beam spot and for the vertically integrated profiles, at the BAMS exit positions and at isocenter, are reported in Table 5.2. For protons (for both energies and foci) the maximal difference is equal to 0.1mm for the vertically integrated profiles and 0.2 mm for the horizontal profile along the spot center. For carbon ions (both energies and foci) the maximal difference is equal to 0.1 mm for the vertically integrated profile and 0.2 mm for the profile sampled along the spot center. For both particles type, the difference to the nominal expected values at the isocenter from the database is under 3.5% and 0.5mm with the FWHM values in vacuum obtained from section 5.3.1.1.

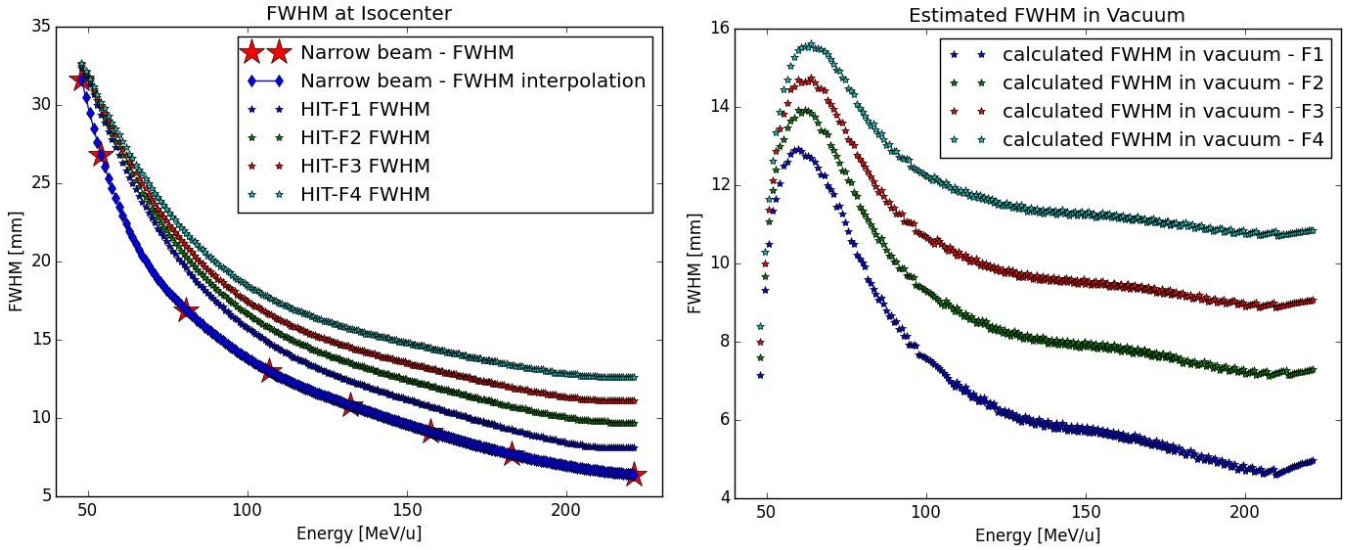

Figure 5.4**:** Calculation of the protons Gaussian FWHM in vacuum: on the left panel, the different FWHM size of the proton foci at isocenter from the LIBC are displayed as a function of the energy, as well as the calculated FWHM size for the narrow beam approach (star) and its interpolation; on the right panel, the results of the quadratic subtraction between the two previous quantities yielding the initial beam size in vacuum for the different foci as function of the energy.

	Protons						Carbon ions					
	48.12MeV/u			221.06MeV/u			88.83MeV/u			430.10MeV/u		
	μ(%)	σ(%)	max(%)	μ(%)	σ(%)	max(%)	μ(%)	σ(%)	max(%)	μ(%)	σ(%)	max(%)
F1	0.33	0.32	2.30	0.06	0.13	0.91	0.07	0.13	0.93	0.02	0.06	0.83
F4	0.35	0.34	2.20	0.08	0.17	1.30	0.10	0.18	1.26	0.05	0.12	0.85

Table 5.1**:** Primary particle fluence differences at the isocenter (absolute global differences with mean μ, standard deviation σ and maximum value) between the PS and the BL approaches for both focus 1 and 4 for the vertically integrated lateral profile distributions, in percentages compared to the maximum fluence (calculated for spectra regions with a corresponding fluence >0.01% of the maximum one).

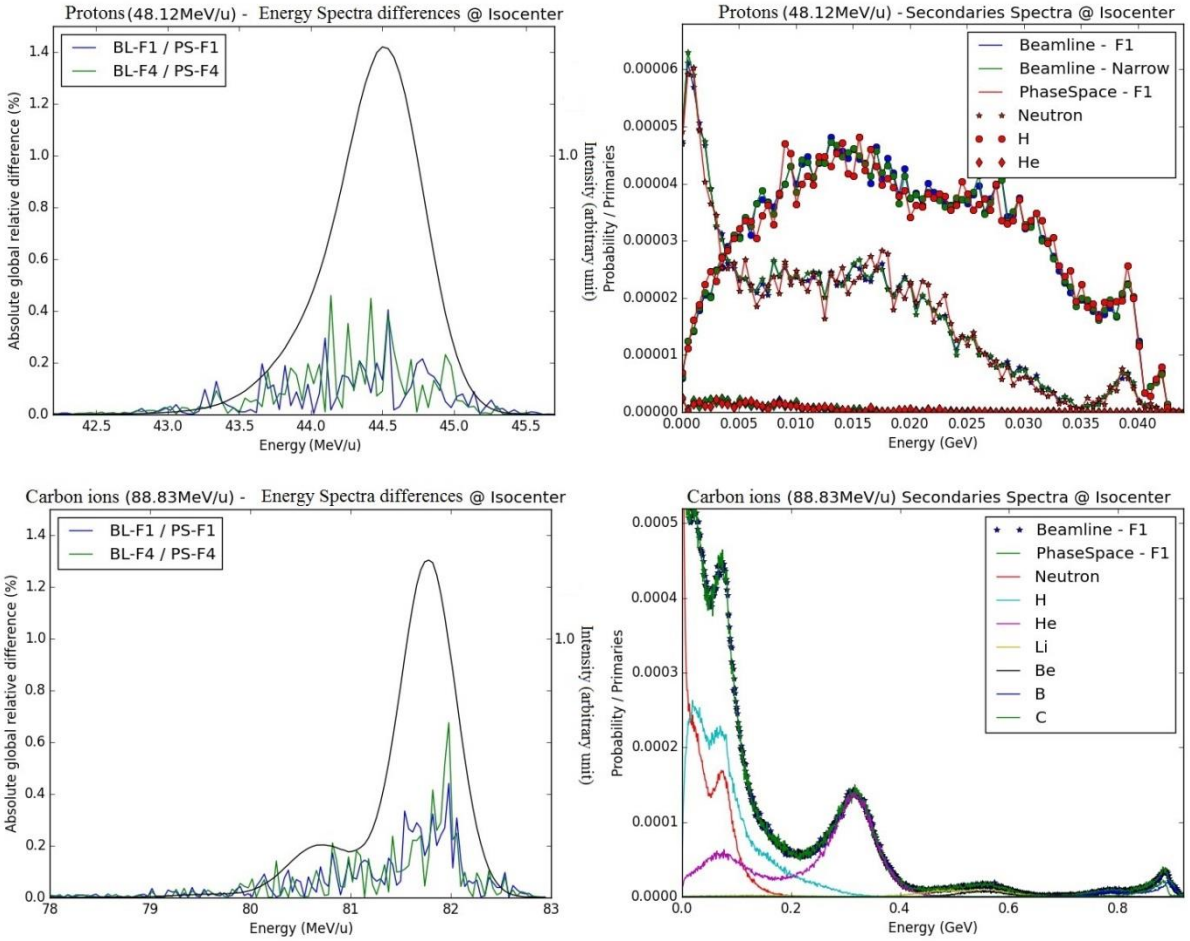

Figure 5.5: Energy spectra difference for protons and carbon ions at the isocenter in air: on the left panels, absolute differences in primary spectra obtained with the PS and BL approaches are displayed for focus 1 and 4 (blue and green) together with the primary spectra shape (in black, similar for focus 1 and 4 and both approaches). On the right panel, secondary spectra at isocenter are displayed for the beamline approach (narrow beam and focus 1) and the PS approach. The upper panels correspond to protons, energy 48.12MeV/u, and the bottom panels correspond to carbon ions, energy 88.83MeV/u.

			48.12MeV/u		221.06MeV/u	
		position	Profiles(mm)	Int. profiles(mm)	Profiles(mm)	Int. profiles(mm)
Protons	DB-F1	Isocenter	32.4	/	8.7	/
	DB-F4	Isocenter	32.6	/	12.6	/
	BL-Narrow	BAMS	4.1	4.2	0.9	0.9
		Isocenter	32.0	34.1	6.8	6.8
	BL-F1	BAMS	8.6	8.6	5.0	5.0
		Isocenter	32.4 (0 %)	34.5	8.9 (2.3%)	9.1
	BL-F4	BAMS	9.4	10.6	10.8	10.8
		Isocenter	32.5 (-0.3%)	35.0	13.0 (3.2 %)	13.5
	PS-F1	Isocenter	32.3 (-0.3 %)	34.6	9.0 (3.4%)	9.2
	PS-F4	Isocenter	32.6 (-0.6 %)	35.0	12.8 (1.6 %)	13.5

			88.83MeV/u		430.10MeV/u	
		position	Profiles(mm)	Int. profiles(mm)	Profiles(mm)	Int. profiles(mm)
Carbon ions	DB-F1	Isocenter	9.8	/	3.4	/
	DB-F4	Isocenter	13.4	/	9.8	/
	BL-Narrow	BAMS	1.3	1.3	0.4	0.4
		Isocenter	9.6	9.6	2.5	2.5
	BL-F1	BAMS	2.9	2.9	2.7	2.7
		Isocenter	10.0 (2%)	10.4	3.5 (3%)	3.6
	BL-F4	BAMS	9.7	10.3	9.6	9.6
		Isocenter	13.7 (2.2%)	14.2	9.9 (1%)	9.9
	PS-F1	Isocenter	9.8 (0%)	10.4	3.5 (3%)	3.5
	PS-F4	Isocenter	13.6 (1.5%)	14.2	9.8 (0%)	9.9

Table 5.2**:** FWHM, in mm, of the different fluence distributions for protons and carbon ions, with respect to the reference one from the LIBC: FWHM values for profiles sampled at the center of the beam spot and for vertically integrated profiles (Int. profiles), for two positions in depth in air (exit of the BAMS and isocenter) for both focus 1 and 4. For the different foci at isocenter, the variations in percentage to the LIBC foci value are shown in bracket. DB- stands for the LIBC database values, BL- for the BL approach values and PS- for the PS approach.

5.3.1.2.2. Energy spectrum

From visual analysis, the different energy spectra for the primary particles of both carbon ions and protons at the isocenter are similar for the different foci simulated with the BL (focus 1, 4 and narrow beam) or while using the PS approach for the focus 1 and 4. Quantitatively, the energy spectra at the isocenter of the BL and the PS approaches are highly similar regarding their differences (figure 5.6). The absolute global differences between the BL and the PS approaches are reported in the Table 5.3. The maximal deviation for protons is 0.46% and for carbon ions 0.68%.

For the less abundant secondary particles, the different approaches show profiles with the same trend for both protons and carbon ions (figure 5.6).

5.3.1.3. Line scan validation

The line scan validation step exhibits similar results for the simulations performed with the BL and the PS approaches, both in terms of depth as well as lateral dose profiles (figure 5.7).

For both type of particles and all explored combinations of energy and focus values, the absolute global dose relative difference between the PS and the BL approaches is below 0.5% for the laterally integrated depth dose profiles, and the local dose relative difference is below 0.8%. For the lateral profiles, the maximal absolute global dose relative differences are less than 0.5%, while the absolute local dose relative differences reach higher values in low dose regions, but still well below the MC percentage errors (figure 5.7), as calculated over the 100 statistically independent runs.

5.3.1.4. SOBP validation

In terms of extended SOBP fields, both the simulated approaches yield depth and lateral dose profiles in excellent agreement with each other (figure 5.8), with absolute global dose relative differences below under 0.5% regardless of the considered ion species.

	Protons						Carbon ions					
	48.12MeV/u			221.06MeV/u			88.83MeV/u			430.10MeV/u		
	μ(%)	σ(%)	max(%)	μ(%)	σ(%)	max(%)	μ(%)	σ(%)	max(%)	μ(%)	σ(%)	max(%)
F1	0.05	0.07	0.41	0.04	0.06	0.31	0.06	0.08	0.44	0.07	0.08	0.35
F4	0.06	0.10	0.46	0.05	0.07	0.30	0.06	0.10	0.68	0.08	0.10	0.42

Table 5.3: Primary particles energy spectra differences at the isocenter (absolute global differences with mean μ, standard deviation σ and maximum value) between the PS and the BL simulation approaches for both focus 1 and 4, in percentages compared to the maximum fluence (calculated for spectra regions with a corresponding fluence >0.01% of the maximum one).

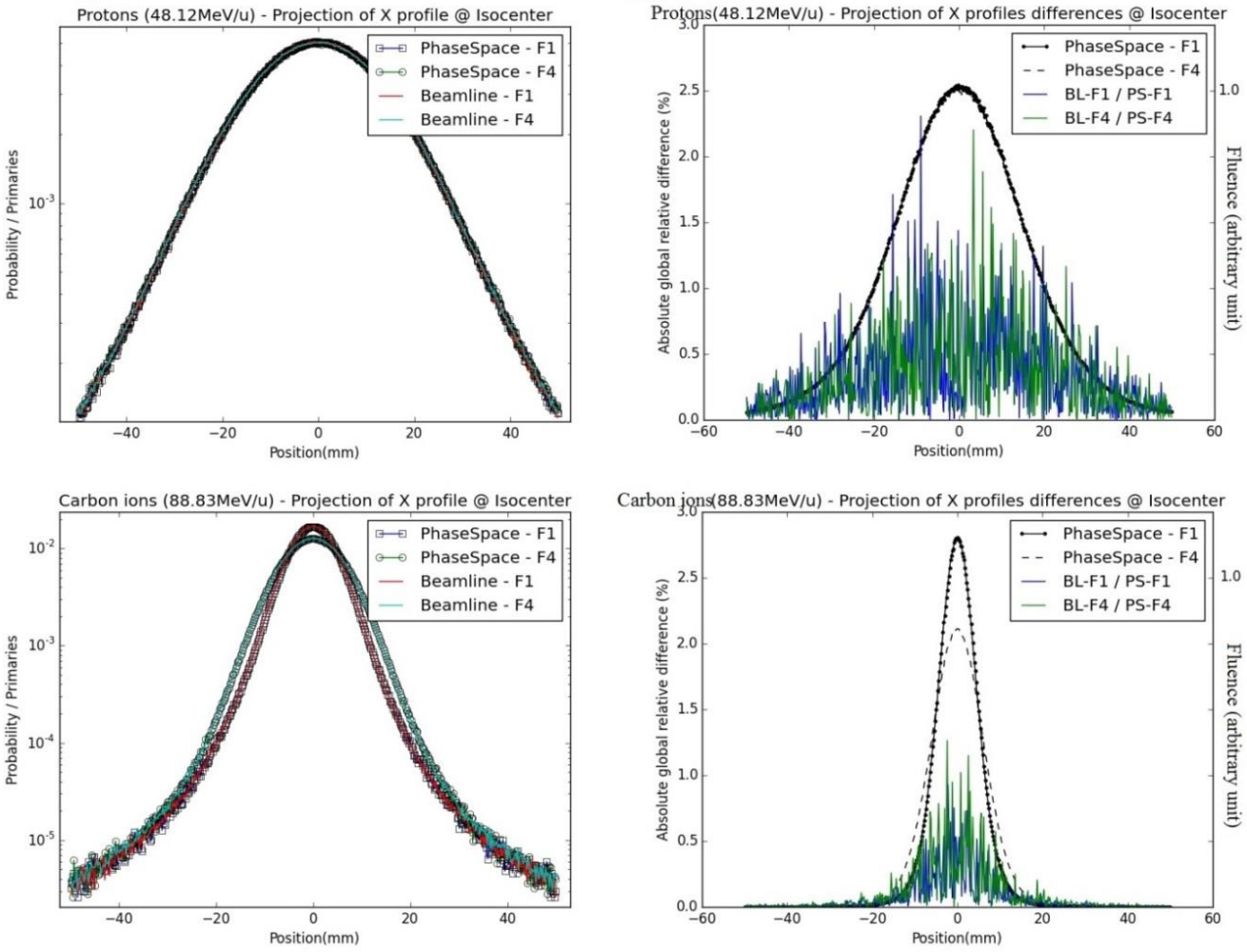

Figure 5.6: Fluence distributions for protons and carbon ions at the isocenter in air – vertically integrated profiles: on the left panels, vertically integrated profiles (projections of X profiles) from BL and PS approaches are displayed for focus 1 and 4 in semi-logarithmic scale; on the right panels, absolute relative differences between lateral distributions from PS and BL approaches are displayed for focus 1 and 4 of the smallest energy (blue/green) together with their respective shapes (black). The upper panel corresponds to protons (48.12MeV/u), the bottom panel corresponds to carbon ions (88.83MeV/u).

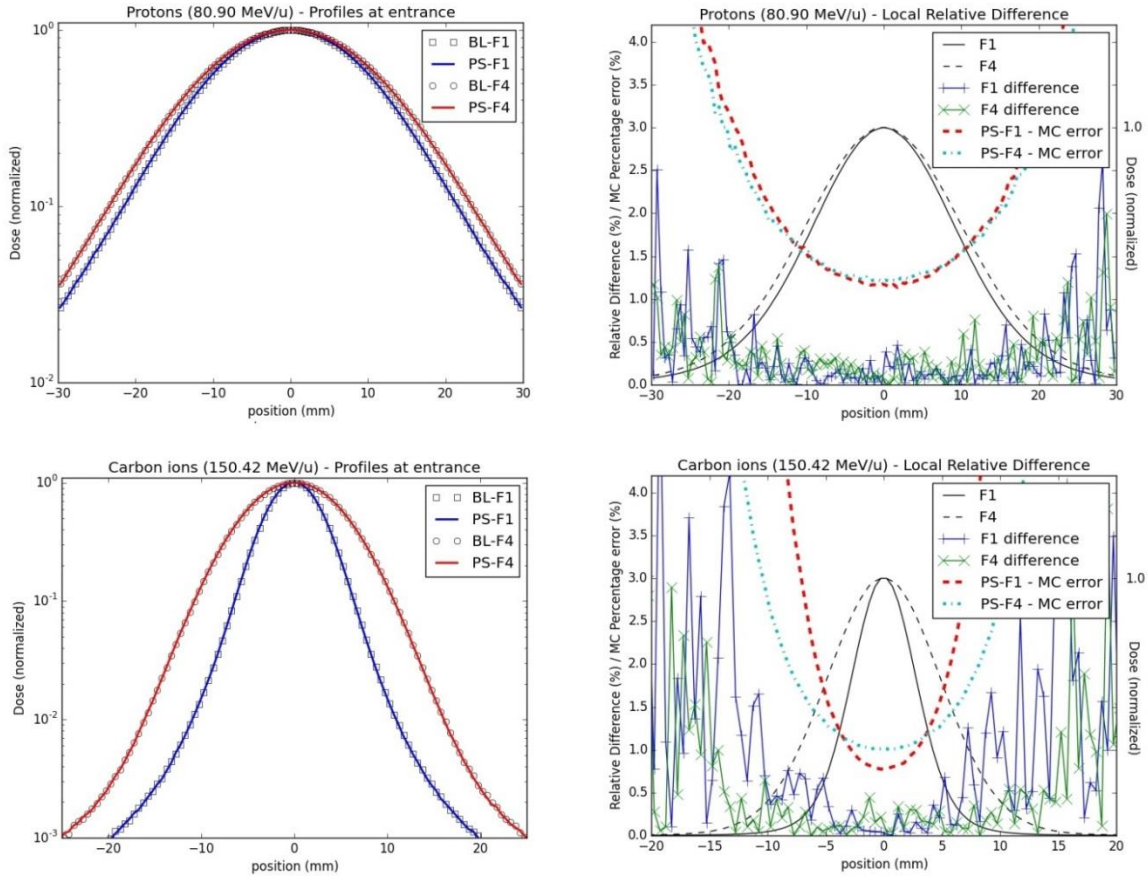

Figure 5.7: Lateral dose profiles for line scan validations: Lateral dose profiles for the lowest energy studied for both protons (upper panels, 80.90 MeV/u) and carbon ions (bottom panels, 150.42 MeV/u) at the isocenter in water. The left panels display the profiles from focus 1 and focus 4 for the PS (full line) and the BL approaches (stripes) in a semi-logarithmic scale; On the right panels, the profiles (black lines) together with their local relative difference (cross) and MC percentage errors (dashed lines) for focus 1 and 4 are shown.

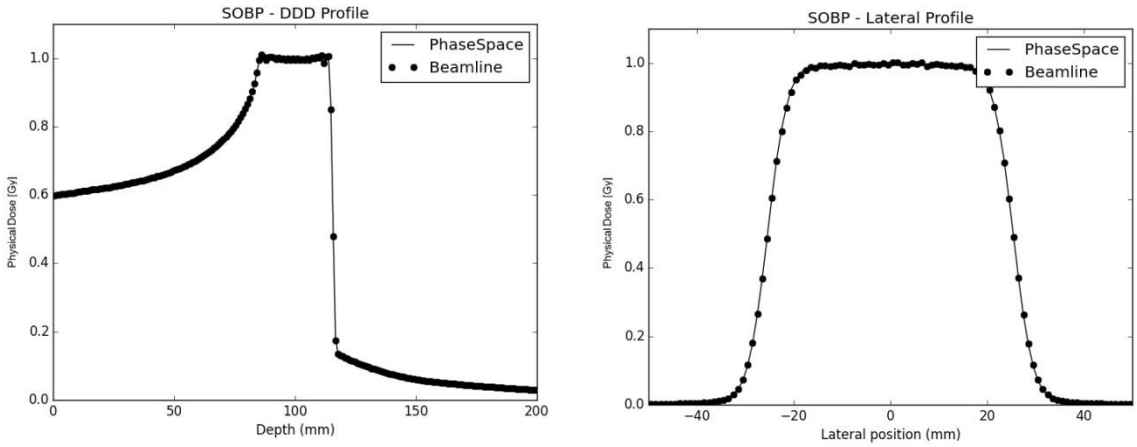

Figure 5.8: SOBP Profiles in water: on the left panel, the depth dose profiles of both the PS (full line) and the beamline (dot line) approaches are plotted together; on the right panel the lateral dose profiles at the center of the SOBP for both the PS (full line) and the BL (dot line) approaches are shown.

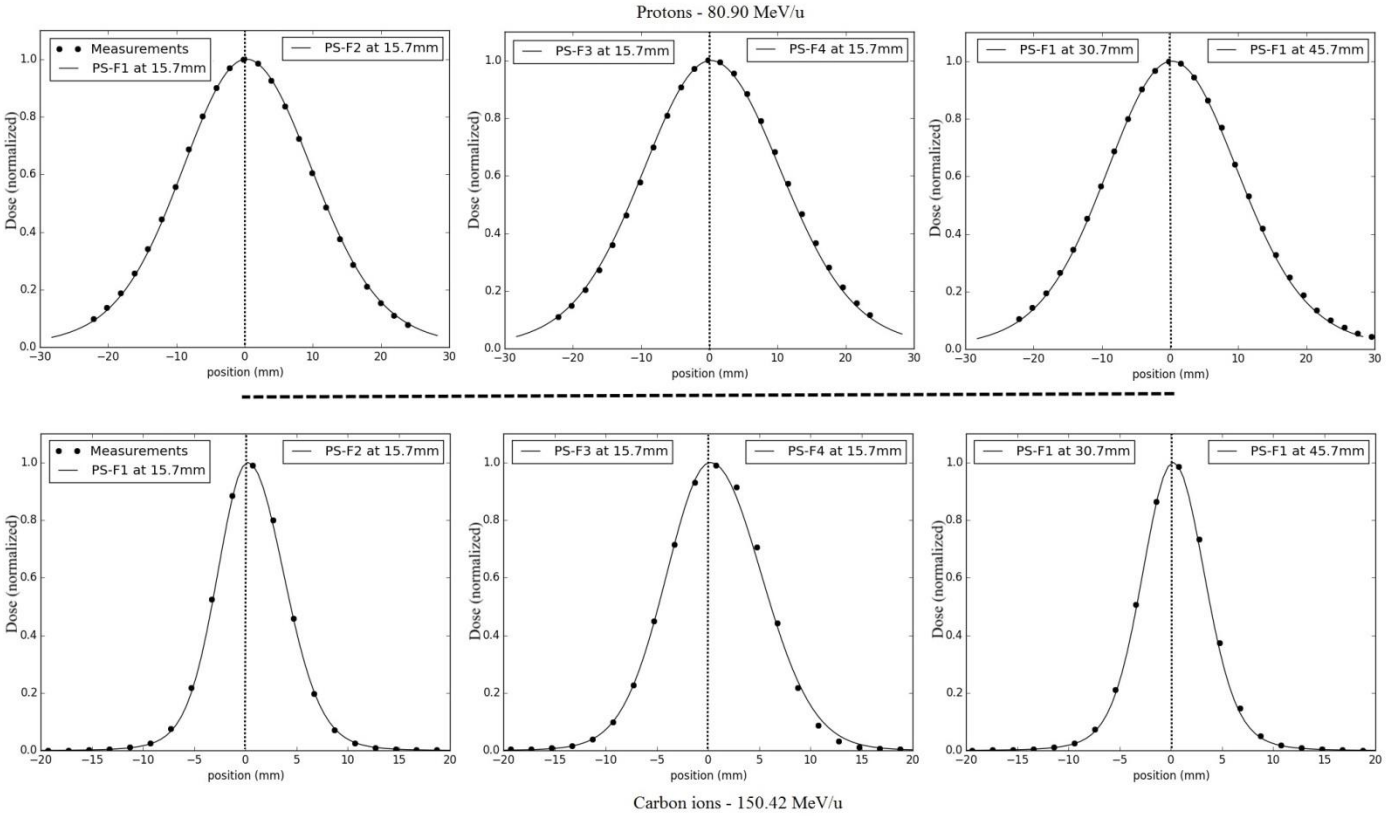

Figure 5.9: Dose calculations and measurements for lateral dose profile comparisons from line scans: half-profiles of the different foci are plotted for the same low energy, from left to right for focus 1 to focus 4 at 15.7 mm in water, and for two other depths for focus 1 (30.7 and 40.7 mm). The upper panels correspond to protons comparisons (energy 80.90MeV/u), the bottom panels to carbon ions comparisons (energy 150.42MeV/u). Results are normalized to the maximum.

5.3.2. Comparison of PS-based simulations with dosimetric measurements

The different water phantom dosimetric measurements show good agreements with the PS approach simulations (figure 5.9). In terms of lateral profiles sampled at three different depths in water, the differences (in mm and percentage) of the fitted FWHM values are displayed in Table 5.4 for both particles types, and all investigated combinations of energies/foci. The maximum relative FWHM differences found for protons are about 6.5% and 5.8% corresponding respectively to FWHM differences of 0.8 mm and 1.1 mm. The mean absolute difference of the value is 0.5 mm with a standard deviation of 0.3 mm. The maximal absolute difference found for carbon ions is of -0.9 mm (relative difference of -7.5%), the mean absolute difference is 0.2 mm with a standard deviation of 0.2 mm.

		Protons				Carbon ions			
	Depth (mm)	F1	F2	F3	F4	F1	F2	F3	F4
Low energy	15.7	-0.2mm -1.0%	0.5mm 2.2%	0.4mm 1.8%	-0.9mm -3.7%	-0.4mm -5.7%	-0.2mm -1.8%	-0.2mm -1.5%	-0.3mm -2.1%
	30.7	-0.3mm -1.3%	-0.4mm -1.5%	-0.3mm -1.1%	-0.8mm -3.1%	-0.3mm -3.5%	0.0mm 0.0%	0.0mm 0.0%	-0.1mm -0.1%
	45.7	-0.5mm -2.2%	0.0mm 0.0%	0.2mm 0.8%	-0.7mm -2.8%	-0.2mm -3.2%	0.1mm 0.9%	-0.1mm -0.5%	-0.2mm -1.4%
Middle energy	15.7	-0.1mm -0.7%	0.2mm 1.2%	0.4mm 3.1%	-0.5mm -2.8%	-0.1mm -2.8%	0.1mm 2.0%	-0.2mm -1.7%	**-0.9mm -7.5%**
	85.7	0.3mm 2.1%	0.4mm 2.7%	0.6mm 3.5%	0.2mm 1.0%	0.3mm 6.6%	0.4mm 5.44%	0.0mm 0.0%	-0.7mm -5.7%
	151.7	0.3mm 2.0%	0.8mm 5.0%	0.8mm 4.4%	0.5mm 2.6%	0.2mm 2.7%	0.4mm 6.1%	0.3mm 3.6%	-0.1mm -1.3%
High energy	15.7	0.3mm 2.9%	0.4mm 4.1%	**0.8mm 6.5%**	0.2mm 1.3%	0.2mm 3.7%	0.1mm 2.0%	0.0mm 0.0%	-0.1mm -1.1%
	195.7	0.3mm 2.4%	0.7mm 4.6%	0.1mm 0.3%	0.9mm 5.2%	-0.1mm -1.5%	0.1mm 1.6%	0.1mm 1.0%	-0.3mm 2.7%
	267.7	0.3mm 1.8%	0.7mm 3.8%	**1.1mm 5.8%**	0.9mm 4.5%	-0.1mm -1.1%	0.3mm 4.0%	0.4mm 4.4%	0.1mm 1.0%

Table 5.4: FWHM differences (in millimeter) and percentages differences (%), between the PS simulation approach and dosimetric measurements, at different depths in water, for all investigated combinations of particles/energies/foci. Measurements are the reference FWHM. “Low energy” corresponds, respectively for protons and carbon ions, to 80.90 and 150.42MeV/u, “Middle energy” to 157.43 and 299.94 MeV/u, and “High energy” to 221.06 and 430.10 MeV/u. Numbers in bold represent the maximal differences found for protons and carbon ions.

5.3.3. Application to a small target clinical case

After validation of the PS approach against dosimetric experiments as presented previously in a water phantom, the PS implementation in the framework was tested successfully against the TPS for several scenarios. Rotation of the CT geometry emulates the adjustments made to the patient table (as explained in section 5.2.3) and of the gantry during treament. Subsequently, the framework was tested for the challenging clinical case selected.

The comparison of the measurements acquired at different depths in water exhibits absolute global differences below 6% with the conventional PS approach (i.e. utilizing the beam width in vacuum discussed in section 5.2.3.1.), while under 2% with the optimized PS approach which takes into account the actual deviation of +1 mm for the delivered foci with respect to the nominal TPS (LIBC) values. In such extreme scenarios, the TPS-like approach implemented in the MC framework, using the nominal TPS FWHM values, yields deviations up to 25% (figure 5.10) consistent with the expectations from previous work (Magro *et al* 2015, Parodi *et al* 2012).

Using the nominal FWHM values at isocenter the results of the dose predictions for the full plan projected on the CT patient geometry show the same tendency in terms of the lateral profiles and dose volume histogram (figure 5.11). Specifically, the main findings can be summarized as follows:

- 95% of the volume receives 16.9 Gy for PS approach against 19.44 Gy for the TPS-like one.
- 5% of the volume receives 22.5 Gy for PS approach against 26.1 Gy for TPS-like one.

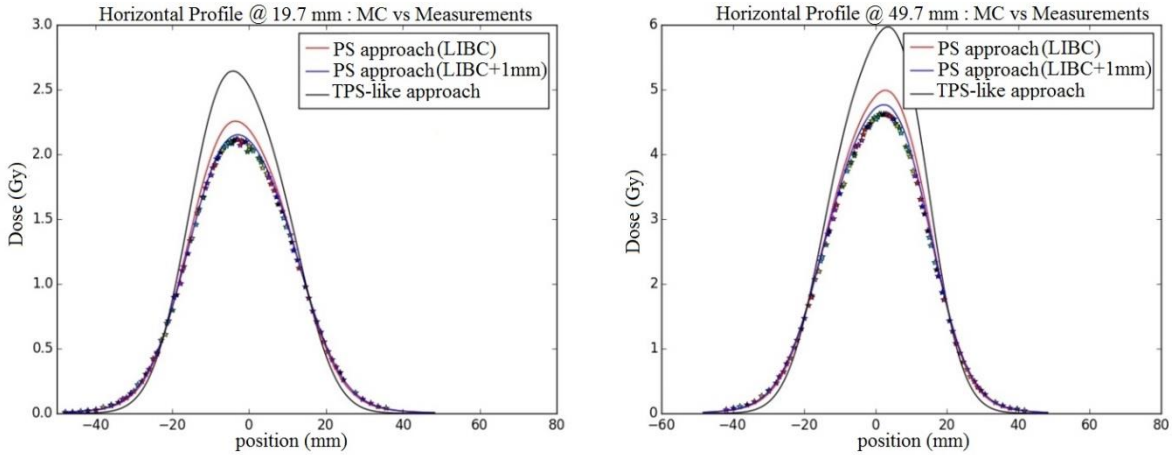

Figure 5.10: PS approach against TPS-like approach for a small target clinical case – dose verification in a water phantom : dose verification measurements (stars) are displayed against simulations with the TPS-like approach using the database foci values (black), the normal PS approach (red) with the foci in vacuum estimated from the database foci values, and the modified PS approach (blue) using the foci values in vacuum calculated from the beam records, at two different depths in water (19.7 mm and 49.7 mm);

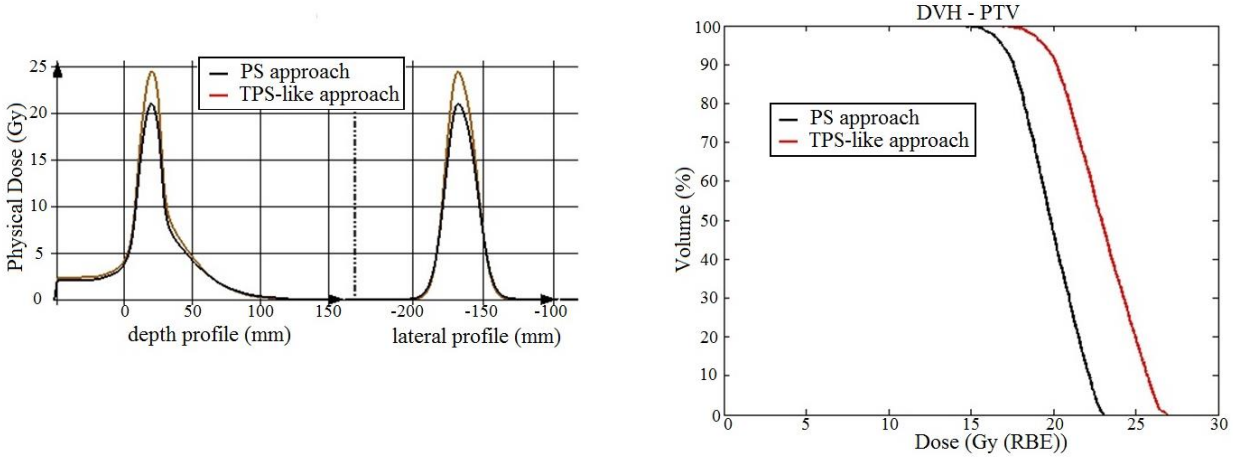

Figure 5.11: PS approach against TPS-like approach for a small target clinical case – dose predictions on the CT geometry: the dose profile at the PTV level in the CT patient geometry is plotted in red for the TPS-like approach and black for the PS approach, using the reference LIBC foci, for one beam; the bottom right panel displays dose volume histograms of the dose calculated with the two studied approaches.

5.4. Discussions

5.4.1. Validation of the PS

MC simulations using the proposed PS approach are overall in good agreement with results using the the explicit beamline modeling approach, typically within 0.5% for the absolute global dose difference.

The initial sampling of the infinitely narrow beam randomly spread within a 5 mm x5mm area before the beamline allows to include into the PS the information of the different interactions which can occur in the beamline, particularly between the impinging particules and the multiwire proportional chambers, where the wires are separated by a 1mm distance. Without this sampling, the spectra of the particles would have been different between the PS and the BL approaches, since some particles of the narrow beam approach would not interact as expected with the beamline. This would also cause to the fluence distribution and dose deposition deviations due to incorrect direction cosines, reducing the FWHM for the fluence distributions of the PS approach, ultimately boosting dose deposition in the center of the beam spot. The energy spectra of the particles obtained with the BL approach were found to be similar for both focus 1 and 4, regardless of the sampling position at the end of the BAMS or at the isocenter. This means that either with a small or a large FWHM Gaussian size in vacuum, there is no major impact on the energy spectra, thus confirming that the used initial sampling area 25mm² is adequate. Furthermore, while investigating the impact of the sampling area in more detail, new PS were generated for a 100mm² area. The fluence distribution comparison between the original and new PS did not show any relevant differences. No major differences were found for the director cosines distribution or the energy spectra either for the PS generated with the different foci or PS generated with the different sampling area, since in all these cases the initial beam is large enough to cover the

multiwire proportional chambers pattern, where the wires are separated by 1mm in the horizontal and vertical directions.

The absolute differences for the vertically integrated fluence distributions, obtained for the pencil-beam validation, are mainly due to the bin size and the resulting lower statistics per bin. When changing the bin size from a 0.2 mm to 0.6 mm, the maximal differences drop from 2.5% to 0.6% for protons and from 1.3% to 0.5% for carbon ions.

The dose differences between the PS and the BL simulation approaches for the line scans and the SOBP validation are within the statistical uncertainties.

These results show that we could fulfill the initial requirements on the adaptation of a unique PS to the different foci and the consistency of the propagation starting from the PS sampling plane, including the handling of the raster scanning process.

5.4.2. Comparisons of the PS-based simulations to dosimetric measurements

Overall, there was good agreement between the PS approach simulations to the lateral profile measurements in water, with a maximal FWHM deviation of -7.5 % or 1.1 mm for the extreme cases and a mean deviation below 0.5 mm, which corresponds to the bin size. These results are well within the range of acceptability, taking into account the even larger tolerance of experimental foci deviations at HIT, which is from +25% to -15%. For larger foci, particularly for carbon ions, the measured profiles exhibit asymmetric shapes in the horizontal directions, which are not modeled in our simulation. This shape is the resulting effect of the knock-out extraction process of the beam in the synchrotron, occurring in the horizontal plane, which is of trapezoidal shape (Ondreka and Weinrich 2008). However, its effects are smeared out due to the scattering in the beamline, air and water, particularly for small foci and lower energies.

5.4.3. Application to a small target clinical case

The PS approach shows good results compared to dosimetric measurements in the water phantom, with an acceptable maximal deviation of 5.8%, taking into account uncertainties in the dose gradient for such an extreme case of a small target volume. Moreover, our findings also prove the power of the PS approach to adapt easily to the “real” conditions of irradiation as monitored by the BAMS, improving the results significantly. In particular, we show that MC simulations with the PS approach can use the record of the irradiation to refine from the measured foci the estimate of the actual beam size in vacuum for each energy slice. Combined with the approach used in Tessonnier *et al* (2013), using the measured positions of every single raster scanning spot and its associated number of particles, it could provide a powerful tool for forward calculation closer to the “real” irradiation conditions.

On the other hand, the simplified TPS-like approach of the MC-framework exhibits a large overestimation of the dose with a smaller size of the irradiated volume. This is because it underestimates the large angle spread of the beam due to the BAMS and the air between the end of the beamline and the target position, resulting in higher dose values in the center of every spot. This is shown in the comparison for the lowest beam energy and focus for protons used in the line scan comparisons between the new PS approach, the TPS-like one and measurements (figure 5.12). These results show that beyond the accurate transport of particles in the target, the initial conditions of the beam are also fundamental. This observation is consistent with the results of Magro *et al* (2015) between the same TPS and MC simulations

for small targets at shallow depths, and as expected from Parodi *et al* (2012) evaluating the TPS-like approach against a more detailed approach (accounting for the BAMS elements but without the at that time not yet available detailed modeling). Beamline approximations used for MC simulations are giving in general good results, as shown in Bauer *et al* (2014) for the MC-framework, where the differences between simulations and measurements are in average below 3% or in Grassberger et al (2015 where their model compared to a full beamline propagation show differences inferior to 1% in the middle of a SOBP. As mentioned in section 5.2.1.1, the previous TPS-like approach was implemented for consistency and validation of the TPS beam modeling, and before the MC modeling of the beam nozzle (cf section 5.3.1.1). However a precise model is fundamental for extreme cases of small targets sensitive to the exact modeling of the few individual pencil beams.

In addition to the advantages provided by a good description of the beamline, the new MC framework using the PS provides a full description of the patient set-up as well as the possibility to readily take into account all rotations related to the plan. These features were made possible by the new capabilities of the MC code FLUKA for handling geometry implemented in the newest version (version 2011 and above). The implementation of additional elements such as RiFi, or range shifter is facilitated due to the fix geometry of the upstream beam.

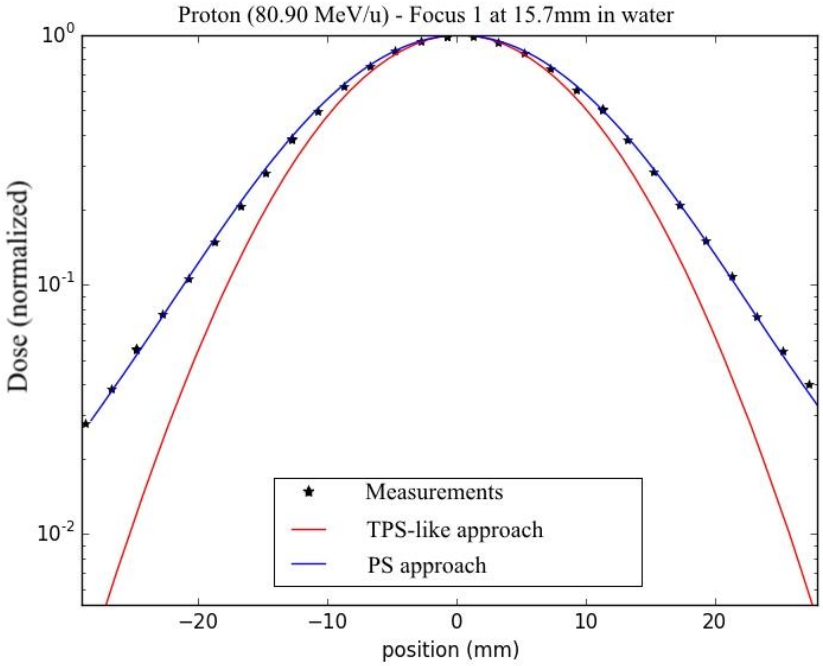

Figure 5.12: Dose results and measurements at 15.7 mm in water, for lateral dose profiles from line scans for the lowest energy protons and focus 1 with a semi-logarithmic scale. The TPS-like approach is displayed in red, the PS approach in blue and the measurements with the star dots

5.5. Summary

In this chapter, a novel PS approach has been successfully introduced, validated against simulations with the full beamline geometry and implemented in the in-house MC framework. It provides an accurate description of the beam to be propagated to a target (phantom/patient) as it includes the information of the interaction in the beamline in a generic way (so called narrow beam approximation), allowing adaptation to different beam foci with the same data. The PS approach can bring significant improvement to the dose calculation compared to the simplified approach implemented in the current MC framework (for consistency with the TPS). This is especially important, for similar extreme situations of a small target at shallow depths, as the patient case investigated in this chapter.

The generation of PS files for other particles (helium and oxygen ions) has been carried out successfully to allow a full description of the particle species available at HIT.

The generated phase spaces were made available for external teams upon request and have been used for several projects (Kelleter *et al* 2017, Bellinzona *et al* 2016, Meyer *et al* 2017).

Chapter 6. Dosimetric verification in water of a Monte Carlo treatment planning tool for ^{1}H, ^{4}He, ^{12}C and ^{16}O ion beams at HIT

In this Chapter, the validation of a Monte Carlo treatment planning tool will be presented. This work is using the phase space files created for every ion, presented in Chapter 5, after tuning the simulation parameters as explained in Chapter 4. The validation of this tool is the mandatory step toward application for patient planning, to be presented in Chapter 7. After SOBP optimizations in water for each ion available at HIT, Monte Carlo predictions will be compared to dosimetric measurements. The difference between ion dosimetric characteristics will be highlighted for challenging SOBP cases, closer to clinical-like scenario compared to the SOBP presented in Chapter 3. The introduction of the biological model coupled to the Monte Carlo treatment planning tool used for patient planning is shown in Appendix C, together with its validation against biological experiments. A part of the work presented in this Chapter has been submitted for publication (Tessonnier *et al* 2017c).

6.1. Background

The previous Chapter 3 and 4 introduced the particular interest of the particle therapy community into other ions than the therapeutically used protons and carbon ions. At the Heidelberg ion beam therapy center, as previously seen, recent efforts aim to provide further ions species such as helium and oxygen for future clinical use.

In Chapter 3, thorough dosimetric characterization of these particle species was performed (Tessonnier *et al* 2017a). Validation of the MC code FLUKA against experimental dose measurements in water and air was presented in previous published works for protons, carbon and oxygen ions (Parodi *et al* 2012, Parodi *et al* 2013, Kurz *et al* 2012), and in Chapter 4 of this thesis for helium ions (Tessonnier *et al* 2017b).

Prior to clinical deployment, treatment planning studies have to be performed with an experimentally validated engine. As already mentioned in Chapters 3 few works are available in literature (Kantemiris *et al* 2011, Kempe *et al* 2007, Fuchs *et al* 2015, Grün *et al* 2015), based on either analytical or MC dose engines, which compare physical properties of different ions and treatment-like plans. These works have been performed, however, without any or with a limited number of experimental dosimetric benchmarks supporting their predictions. Therefore this Chapter addresses the validation of a novel FLUKA-based Monte Carlo Treatment Planning tool (MCTP, Mairani *et al* 2013, Böhlen *et al* 2013) against dosimetric measurements for challenging targets, i.e., small spread-out Bragg peaks (SOBPs) of 3 cm × 3 cm × 3 cm size, or larger SOBPs of 6 cm × 6 cm × 6 cm, at different depths in water (5, 12.5 and 20 cm), which are representative for clinically-relevant scenarios. Furthermore, the experimental dosimetric SOBP properties collected for the different ions, such as distal/lateral fall-off or the entrance/tail doses, were compared to complete the dosimetric studies presented in Chapter 3.

6.2. Materials and Methods

6.2.1. Monte Carlo Treatment Planning tool

The physical optimization of the SOBPs was performed with the FLUKA-based MCTP tool. The optimization was carried out for 3 cm × 3 cm × 3 cm and 6 cm × 6 cm × 6 cm targets, centered at 5 cm (SOBP1), 12.5 cm (SOBP2) and 20 cm (SOBP3), with a planned homogeneous absorbed dose of 1 Gy within the SOBP. The step in depth between two consecutive energy slices was about 2 mm, while the lateral spacing between two pencil beams was 3mm. The simulations were performed using a detailed model of the HIT beamline as described in Parodi *et al* (2013) and Tessonnier *et al* (2016), with a water tank positioned with its entrance window at the isocenter, as seen in Chapter 4 and Chapter 5. As investigated in Parodi *et al* (2012) and Kurz *et al* (2012), the optimal initial energy momentum spread and ionization potential values in water (76.8 eV for helium, carbon and oxygen ions and 77.3 eV for protons) were used for simulation, for a water density of $0.998 g.cm^{-3}$, reproducing the experimental conditions as seen in Chapter 4. The ripple filter (RiFi) was implemented for carbon ions and oxygen ions as routinely applied for patient treatment with carbon ion beams. For protons and helium ions, the beam spot size at isocenter was chosen following the clinical practice with protons, i.e., using the lowest focus available in the HIT accelerator library, thus meaning full-width at half-maximum (FWHM) at isocenter of [24.2-16.8] mm and [13.7-10.0] mm for SOBP1, [13.1-11.7] mm and [7.9-7.0] mm for SOBP2, [10.3-9.3] mm and [6.0-5.5] mm for SOBP3 for protons and helium ions, respectively. For carbon and oxygen ions, the third focus value was chosen as generally performed in clinical routine of carbon ion therapy. Thus, this choice means FWHM values at isocenter without RiFi of [10.4-9.0] mm and [9.9-8.9] mm for SOBP1, [8.4-8.2] mm and [8.5-8.4] mm for SOBP2, [8.0] mm and [8.2-8.1] mm for SOBP3 for carbon and oxygen ions, respectively. In the optimization, a constraint on the maximum dose in the target was set to 107% of the planned dose. The scoring grid for dose calculation was set to 1 mm × 1 mm × 1 mm, smaller than used in routine with the clinical treatment planning system (generally between 2 mm × 2 mm × 2 mm and 3 mm × 3 mm × 3 mm). After optimization, the final plan for each SOBP and for each beam modality was re-calculated using the full beamline and a model of the water tank used at HIT for measurement verification (Tessonnier *et al* 2016 and Chapter 5), with $2x10^8$ primary histories in 200 statistically independent parallel runs. A summary of the optimization workflow is provided in Appendix C.

6.2.2. Dosimetric Measurements

The measurements of the MCTP-optimized plans were acquired in the experimental room of HIT. The delivery was performed with the active beam scanning system available at HIT (Chapter 2), with the beam impinging on a water tank positioned with its entrance window at isocenter and equipped with a block of 24 pinpoint ionization chambers (ICs, 0.030cm^3; PTW) as described in Chapter 5 and Tessonnier *et al* (2016).

Depth dose measurements were recorded from 16 mm depth to at least 20 mm after the 80% dose fall-off position (R_{80}) of the SOBP. Depth measurement step size in both regions of high dose and sharp gradients was about 1 mm. For each irradiation, six depth positions were acquired at the same time, with at least two ICs within the radiation field per depth. Depth dose positions are relative to the entrance window and expressed in water-equivalent depth.

Lateral dose measurements were performed at several depths. Measurements from -25 mm to +30 mm were achieved with a particular emphasis on the 0 to +30 mm region with step sizes of about 1 mm for 3 cm × 3 cm × 3 cm SOBPs. For 6 cm × 6 cm × 6 cm SOBPs, measurements were acquired from -25 to +50 mm, with a special focus on the 15 to 50 mm region and are presented in Appendix C.

6.2.3. Analysis of the experimental results and comparisons to MC predictions

From the experimental dosimetric measurements, for each ion and SOPB, parameters were extracted for both depth and lateral dose distributions, similar to Chapter 3.

For each depth dose distribution, the mean dose in the inner 80% of the SOBPs was compared to the planned dose of 1 Gy. Subsequently, the mean dose was used as a normalization factor for all measurements for all comparisons (depth and lateral), thus being independent of beam monitor calibration or daily dose delivery deviation. The dose homogeneity, defined as the ratio between the lowest and the highest measured dose within the inner 80% of the SOBP, was calculated. The R_{80}, the distal position of the SOBP reaching 80% of the planned dose, and the 90% SOBP size, defined as the distance between the proximal and distal position reaching 90% of the planned dose, were estimated. The dose distal fall-off 80%-20% ($DFO_{80/20}$), defined as the distance between the 80% and 20% distal dose positions, was assessed. The distal fall-off 80%-40% ($DFO_{80/40}$), free from the influence of the fragmentation tail, was also evaluated. The entrance-to-plateau region (EPLR) ratio, between the absorbed dose at 16 mm and the mean dose in the inner 80% of the SOBP, as well as the tail-to-plateau ratio (TPLR) ratio, between the dose 10 mm after the R_{80} and the SOBP mean dose, were extracted.

For the lateral dose distributions, the following parameters were extracted from each lateral profile within the SOBP region, and then averaged:

- the 90% lateral SOBP size defined as the distance between the lateral position reaching 90% of the planned dose,
- the lateral fall-off 80%-20% (LFO),
- the lateral irradiated size defined as the distance between the position reaching the 50% dose.

The dosimetric parameters described above were then extracted from the MC predictions as well, with the exact same procedure, and compared to the experimental results.

6.3. Results

6.3.1. Small SOBP (3 cm × 3 cm × 3 cm)

The next sections present detailed results related to the 3 cm × 3 cm × 3 cm SOBPs. As described in Magro et al (2015), this scenario represents a challenging target for a treatment planning system, with high sensitivity to delivery uncertainty and beam modifications (e.g. spot sizes).

6.3.1.1. Depth dose distributions

Measured and predicted depth dose distributions are shown in figure 6.1 for the three 3 cm × 3 cm × 3 cm SOBPs for protons, helium, carbon and oxygen ions.

6.3.1.1.1. Measurements results and comparisons between ions

The experimental depth dose SOBPs parameters are displayed in table 6.1 (left column). The error on the dose is the standard deviation of the measurements. The positioning error, linked to the IC position uncertainty, is about 0.5 mm, accounting for the 0.1 mm accuracy of the step motor, the uncertainty in water tank position of the IC and the error on the position of the effective measurement point (Karger *et al* 1999). Deviations between planned and measured dose were below about 3.5% for every ion species and SOBP sizes. For proton and helium ion SOBPs, the absolute dose deviations were below 1.1% and below 1.0%, respectively. For heavier ions, the differences to the planned dose were below 3.5% with the largest discrepancies found for the deepest ^{12}C ion SOBP. The homogeneity was in general above 95% except for the shallowest helium ion SOBP with a registered homogeneity of around 93%. The range was found to be similar between ions: about 65.5 mm for SOBP1, about 140.2 mm for SOBP2 and about 215.4 mm for SOBP3. For SOBP1 the $DFO_{80/40}$ was around 1 mm for protons, oxygen- and carbon ions, and 0.3 mm for helium ions. For SOBP2 the $DFO_{80/40}$ was around 1.7 mm for protons, oxygen and carbon ions, while being 0.8 mm for helium ions. For SOBP3 the $DFO_{80/40}$ was around 2.6 mm for protons and 1.7 mm for helium, oxygen and carbon ions.

The SOBPs size was similar for all depths and ions with an average size of 31.6 mm with a maximum difference of about 1 mm. The EPLR of the different ions for the SOBP1 were similar and around 72.3%. For the SOPB2 the EPLR was around 54% for the lighter ions and 63.5% for the heavier ions. At the largest depth, greater differences were found with EPLR values of 49.7% for protons, 54.3% for helium ions, 66.9% for carbon ions and 73.7% for oxygen ions. The TPLR for protons were 0% except for the deeper SOBP with 0.4%. From the shallowest to deepest SOBPs the TPLRs were about 1.6%, 2.9%, and 3.4% for helium ions, 6.0%, 12.9%, and 17.9% for carbon ions, and 6.6%, 16.7%, and 24.9% for oxygen ions.

6.3.1.1.2. Simulations results and comparisons to measurements

The depth dose SOBPs parameters extracted from the simulations are shown in table 6.1 (right columns) and the deviation of the main parameters to the measurements are summarized in figure 6.2. The errors for the R_{80}, DFO and size parameters take into account the errors on the simulated position, about half of the dose scoring bin-size (0.5 mm). The uncertainties on the dose parameter (EPLR, TPLR, homogeneity and absolute dose deviation to the planned dose) were linked to the standard deviation of the underlying dose. The Monte Carlo statistical uncertainty was below 0.1% in the high dose region and below 0.5% in the low dose regions for all investigated ions and SOBPs. Consistently with the experimental results, the homogeneity was in general above 96% except for the shallowest helium ion SOBP with homogeneity around 92.1%.

The differences in mean dose were close to those found between experimental and planned dose since simulated mean absolute dose deviations to planned dose were found to be about -

0.3 ±0.6%. EPLR and TPLR differences between simulations and measurements were within 3% with the largest difference observed for the deepest SOBPs and heavier ions (carbon ions EPLR for the SOBP3 was about 2.9% larger for simulations). Concerning variation in R_{80}, the differences were below 1 mm for every ion/SOBP combination. Similar results were found for the SOBP size, with differences below 1 mm except for He SOBP1, with a difference of 1.9 ± 1.0 mm. The $DFO_{80/20}$ differences were below 1 mm except for the ^{16}O SOBP3 with 2.3 ±1.0 mm difference.

The figure 6.3 presents dose comparisons between measurements and simulations along the depth for all ions investigated, after normalization of both depth dose curves to the dose in the inner 80% of their respective SOBP. Dose deviations are presented in units of percent difference (**Δ** %), with the display of the ±1% difference in green and ±3% difference in red, as well as the blue vertical lines which represent the SOBP target region. The four ions are presented: protons, helium, carbon and oxygen ions from left to right panels respectively, for the three SOBPs investigated from top to bottom panels, respectively). After normalization of each SOBP to the mean dose within 80% of their sizes, for both measurements and simulations, all measurement points in the high dose region were found with differences for protons below 1% in the target region and below 2.5% in the whole distribution for all SOBPs. For helium and oxygen ions, the differences were found to be below 2% for the whole distribution, while being below 2.1% in the target for carbon ions and below 3% for the overall distribution.

SOBP position		Experimental measurement parameters						FLUKA simulation parameters					
		5,0		12,5		20,0		5,0		12,5		20,0	
		mean	σ	mean	σ	mean	σ	mean	σ	mean	σ	mean	σ
H	EPLR (%)	71,3	2,6	53,1	0,6	49,7	1,1	71,0	0,3	52,3	0,2	49,3	0,4
	R_{80} [mm]	65,0	0,7	140,5	0,7	216,4	0,7	64,8	0,7	140,3	0,7	216,0	0,7
	Size [mm]	31,8	0,7	32,5	0,7	32,8	0,7	31,9	0,7	32,7	0,7	33,0	0,7
	TPLR (%)	0,0	0,7	0,0	0,3	0,4	0,5	0,0	0,3	0,0	0,2	0,5	0,4
	$DFO_{80/20}$ [mm]	1,5	0,7	2,8	0,7	4,1	0,7	1,8	0,7	2,8	0,7	4,3	0,7
	$DFO_{80/40}$ [mm]	0,9	0,7	1,8	0,7	2,6	0,7	1,0	0,7	1,8	0,7	2,7	0,7
	Hom. [%]	97,0	1,2	99,0	1,1	97,8	1,1	98,7	0,1	99,3	0,1	97,9	0,1
	Dose dev.	-1,1	0,7	0,1	0,3	-0,3	0,5	-0,2	0,3	0,0	0,2	0,2	0,4
He	EPLR (%)	70,5	1,9	55,3	0,8	54,3	2,4	71,7	0,2	55,4	0,1	54,0	0,1
	R_{80} [mm]	66,1	0,7	140,0	0,7	214,4	0,7	65,9	0,7	140,0	0,7	214,6	0,7
	Size [mm]	30,0	0,7	31,9	0,7	31,8	0,7	31,9	0,7	32,0	0,7	31,6	0,7
	TPLR (%)	1,6	1,9	2,9	0,7	3,4	0,8	1,2	0,2	2,0	0,1	2,7	0,1
	$DFO_{80/20}$ [mm]	0,5	0,7	1,3	0,7	2,3	0,7	0,8	0,7	1,4	0,7	2,0	0,7
	$DFO_{80/40}$ [mm]	0,3	0,7	0,8	0,7	1,3	0,7	0,4	0,7	0,9	0,7	1,2	0,7
	Hom. [%]	93,0	1,2	97,8	1,1	96,9	1,1	92,1	0,1	99,5	0,1	99,3	0,1
	Dose dev.	-0,1	1,9	0,2	0,7	0,8	0,8	0,0	0,2	-0,3	0,1	-0,9	0,1
C	EPLR (%)	72,9	0,9	62,1	0,9	66,9	1,1	73,4	0,3	63,1	0,1	69,7	0,6
	R_{80} [mm]	65,5	0,7	140,2	0,7	214,9	0,7	65,4	0,7	140,1	0,7	214,7	0,7
	Size [mm]	31,1	0,7	31,5	0,7	31,0	0,7	31,9	0,7	32,0	0,7	31,4	0,7
	TPLR (%)	6,0	0,7	12,9	0,8	17,9	1,1	6,4	0,3	12,8	0,1	17,6	0,6
	$DFO_{80/20}$ [mm]	1,8	0,7	3,1	0,7	4,8	0,7	2,0	0,7	2,9	0,7	4,2	0,7
	$DFO_{80/40}$ [mm]	1,1	0,7	1,5	0,7	1,6	0,7	1,4	0,7	1,4	0,7	1,4	0,7
	Hom. [%]	97,7	1,0	96,3	1,3	95,2	1,2	98,8	0,1	99,4	0,1	96,7	0,1
	Dose dev.	1,7	0,7	2,7	0,8	3,5	1,1	-0,6	0,3	-0,3	0,1	0,0	0,6
O	EPLR (%)	74,3	0,6	65,0	1,5	73,7	1,3	73,6	0,2	65,6	0,2	75,3	0,5
	R_{80} [mm]	65,4	0,7	140,1	0,7	216,0	0,7	65,2	0,7	140,1	0,7	215,9	0,7
	Size [mm]	31,5	0,7	31,4	0,7	32,3	0,7	31,7	0,7	32,3	0,7	33,2	0,7
	TPLR (%)	6,6	0,5	16,7	1,0	24,9	0,9	6,5	0,2	15,8	0,2	23,6	0,5
	$DFO_{80/20}$ [mm]	1,5	0,7	4,2	0,7	14,7	0,7	1,8	0,7	3,3	0,7	17,0	0,7
	$DFO_{80/40}$ [mm]	0,9	0,7	1,7	0,7	1,5	0,7	1,2	0,7	1,7	0,7	1,5	0,7
	Hom. [%]	97,7	1,1	96,9	1,1	96,6	1,2	99,3	0,1	99,2	0,1	96,9	0,1
	Dose dev.	1,7	0,5	3,0	1,0	2,8	0,9	-0,7	0,2	-0,5	0,2	-0,5	0,5

Table 6.1: 3 cm × 3 cm × 3 cm SOBP depth dose distribution parameters: the different parameters are shown for the ions investigated at the different SOBP positions, for both measurements (left columns) and simulations (right columns).

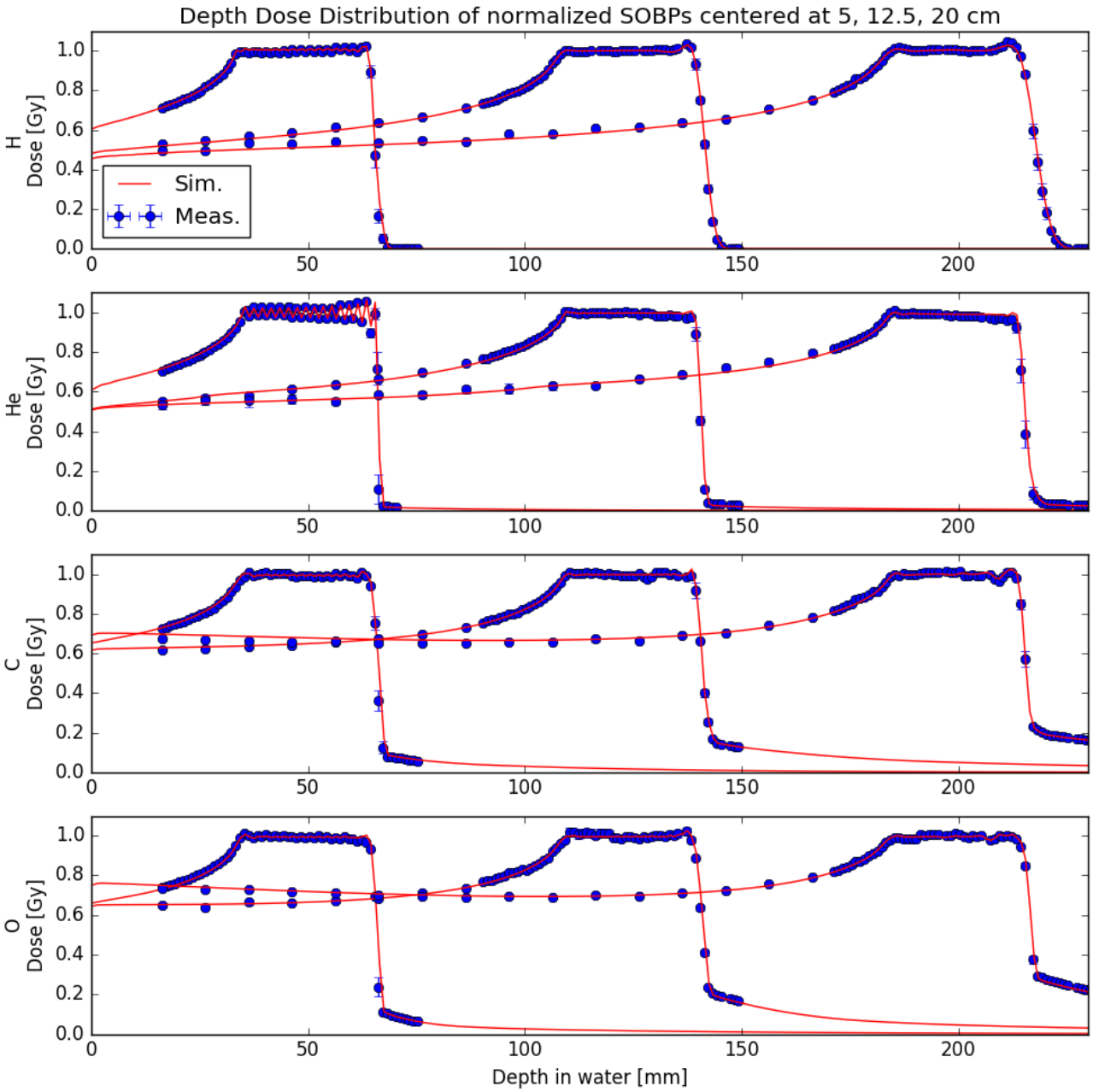

Figure 6.1: Depth dose distributions in water of the 3 cm × 3 cm × 3 cm SOBPs centered at 5, 12.5 and 20 cm for protons, helium, carbon and oxygen ions (from top to bottom panels). Measurements are shown as points with circles (with error bars) while MC predictions are represented by solid lines.

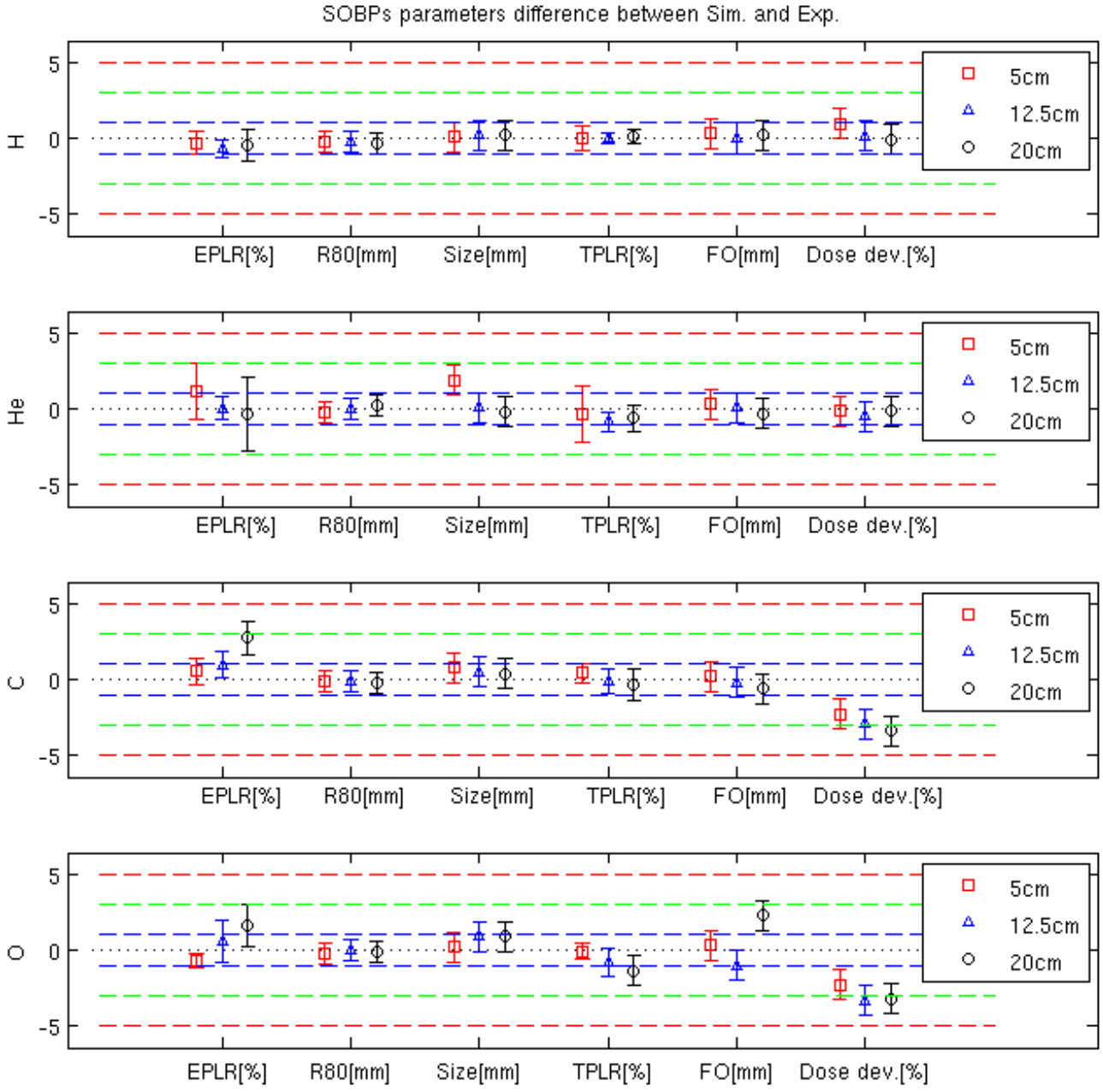

Figure 6.2: Difference between SOBP parameters extracted from the measured and simulated depth dose distributions. SOBP centered at 5 cm are represented by the square, at 12.5 cm by the triangle, and at 20 cm by the circle. From top to bottom the differences are displayed for protons, helium, carbon and oxygen ions. The dotted lines stand for difference of either 0 % or 0 mm, the dashed lines represent successively the 1, 3 and 5 difference in % or mm.

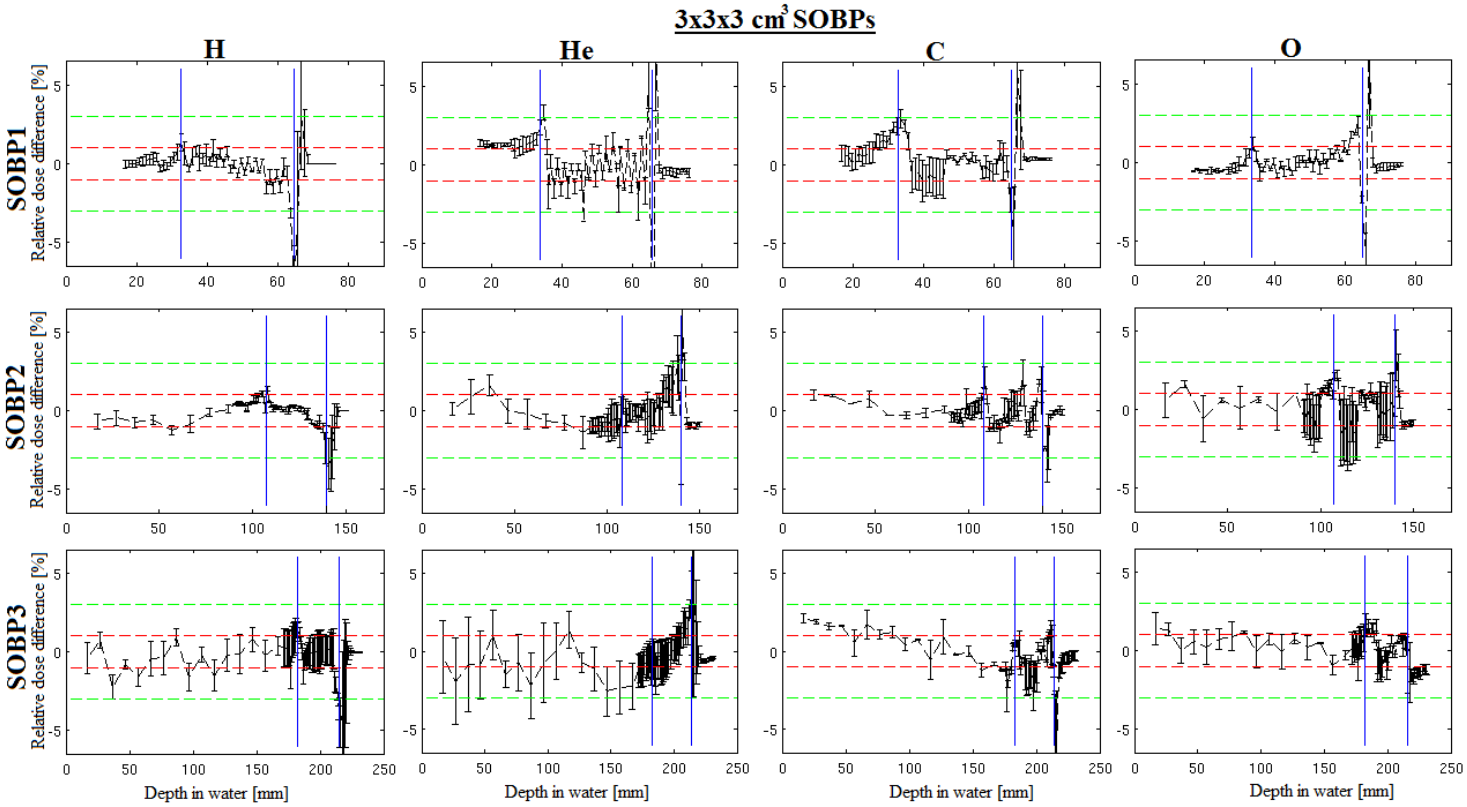

Figure 6.3: Dose differences along the depth between MC and measurements in water, after normalization, for the 3 cm × 3 cm × 3 cm SOBPs presented in Chapter 6. The 1% deviation line is displayed in red, the 3% in green. The target region is within the blue vertical lines.

6.3.1.2. Lateral dose distributions

Lateral profiles in the middle of the SOBP for measurements and simulations are shown in figure 6.4, for all three cases of the small 3 cm × 3 cm × 3 cm SOBP (left to right: SOBP1, SOBP2 and SOBP3), for all ion species (top to bottom: protons, helium, carbon and oxygen ions).

Parameters for the lateral distributions extracted from the measurements are shown in the table 6.2 (left columns). The errors have been estimated as described for the depth dose distributions. The LFO values for protons were ranging from 12.7 mm for the shallowest SOBP to 9.6 mm for the deepest one. The LFO values for helium ions were ranging from 6.9 mm for SOBP1 down to 5.4 mm for SOBP3. The LFO values for carbon ions were ranging from 6.3 mm down to 4.9 mm. The LFO values for oxygen ions were about 5.2-5.4 mm for all SOBPs. The average SOBP sizes were similar for every ion, with a better conformity for oxygen ions of about 30.3 mm, followed by carbon ions with 30.6 mm, then helium ions with 31.4 mm and finally protons with 31.7 mm. The irradiated SOBP size was about 51.7 mm at the shallowest depth for protons and around 45 mm for other depths. For helium ions, the irradiated size was about 41.2 mm for SOBP1 and around 38.3 mm for the other two SOBPs. In case of carbon- and oxygen ions, the irradiated size was around 38.5-38 mm for all SOBPs.

The parameters of the lateral distributions extracted from the SOBP simulations are shown in table 6.2 (right columns) and the difference to the parameters extracted from the measurements are summarized in figure 6.5.

The differences between measured and simulated parameters are below 1 mm except for the SOBP size of the proton SOBP1 and SOBP2, where variations of about 2 mm are observed.

SOBP position		Experimental measurement parameters						FLUKA simulation parameters					
		5,0		12,5		20,0		5,0		12,5		20,0	
		mean	σ	mean	σ	mean	σ	mean	σ	mean	σ	mean	σ
H	Irrad. Size [mm]	50,4	1,3	44,9	0,7	45,3	0,8	49,4	0,8	44,6	0,7	44,9	0,8
	Lat. Size [mm]	31,8	0,9	31,1	0,7	32,2	0,8	33,7	0,7	32,7	0,7	32,7	0,7
	$LFO_{80/20}$ [mm]	12,9	1,4	10,1	0,8	9,6	0,9	12,2	0,8	9,3	0,7	9,6	0,8
He	Irrad. Size [mm]	41,2	0,7	37,7	0,7	38,9	0,7	41	0,7	37,4	0,7	38,2	0,7
	Lat. Size [mm]	31,7	0,8	30,5	0,7	32	0,7	31,5	0,7	30,6	0,7	31,8	0,7
	$LFO_{80/20}$ [mm]	7	0,8	5,4	0,7	5,4	0,8	7,2	0,7	5,3	0,7	5,1	0,8
C	Irrad. Size [mm]	38,9	0,8	38,3	0,7	38,3	0,7	38,5	0,7	37,9	0,7	37,8	0,7
	Lat. Size [mm]	29,9	0,9	30,7	0,7	31,2	0,7	30,7	0,7	30,9	0,7	30,5	0,7
	$LFO_{80/20}$ [mm]	6,3	0,7	5	0,7	5	0,7	6	0,7	5,3	0,7	5,6	0,7
O	Irrad. Size [mm]	38,7	0,7	37,8	0,7	38,6	0,7	38,1	0,7	37	0,7	37,7	0,7
	Lat. Size [mm]	31	0,7	29,7	0,7	30,1	0,8	31,2	0,7	30,2	0,7	30,6	0,7
	$LFO_{80/20}$ [mm]	5,2	0,7	5,3	0,7	5,4	0,7	5,3	0,7	5,2	0,7	5,4	0,7

Table 6.2: 3 cm × 3 cm × 3 cm SOBP lateral dose distribution parameters: the different parameters are shown for the ions investigated at the different SOBP positions, for both measurements (left columns) and simulations (right columns)

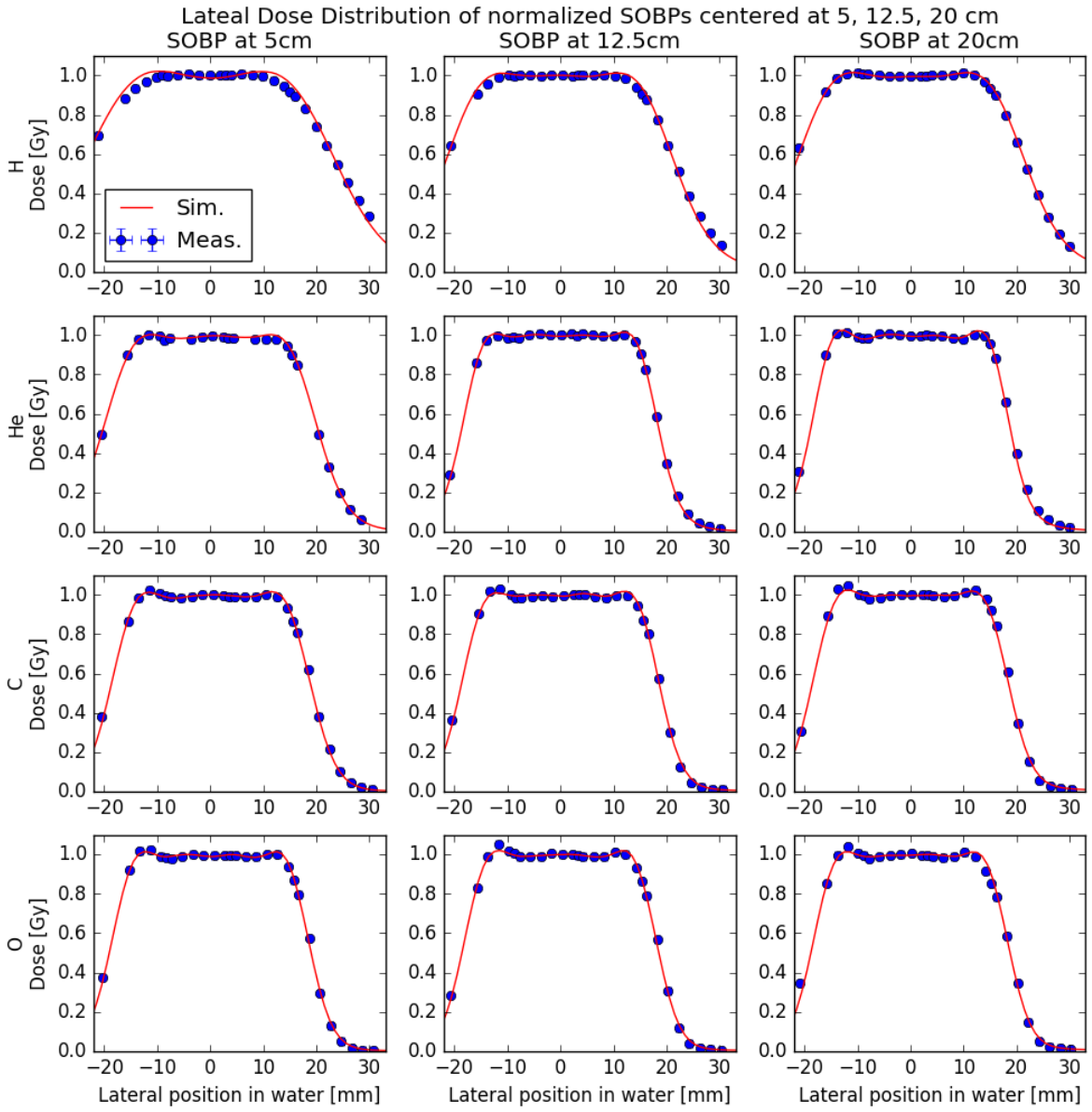

Figure 6.4: Lateral dose distributions at the mid-SOBP position for the 3 cm × 3 cm × 3 cm SOBPs centered at 5, 12.5 and 20 cm (from left to right panels) for protons, helium, carbon and oxygen ions (from top to bottom panels). Measurements are shown as points with circles, while MC predictions are represented by the solid lines.

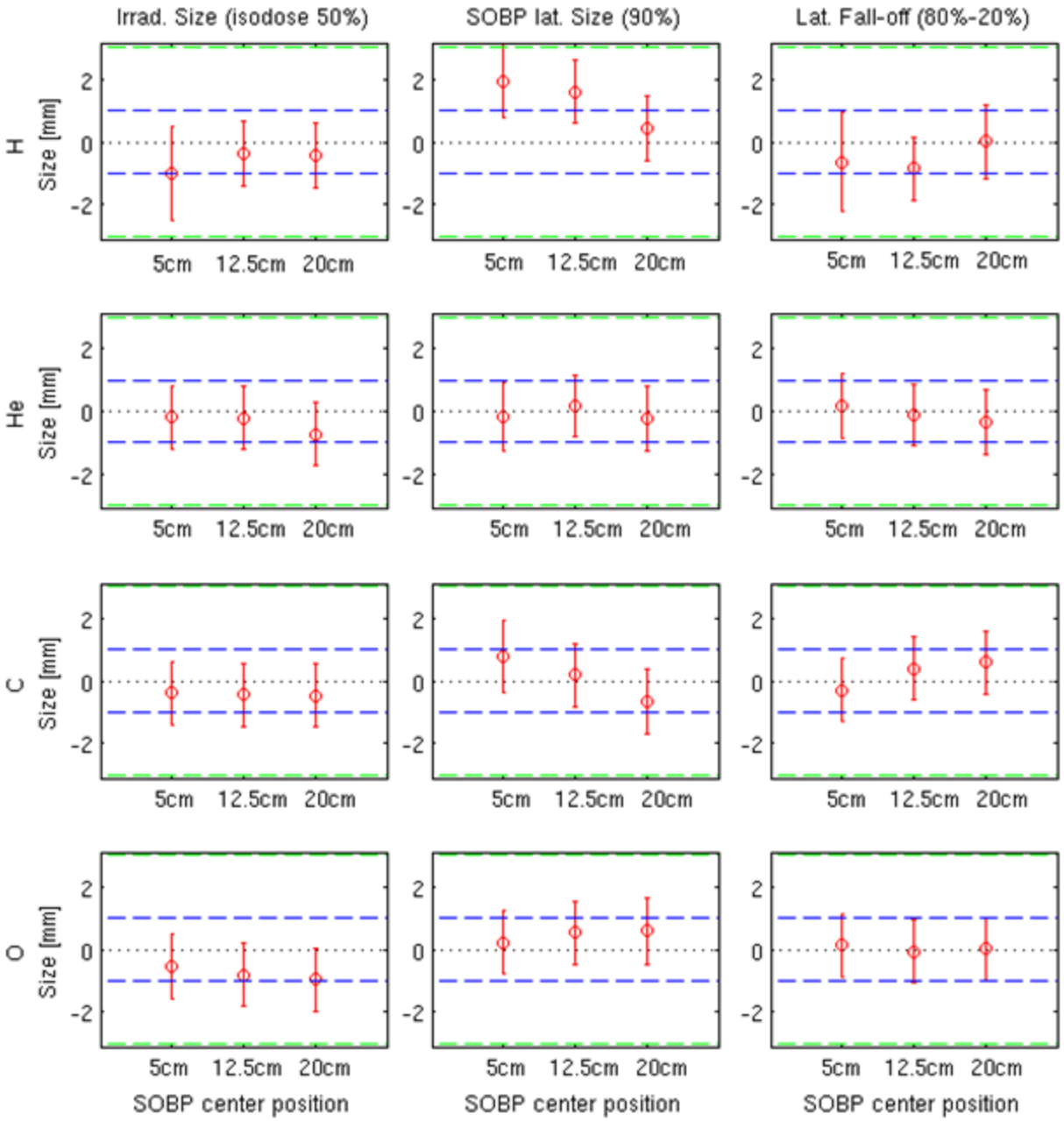

Figure 6.5: Difference between parameters extracted from the simulated and measured lateral dose distributions in the SOBP region. From the left to the right panels, the irradiated lateral size, the SOBP lateral size and the lateral dose fall-off are presented for protons, helium, carbon and oxygen ions (from top to bottom panels). The dotted lines stand for 0 mm difference, the dashed lines represent differences of 1 and 3 mm, respectively.

6.3.2. Large SOBP (6 cm × 6 cm × 6 cm)

The next sections present detailed results related to the 6 cm × 6 cm × 6 cm SOBPs.

6.3.2.1. Depth dose distributions

6.3.2.1.1. Measurements results and comparisons between ions

Measured and predicted depth dose distributions are shown in figure 6.6 for the three SOBPs for protons, helium, carbon and oxygen ions. The experimental depth dose SOBPs parameters are displayed in table 6.3 (left column). The error on the dose and positioning are similar to those previously seen in section 6.3.1. Absolute dose deviations between planned and measured dose were below about 3.5% for every ion species and SOBP.

For proton and helium ion SOBPs, the absolute mean dose deviations within the SOBP were below 0.5% and below 1.5%, respectively. For heavier ions, the differences to the planned dose were below 3.3% with the largest discrepancies found for the deepest 12C ion SOBP. The homogeneity was in general above 95% except for the shallowest helium ion SOBP centered at 5cm, with an homogeneity of about 94.7%. The range was found to be similar between ions: about 79.5 mm for SOBP1, about 153.5 mm for SOBP2 and about 229 mm for SOBP3, except for oxygen ions with 226mm. For SOBP1, the DFO80/40 was roughly 1 mm for all ions, around 1.3 mm for SOBP2 and around 2.0 mm for SOBP3. The SOBPs size was similar for all depths and ions with an average size of 62.5 mm with a standard deviation of about 1.5 mm. The EPLR of the different ions for the SOBP1 were similar and around 93.2%. For the SOPB2 the EPLR was around 66% for the lighter ions and 76% for the heavier ions. At the largest depth, greater differences were found with EPLR values of 61% for protons, 66% for helium ions, 82% for carbon ions and 89% for oxygen ions. The TPLR for protons were about 0% except for the deeper SOBP with 2.6%. From the shallowest to deepest SOBPs the TPLRs were about 2.1%, 4.5%, and 6.0% for helium ions, 10.6%, 17.4%, and 23.3% for carbon ions, and 9.5%, 20.5%, and 29.7% for oxygen ions.

6.3.2.1.2. Simulations results and comparisons to measurement

The depth dose SOBPs parameters extracted from the simulations are shown in table 6.3 (right columns) and the deviation of the main parameters to the measurements are summarized in figure 6.7. The errors on the extracted parameters are calculated in a similar way as previously explained. The MC statistical error was below 0.1% in the high dose region and below 0.5% in the low dose regions for all the ions and for all the SOBP. Consistently with the experimental results, the homogeneity was in general above 98% except for the shallowest helium ion SOBP, showing homogeneity of about 96.5%, and the oxygen ion SOBP3, at about 94.8%. The differences in mean dose were close to those found between experimental and planned dose, since simulated absolute mean dose deviations to planned dose were found to be about +0.01 +/-0.3%. EPLR and TPLR differences between simulations and measurements were within 3%, with the largest difference observed for the deepest SOBPs and heavier ions (carbon ions EPLR difference for the SOBP3 was about 3.3% larger for simulations). Concerning variations in R_{80}, the differences were below 1 mm for every ion/SOBP combination. Regarding the SOBP size, the differences are below 1 mm for SOBP1 but larger for SOBP2 and SOBP3. The $DFO_{80/20}$ differences were below 1 mm except for protons, helium ions and the SOBP1 from carbon and oxygen ions. For SOBP2 and SOBP3 of oxygen and carbon ions larger differences are found up to12mm. However, the $DFO_{80/40}$ is showing excellent agreements within 1 mm for all investigated ions.

After normalization of each SOBP to the mean dose within 80% of their sizes, for both measurements and simulations, all measurement points in the high dose region were found

with differences for protons below 1.5% in the target region and below 3% in the whole distribution for all SOBPs, as seen in figure 6.8. For helium, carbon and oxygen ions, the differences were found below 3% on the whole distribution, except for the entrance measurements of carbon ion SOBP at 3.3%, as seen in figure 6.8.

SOBP position		Experimental measurement parameters						FLUKA simulation parameters					
		5,0		12,5		20,0		5,0		12,5		20,0	
		mean	σ	mean	σ	mean	σ	mean	σ	mean	σ	mean	σ
H	EPLR (%)	92,1	2,6	65,1	0,6	60,8	1,1	92,1	0,3	63,6	0,2	59,1	0,4
	R_{80} [mm]	79,0	0,7	154,0	0,7	229,0	0,7	79,0	0,7	153,7	0,7	228,5	0,7
	Size [mm]	60,7	0,7	62,6	5,1	61,7	5,1	61,0	0,7	61,3	0,7	60,8	0,7
	TPLR (%)	0,1	0,7	0,1	0,3	2,6	0,5	0,1	0,3	0,1	0,2	0,3	0,4
	$DFO_{80/20}$ [mm]	1,4	0,7	2,5	0,7	3,8	0,7	1,2	0,7	2,5	0,7	3,7	0,7
	$DFO_{80/40}$ [mm]	0,8	0,7	1,5	0,7	2,3	0,7	0,8	0,7	1,5	0,7	2,3	0,7
	Hom. [%]	95,9	1,2	96,9	1,1	96,4	1,1	98,1	0,1	99,7	0,1	98,7	0,1
	Dose dev.	0,1	0,7	-0,1	0,3	0,0	0,5	0,7	0,3	-0,2	0,2	0,3	0,4
He	EPLR (%)	92,5	1,9	67,0	0,8	66,6	2,4	92,9	0,2	67,2	0,1	65,3	0,1
	R_{80} [mm]	79,8	0,7	153,9	0,7	229,1	0,7	79,9	0,7	154,0	0,7	229,3	0,7
	Size [mm]	61,8	0,7	63,0	5,1	64,6	5,1	62,2	0,7	61,5	0,7	63,1	0,7
	TPLR (%)	2,1	1,9	4,5	0,7	6,0	0,8	2,9	0,2	3,3	0,1	4,7	0,1
	$DFO_{80/20}$ [mm]	1,1	0,7	1,7	0,7	2,4	0,7	0,9	0,7	1,6	0,7	4,7	0,7
	$DFO_{80/40}$ [mm]	0,8	0,7	1,0	0,7	1,6	0,7	0,5	0,7	1,0	0,7	1,4	0,7
	Hom. [%]	94,7	1,2	96,2	1,1	97,0	1,1	96,6	0,1	99,5	0,1	98,9	0,1
	Dose dev.	1,3	1,9	1,2	0,7	1,2	0,8	-0,2	0,2	0,0	0,1	0,0	0,1
C	EPLR (%)	93,9	0,9	74,9	0,9	82,3	1,1	94,3	0,3	76,6	0,1	85,6	0,6
	R_{80} [mm]	79,9	0,7	153,1	0,7	229,2	0,7	79,9	0,7	153,2	0,7	229,1	0,7
	Size [mm]	62,3	0,7	62,0	5,1	63,0	5,1	62,6	0,7	60,8	0,7	65,3	0,7
	TPLR (%)	10,6	0,7	17,4	0,8	23,3	1,1	8,6	0,3	16,1	0,1	22,8	0,6
	$DFO_{80/20}$ [mm]	2,0	0,7	7,6	0,7	14,5	0,7	1,8	0,7	2,1	0,7	20,7	0,7
	$DFO_{80/40}$ [mm]	1,2	0,7	1,3	0,7	2,0	0,7	1,1	0,7	1,0	0,7	1,8	0,7
	Hom. [%]	95,9	1,0	95,9	1,3	98,8	1,2	99,3	0,1	99,6	0,1	98,5	0,1
	Dose dev.	2,1	0,7	2,5	0,8	3,3	1,1	-0,4	0,3	0,3	0,1	0,0	0,6
O	EPLR (%)	94,4	0,6	78,2	1,5	88,9	1,3	94,1	0,2	79,3	0,2	90,5	0,5
	R_{80} [mm]	79,7	0,7	152,3	0,7	226,9	0,7	79,9	0,7	152,2	0,7	226,9	0,7
	Size [mm]	62,2	0,7	61,7	5,1	65,0	5,1	62,5	0,7	60,2	0,7	69,9	0,7
	TPLR (%)	9,5	0,5	20,5	1,0	29,7	0,9	9,2	0,2	19,0	0,2	27,8	0,5
	$DFO_{80/20}$ [mm]	2,1	0,7	10,4	0,7	16,8	0,7	2,0	0,7	7,8	0,7	28,0	0,7
	$DFO_{80/40}$ [mm]	1,3	0,7	1,0	0,7	1,9	0,7	1,2	0,7	0,9	0,7	1,4	0,7
	Hom. [%]	98,3	1,1	97,7	1,1	97,8	1,2	99,5	0,1	99,5	0,1	94,8	0,1
	Dose dev.	1,7	0,5	2,5	1,0	2,5	0,9	-0,4	0,2	0,0	0,2	0,0	0,5

Table 6.3: 6 cm × 6 cm × 6 cm SOBP depth dose distribution parameters: the different parameters are shown for the ions investigated at the different SOBP positions, for both measurements (left columns) and simulations (right columns).

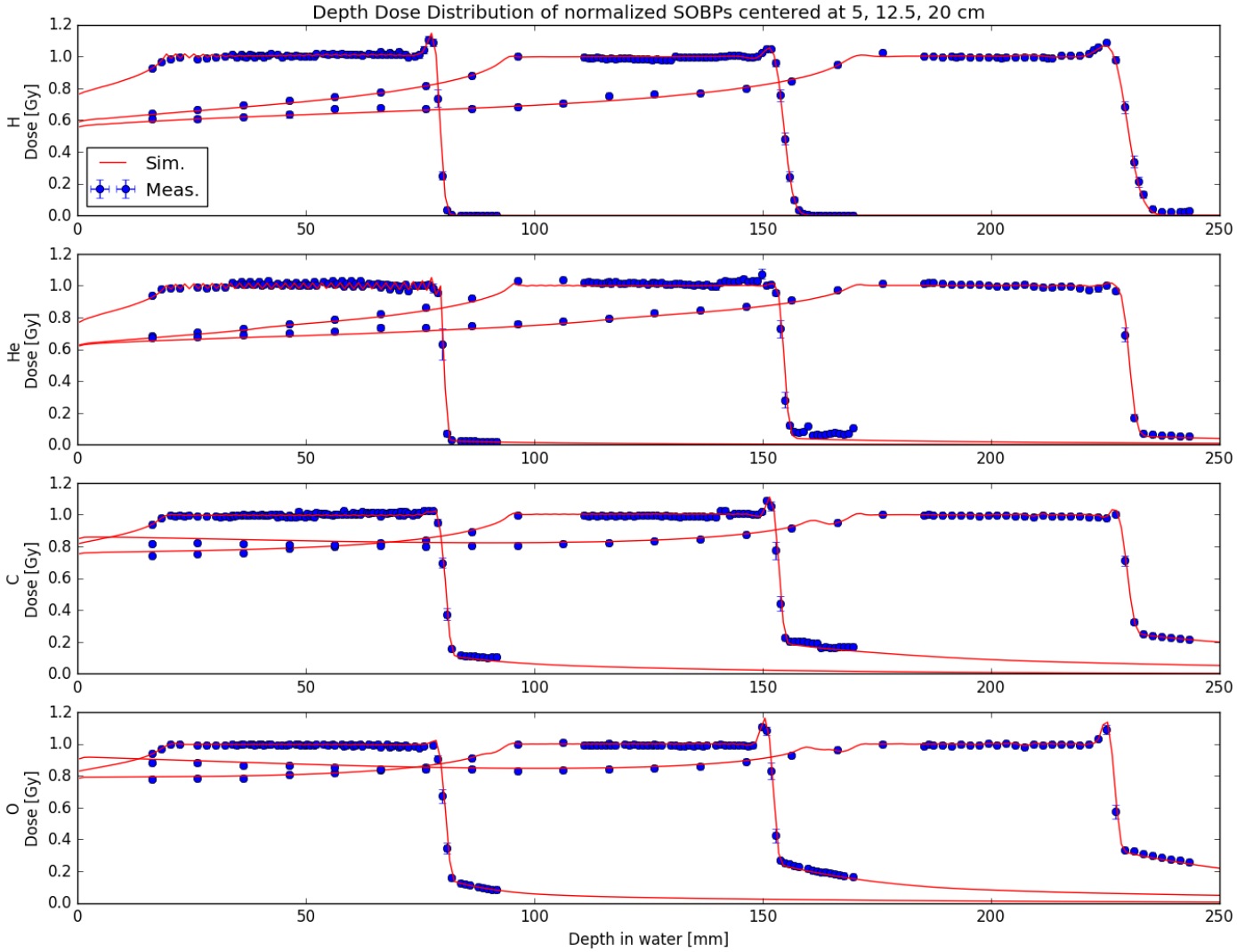

Figure 6.6: Depth dose distributions of the 6 cm × 6 cm × 6 cm SOBPs centered at 5, 12.5 and 20 cm for protons, helium, carbon and oxygen ions (from top to bottom panels). Measurements are shown as points with error bars while MC predictions are represented by solid lines.

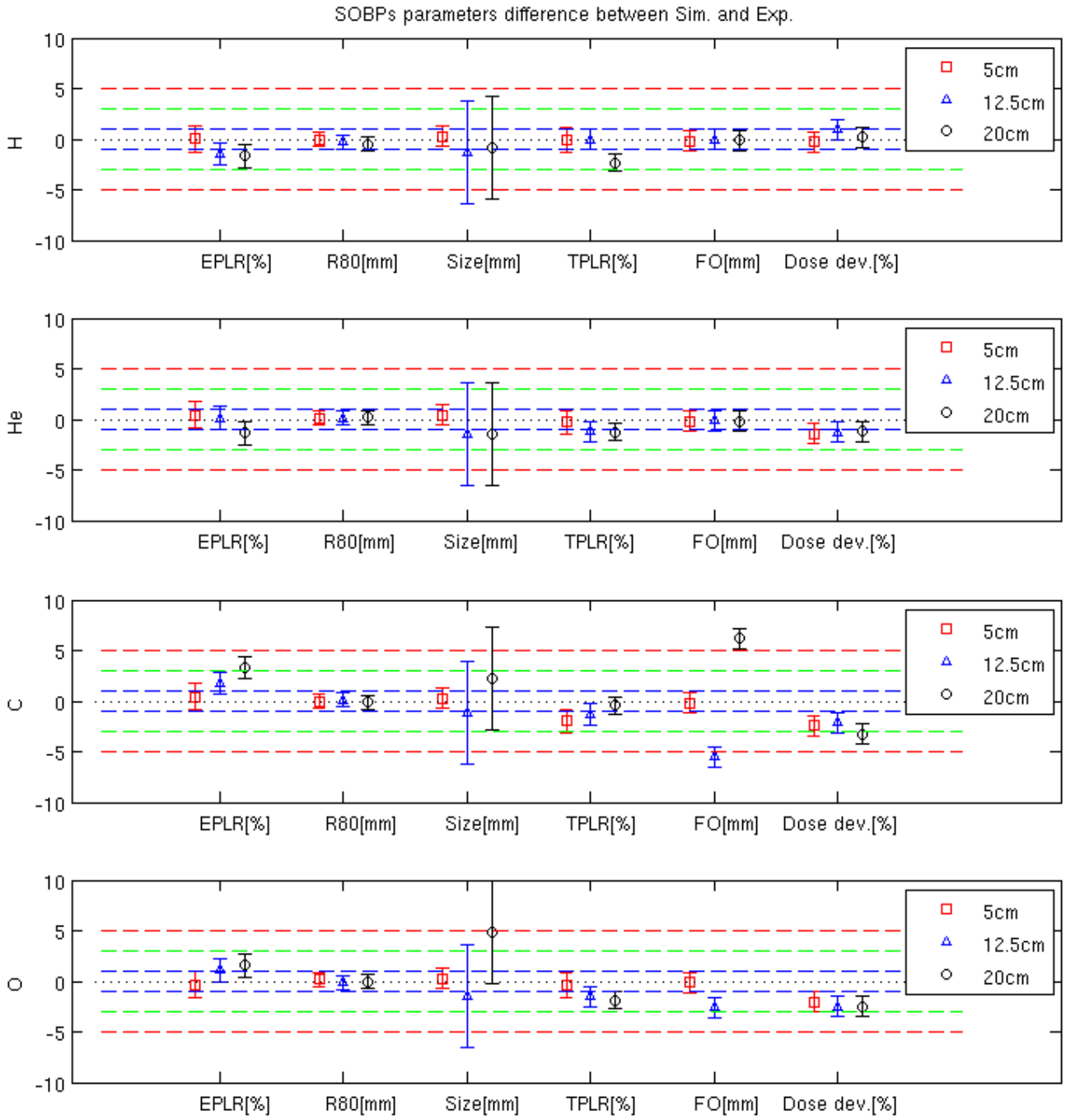

Figure 6.7: Difference between simulations and measurements for the 6 cm × 6 cm × 6 cm SOBP parameters extracted/calculated from the depth dose distributions. SOBP centered at 5 cm are represented by the square, at 12.5 cm by the triangle, and at 20 cm by the circle. From top to bottom the differences are displayed for protons, helium, carbon and oxygen ions. The dotted lines stand for difference of either 0 % or 0 mm, the dashed lines represent successively the 1, 3 and 5 difference in % or mm.

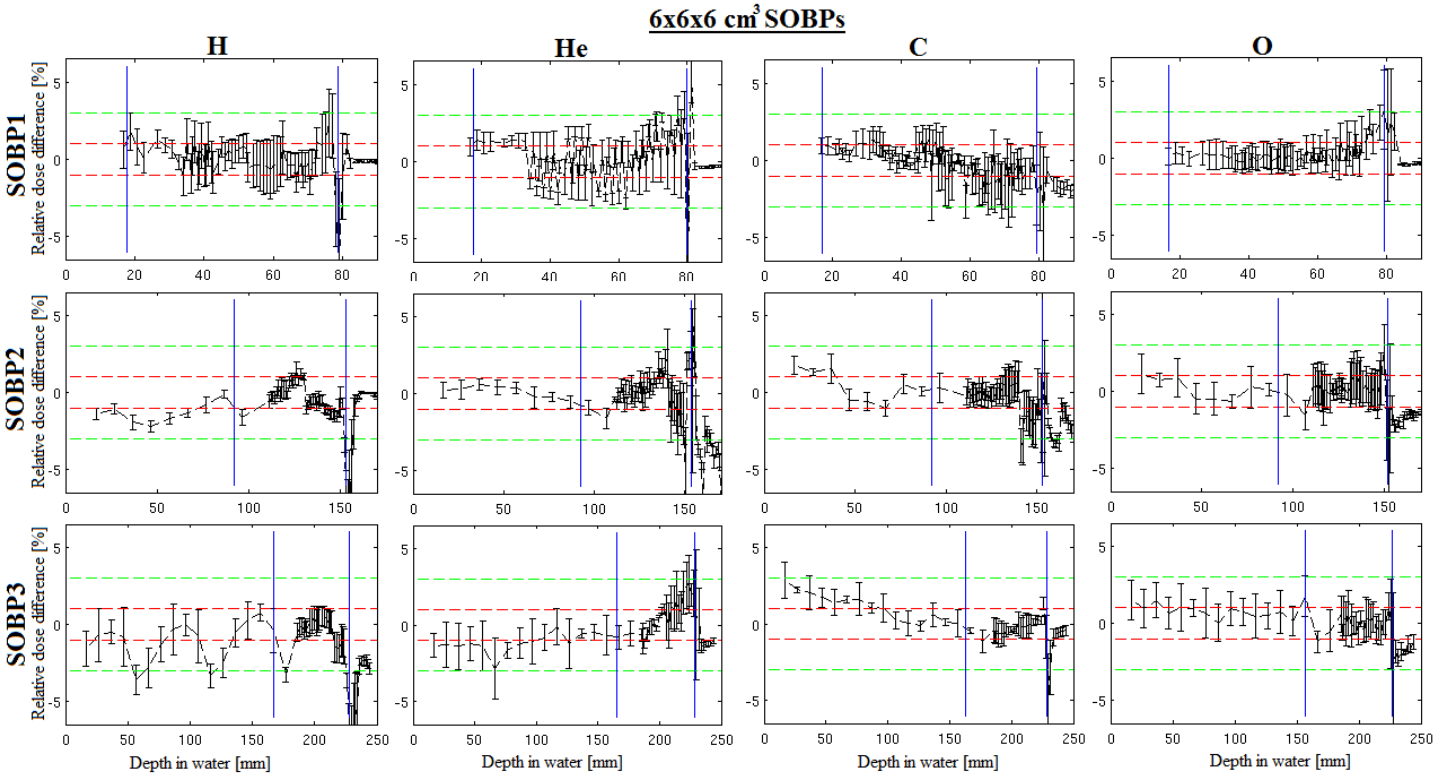

Figure 6.8: Dose differences along the depth between MC and measurements in water, after normalization, for the 6 cm × 6 cm × 6 cm SOBPs 6. The 1% deviation line is displayed in red, the 3% in green. The target region is within the blue vertical lines.

6.3.2.2. Lateral dose distributions

Lateral profiles in the middle of the SOBP for measurements and simulations are shown in figure 6.9, for all three 6 cm × 6 cm × 6 cm SOBP cases (left to right: SOBP1, SOBP2 and SOBP3) and for all ion species (top to bottom: protons, helium, carbon and oxygen ions). Parameters for the lateral distributions extracted from the measurements are shown in the table 6.4 (left columns). The errors have been estimated as described for the depth dose distributions. The LFO values for protons ranged from 12.7 mm for the shallowest SOBP to about 10.0 mm for the SOBP2 and SOBP3. The LFO values for helium ions ranged from 6.5 mm for SOBP1 down to 5.6 mm for SOBP2. The LFO values for carbon ions varied from 6.1 mm down to 5.1 mm. The LFO values for oxygen ions were about 5.0-5.7 mm for all SOBPs. The average SOBP sizes were similar for every ion and about 61.5 mm. The irradiated protons SOBP size was about 76 mm. For helium and carbon ions, the irradiated size was about 69 mm. For oxygen ions, the irradiated size was about 68 mm.

The parameters of the lateral distributions extracted from the SOBP simulations are shown in table 6.4 (right columns) and the difference to the parameters extracted from the measurements are summarized in figure 6.10.

The differences between measured and simulated parameters are below 1 mm for most of the SOBP parameters except the for the irradiated sizes of the protons SOBP2 and helium ions SOBP3, and the lateral size and lateral fall off of protons SOBP1.

SOBP position		Experimental measurement parameters						FLUKA simulation parameters					
		5,0		12,5		20,0		5,0		12,5		20,0	
		mean	σ	mean	σ	mean	σ	mean	σ	mean	σ	mean	σ
H	Irrad. Size [mm]	76,1	0,97	76,5	1,72	75,9	1,15	76,2	0,7	75,1	0,8	75,3	0,8
	Lat. Size [mm]	59,9	0,75	62,5	1,44	62,3	1,1	62,8	0,8	63,4	0,7	63,3	0,7
	$LFO_{80/20}$ [mm]	12,7	0,75	9,8	0,85	10	0,75	11	0,8	9,2	0,7	9,7	0,8
He	Irrad. Size [mm]	68,5	0,85	68,3	0,85	70,5	0,97	69,1	0,7	68,4	0,7	69,1	0,7
	Lat. Size [mm]	60,6	0,75	61,2	0,97	63,1	0,97	61,2	0,8	62	0,7	62,6	0,7
	$LFO_{80/20}$ [mm]	6,5	0,85	5,6	0,71	6,2	0,6	6,4	0,7	5,1	0,7	5,3	0,8
C	Irrad. Size [mm]	67,7	0,79	69,3	0,97	69,5	0,97	67,2	0,9	68,9	0,7	69,4	0,7
	Lat. Size [mm]	59,3	1,02	62,3	1,33	62,9	0,85	59,9	1,1	62	0,7	62,2	0,7
	$LFO_{80/20}$ [mm]	6,1	0,71	5,1	0,85	5,6	0,85	5,8	0,7	5,3	0,7	5,7	0,7
O	Irrad. Size [mm]	65,6	1,98	69	0,85	69,2	1,55	66,1	0,7	68,3	0,7	68,9	0,7
	Lat. Size [mm]	60	0,85	62,5	1,21	61,3	0,85	59,3	0,7	61,7	0,7	61,9	0,7
	$LFO_{80/20}$ [mm]	5	0,71	5,2	0,85	5,7	0,71	5,3	0,7	5,1	0,7	5,4	0,7

Table 6.4: 6 cm × 6 cm × 6 cm SOBP lateral dose distribution parameters: the different parameters are shown for the ions investigated at the different SOBP positions, for both measurements (left columns) and simulations (right columns).

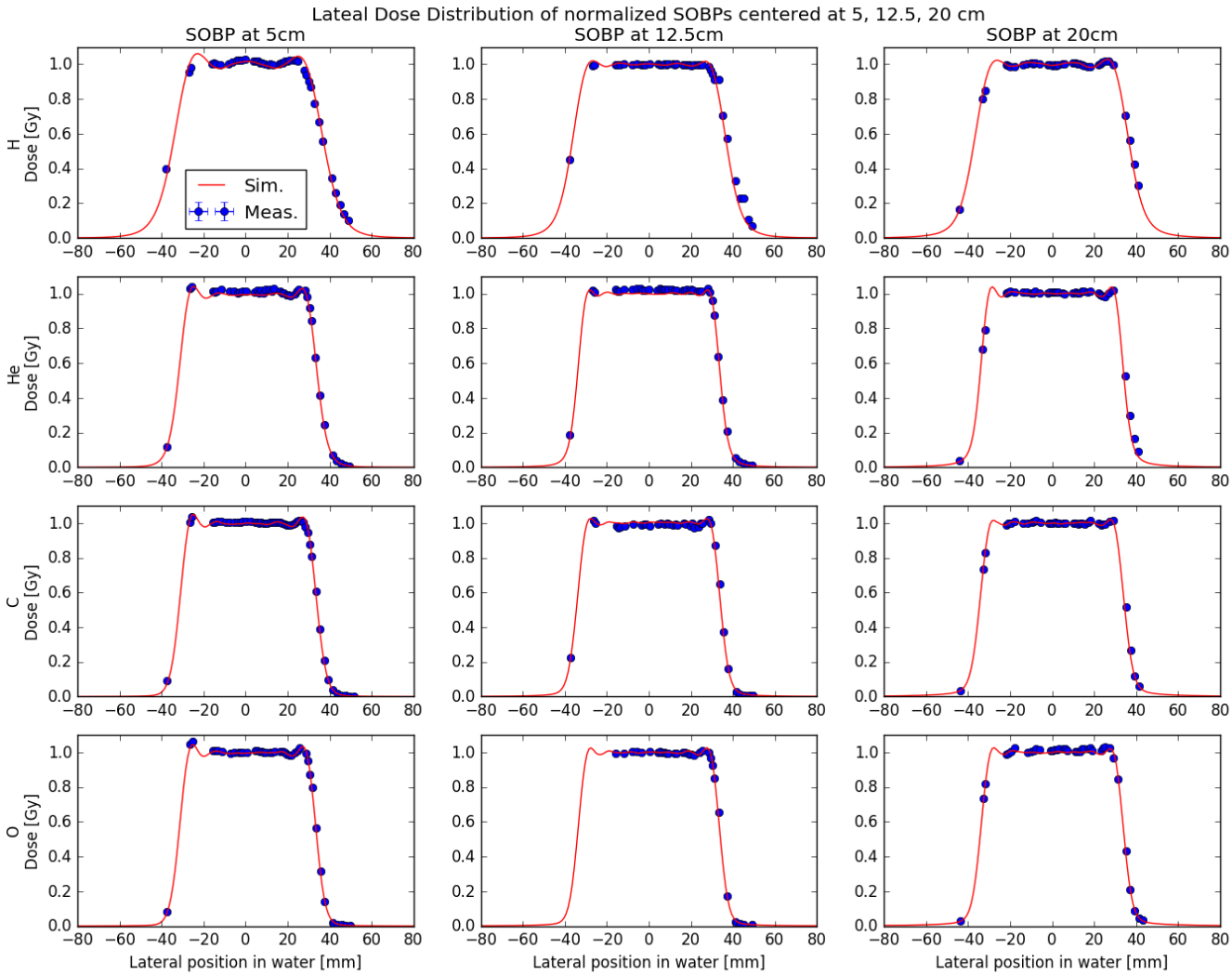

Figure 6.9: Lateral dose distributions at the mid-SOBP position for the 6 cm × 6 cm × 6 cm SOBPs centered at 5, 12.5 and 20 cm (from left to right panels) for protons, helium, carbon and oxygen ions (from top to bottom panels). Measurements are shown as points with error bars, while MC predictions are represented by the solid lines.

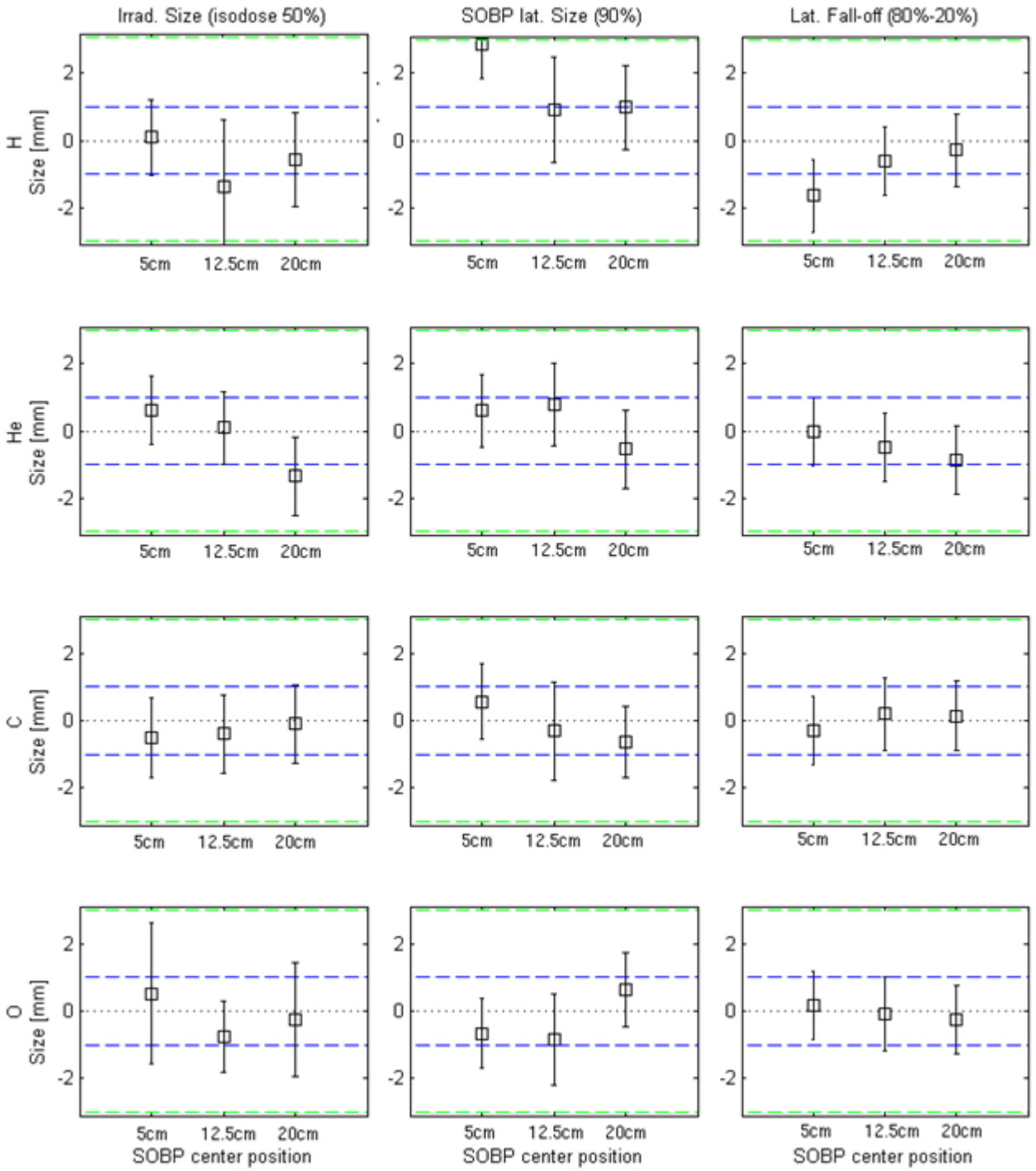

Figure 6.10: Difference between parameters extracted from the simulated and measured lateral dose distributions in the 6 cm × 6 cm × 6 cm SOBP region. From the left to the right panels, the irradiated lateral size, the SOBP lateral size and the lateral dose fall-off are presented for protons, helium, carbon and oxygen ions (from top to bottom panels). The dotted lines indicate a 0 mm difference, while the dashed lines represent differences of 1 (blue) and 3 mm (green), respectively.

6.4. Discussion

As previously stated, the small 3 cm × 3 cm × 3 cm is the most challenging case and will be discussed into details. Uncertainties in the planning, delivery and measurements of the the 6 cm × 6 cm × 6 cm will be described to explain discrepancies in the results, compared to the trend reported in detail for the small SOBP.

6.4.1. Dosimetric parameters comparisons between the different ions and to MCTP plans

6.4.1.1. Depth dose distributions

On the depth dose distribution parameters for the 3 cm × 3 cm × 3 cm SOBPs, for the EPLR at 5 cm no particular differences were observed between the different ions with an EPLR value of around 72%. For deeper SOBPs, light ions were showing net advantages with at least 10% less EPLR at 12.5 cm and up to around 20% for protons and helium ions compared to oxygen ions at 20 cm. These effects of increased EPLR, already described in Chapter 3 with the entrance-to-peak ratio for pristine Bragg peaks measured at HIT, are mainly due to the higher fragmentation of ions. Additionally, the RiFi used for heavy ions is increasing the peak width of the pristine peaks, thus leading to an increase of EPLR. In Chapter 3, the difference between the entrance-to-peak ratio of pristine peaks at about 20 cm of oxygen ions with RiFi and protons without RiFi was about 9%. For SOBP3, this difference was found larger (~20%) due to the overlapping contribution of each Bragg curve building up the SOBP. For physical SOBPs optimized for a 6 cm × 6 cm × 6 cm target the contribution of more Bragg curves increased this difference, up to 29%.

For the 3 cm × 3 cm × 3 cm SOBPs the $DFO_{80/20}$ of SOBP1 showed similar results for protons without RiFi and carbon/oxygen ions with RiFi. A value of about 1.5 mm has been found which is in agreement with the results shown in Chapter 3 for pristine peak of the same range (~1.3 mm). Helium ions were showing for this depth a reduced $DFO_{80/20}$ of 0.5 mm due the reduced range straggling compared to protons and steeper fall-off than heavier ions using RiFi. The RiFi, in fact, increases the range spread. For larger depths, the $DFO_{80/20}$ were not comparable due to the contribution of the fragmentation tail to the 20% fall-of dose, thus making $DFO_{80/40}$ the preferable parameter for comparisons. The $DFO_{80/40}$ of the 12.5 cm centered SOBP were similar (~1.7 mm) for protons, carbon- and oxygen ions, while it was smaller (~0.8 mm) for helium ions (without RiFi). For the deepest SOBP helium, carbon and oxygen ions exhibit the same $DFO_{80/40}$, in agreement with the trend of the $DFO_{80/20}$ at this depth for pristine peaks, while the range straggling of protons led to a larger DFO. However, it can be observed that the $DFO_{80/40}$ values are found larger than the $DFO_{80/20}$ of pristine peaks for carbon and oxygen ions. For the lighter ions, the SOBP $DFO_{80/20}$ is larger than the one with pristine peaks. This could be explained by the sum of the Bragg curves and their dose contributions to the fall-off of the most distal ones. Thus, for protons the $DFO_{80/20}$ of the SOBP, compared to the corresponding highest energy pristine Bragg peak, was raised by about 0.3 mm at 5cm, 0.8 mm at 12.5 cm and 1.3 mm at 20 cm. For helium ions, the increase was about 0.1, 0.5 and 0.6 mm for the SOBP1, SOBP2 and SOBP3, respectively. The effect is enhanced at greater depth since the $DFO_{80/20}$ gets larger than the distance between two consecutive Bragg peaks in depth. Experiments with 6 cm × 6 cm × 6 cm optimized SOBPs, centered at the same investigated depths, showed similar values for the DFO parameters.

Concerning the TPLR, for the 3 cm × 3 cm × 3 cm SOBPs, the light ions showed advantages with null TPLR for protons except small values of 0.4% at large depths due to the enhanced distal fall-off, and reaching a maximum of around 3.5% for helium ions for SOBP3. The heavier ions showed significantly larger TPLR values up to 18% and 25% for carbon- and oxygen ions, respectively. The fragments produced all along the beam paths for each Bragg

curves are summed up in the SOBP, leading to TPLR results larger than the ones found in Chapter 3 for pristine peaks, exhibiting at 20 cm tail-to-peak ratios of about 10% for carbon ions and 15% for oxygen ions. For experiments using 6 cm × 6 cm × 6 cm SOBPs the TPLR got even higher due to the contribution of a larger number of Bragg curves, resulting in TPLR of about 23% and 29% for carbon- and oxygen ions, respectively, in the case of SOBP3.

Except for the R_{80} of the oxygen 6 cm × 6 cm × 6 cm SOBP3, the range of the different SOBPs are similar. For the large oxygen SOBP3, this discrepancy in range results from the high dose region observed at the end of the SOBP, impacting the range evaluation. It results from a lack of constraint on the optimizer for maximal dose within the target (cf. Appendix C), which was corrected for the 3 cm × 3 cm × 3 cm SOBPs optimization.

The size of the small SOBPs in depth was found similar with a value of about 31.6 mm, showing good conformity of all ions to the target, except for the shallowest helium SOBP (~30 mm) where, due to the ripples, the proximal 90% position is overestimated. Due to the same effect, the homogeneity of helium ions for SOBP1 is lower than that of other ions or at other depths. In order to achieve homogeneous distribution with low energy helium ions, the RiFi should be used as proposed in Chapter 3 and used in Krämer *et al* (2016). However, it could degrade some parameters such as EPLR, TPLR, DFO and LFO, thus bringing more doses to the surrounding tissues. Furthermore, even though the homogeneity was found below 95%, the maximum and minimum doses differ less than 4% from the planned dose value, which could still make a delivery without RiFi acceptable. Dose planning using a reduced depth separation between consecutive Bragg peaks of about 1mm could provide also an improved dose distribution homogeneity within the target. The main drawback of such an approach is the increase delivery time. For the larger 6 cm × 6 cm × 6 cm SOBPs, the SOBP1 size was found consistent between all ions. However for the deepest SOBP2 and SOBP3, differences to the planned size of 60mm were observed. The large difference up to 5 mm in size can be attributed to the lack of measurement points in the proximal rising edge region of the SOBP, as seen in figure 6.6, translated into the large standard deviations reported in table 6.3.

The observed absolute dose deviations between measurements and MC predictions below 3.5% for all investigated SOBPs, as well as the overall homogeneity higher than 95%, are promising results indicating a proper beam monitor calibration in the experimental room for all ions.

In Chapter 3, larger deviations between planned and delivered dose were found, before performing a refinement of the beam monitor calibration, with about 5% dose difference in the SOBP region for helium ions and 8% for oxygen ions. Also, the dose differences between measurements and plans performed with the research analytical TPS were found about -1.8% for carbon ions, while being about +2.7% for the small SOBP2 planned with the research MCTP. The small carbon SOBP2 is similar in longitudinal size and close to the range of the SOBP presented in Chapter 3. The main reason is ascribed to the fact that the beam monitor calibration is tuned for the clinical and research analytical TPS. MC dose prediction of the SOBP described in Chapter 3 was found to deviate by about -4.5% from the planned dose, as shown in Appendix C. Therefore, a similar disagreement of about 3% is found with respect to measurements, consistent with the findings of this work with deviations between 1.7 and 3.5%.

Regarding the evolution of the differences between measurement and simulations shown in figure 6.3 and 6.8 for small and large SOBPs respectively, due to dose gradient effects and position uncertainties, large deviation are observed for all ions near the blue lines representing the SOBP limits. Compared to the measurements of the 3 cm × 3 cm × 3 cm SOBPs, the

measurements were noisier and presented unexpected values due to measurement drift (helium SOBP2 tail, measurements above 3% for protons), mainly due to the delivery time at least 8 times higher than for the small SOBPs, associated to a higher number of measurement points to cover the whole SOBPs.

While for protons, carbon and oxygen ions the dose difference is relatively stable around the line of 0% deviation (after normalization) in the SOBP region, helium ions show trends of increasing dose difference in the SOBP with increasing depth. This could be the effect of the beam monitor calibration performed with only two parameters. One is applied to adjust the level of the calibration for all energies, while the other one is used to introduce a linear dependency between dose and energy. A possible modification of this second component could flatten out the dose difference within the SOBP. However, this would lead to a larger dose difference in the entrance channel, similar to the trend observed with carbon ions in figure 6.3 and 6.8 before the SOBPs position. The beam monitor calibration for helium ions could be refined in future, even though the results presented are dosimetrically acceptable.

6.4.1.2. Lateral dose distributions

For the lateral dose distributions of the 3 cm × 3 cm × 3 cm SOBPs, due to the use of different spot-sizes, the LFO values of helium and heavy ions were found quite similar in the SOBPs region while being larger by about 5 mm for protons due to a non-negligible lateral scattering. In the entrance of the water tank, smaller LFO values were found for helium ions compared to heavier ions. This finding results from (1) the delivery of helium ions without RiFi compared to heavier ions with RiFi and (2) due to the use of a different focus size at isocenter (first focus size for helium, third focus for heavier ions) as stated in section 6.2.1, being the nominal focus size smaller by about 3mm for helium ions at high energies (without taking into account the additional broadening effect from the RiFi for heavier ions). In the tail, the lateral fall-off of carbon ions was found larger than the one for oxygen ions due to the production of heavier fragments with less lateral spread for oxygen ions. Similar LFO results were found for the 6 cm × 6 cm × 6 cm SOBPs.

The irradiated lateral size was found to be similar for helium, carbon and oxygen ions, while being up to 8-12 mm larger for protons, respectively, for the large and small SOBPs, as a direct consequence of their reported larger LFO.

Concerning the SOBP sizes, the results were in agreement with the planned size of 30 mm and 60mm, with better conformity to the target for oxygen ions, followed by carbon ions, helium ions and protons.

These results are consistent with the trend of the mono-energetic pencil-beams data investigated in Chapter 3. Compared to the 4 cm SOBP centered at 10 cm which is presented in Chapter 3, optimized only in depth, similar DFO were observed than the small SOBP2. However the LFO values of SOBPs optimized with 3 dimensional techniques is improved, particularly for light ions. The LFO reported in Chapter 3 was about 4 mm larger for protons, 3 mm larger for helium ions, about 1 mm larger for carbon ions and 0.5 mm larger for oxygen ions, compared to the small and large SOBP2 reported in this Chapter.

These results indicate that helium and oxygen ions are provided with a similar clinical quality than the therapeutic protons and carbon ion beams used at HIT. It also shows that the MCTP engine is able to optimize correctly different regular fields with the requested size, depth and dose for both small and large targets, respecting as well the constraints of the HIT delivery system.

6.4.2. Dosimetric parameters comparisons between MC predictions and measurements

In the comparisons between MC predictions and measurements after dose normalization to the mean dose inside the inner 80% of the SOBP, the dose parameters EPLR and TPLR were found all in good agreement within 3% for both SOBP sizes. The MC absolute dose deviation with respect to the measurements were similar to those presented previously for SOBP dose measurements and planned doses, with a maximum absolute dose deviation of 3.5%, since the simulated dose agreed within 1% with the dose planned from the MCTP.

R_{80} values from simulations and measurements were found to be in excellent agreement, for 3 cm × 3 cm × 3 cm and 6 cm × 6 cm × 6 cm SOBPs.

Similar agreement was found for the 3 cm × 3 cm × 3 cm SOBP size comparisons, with the exception of the shallowest SOBP for helium ions. As explained previously, this is owed to an overestimation of the position of the 90% proximal dose due to the pronounced ripples, thus reducing the calculated size of the experimental SOBP. For the 6 cm × 6 cm × 6 cm SOBPs difference in size for all ions deepest SOBP2 and SOBP3 were found due to the lack of measurement points in the SOBP proximal rising edge region, as seen in figure 6.6. However the measurements and simulations depth dose curves are matching in the SOBP region.

For 3 cm × 3 cm × 3 cm, the agreements on the $DFO_{80/20}$ are within 1 mm except for the deepest oxygen SOBP, due to the worsening of the agreement between measurements and predictions in the fragmentation tail. For the 6 cm × 6 cm × 6 cm SOBPs, while the agreement remains good for light ions, for SOBP2 and SOBP3 of oxygen and carbon ions, the $DFO_{80/20}$ parameter is not reliable due to the dose measurement fluctuation of the tails and the hot spots at the end of the SOBP regions. However for both SOBP sizes, when comparing the $DFO_{80/40}$, the difference between measurement and simulation was found to be below 0.5 mm.

Concerning the comparisons of the geometrical lateral dose parameters of the small SOBP size, all investigated quantities were found within 1 mm between MC and experiments, except for protons. For protons differences up to 1.9 mm were found for SOBP1 and SOBP2. It was found that for these two SOBPs the spot size delivered at isocenter was larger than the one expected from the HIT library by about 10%, which is still within the tolerance of HIT. It has already been investigated in Parodi *et al* (2010) that, on small targets, spots size deviations can impact the target dose distribution. By adjusting the spot size to the actual measurements, as described in Chapter 5 and Tessonnier *et al* (2016), the newly calculated dose distributions were matching well the measurements, resulting in an agreement of the new parameters within 1mm (figure 6.11, referring to the small SOBPs). For the largest SOBPs, relevant difference on the lateral parameters were observed only for the shallowest proton SOBP1, due to the reason previously explained for the small SOBP1 and SOBP2.

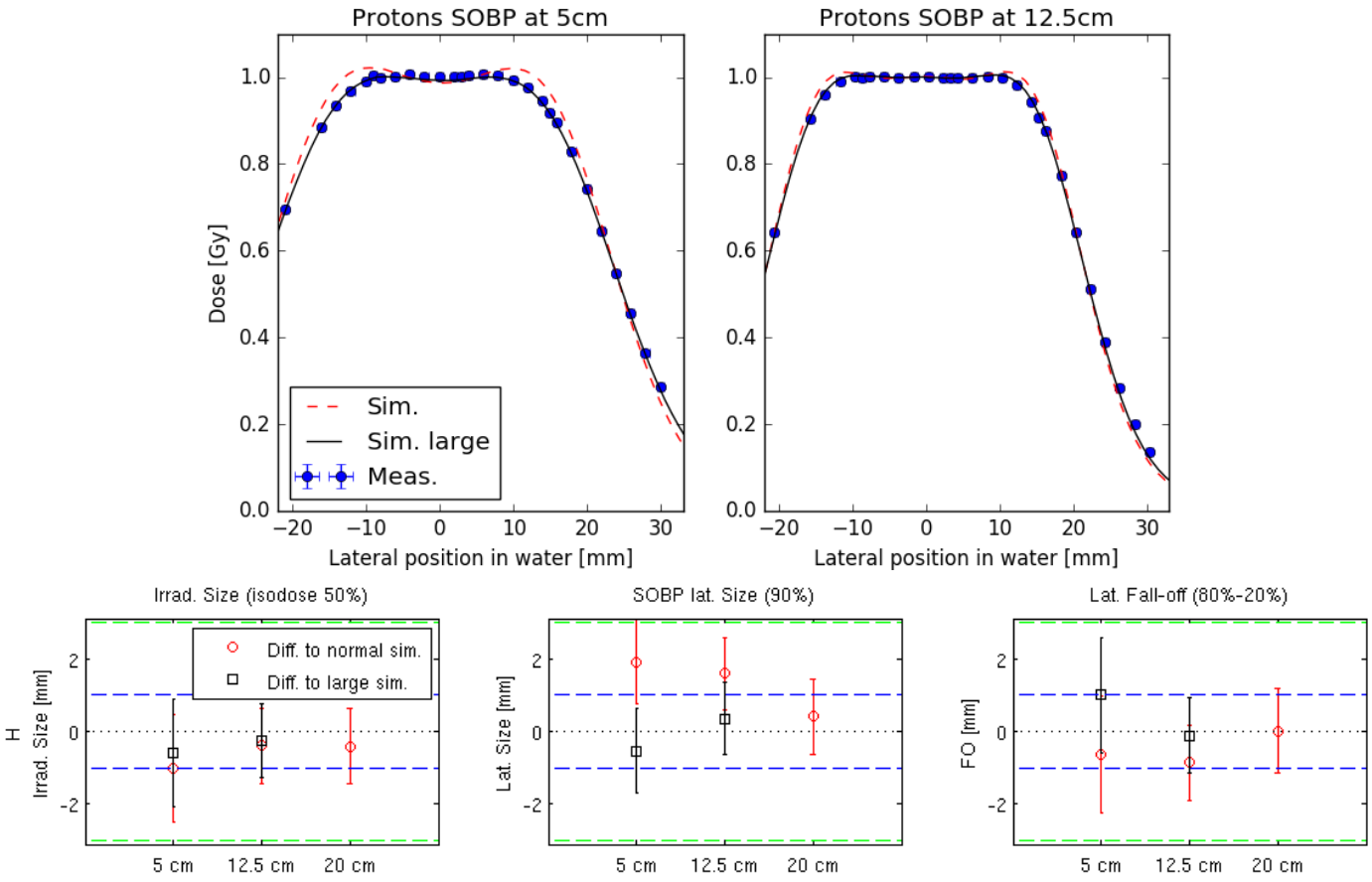

Figure 6.11: Lateral dose distributions at the mid-SOBP position of the 3 cm × 3 cm × 3 cm SOBPs centered at 5, and 12.5 cm (from upper left to right panels) for protons. Measurements are shown with dots while MC predictions are represented by the lines. The simulations using planned parameters are displayed with dashed lines ("Sim.") while the simulations using larger spot sizes are represented with solid lines ("Sim. Large"). The bottom panels depict the evolution of the extracted parameters from the lateral dose distributions in the SOBP region for protons. From the left to the right panels the irradiated lateral size, the SOBP lateral size and the lateral dose fall-off are presented. Circles depict the comparisons between normal simulations against measurements, while square symbols represent the comparisons between simulations with larger spot sizes and measurements.

The high level of agreement between MC predictions and measurements is encouraging and supports the possibility of patient plan comparisons, as addressed in Chapter 7 for protons and helium ions. The quality of the predictions is relying on both the FLUKA physics models as well as the detailed model of the HIT irradiation system (beamline, focus size). As shown in Parodi *et al* (2010), Parodi *et al* (2012) and Chapter 5 changes in the description of the beamline model, such as the spot size, can highly impact the dose distribution in small and challenging targets. In Krämer *et al* (2016), for helium ions SOBP, disagreement has been observed in the lateral fall-off distributions, using their analytical TPS compared to measurements. In our study, MC predictions were found to match the data within 1.5 mm for all helium ion SOBPs, ensuring a correct estimate of the absorbed dose in surrounding healthy tissues for future planning studies. A previous FLUKA-based MC work from Kantemiris *et al* (2011) was estimating $DFO_{80/20}$ values of about 2.4, 1.6, 1.6, 1.6 mm, respectively, for protons, helium, carbon and oxygen ions for a 5cm SOBP centered at 10.5 cm optimized in depth. For light ions these values are close to the measurements and simulation predictions presented in this work for the 12.5 cm SOBP, with differences most likely due to the variation in the initial beam setup (beamline, initial momentum spread) or to the different position of the investigated SOBP. However, an underestimation of the fragmentation can be observed in the work of Kantemiris *et al* (2011), as no dose contribution from the tail to the $DFO_{80/20}$ is seen for carbon and oxygen ions, contrary to the expectations. Actually an even enhanced fragmentation tail would have been anticipated for that work compared to the small SOBP2 reported in this Chapter, as a result of the sum of a higher number of pristine Bragg curves needed to cover the considered larger target. This effect is probably linked either to a previous version of the FLUKA code or different simulation settings. Hence, these observations are highlighting the importance of the validation of calculation engines (either analytical or MC) against measurements before performing in-depth planning studies.

This physically validated MCTP system can be interfaced with experimentally validated biological models, such as phenomenological (Wedenberg *et al* 2013, Mairani *et al* 2016a, Mairani *et al* 2016b) or biophysical (Elsässer *et al* 2010, Inaniwa *et al* 2010) models. Appendix C shows results of biological calculations performed with FLUKA using the model from Mairani *et al* (2016a, 2016b, 2017a). Thus, the MCTP tool can be used to calculate biologically optimized treatment plans. As already explained in Grün *et al* (2015) and Burigo *et al* (2015) and anticipated in Chapter 3, the superiority of one ion species over another for clinical scenarios is not trivial and may depend on various parameters, involving amongst others the beam ballistics (number of fields, angles), the fractionation and the tissue types and condition (oxygenation) of the target and the surrounding healthy tissues. Thus, the validated FLUKA-based MCTP engine presented in this Chapter will provide a solid platform for plan comparisons with the available ions at HIT.

6.5. Summary

In this part of the thesis work, thorough comparisons between the measured dosimetric properties of SOBPs physically optimized with the FLUKA-based MCTP tool for different ion species were presented, considering small targets of 3 cm × 3 cm × 3 cm and larger targets of 6 cm × 6 cm × 6 cm placed at different depths in water. The FLUKA forward recalculation of the SOBP plans was validated against measurements with satisfactory agreement for all investigated parameters. Using clinical-like irradiation settings, the dosimetric properties of helium ions are found close to those of heavier ions. Between protons and helium ions, which are in the same low LET range, helium ions could provide better sparing of surrounding healthy tissues through better dosimetric characteristics. Oxygen ions show similar dosimetric characteristics as clinically used carbon ions. Due to their high LET characteristics, oxygen ions could be of particular interest in treatment of radio-resistant tumors such as high-risk meningiomas in combination with conventional radiotherapy as discussed by Combs *et al* (2010). Planning studies with patient data are foreseen with this tool in combination with recently validated biological models, as will be shown in Chapter 7, thus paving the way towards the envisioned clinical introduction of these new ions at HIT. Furthermore, investigations on the combination of several ions within the same plan can also be performed using this validated platform, following the work of Böhlen *et al* (2013).

Chapter 7. Proton and helium ion radiotherapy for meningioma tumors: a Monte Carlo-based planning study

A comparison of proton and helium ion treatment plans is shown in this chapter. It relies on validated Monte Carlo simulations as presented in Chapter 4 for helium ions, as well as the Monte Carlo Treatment planning tool described in Chapter 6. With the improved simulation framework described in Chapter 5, treatment plans for four patients with meningioma tumor were biologically optimized for both protons and helium ions. This biological optimization takes into account the different tissue-types of tumorous and normal tissues (based on the biological modeling presented in Appendix C for helium and protons). Two tissue-types were considered for the target, meningioma and arterio-venous-malformation, representing an example of biological diversity of treated brain tissues which yields varying biological dose outcomes during optimization.

7.1. Background

Clinical application of helium ions with state-of-the-art delivery techniques has the potential to improve particle therapy, i.e., patient treatment outcome. Compared to the first clinical experience at the Berkeley institute with passively scattered beam delivery (Castro et al. 1994, Kaplan et al. 1994), treatments at HIT can be achieved with a fully active beam delivery, as presented in Chapter 2.

The physical advantages of helium ions with reduced range and lateral straggling in comparison to protons could result in greater healthy tissue sparing and improved dose-to-target conformity, as presented in the previous Chapters 3 and 6. As already introduced in Chapter 4, compared to protons, helium ions exhibit a higher linear energy transfer (LET) and

therefore a higher relative biological effectiveness (RBE), as well as a smaller oxygen enhancement ration (OER). Compared to heavier ions, such as carbon and oxygen ions, presenting higher LET values, higher RBE and reduced straggling than helium ions, helium ions can be still considered favorable in terms of reduced fragmentation after the Bragg peak and subsequently lower dose after the target, as seen in the dosimetric results from Chapter 4 and 6. Even though differential RBE effects between tumor and normal tissues are reduced compared to the heavier ions, the reduced RBE range makes biological dose predictions of helium ions less prone to uncertainties, particularly in normal tissues. Moreover, possibilities of dose escalation seem promising for helium ions, owing to their reduced penumbra compared to protons and the low dose fragmentation tail compared to heavier ions. Thus, the helium ion treatment modality could effectively reduce dose in cases where organs at risk (OAR) are commonly found in proximity to the target, e.g., brain tissue, as well as reduce the integral dose delivered to the patient and the related risk of radiation induced secondary cancer. Vernimmen et al. (2001) noted the particular interest of proton beam therapy for complex brain tumour cases such as meningiomas, where helium ions could further improve the therapeutic gain with respect to proton therapy.

As stated in the previous Chapter 4 and 6, recent works investigated the advantages of helium ions for planning studies (Grün et al. 2015, Knäusl et al. 2016) with research platforms not validated against experimental dosimetric data. A thorough dosimetric investigation of helium ions and in-depth validation of the MC code FLUKA with related MC-based treatment planning tool has been achieved in this thesis, as presented in the previous Chapter 4 and 6. In combination with a validated phenomenological biological model (Appendix C), which has been benchmarked against data for proton and helium ions and considers the entire mixed radiation field generated in nuclear interaction (Mairani et al. 2016a, Mairani et al. 2016b, Mairani et al 2017), this chapter presents a treatment plan comparison of four different brain meningioma cases, using protons and helium ions. Additional MC investigations were performed, replacing the target with arteriovenous malformation (AVM) tissue in order to evaluate the influence of different brain tissue types on dose optimization and biological outcome. AVMs, even if being non-tumorous tissues as described in Chapter 5, represent a tissue type which could be related to a high α_x/β_x in comparison to meningioma (Vernimmen *et al* 2010) and hence is used as a high α_x/β_x tissue surrogate in the MC study. The effect of dose fractionation scheme was investigated for one challenging patient case with helium ions for both target tissue types. Additionally, the impact of the ripple filter (RiFi) presence was evaluated for a patient case with a target at shallow depth. In Appendix D, a comparative study between helium ions and protons for a prostate case is additionally presented.

7.2. Patient selection and methods

7.2.1. Optimization and dose calculation methods

Four meningioma patient cases irradiated with protons at HIT were used in this study. In clinical practice, treatment planning with protons assumed a RBE of 1.1. Details of each treatment are presented in table 7.1:

- three brain meningiomas with two beams (patients A-C);
- one optical meningioma (patient D), at shallow depth, with a single beam.

Critical OARs for each case are listed in table 7.1 and their spatial locations relative to the planned target volume (PTV) are displayed in figure 7.1. The original proton plans from the commercial TPS (SyngoPT, Siemens) were re-optimized with MCTP (cf. Chapter 6) for both protons and helium ions, using a variable RBE model for both ions, as well as a fixed RBE

value of 1.1 for protons. Proton RBE in clinical practice is defined at 1.1 (Paganetti *et al* 2002), since, as explained in Carabe et al (2012), data are not sufficient to support a variable RBE approach. However some studies against cell data have shown a rise in RBE with the increase of LET (Wedenberg *et al* 2013, Mairani *et al* 2017) justifying the implementation of such variable model in the MCTP, as also supported by the recent work from Peeler *et al* (2016) showing clinical evidence for pediatric patient brain treatments. In our study, for variable RBE calculation, different α_x and β_x terms from the linear quadratic equation (Fowler 1989 as seen in Chapter 2) for photon irradiations were attributed to OAR and PTV. For PTV, two different tissue types were investigated as explained in the following.

The optimization process was performed as follows. Firstly, the optimization constraints were determined by initially running the proton plans in the MCTP with a fixed RBE of 1.1 in order to obtain similar or better dose volume histograms (DVH) than the original plan from the analytical TPS. After determination of the various constraints and obtaining the resulting plan for protons with fixed RBE, optimizations for protons and helium ions with a variable RBE model were performed. The two main advantages of finalizing the constraints for protons using a fixed RBE are: (1) it makes the DVH results readily comparable to those of the clinical TPS plans and (2) no additional changes will occur on biological dose while changing tissue type or fractionation size. The different constraints are shown in table 7.2 with their respective weights required to achieve dose levels comparable to the ones presented in table 7.3 for the TPS proton plans taking into account all treatment fractions (full plan delivery, i.e., *planned fraction dose* times the *number of fractions*). For the PTV, a constraint to achieve a biological dose of 1.8 GyRBE per fraction was initially applied, as well as a constraint on the maximum dose where 5% or more of the volume ($D5_{PTV}$) should not receive more than 107% of the planned dose. For the OAR, a constraint on $D5_{OAR}$ was set as seen in table 7.2, close to the $D5_{OAR}$ extracted from the TPS plan DVH. The D5 is chosen instead of D2 to define the maximum dose, since this indicator is less prone to statistical variation in the MC simulation (Paganetti et al. 2008). Additionally to the constraint on the OAR maximum dose, low dose constraints were applied with smaller weights. The goal is to reduce as much as possible the volume of OAR receiving low dose, and thereby the integral dose, by increasing the dose gradient between PTV and surrounding normal tissue. DVH constraints on dose and volumes can be easily applied in the clinical TPS, however this feature for the MCTP tool is currently under development.

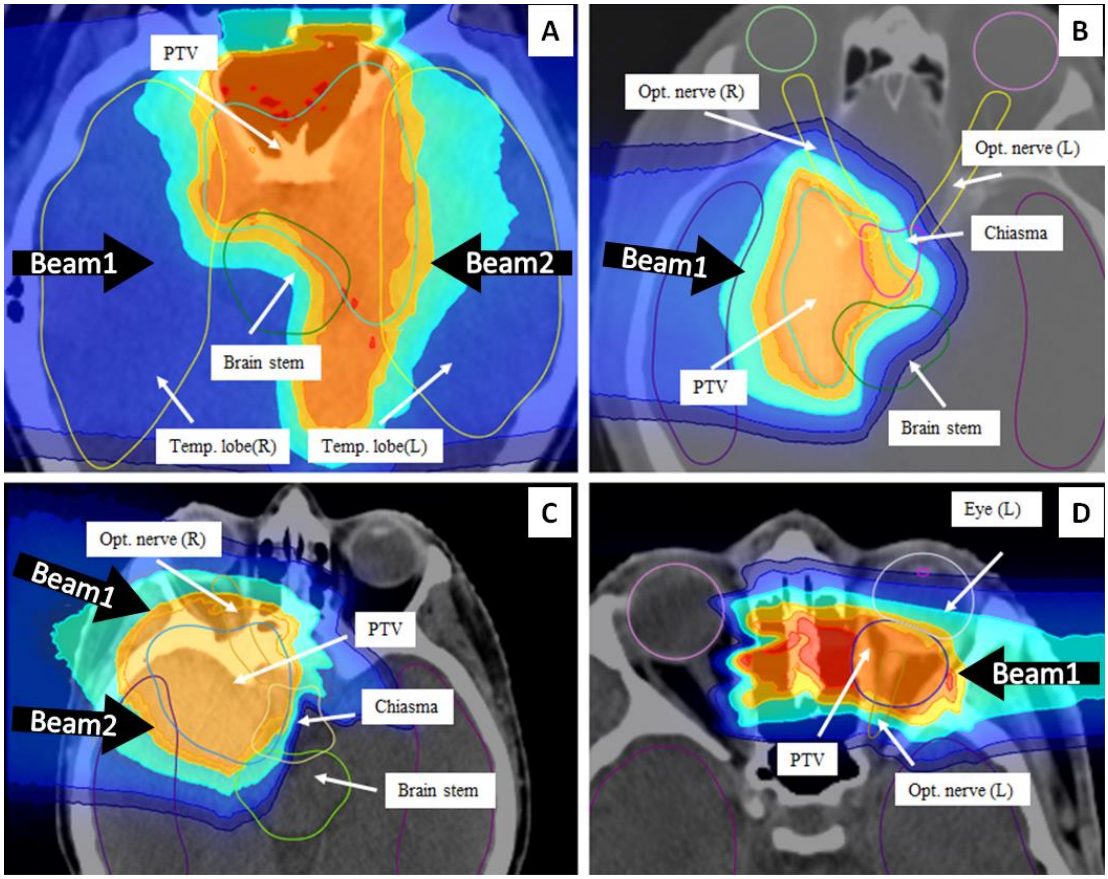

Figure 7.1: The four panels above display the complex relation between the contoured PTV and OARs for the four considered patient cases on the X-ray computed tomography axial images (gray scale) with the overlaid dose distributions (color wash) for proton plans calculated with MCTP (section 7.3.1). Second beam for patient B is not visible for this image, but can be seen in figure 7.3.

	Planned dose / fraction [GyRBE]	Number of fractions	Number of beams	Angles between beams [°]	Critical organ at risks
Patient A (H02202)	1,8	29	2	180	*Temporal lobes (left/right)*
					Brain stem
					Optical system
Patient B (H02433)	1,8	30	2	75	*Brain stem*
					Chiasma
					Optic nerves (left/right)
					Intra-auricular nerve (right)
Patient C (H02524)	1,8	30	2	32	*Brain stem*
					Chiasma
					Optic nerve (right)
Patient D (H02552)	1,8	28	1	\	*Optic nerve (left)*
					Eye (left)

Table 7.1: Patient proton plans characteristics from TPS. The information about the dose per fraction, number of fractions and beams are reported. It provides information on the angles between beams and the close by OARs taken into account for the optimization.

		Dose constraint [GyRBE]	weight	Dose constraint [GyRBE]	weight
Patient A (H02202)	**PTV**	***1,8***	***20***	1,93	20
	Temporal lobe left	1,15	5	0,4	1
	Temporal lobe right	0,98	5	0,3	1
	Brain stem	1,21	5	0,5	1
	Optical system	1,7	10	/	/
Patient B (H02433)	**PTV**	***1,8***	***15***	1,93	20
	Brain stem	1,77	10	0,8	1
	Chiasma	1,72	8	0,8	1
	Optic nerve left	0,8	5	/	/
	Optic nerve right	1,7	5	0,8	1
	Intra-auricular nerve (right)	1,36	5	0,6	1
Patient C (H02524)	**PTV**	***1,8***	***12***	1,93	20
	Brain stem	1,35	5	0,5	1
	Chiasma	1,38	30	0,7	1
	Optic nerve (right)	1,71	30	0,7	1
Patient D (H02552)	**PTV**	***1,8***	***14***	1,93	20
	Optic nerve (left)	1,55	20	0,8	1
	Eye (left)	1,45	20	1	2
Patient E (H01949)	**PTV**	***3,3***	***14***	3,53	20
	Rectum	2,9	20	1,4	1

Table 7.2: Optimal constraint parameters for PTV and OAR found with MCTP to reproduce the TPS proton DVH characteristics presented in table 7.3. Hard constraints are defined for D_{50} and D_5 in the PTV, while only for D_5 in the OAR. However, as the MCTP works only with maximum dose up to now (Appendix C), a second D_5 at lower dose with a softer constraint is used for OAR, to reduce the irradiated volume of normal tissues.

		DVH analysis : H (RBE=1.1) TPS Plan							
		D5	D10	D20	D33	D50	D66	D75	D95
Patient A (H02202)	**PTV**	53,1	52,8	52,5	52,2	51,6	50,8	50,2	48,1
	Temporal lobe left	33,6	29,0	22,9	18,6	15,1	11,9	9,3	2,3
	Temporal lobe right	28,7	22,6	18,9	14,5	12,5	10,7	8,4	1,5
	Brain stem	35,1	32,2	27,0	22,6	18,0	14,5	11,6	3,5
	Optical system	49,9	47,9	42,1	33,9	25,8	17,4	10,2	2,0
Patient B (H02433)	**PTV**	55,2	54,9	54,6	54,0	53,4	52,8	52,5	49,8
	Optic nerve left	23,4	17,7	8,4	1,8	0,6	0,3	0,3	0,3
	Chiasma	51,6	51,0	50,4	49,2	44,1	35,4	29,4	12,0
	Optic nerve right	51,0	50,4	49,5	45,6	27,9	6,9	2,4	0,3
	Brain stem	53,4	52,5	46,8	32,1	14,1	5,1	3,0	0,6
Patient C (H02524)	**PTV**	55,8	55,2	54,9	54,0	53,1	52,5	51,6	49,2
	Optic nerve (right)	51,3	50,7	50,1	49,5	47,1	41,1	36,6	22,5
	Chiasma	50,7	49,8	48,9	43,5	25,5	9,9	1,8	0,3
	Brain stem	41,4	27,9	10,5	2,7	0,6	0,3	0,3	0,3
Patient D (H02552)	**PTV**	51,8	51,2	50,7	50,1	49,6	48,7	47,9	44,2
	Eye (left)	41,4	38,6	33,6	28,0	21,0	15,1	12,0	5,3
	Optic nerve (left)	43,4	40,3	34,2	23,8	9,5	3,4	1,4	0,3

Table 7.3: DVH parameters extracted from the clinical TPS proton plans. The dose volume parameters for each ROI, in GyRBE - D5, D10, D20, D33, D50, D66, D75 and D95 - are presented for a full plan delivery. The MCTP optimization with fixed RBE protons tries to reproduce these values.

For each plan, the optimization is performed with a method similar to Mairani et al. (2013) and already applied in Chapter 6 for physically optimized SOBPs (cf. also Appendix C):

- Dose matrices for each regions of interest (ROI), i.e., the target and the OARs presented in table 7.2, are pre-calculated using the FLUKA MC. These calculations include the patient voxelized geometry a detailed model of the HIT beamline with the RiFi model for helium ions. If needed, the biological model presented in Mairani et al. (2016a) and described in Appendix C is used for biological dose calculation with a variable RBE. Thus, for each ion, physical matrices are created for each ROI, along with the requested biological dose matrices for each tissue type investigated.
- Initial optimization is performed with protons, for a fixed RBE, to obtain the optimal constraints for each ROI in comparison to the original clinical TPS plan.
- Optimization for each ion is performed with the above presented biological model.

The resultant plans are simulated with MC FLUKA using the simulation framework presented in Chapter 5 and linked to the biological model. As previously stated for the pre-optimization process, the planning and simulations for helium ions were performed with the RiFi to avoid target dose inhomogeneity as seen in Chapter 6. The final calculations are performed using $50x10^6$ primary histories, in 50 independent runs, with online calculation of the α_{ion} and β_{ion} parameters, at 1x1x3 mm^3 resolution. Dose distribution and DVH analysis are calculated and plotted with an in-house software (Bauer et al. 2014).

7.2.2. Tissue-types attributions

For the biological dose calculations using variable RBE, tissue-types need to be designated. From the ROI, two categories can be distinguished for this study: the target (PTV) and the OAR. For the non-tumorous regions, a tissue type with a α_x/β_x ratio of 2.0 Gy (Santacroce et al. 2013) was chosen. For the PTV, two tissue-types were considered describing two kinds of target with distinct α_x/β_x ratio, characteristic of the biological diversity of brain tumors. The first target type is meningioma, corresponding to the patient cases selected and representing one of the potential tumor types for helium therapy. As recommended in Vernimmen et al. (2010), an α_x/β_x ratio of 3.7 Gy for tumor tissue was selected. For the second target tissue types, the α_x/β_x ratio of the target was changed to 10.0 Gy, representative of the α_x/β_x order for AVM tissues (Vernimmen et al. 2010). It has to be noted that for the selected biological model, only the α_x/β_x ratio is of importance, not the α_x and β_x individual values.

7.2.3. Change in fractionation scheme

For the challenging patient C, exhibiting the smallest angle between the two beams and many sensitive OARs near the PTV, a different daily fractionation scheme of 3 GyRBE instead of 1.8 GyRBE was investigated for helium ions and both target tissue-types. The results using the two fractionation schemes were then compared to protons, calculated with and without variable RBE for a dose per fraction of 1.8GyRBE.

It should be however noticed that by using a different fractionation scheme, the biological endpoints could be different, as explained in the report of Suit et al (2010), reviewing the clinically used fractionation scheme and the introduction of the biologically effective dose (BED). BED takes into account the total dose (D_{tot}), the dose per fraction (d), and the cell type (α_x/β_x) and can be defined, compared to a reference dose per fraction of 2Gy, as:

$$BED = D_{tot}\frac{(\alpha_x/\beta_x)+d}{(\alpha_x/\beta_x)+2} \quad . \tag{7.1}$$

Thus, the BED (in GyBED) can be expressed in the presented situations for the PTV as well as the OAR, assuming that the OAR is receiving the same dose as the planned one. For the meningioma case with α_x/β_x=3.7, the calculated BED for 1.8GyRBE achieved in for example 30 fractions is 52GyBED. To achieve the same BED with a 3GyRBE fractionation, about 15 fractions are necessary. This implies for the OAR (α_x/β_x=2) a BED of 51GyBED and 56GyBED, respectively, for the 1.8GyRBE and 3GyRBE daily fractionation scheme. For the AVM case with α_x/β_x=10, the calculated BED for 1.8GyRBE achieved in 30 fractions is 53GyBED. To achieve the same BED with a 3GyRBE fractionation, about 16 fractions are necessary. This implies for the OAR (α_x/β_x=2) a BED of 52GyBED and 60GyBED, respectively, for the 1.8 GyRBE and 3GyRBE fractionation schemes. However, while BED calculation are straightforward concerning the tumor, for OAR such approach is more complex due to the non-uniform dose and the spatial location with respect to the tumor. To achieve the constraint mentioned in table 7.2, a voxel per voxel approach could be used to calculate the new BED of OAR such as in Unkelbach et al (2013). However, such an approach was not available for this study, although it could be considered in future implementation within the MCTP framework at HIT.

Hence, in a first approach without using a more refined BED model of the OARs, the 1.8GyRBE fractionation scheme was set as reference for the target dose, in order to compare the two fractionation schemes. Subsequently, the number of fractions to achieve the same BED was calculated for the 3GyRBE fraction dose. According to the originally considered number of fractions, for α_x/β_x=3.7 and α_x/β_x=10, the new number of fractions were respectively about 15 (14.8) and 17 (16.4) for patient B and C, about 14 (14.3) and 16 (15.8) for patient A, and about 14 (13.8) and 15 (15.3) for patient D. The numbers into brackets indicate the exact number of fractions to achieve the same BED. While using such numbers is not realistic in clinical practice, it will be used in the following to allow a more straightforward comparison between the two fractionation schemes, acknowledging the limitations that such approach holds.

Thus, for the optimization, the same weight constraints as previously described were applied for the planning of a given daily fraction, however, all dose constraints were scaled by a $\frac{3}{1.8}$ factor to account for the difference in prescribed dose. The dose for helium ions in the DVH figures and tables is displayed in GyRBE, but is calculated for the full delivery taking into account the new fractionation scheme and the new number of fractions. Calculations for protons were not performed with the new fractionation scheme of 3GyRBE, but it should be noted that at this dose level, the RBE tends toward a value of 1.1, as it will be discussed in section 7.4.

7.2.4. Investigation of the RiFi potential benefits

In Chapter 3 and Chapter 6, the possibility to use the RiFi for helium ion treatments of shallow tumors was discussed, due to the small Bragg peak width presented at low energies. In Chapter 6, the physically optimized spread-out Bragg peaks (SOBP) at 5cm depth exhibited dose ripples within the target regions due to the chosen absence of RiFi. However, for the patient D, presenting a tumor at shallow depth with a single beam, the evaluation on a clinical scenario of a delivery without RiFi was investigated, in addition to the optimization presented previously with RiFi. The optimization dose matrices were recalculated without RiFi and optimized for the meningioma tissue-type target with fraction dose of 1.8 GyRBE. Additional optimizations were performed for irradiation schemes without RiFi considering a reduced distance between consecutive Bragg peaks, to compensate for the smaller Bragg peak width. For this purpose, new matrices were calculated for energy slices separated by about 1mm instead of the initially planned 2mm, which are commonly used for protons at such depths.

7.3. Results

This section presents the results of the patient plans optimizations, their final MC calculations and related dosimetric comparisons. The tables present the differences between DVH parameters (in GyRBE), for the full treatment total dose (*planned dose* x *number of fractions*) as well as the DVHs of the different ROIs. For patient B, the intra-auricular nerves results are not displayed to facilitate the comprehension of DVH and tables. For the new fractionation scheme, results are taking into account the effect of dose and fractionation on the full delivery course.

7.3.1. MCTP optimization results compared to TPS

The DVH results of proton optimization (with fixed RBE) for the MCTP compared to the TPS are shown in table 7.4, representing the dose difference between dose volume parameters of the MCTP plans against the TPS plans. For the PTV of the four patients, the $D5_{PTV}$ value obtained with MCTP was found higher by a maximum of about 2GyRBE compared to TPS. However, in general a similar coverage of the target was observed, with on average less than 1.5GyRBE difference for all extracted DVH parameters. The maximum deviation found was for $D95_{PTV}$ at 3GyRBE for patient A.

Regarding the OARs, a relatively good agreement in terms of the maximum dose is found, with less than 2.1 GyRBE difference in the $D5_{OAR}$. For the other OAR DVH parameters, the difference between MCTP and TPS is below 2GyRBE, except for patient D and the brainstem of patient B. For patient D and the brainstem of patient B, MCTP was giving higher dose on average to the OAR, up to 3.6 GyRBE for the left eye of patient D. On the other hand, the MCTP was able to reduce the dose up to 10GyRBE in regions such as the optical system of patient A. For this latter patient, all OARs indicated a reduced dose with MCTP compared to the TPS plan. For patient C, $D5_{brainstem}$ of brainstem is reduced by 9.6GyRBE with MCTP, as well as the $D33_{chiasma}$ of chiasma by about 9GyRBE. As it will be discussed in section 7.4, these results are acceptable and demonstrate the capabilities of MCTP as treatment planning engine. The constraints and weights chosen to achieve these DVH results were then used for further planning.

7.3.2. Meningioma target tissue-type

The dose distributions for patient A, B, C and D are displayed in figure 7.2 to 7.5 respectively, with the helium ion dose prediction (top) and the one for protons (bottom), both obtained with a variable RBE scheme. The figure 7.6 displays the dose difference between the helium dose distributions minus the protons dose predictions (top), and protons dose minus heliums doses (bottom), to highlight the difference between the plans. The dose display uses a color-wash system showing certain dose levels w.r.t. the planned dose of 1.8GyRBE. These dose levels are as follows: >10%, >20%, >50%, >80%, >95% and >107% of the prescribed dose. The 10%, 20% and 50% dose level regions are larger for protons than for helium ions, and are best visualized in the dose difference maps. The dose gradients outside the PTV are sharper for helium ions than for protons in all directions, as expected. In figure 7.2 for patient A, some hotspots can be observed for helium ions outside of the target volume or near the vicinity of the PTV. In addition to the shallow dose gradient found for protons for patient D, doses above 107% exist within the PTV for the proton patient D plan, as it can be seen in the related DVH in figure 7.7. DVH plots for the different ROIs are displayed in figure 7.7.

		DVH analysis : H (MCTPS, RBE=1.1) - H (TPS, RBE=1.1)							
		D5	D10	D20	D33	D50	D66	D75	D95
Patient A (H02202)	**PTV**	2,0	1,7	1,2	0,9	0,6	0,0	0,0	-3,2
	Temporal lobe left	-4,1	-2,3	0,0	0,6	0,9	0,6	0,6	0,0
	Temporal lobe right	-6,7	-3,8	-4,4	-1,7	-1,5	-1,7	-2,0	-0,3
	Brain stem	-0,9	-2,0	-1,7	-1,5	-0,6	0,0	-0,3	0,0
	Optical system	-3,5	-4,9	-7,5	-9,9	-8,1	-5,2	-1,2	0,0
Patient B (H02433)	**PTV**	1,5	0,9	0,3	0,6	0,3	0,3	0,3	-1,8
	Optic nerve left	-0,9	-1,5	-0,3	0,3	-0,3	0,0	0,0	-0,3
	Chiasma	1,5	1,2	0,3	-1,8	-2,1	0,6	2,1	2,1
	Optic nerve right	2,1	1,8	0,9	-0,9	-0,6	0,9	0,6	0,0
	Brain stem	-3,0	-5,1	-9,0	-5,4	1,5	3,6	2,7	0,9
Patient C (H02524)	**PTV**	0,6	0,6	0,0	0,3	0,3	0,6	0,6	-0,9
	Optic nerve (right)	1,2	1,5	1,2	0,6	0,9	0,9	0,9	1,8
	Chiasma	0,3	0,0	-2,7	-9,0	-3,9	-5,4	-0,3	-0,3
	Brain stem	-9,6	-7,2	-1,5	0,9	0,3	0,0	0,0	-0,3
Patient D (H02552)	**PTV**	2,0	1,7	1,4	0,6	0,3	0,3	0,3	1,1
	Eye (left)	1,4	2,2	3,4	3,6	3,6	3,1	2,8	1,4
	Optic nerve (left)	-3,1	-2,5	-2,5	-0,8	2,8	3,4	2,8	0,8

Table 7.4: DVH parameters difference for the ROI of the four patients, in GyRBE, between the MCTP optimized proton plans with fix RBE and the original TPS plans.

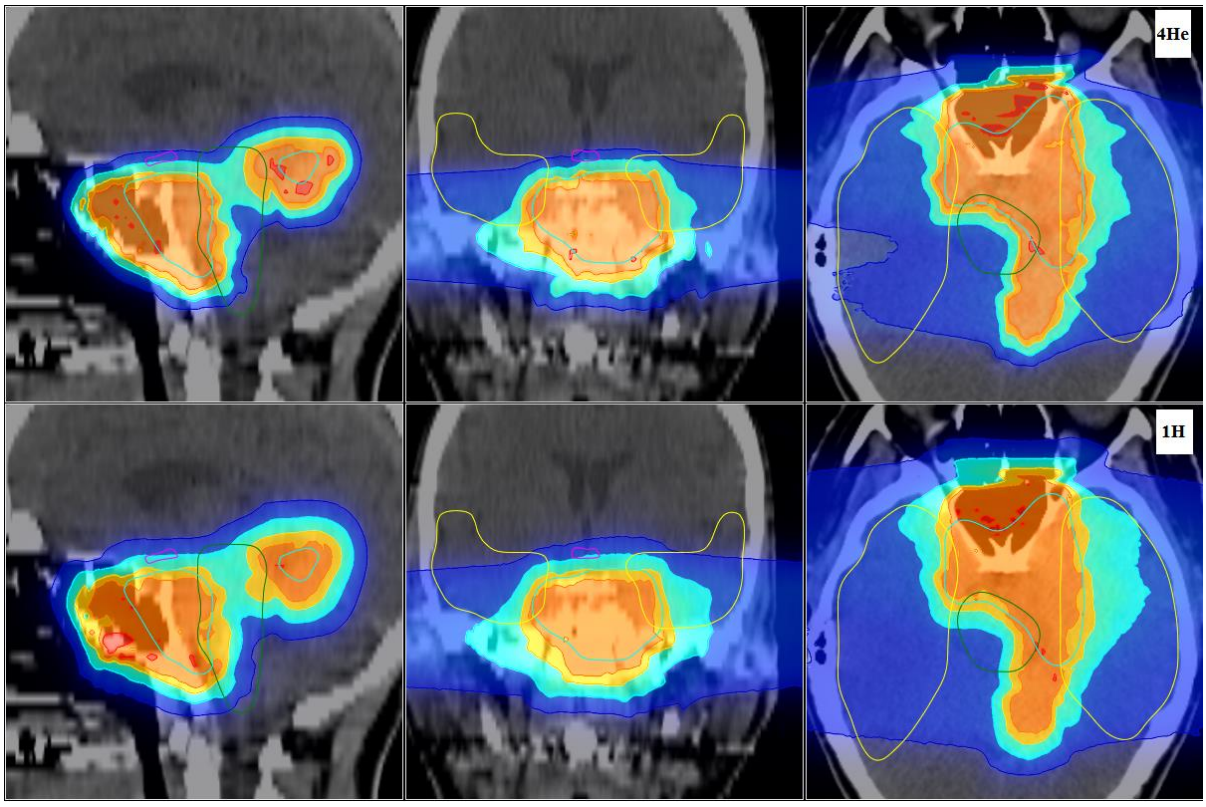

Figure 7.2: Dose distributions superimposed on the gray scale CT images are shown for patient A, with on the top panels helium ions (4He) and bottom panels protons (1H) for the sagittal, coronal, axial slices.

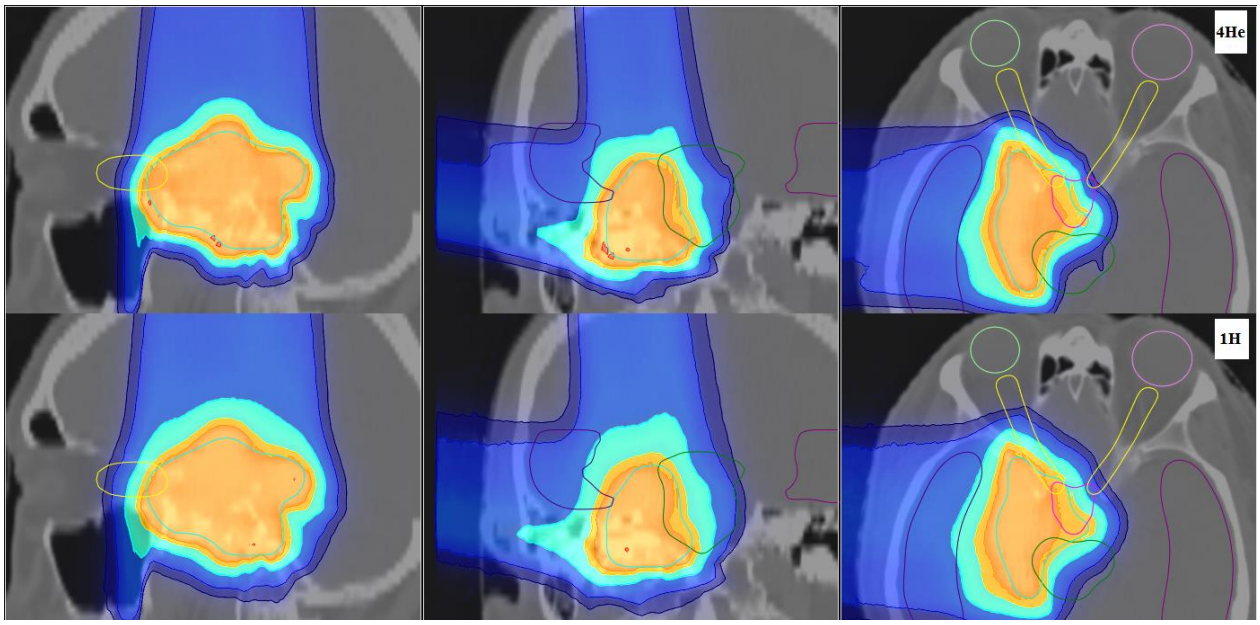

Figure 7.3: Dose distributions superimposed on the gray scale CT images are shown for patient B, with on the top panels helium ions (4He) and bottom panels protons (1H) for the sagittal, coronal, axial slices.

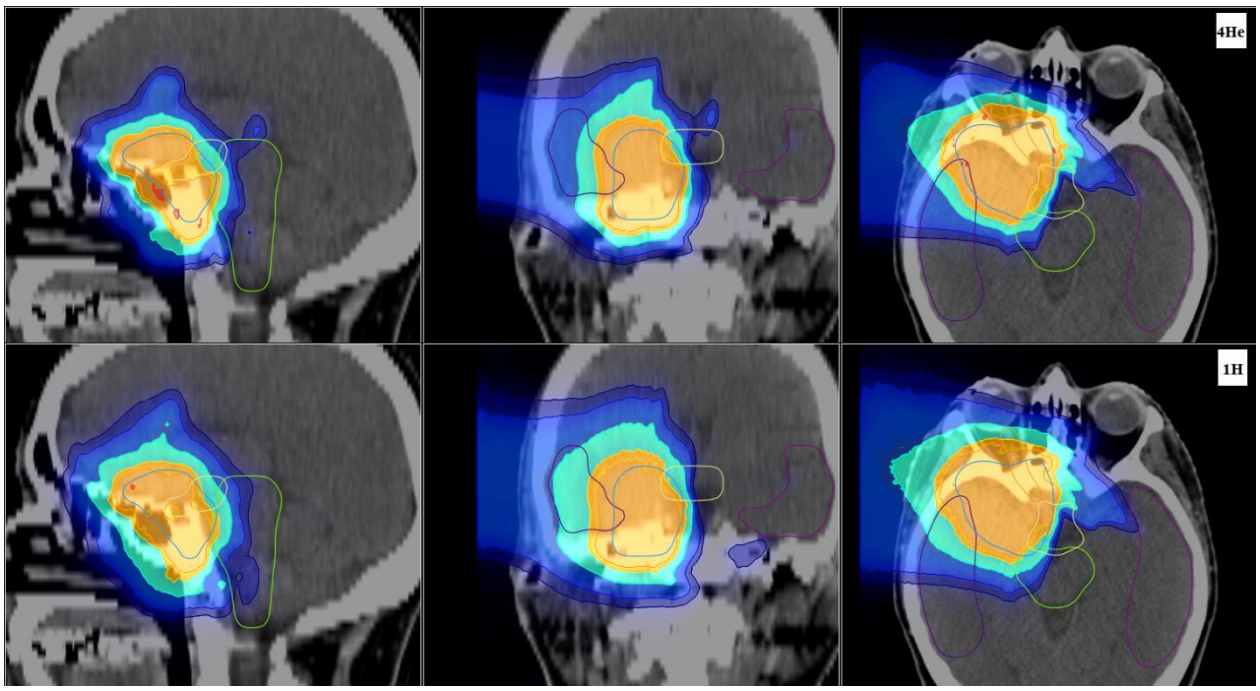

Figure 7.4: Dose distributions superimposed on the gray scale CT images are shown for patient C, with on the top panels helium ions (4He) and bottom panels protons (1H) for the sagittal, coronal, axial slices.

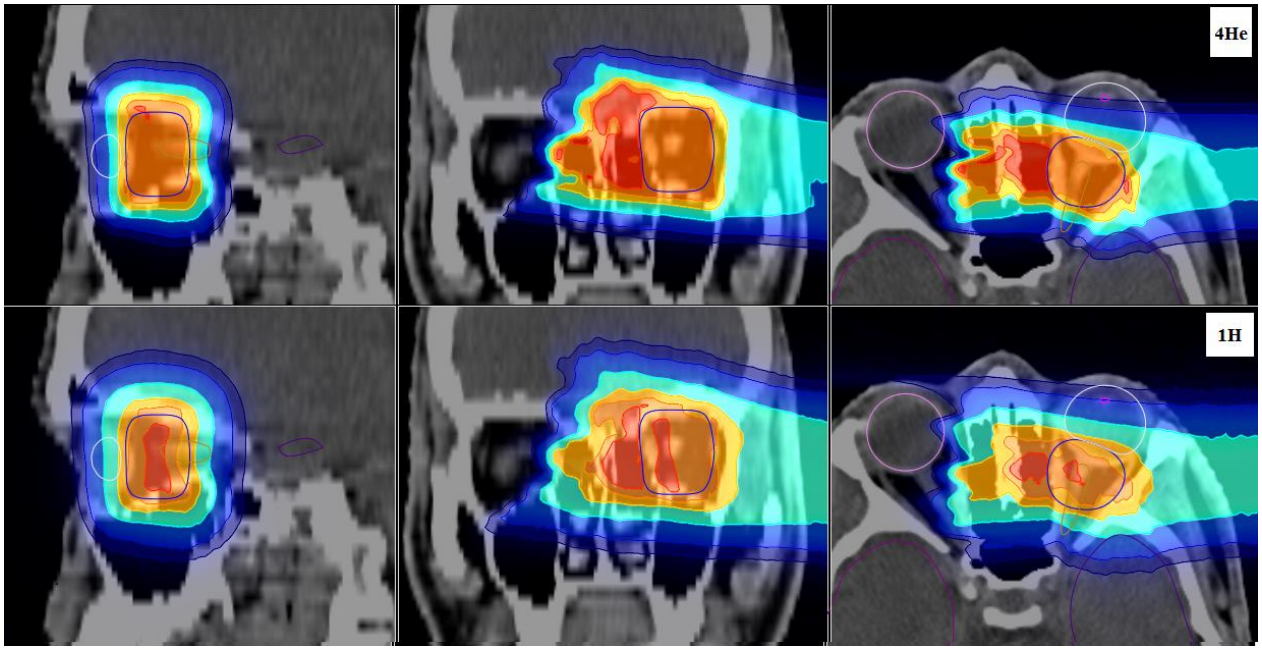

Figure 7.5: Dose distributions superimposed on the gray scale CT images are shown for patient D, with on the top panels helium ions (4He) and bottom panels protons (1H) for the sagittal, coronal, axial slices.

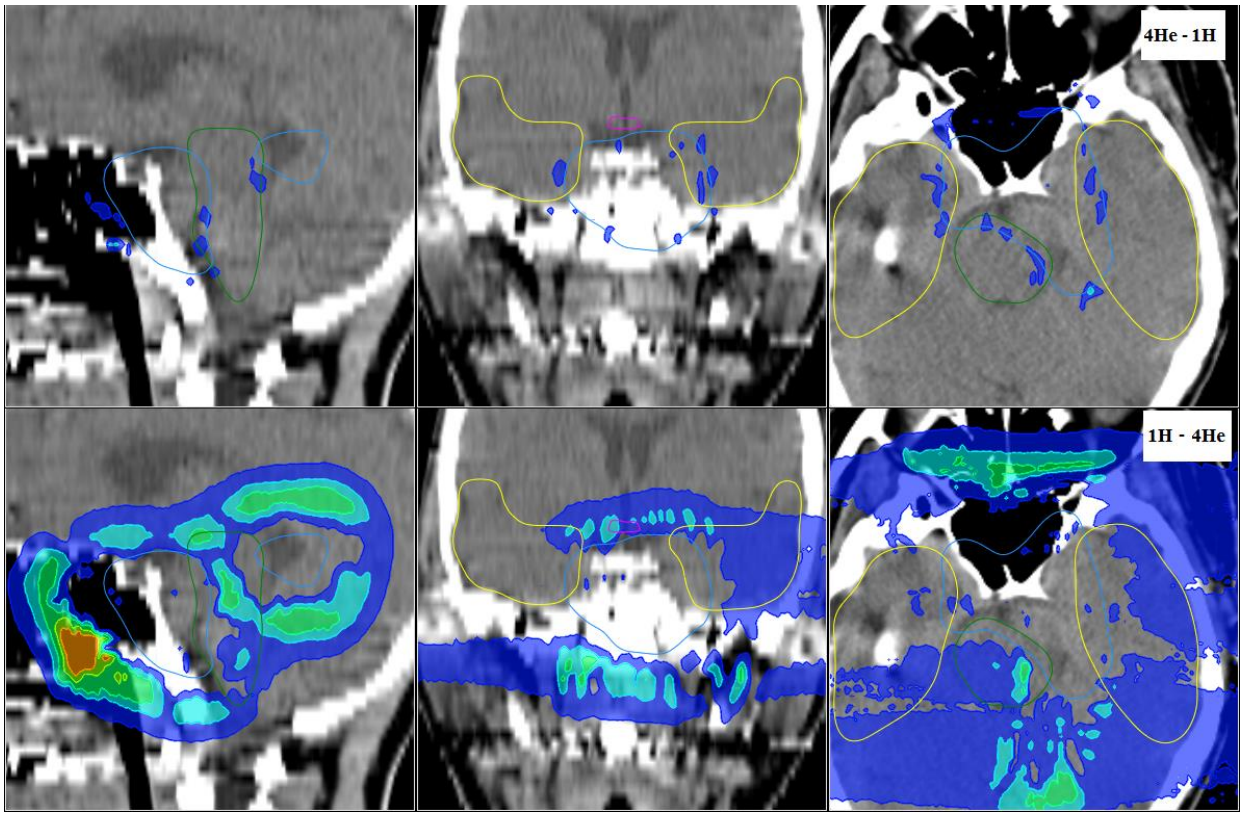

Figure 7.6: Dose difference between the helium ions and proton dose predictions for patient A: the top panel displays the overdosages due to helium ions (^{4}He-^{1}H), the bottom panels shows the overdosages due to protons (^{1}H-^{4}He). The isocontours displays the dose per fraction >0.1GyRBE, >0.2GyRBE, >0.3GyRBE, >0.4GyRBE, >0.5GyRBE and >0.6GyRBE.

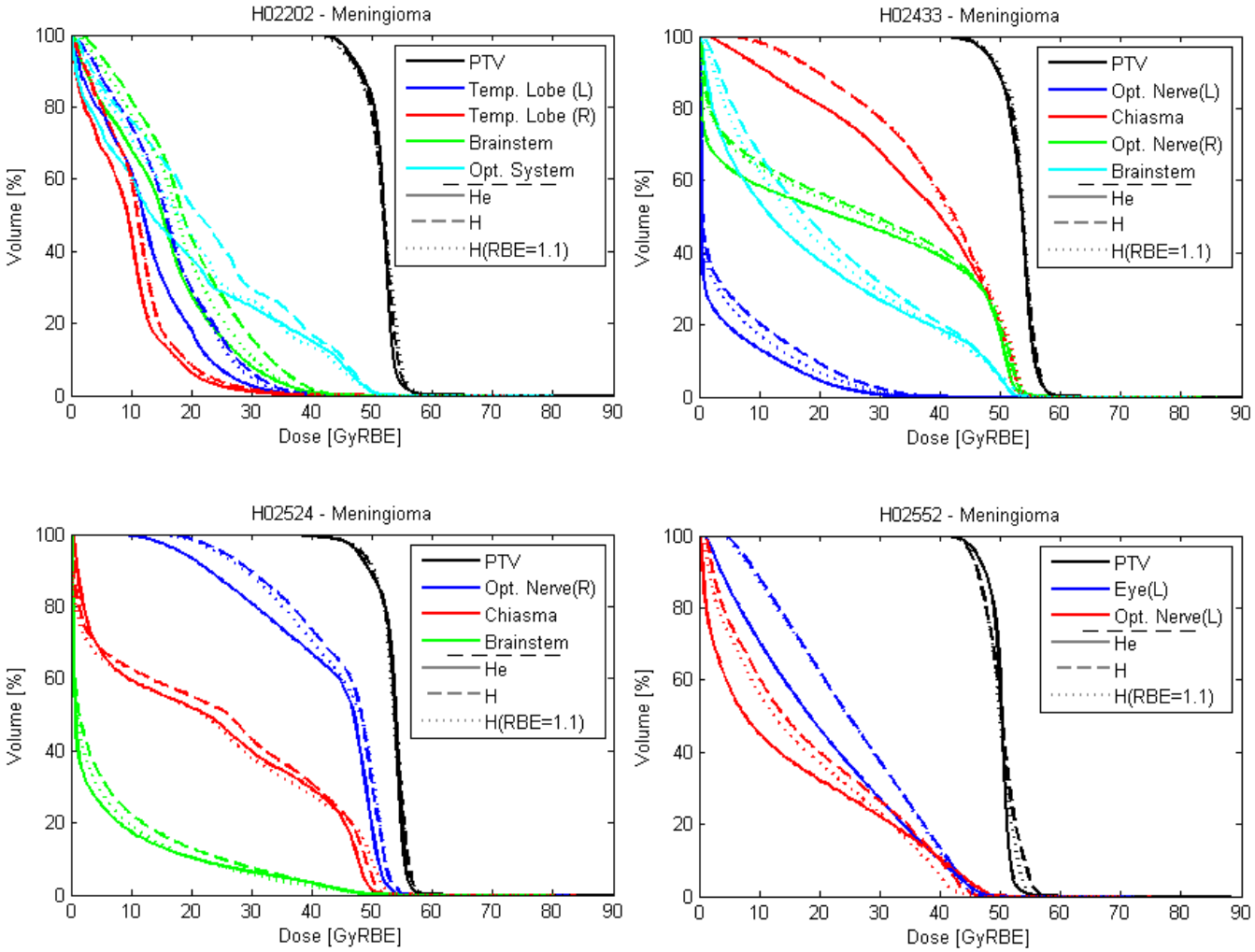

Figure 7.7: DVH for the four patient with meningioma as target tissue-type. The different ROIs investigated are displayed. Protons are shown for both fixed (dotted lines) and variable RBE (dashed lines). Helium ions are displayed with solid lines.

Proton results are shown for both fixed (dotted lines) and variable RBE (dashed lines). Helium ions are displayed with solid lines. Tables 7.5 and 7.6 show differences between DVH parameters extracted from helium ion and proton plans, with either a fixed or variable RBE, respectively. It can be seen from figure 7.7, as well as from tables 7.5 and 7.6, that the PTV coverage is similar for all cases except patient D, where helium ions afford better coverage, with a sharper PTV DVH. For this patient D, the $D5_{PTV}$ is larger with protons by about 2GyRBE, due to the hot spots previously mentioned. For most of the dose volume parameters, the dose is reduced with helium ions compared to protons with a fixed RBE (table 7.5,) with dose sparing up to 7.5GyRBE for $D95_{chiasma}$ of Patient B. Only the $D5_{brainstem}$ of patient C and $D5_{Opt.Nerve}$/ $D10_{Opt.Nerve}$ of patient D present for helium ions higher doses above 2GyRBE, with values of about 3 and 3.9/2.5 GyRBE, respectively. When comparing helium ions to protons with variable RBE, the dose is reduced with helium ions compared to protons (table 7.6) with dose sparing up to 7.8GyRBE for $D50_{Opt.System}$ of Patient A. Only the $D5_{Opt.Nerve}$ of patient D is having higher dose with helium ions by about 1.7GyRBE. Proton optimized plans show in the OARs a DVH slightly shifted toward higher dose, about 1-2GyRBE, particularly for small volumes close to the PTV, for example leading to higher D5/D10 values.

		DVH analysis : He (Meningioma) - H (RBE=1.1)							
		D5	D10	D20	D33	D50	D66	D75	D95
Patient A (H02202)	**PTV**	-0,9	-1,2	-0,9	-0,6	-0,3	0,6	0,9	1,2
	Temporal lobe left	-2,9	-3,8	-3,8	-4,1	-4,1	-3,5	-3,5	-1,7
	Temporal lobe right	-1,2	-1,2	-1,5	-1,5	-1,7	-2,9	-2,9	-0,9
	Brain stem	-1,5	-1,5	-2,3	-2,9	-2,3	-3,5	-3,8	-2,0
	Optical system	0,6	1,2	0,3	-2,0	-4,4	-4,6	-4,4	-1,7
Patient B (H02433)	**PTV**	-0,3	-0,3	0,3	-0,6	0,0	-0,3	-0,9	-0,6
	Optic nerve left	-3,3	-3,0	-3,6	-1,5	0,0	0,0	-0,3	0,0
	Chiasma	-1,2	-1,2	-0,9	-0,9	-2,1	-5,1	-6,3	-7,5
	Optic nerve right	-1,2	-1,2	-0,9	0,3	-4,2	-4,8	-2,1	-0,3
	Brain stem	-0,3	0,3	0,3	-3,0	-3,9	-3,3	-2,7	-0,6
Patient C (H02524)	**PTV**	-0,6	-0,6	0,0	0,0	0,6	0,0	0,3	-0,6
	Optic nerve (right)	-0,6	-1,2	-1,5	-1,5	-1,2	-1,5	-3,3	-6,0
	Chiasma	-2,4	-2,1	-0,6	2,1	0,9	0,9	1,5	0,9
	Brain stem	3,0	0,0	-1,2	-1,5	0,0	0,0	0,0	0,0
Patient D (H02552)	**PTV**	-1,7	-1,1	-0,8	0,0	0,6	0,8	1,4	0,6
	Eye (left)	0,6	-1,1	-3,1	-5,0	-6,4	-6,4	-6,4	-4,5
	Optic nerve (left)	3,9	2,5	0,0	-3,6	-4,8	-3,6	-2,8	-0,8

Table 7.5: DVH parameters difference for the ROIs of the four patients with meningioma tissue-types as target, in GyRBE, between the MCTP optimized helium plans and proton plans with fixed RBE.

		DVH analysis : He (Meningioma) - H (Meningioma)							
		D5	D10	D20	D33	D50	D66	D75	D95
Patient A (H02202)	**PTV**	-0,6	-0,9	-0,6	-0,3	0,0	0,3	0,6	0,6
	Temporal lobe left	-4,4	-4,6	-4,6	-4,1	-3,8	-3,5	-3,5	-2,0
	Temporal lobe right	-2,3	-1,5	-1,5	-1,5	-1,5	-2,6	-2,9	-0,9
	Brain stem	-3,8	-4,3	-5,2	-4,6	-3,5	-4,4	-5,2	-3,2
	Optical system	-0,6	-1,2	-3,2	-5,8	-7,8	-7,3	-5,8	-1,7
Patient B (H02433)	**PTV**	-0,3	-0,6	0,0	-0,3	0,0	0,0	0,0	-0,6
	Optic nerve left	-6,0	-6,0	-5,7	-2,4	-0,3	0,0	-0,3	0,0
	Chiasma	-0,9	-0,9	0,0	-0,3	-2,4	-5,1	-6,3	-7,8
	Optic nerve right	-0,6	-0,6	-0,6	-0,9	-6,0	-5,7	-2,1	-0,3
	Brain stem	0,3	0,0	-2,1	-5,1	-6,0	-5,1	-4,2	-1,5
Patient C (H02524)	**PTV**	-0,6	-0,6	0,0	-0,3	0,0	0,0	0,3	-0,6
	Optic nerve (right)	-0,9	-0,9	-1,2	-1,2	-1,5	-3,6	-5,4	-6,9
	Chiasma	-1,2	-1,2	-0,9	-1,5	-3,3	-0,9	0,9	0,9
	Brain stem	-0,9	-4,2	-3,9	-2,7	-0,3	0,0	0,0	0,0
Patient D (H02552)	**PTV**	-2,5	-2,0	-1,1	-0,6	0,0	0,8	1,4	0,8
	Eye (left)	-0,3	-1,7	-3,4	-5,0	-6,4	-6,7	-7,0	-5,0
	Optic nerve (left)	1,7	0,3	-2,8	-5,9	-6,4	-5,0	-3,9	-1,4

Table 7.6: DVH parameters difference for the ROI of the four patients, with meningioma tissue-types as target, in GyRBE, between the MCTP optimized helium plans and proton plans with variable RBE.

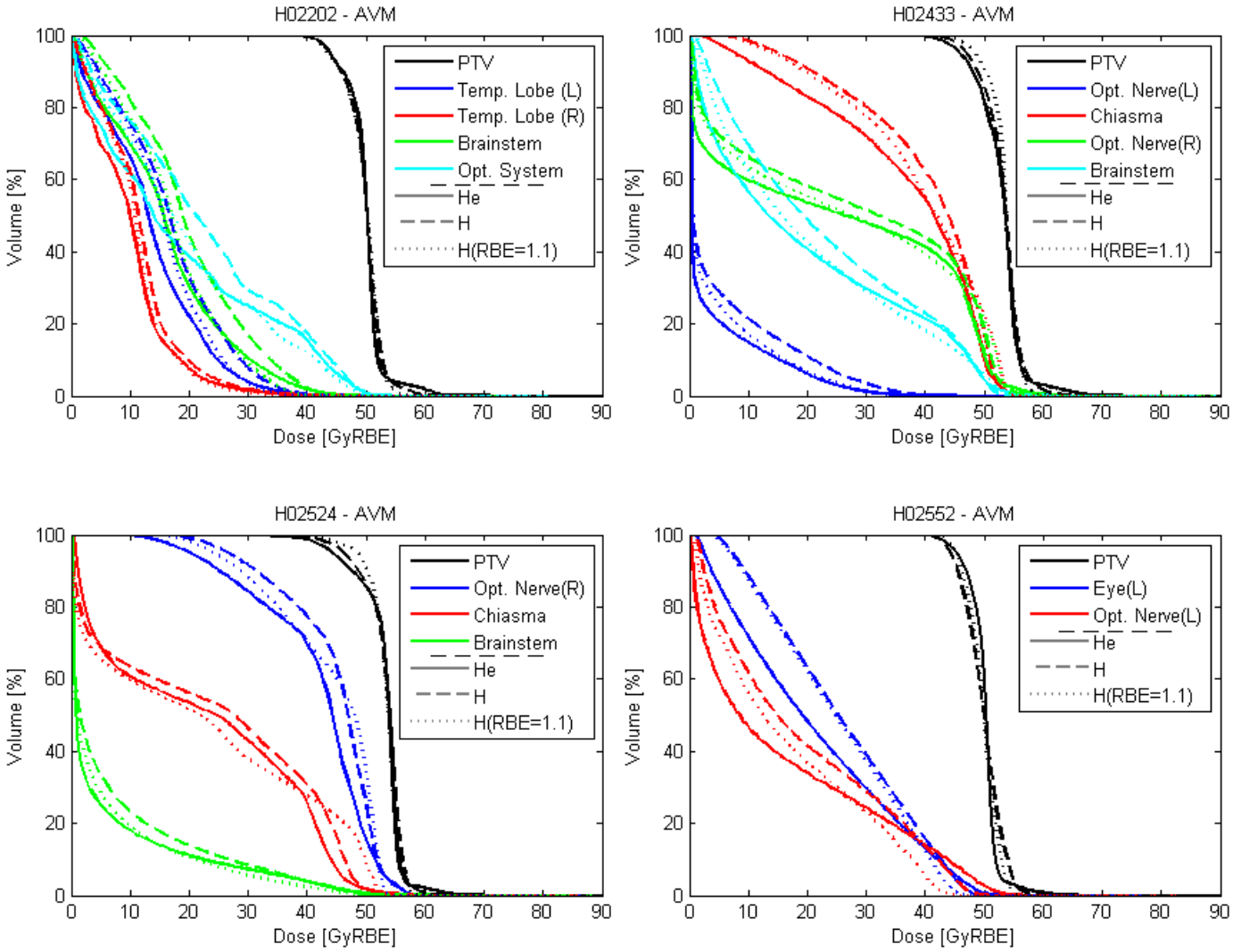

Figure 7.8: DVH for the four patients with AVM as target tissue-type. The different ROIs investigated are displayed. Protons are shown for both fixed (dotted lines) and variable RBE (dashed lines). Helium ions are displayed with solid lines.

7.3.3. AVM target tissue-type

The DVH for AVM cases are shown in figure 7.8. Dose distributions are not displayed, however, as it can be seen in the DVH (figure 7.8), more hot spots are present within the PTV, as well as within the normal tissues close to the PTV boundary, for both protons and helium ions with variable RBE, compared to protons with fixed RBE. The difference between the ROI DVH parameters of helium plans against protons with fixed or variable RBE are presented in table 7.7 and table 7.8, respectively. For meningioma tissue-types cases, the coverage was similar between protons with fixed RBE or protons and helium ions with variable RBE. However, for AVM tissue-type cases, the PTV coverage is degraded for helium ions and protons with variable RBE. It can also be seen that a small volume of the PTV (below $D5_{PTV}$) is receiving high dose for protons and helium ion plans with variable RBE for patients B and C, particularly for helium ions. For patient A, except for the presence of hot

spots for a small portion of the PTV, the PTV coverage is similar for helium and proton plans with variable RBE compared to the proton plans with fixed RBE. For patient D, no difference in the PTV coverage is observed compared to the meningioma cases, regardless of the presence of hotspots (volume <5%). For the OARs, protons with a variable RBE present a DVH shifted towards higher doses in comparison to fixed RBE schemes, and more pronounced than for meningioma cases, with dose values increased by about 3-4 GyRBE (for D_5/D_{10}). This happens for volumes of the OARs close to the PTV. For large volume of the OARs (>D33), helium ions, in general, deliver less dose compared to protons with fixed RBE, up to 6.2GyRBE for $D66_{eye}$ of patient D. However, compared to protons with fixed RBE, helium ions tend to give higher doses to small volumes of OAR close to the high dose region of the PTV. Quantitatively, as seen in table 7.7, it means that helium ions for AVM tissue-type cases compared to protons with a fixed RBE exhibit higher $D5_{OAR}$ for OARs close to the PTV, e.g. up to 7.6 GyRBE for $D5_{Opt.Nerve}$. In comparison, the maximum overdosage for meningioma tissue case was only up to 3.9GyRBE with respect to protons with fix RBE for the same patient D $D5_{Opt.Nerve}$. Helium ions compared to protons with variable RBE present a dose reduction over large OAR volumes, e.g., about 7.3GyRBE less on $D66_{OptSystem}$ for patient Awith a similar PTV coverage. The only OAR presenting a higher dose for the extracted DVH parameters with helium ions compared to protons with variable RBE is for patient D, showing a $D5_{Opt.Nerve}$ value increased by about 3.4GyRBE.

		DVH analysis : He (AVM) - H (RBE=1.1)							
		D5	D10	D20	D33	D50	D66	D75	D95
Patient A (H02202)	**PTV**	0,0	-0,9	-0,6	-0,6	-0,3	0,6	0,6	0,3
	Temporal lobe left	0,3	-0,9	-1,5	-2,0	-2,6	-2,0	-2,6	-1,5
	Temporal lobe right	0,9	0,0	0,0	-0,3	-0,9	-2,0	-2,3	-0,9
	Brain stem	2,3	1,2	-0,3	-1,2	-1,2	-2,6	-3,5	-2,0
	Optical system	1,4	1,2	2,3	0,6	-2,9	-4,4	-4,1	-1,7
Patient B (H02433)	**PTV**	0,0	0,0	0,3	-0,6	-0,3	-0,6	-2,1	-2,1
	Optic nerve left	-1,2	-0,9	-2,7	-1,5	0,0	0,0	-0,3	0,0
	Chiasma	-1,8	-2,1	-2,1	-1,5	-0,3	-2,4	-4,2	-6,6
	Optic nerve right	-1,2	-1,8	-2,4	0,6	-0,9	-3,9	-2,1	-0,3
	Brain stem	-0,9	0,3	3,9	0,0	-2,1	-2,7	-2,1	-0,6
Patient C (H02524)	**PTV**	-0,3	0,0	0,3	0,3	0,3	0,0	0,3	-4,2
	Optic nerve (right)	0,6	-0,9	-2,1	-3,3	-3,9	-0,6	-0,6	-3,9
	Chiasma	-5,1	-6,0	-4,5	1,8	3,0	1,5	1,8	0,9
	Brain stem	4,8	1,5	-1,2	-1,2	0,0	0,3	0,3	0,0
Patient D (H02552)	**PTV**	-0,8	-1,1	-0,8	0,3	0,6	0,3	0,8	-0,3
	Eye (left)	2,5	1,1	-1,7	-3,6	-5,6	-6,2	-6,2	-4,2
	Optic nerve (left)	7,6	5,9	2,2	-2,0	-3,9	-3,4	-2,5	-0,8

Table 7.7: DVH parameters difference for the ROIs of the four patients with AVM tissue-types as target, in GyRBE, between the MCTP optimized helium plans and proton plans with fixed RBE.

		DVH analysis : He (AVM) - H (AVM)							
		D5	D10	D20	D33	D50	D66	D75	D95
Patient A (H02202)	**PTV**	-0,6	-0,9	-0,6	-0,6	0,0	0,3	0,3	0,0
	Temporal lobe left	-3,5	-3,8	-3,8	-3,8	-4,1	-3,2	-3,5	-1,7
	Temporal lobe right	-2,0	-1,7	-1,2	-1,2	-1,5	-2,3	-2,9	-0,9
	Brain stem	-2,3	-3,8	-4,6	-4,4	-3,2	-4,4	-5,5	-3,2
	Optical system	-0,3	-1,5	-2,9	-4,4	-7,0	-7,3	-6,1	-1,7
Patient B (H02433)	**PTV**	-0,9	-0,3	0,0	-0,6	-0,3	-0,3	-0,9	-0,9
	Optic nerve left	-6,0	-5,7	-5,7	-2,4	-0,3	0,0	-0,3	0,0
	Chiasma	-0,6	-0,9	-0,9	-1,5	-2,1	-4,8	-6,6	-7,8
	Optic nerve right	-0,3	-0,9	-1,5	-1,2	-6,0	-6,3	-2,7	-0,3
	Brain stem	-0,3	0,0	-0,9	-4,2	-6,0	-5,1	-4,2	-1,2
Patient C (H02524)	**PTV**	-0,9	-0,3	0,0	0,0	0,0	0,0	0,3	-2,1
	Optic nerve (right)	-0,3	-0,3	-1,2	-2,4	-3,0	-3,0	-3,9	-6,3
	Chiasma	-1,8	-2,7	-2,4	-2,4	-3,0	-1,2	1,2	0,9
	Brain stem	-1,2	-4,5	-4,8	-2,7	-0,3	0,3	0,3	0,0
Patient D (H02552)	**PTV**	-1,7	-2,2	-1,4	-0,3	0,6	0,8	1,4	0,8
	Eye (left)	0,6	-0,3	-2,8	-4,5	-5,9	-6,7	-6,7	-4,8
	Optic nerve (left)	3,4	1,4	-2,2	-5,6	-6,4	-5,0	-3,9	-1,7

Table 7.8: DVH parameters difference for the ROI of the four patients, with AVM tissue-types as target, in GyRBE, between the MCTP optimized helium plans and proton plans with variable RBE.

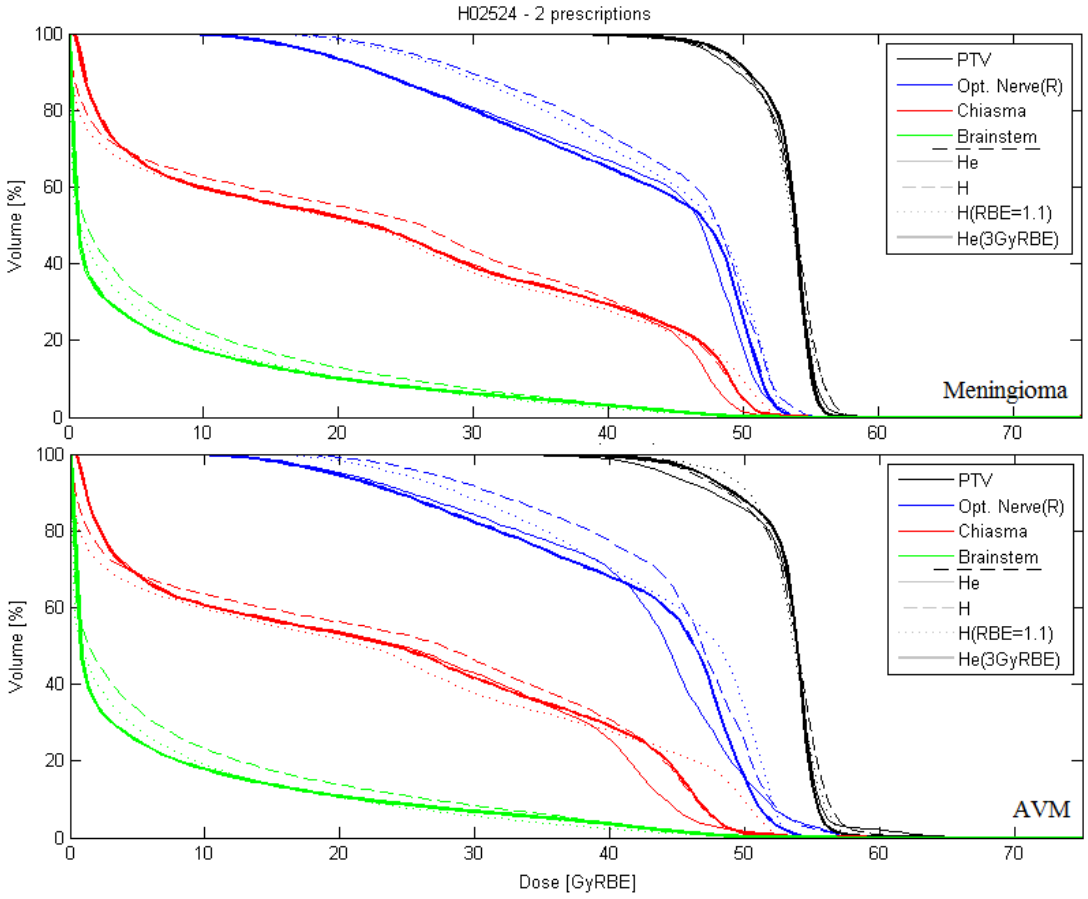

Figure 7.9: DVH for Patient C with meningioma (top panel) and AVM (bottom) as target tissue-type. The various ROIs investigated are displayed. Protons are shown for both fixed (dotted lines) and variable RBE (dashed lines for 1.8GyRBE per fraction). Helium ions are displayed with continuous lines (thin for 1.8GyRBE and thick for 3GyRBE dose per fraction).

7.3.4. Change in fractionation scheme

In figure 7.9, the DVH of the considered ROIs for patient C are displayed for protons with fixed (dotted lines) and variable RBE (dashed lines), as well as helium ions for the two investigated fractionation schemes of 1.8GyRBE (continuous thin line) and 3GyRBE (continuous thick line) for the full delivery with their respective exact numbers of fraction, and taking into account the simple BED approach introduced in 7.2.3. The difference in DVH parameters between helium ions planned for 3GyRBE and 1.8GyRBE is shown in table 7.9. Table 7.10 shows the difference between helium ions planned for 3GyRBE and protons plans with fixed RBE for 1.8GyRBE. Table 7.11 reports the difference between helium ions planned for 3GyRBE and protons plans with variable RBE planned for 1.8GyRBE. Tables 7.9-11 present both meningioma and AVM tissue-type cases.

For the meningioma tissue-type target it can be observed that the PTV coverage is similar between the two helium dose fractionation schemes, slightly improved with the 3GyRBE plans with reduced high dose and improved conformity (lower $D5_{PTV}$ and higher $D95_{PTV}$). Compared to protons with fixed or variable RBE, the new helium dose fractionation of 3GyRBE presents a similar PTV coverage, with DVH parameter differences below 1GyRBE. For the OAR, between the dose fractionation schemes, dose difference in the parameters are below 1.4GyRBE, with a general trend of helium ions planned with 3GyRBE to exhibit higher doses for OAR volumes below 33%, such as for chiasma. The difference in dose between helium ions at 3GyRBE and protons with fixed RBE shows in general better dose sparing with helium ions compared to protons, up to 5.9GyRBE for $D95_{Opt.Nerve}$. This holds true except for the $D5_{Brainstem}$, where the dose is about 1.9GyRBE lower with protons than with helium ions as well as reduced down to 1.7GyRBE for a part of the chiasma with volume above 33%. Compared to the protons with variable RBE, helium ions with the new fractionation scheme present higher dose sparing potential, similar to what was obtained for helium with 1.8GyRBE fractionation.

For the AVM tissue type target, the PTV coverage for helium ions is improved with the new 3GyRBE fractionation scheme compared to the calculation for 1.8GyRBE. The $D5_{PTV}$ is similar but the high dose in smaller volumes below 5% is lowered with the 3GyRBE fractionation, while the $D95_{PTV}$ is improved by about 2.3GyRBE. Compared to protons with fixed RBE the PTV coverage is similar, except for the PTV volume above 85%, where the dose level is lowered by 1.9GyRBE with helium ions at 3GyRBE. The DVH parameter differences for the PTV between helium ions at 3GyRBE and the protons planned with 1.8GyRBE with variable RBE are below 1GyRBE, with a slight improvement for volumes below 5% where less high dose due to hot spots is observed, as seen in figure 7.9. For the OAR, between the two helium ions fraction dose sizes, the DVH are similar for brainstem, as well as for chiasma for more than 33% of the OAR volume. Below 33% of the chiasma volume and for the optical nerve below 70% of its volume, higher doses are delivered with helium ions at 3GyRBE compared to 1.8GyRBE, even if less hot spots are presents with the 3GyRBE fractionation (for less than 5% of the volume). Compared to the fixed RBE proton plans, helium ions at 3GyRBE present a better sparing of optical nerve up to 5GyRBE for $D95_{Opt.Nerve}$. For the $D5_{brainstem}$ the dose is lower with protons by about 3.7GyRBE than helium ions, as well as up to 1.7GyRBE for a part of the chiasma for volume above 33%. Compared to protons with variable RBE, helium ions with the new fractionation scheme present higher dose sparing potential, up to 7.4GyRBE for $D95_{Opt.Nerve}$.

		DVH analysis : Fraction Dose He(3GyRBE) - He(1.8GyRBE)							
		D5	D10	D20	D33	D50	D66	D75	D95
Patient C (H02524) - He Meningioma	**PTV**	-0,4	-0,1	-0,2	-0,1	-0,2	0,2	0,4	0,9
	Optic nerve (right)	0,1	0,1	0,6	0,9	0,7	-1,3	-1,1	0,1
	Chiasma	1,4	1,1	0,8	-0,4	-0,2	0,4	-0,1	0,0
	Brain stem	-1,1	-0,4	-0,4	0,2	-0,2	0,1	0,1	0,0
Patient C (H02524) - He AVM	**PTV**	-0,1	-0,4	-0,7	-0,1	0,3	0,0	0,1	2,3
	Optic nerve (right)	-1,3	-0,7	0,1	1,3	2,3	0,0	-1,8	-1,1
	Chiasma	2,0	2,6	2,6	0,6	-0,8	0,1	-0,2	0,0
	Brain stem	-1,1	-0,6	0,3	-0,2	0,0	-0,2	-0,2	0,0

Table 7.9: DVH parameters differences for the ROIs of patient C, with meningioma or AVM tissue-types as target, in GyRBE, between the MCTP optimized helium plans for 3GyRBE and 1.8GyRBE

		DVH analysis : He (3GyRBE) - H (RBE=1.1)							
		D5	D10	D20	D33	D50	D66	D75	D95
Patient C (H02524) - Meningioma	**PTV**	-1,0	-0,7	-0,2	-0,1	0,4	0,2	0,7	0,3
	Optic nerve (right)	-0,5	-1,1	-0,9	-0,6	-0,5	-2,8	-4,4	-5,9
	Chiasma	-1,0	-1,0	0,2	1,7	0,7	1,3	1,4	0,9
	Brain stem	1,9	-0,4	-1,6	-1,3	-0,2	0,1	0,1	0,0
Patient C (H02524) AVM	**PTV**	-0,4	-0,4	-0,4	0,2	0,6	0,0	0,4	-1,9
	Optic nerve (right)	-0,7	-1,6	-2,0	-2,0	-1,6	-0,6	-2,4	-5,0
	Chiasma	-3,1	-3,4	-1,9	2,4	2,2	1,6	1,6	0,9
	Brain stem	3,7	0,9	-0,9	-1,4	0,0	0,1	0,1	0,0

Table 7.10: DVH parameters differences, for the ROI of patient C, with meningioma or AVM tissue-types as target, in GyRBE, between the MCTP optimized helium plans, for 3GyRBE and protons with fixed RBE.

		DVH analysis : He (3GyRBE) - H (1.8GyRBE)							
		D5	D10	D20	D33	D50	D66	D75	D95
Patient C (H02524) - Meningioma	**PTV**	-1,0	-0,7	-0,2	-0,4	-0,2	0,2	0,7	0,3
	Optic nerve (right)	-0,8	-0,8	-0,6	-0,3	-0,8	-4,9	-6,5	-6,8
	Chiasma	0,2	-0,1	-0,1	-1,9	-3,5	-0,5	0,8	0,9
	Brain stem	-2,0	-4,6	-4,3	-2,5	-0,5	0,1	0,1	0,0
Patient C (H02524) - AVM	**PTV**	-1,0	-0,7	-0,7	-0,1	0,3	0,0	0,4	0,2
	Optic nerve (right)	-1,6	-1,0	-1,1	-1,1	-0,7	-3,0	-5,7	-7,4
	Chiasma	0,2	-0,1	0,2	-1,8	-3,8	-1,1	1,0	0,9
	Brain stem	-2,3	-5,1	-4,5	-2,9	-0,3	0,1	0,1	0,0

Table 7.11: DVH parameters differences for the ROI of patient C, with meningioma or AVM tissue-types as target, in GyRBE, between the MCTP optimized helium plans for 3GyRBE and protons with variable RBE for 1.8GyRBE

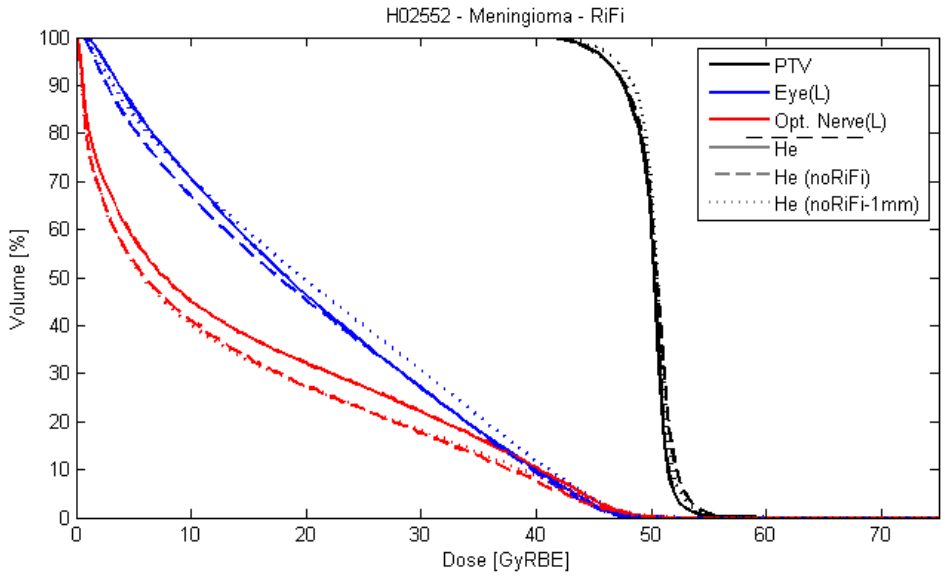

Figure 7.10: DVH for Patient D, with meningioma as target tissue-type for different delivery scenarios: a delivery with RiFi, a delivery without RiFi but the same number of energy slices and a delivery without RiFi with a reduced distance of about 1mm between Bragg peaks, compared to the two first scenarios at about 2mm separation.

7.3.5. Helium ions with/without RiFi

Figure 7.10 depicts the DVH for patient D for the meningioma target. The irradiation scenarios with RiFi are plotted with continuous lines, without RiFi and usual distance of about 2mm between two Bragg peaks with dashed lines, and without RiFi for a reduced distance between peaks of 1mm with dotted lines. The differences between the DVH parameters for helium ions without (for standard distance between Bragg peaks on the top, while reduced distances of about 1mm on the bottom) and with RiFi are listed in table 7.12.
As seen in figure 7.10 and table 7.12, the coverage of the PTV remains similar without RiFi. Differences in DVH parameters are below 1GyRBE. Both irradiation scenarios without RiFi tend to deliver higher dose in the PTV, as seen in the PTV DVH for a volume below 5%. For the irradiation with reduced distance between Bragg peaks, the $D95_{PTV}$ is slightly improved by about 0.8GyRBE. Regarding the optic nerve, the DVH of helium ions without RiFi (both scenarios) is shifted toward lower doses, resulting in a reduction of $D5_{Opt.Nerve}$ by roughly 2GyRBE. For the left eye, higher dose sparing is achieved with the irradiation without RiFi but no change in number of energy slices compared to the irradiation with RiFi. However, for a volume below 80% of the eye, higher dose is delivered (about ~1.5GyRBE) for the irradiation without RiFi but a distance of 1mm between peaks compared to the irradiation with RiFi. On the overall dose distribution, delivery without RiFi reduces the integral dose received by the normal tissues.

		DVH analysis : He (without RiFi) - He (with Rifi) for Meningioma at 1.8GyRBE							
		D5	D10	D20	D33	D50	D66	D75	D95
Patient D (H02552)	**PTV**	0,8	0,8	0,3	0,3	0,0	0,0	0,0	0,0
He (w/o RiFi) -	*Eye (left)*	-0,6	0,0	-0,3	0,3	-0,6	-1,7	-1,7	-0,8
He (with Rifi)	*Optic nerve (left)*	-1,4	-2,8	-4,5	-4,2	-1,7	-1,1	-0,3	0,0
Patient D (H02552)	**PTV**	0,6	0,3	0,0	0,0	0,3	0,0	0,6	0,6
He (w/o RiFi, 1mm) -	*Eye (left)*	0,8	1,4	1,4	2,2	1,7	0,3	-0,3	-0,3
He (with Rifi)	*Optic nerve (left)*	-0,3	-1,7	-3,9	-4,8	-1,7	-1,1	-0,3	0,0

Table 7.12: DVH parameters differences, for the ROIs of patient D, with meningioma tissue-type as target, in GyRBE, between the MCTP optimized helium plans for 1.8GyRBE without and with RiFi. The top part of the table 7.12 shows the difference between the plans withand without RiFI usingthe same number of energy slices. The bottom part compares the same RiFi plan with onewithout RiFi, optimized with a reduced distance of about 1mm between consecutive Bragg peaks.

7.4. Discussions

The observed good agreement in PTV coverage, while successfully fulfilling the constraint criteria on the OARs, for the MCTP and TPS optimized cases of proton irradiation at fixed RBE demonstrates the applicability of MCTP to plan optimization in clinical scenarios. Additionally, these results for proton irradiation demonstrate the capacity of MCTP to provide an even better OAR dose sparing in patient cases, preserving in the PTV a D50 value close (within 1GyRBE) to the TPS calculation at a similar or only slightly reduced D95, as seen in table 7.4. Regarding patient D, the higher dose observed in the OAR can be attributed to the difference in beam modeling at shallow depth between TPS and MCTP. The TPS assumes a beam spread smaller than that of the MCTP, as seen in Chapter 5 for the AVM patient case. In turn, less dose will be given to the OAR using the TPS model at shallow depth. The MCTP is predicting, consistently with experimental data, a larger beam broadening than the TPS (Chapter 5), and thus enhances the weight of the beams delivering dose in the middle of PTV to provide a good PTV coverage, while trying to fulfill the OAR constraints. Although larger $D5_{PTV}$ values can be found in the other patient cases, they are still respecting the limits of 107% set in the constraints. Compared to analytical TPS systems performing calculation in water of variable depth, MC dose predictions generally exhibit higher $D5_{PTV}$ values as well as lowered $D95_{PTV}$ values, due to the beam transport in heterogeneous material. Therefore, the MCTP constraints determined in this work for protons with fixed RBE provide sound treatment plans, comparable in quality to the original TPS plans. Hence, these constraints were also used for the optimization with variable RBE for protons and helium ions. The implementation of constraints on the whole DVH, and not only on the maximal dose, is necessary for MC planning and was achieved in this work by putting a low dose constraint on the OAR. In fact, as described in Dale and Olsen (1997), depending the type of OAR, parallel or serial, the dose constraints should be applied on the OAR mean dose (linked to the whole DVH) or maximum dose, respectively. As stated in section 7.2.1, instead of the maximum dose, indices as D_5 are less prone to MC statistical fluctuation and should be integrated in the foreseen MCTP version.

As seen in figure 7.2-7.4 displaying patient A- C dose ditributions, for helium ions at the boundary of the planning target volume (PTV), hot spots (dose superior to 107% of the prescribed dose) can be observed. It can be due to to the high linear energy transfer (LET) components of helium ion beams at the lateral and distal edge of the tumor, in combination with a lower α_x/β_x ratio (α_x/β_x=2) of the normal tissue. These higher dose contributions could be reduced by adding dose constraints on the surrounding tissue of the PTV, present on the

PTV optimization matrices, but not yet implemented in the Monte Carlo Treatment Planning (MCTP) tool.

The plans optimized for meningioma as target tissue-type show similar coverage for the PTV in patient cases A, B and C with either protons (fixed or variable RBE) or helium ions. For patient D, the PTV coverage is found better with helium ions, with a larger $D95_{PTV}$ value and a smaller $D5_{PTV}$ value, indicator of PTV dose homogeneity. This finding could be be ascribed to the size of the target and the proximity of the OAR. In fact, due to the larger lateral and distal fall-off of proton beams, seen in chapter 3, they cannot cover the target optimally without impacting the surrounding OARs. Thus, to provide a better coverage, the optimizer will choose to allocate higher doses in the middle of PTV as seen in figure 7.5. Compared to protons plans with variable RBE, helium ions provide better sparing of OAR in all cases, excluding the left optic nerve of patient D. Since the left optic nerve exists within the PTV, one could expect higher doses in the OAR due to the better dose homogeneity within the PTV, as previously described. In general, the OAR DVH curves of helium ions are shifted toward lower doses due to: (1) the reduced lateral straggling, impacting the DVH for volume larger than 30% (figure 7.7) and (2) a more favorable ratio between the RBE at high LET for α_x/β_x at 3.7 (target) and RBE at low LET for α_x/β_x at 2 (for the surrounding non-tumour tissue). This ratio is on the order of 15-20% larger for helium ions, as it can be interpreted from figure 7.11, leading to less deposited physical dose, compared to protons. Compared to the proton irradiation with fixed RBE, helium ions still present the advantages of OAR dose sparing, since protons with fixed and variable RBE show similar trends. The largest differences between protons with variable and fixed RBE can be seen for OAR at the end of the beam range, where LET, and therefore RBE, is enhanced, ultimately leading to higher biological dose deposition. This can be seen particularly in the chiasma of patient C in figure 7.7.

Regarding the optimized plan with AVM tissue-type as target compared to the meningioma case, PTV coverage is maintained with both ion species with variable RBE modeling, for patient A with two opposing fields, as well as for patient D. However, the coverage is degraded using protons and helium ions with variable RBE for patients B and C, compared to the meningioma tissue-type case. Furthermore, hot spots are present within the PTV and can be seen in the DVH for volumes smaller than 5% of the PTV, presenting higher dose values than $D5_{PTV}$. In the case of patient A, with the two opposing fields, the high LET components for protons and helium ions are smeared out, similar to the findings of Giovannini et al. (2016), leading to a region of reduced RBE region at the extremity of the PTV and in the adjacent OAR compared to what is seen in figure 7.8 for patient B and C. For patient D, no particular loss in coverage of PTV was found, since no OARs are presents at the end of the ion range. The advantages in dose sparing of helium ions compared to protons with variable RBE are still present, as seen in figure 7.8 and table 7.8, but are reduced. Compared to protons with fixed RBE, the dose sparing advantages of helium ions on OAR are reduced. By changing the tissue type parameter α_x/β_x from 3.7 to 10 for the PTV, a greater number (about 10-15% for protons and helium ions) of primary particles is required to achieve the same biological dose level in the PTV. Thus, on the distal and lateral edges presenting higher LET, higher biological doses are to be expected compared to the meningioma cases and to protons with fixed RBE. Consequently, OAR may exceed the dose limits from the set constraints, and the optimizer will attempt to solve this issue by degrading the coverage and/or increasing the dose within the PTV (hot spots) in order to recover the lost coverage. Similar increases in dose were observed in Grün et al. (2016) for artificial plans with a PTV/OAR presenting similar α_x/β_x ratios as in this work. In patient C the chiasma exhibits a lower $D5_{chiasma}$ value for helium ions and protons with variable RBE compared to protons with fix RBE, but only resulting from a loss of PTV coverage. The difference between protons with and without

variable RBE, which were already present in the meningioma target cases, are found amplified in the AVM target cases. While advantages of helium ions over protons with variable RBE are evident from figure 7.8 and table 7.8, even though with reduced biological advantages, they are more complex to judge against proton with fixed RBE with the considered fractionation scheme for AVM cases.

The behavior of the ions using different tissue types can be explained while looking at the evolution of the RBE as a function of different parameters such as dose, LET and tissue types, as investigated in Giovannini et al. (2016) and Mairani et al. (2017), and shown in figure 7.11. For helium ions, the physical dose needs to be approximatively 20% higher for α_x/β_x of 10 to achieve the same biological dose as for α_x/β_x of 2, which is within the same order of magnitude of the ratio found (~15%) between the AVM (α_x/β_x ratio of 10) and the meningioma target cases (α_x/β_x ratio of 3.7). Subsequently, for the normal tissue surrounding the target (α_x/β_x ratio of 2), which receives about 50% of the physical dose and is still located in the high LET region, the change in α_x/β_x can lead to an increase of dose by approximately 40%. A possible approach to mitigate the influence of the varying α_x/β_x between PTV and normal tissue could be to increase the dose per fraction. In fact, as seen in figure 7.11, for tissue types with α_x/β_x of 2 as both target and normal tissue, the biological dose ratio between target receiving 1.8GyRBE and normal tissue receiving about 50% of the physical dose in the high LET region is about 2. However, for a target with a α_x/β_x of 10, this ratio is lowered to about 1.3. For a prescription dose of 3GyRBE, the biological dose ratio between target and normal tissue is of 1.8 and 1.6, respectively, for a target with an α_x/β_x ratio of 2 and 10. Therefore, using higher dose prescriptions could decrease variability between different tissue types for helium ions.

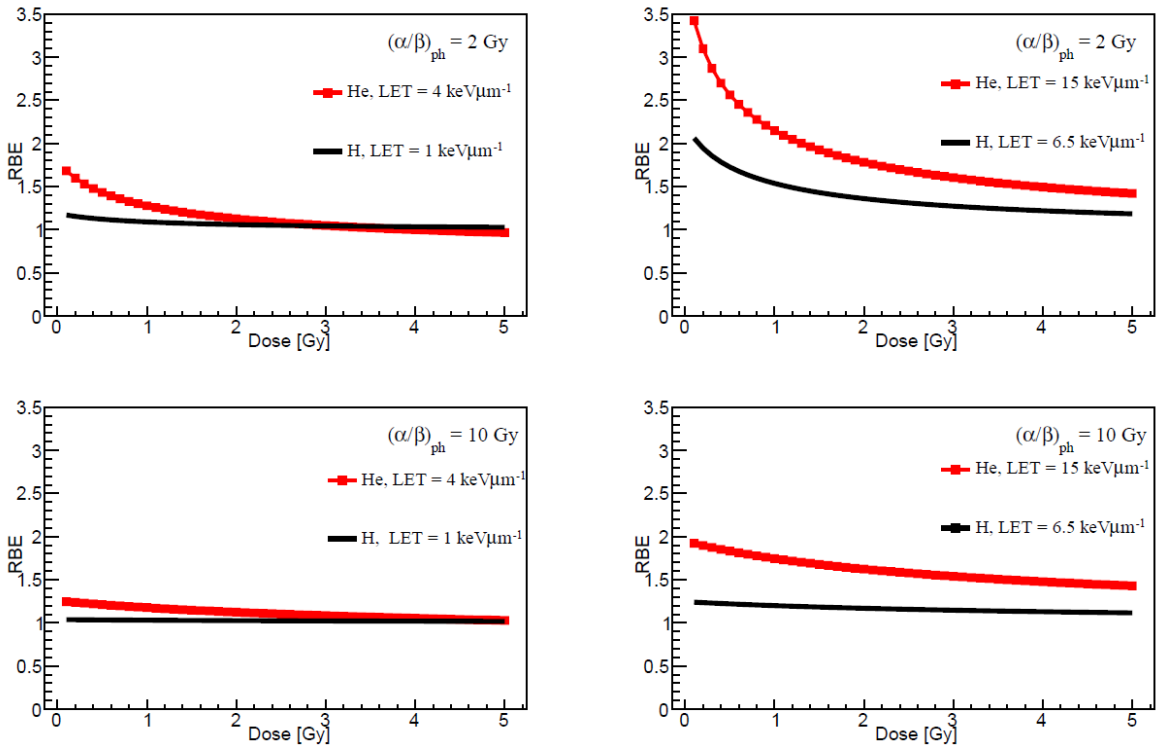

Figure 7.11: RBE model predictions as a function of proton dose in black, for α_x/β_x = 2 Gy (upper panels) and 10 Gy (lower panels), calculated at LET levels of 1 keV/µm (left) and 6.5 keV/µm (right), respectively (adapted from Giovannini et al. 2016). The corresponding dose-dependent predictions for ^{4}He ions are shown in red, again for α_x/β_x = 2 Gy (upper panels) and 10 Gy (lower panels), at 4 keV/µm (left) and 15 keV/µm (right) LET, respectively (adapted from Mairani et al. 2017).

When investigating the complex case of patient C, an increase in the prescribed fraction dose to 3GyRBE for the meningioma target-tissue case allowed helium ions to exhibit a similar coverage as helium ions for the 1.8GyRBE prescription, with improved dose homogeneity (higher D95and lower D5) due to reduced RBE variability as a function of LET and dose. This higher homogeneity in dose in the PTV, together with reduced biological benefits between PTV and normal tissues at higher dose prescriptions, led to an increase in high dose level for OARs, as seen with the enhancement of $D20_{chiasma}$ in figure 7.9 (top panel) and table 7.11. For the AVM target case, the 3GyRBE allowed better PTV coverage compared to the helium plan at 1.8GyRBE fraction dose, as seen in figure 7.9 (bottom panel) and table 7.11, removing the high dose contributions for volumes below 5% of the PTV. Regarding the OAR, the increase in PTV coverage led to higher dose exposure for the OAR volumes close to the PTV. But the maximum OAR dose $D5_{OAR}$ and the dose given to smaller volumes was reduced. In comparison to protons with variable RBE at 1.8GyRBE , helium ions with a 3GyRBE fraction dose prescription presented similar DVH characteristics in the OAR high dose region, e.g. for volumes below 30% in the chiasma, while having a similar PTV coverage. This is due to the fact that with such fractionation the above mentioned biological dose ratio between target and normal tissue for protons is similar to the one of helium ions at 3GyRBE, with values of 1.8 and 1.5, respectively, for a target with a α_x/β_x of 2.0 and 10 (figure 7.11). For larger OAR volumes, helium ions exhibit improved dose sparing due to their physical properties, leading to a reduction in integral dose delivered. However, as stated in 7.2.3, even though introducing a higher dose per fraction is reducing the variability between tissue types, particularly in the case of high α_x/β_x tumors, it could decrease the cell survival of normal tissues compared to a lower fractionation scheme. These assumptions can be linked to the fact that tumors with high α_x/β_x are clinically benefiting from hyperfractionation, while tumor with low α_x/β_x from hypofractionation (Schlaff et al. 2014). However, deeper investigations using more complex approaches such as tumor control probability / normal tissue complication probability (TCP/NTCP) models would be more accurate, particularly regarding the OARs presenting non homogeneous biological dose distributions (Suit et al. 2010). An investigation on the optimal fractionation scheme using methods such as presented in Unkelbach et al. (2013) for these specific cases could be foreseen, combined with known patient outcomes from protons and carbon ion treatments at HIT.

The use of RiFi was suggested in Chapter 6 for the spread-out Bragg peak at shallow depth (5cm) in order to reduce dose ripples within the PTV. However, in the case of patient D with meningioma as target-tissue type, MC predictions without RiFi did not affect PTV coverage and could indicate that a RiFi may not be necessary for helium therapy. Even if higher dosage in the target can be seen for low volumes (<5%), hinting at possible ripples, the constraints on the maximum dose are still fulfilled and the coverage on the larger volume is kept. For the irradiation without RiFi and a reduced distance between Bragg peaks, the coverage was found slightly better, as seen in figure 7.10, due to the increased number of pencil beams available to cover the proximal and distal part of the target, together with the reduced lateral straggling compared to the irradiation with RiFi. For OAR DVH, the curves are shifted to lower dose values for irradiation without RiFi, due to the reduced lateral spread compared to the helium ion delivery with RiFi. However for the left eye, the delivery without RiFi and 1 mm distance between Bragg peaks led to higher dose compared to the delivery with RiFi. This finding can be explained by the higher dose within the PTV and the special location of the left eye, next to the PTV. Higher dose in the PTV was achievable in the scenario of a delivery without RiFi and 1mm distance between Bragg peaks due to the reduced lateral straggling and improved distal/proximal coverage. Delivery of helium ions without RiFi could lead to sparing about 10GyRBE in roughly one third of the optic nerve volume compared to irradiation with

protons (with variable RBE), without considering the improved PTV coverage with helium ions.

Although further investigations are needed, the analyzed case suggests that the RiFi may be unnecessary for helium ion therapy in the clinic. It can be noted that in the prostate case presented in appendix D, the PTV coverage between protons and helium ions without RiFi is similar. However, better OAR dose sparing can be achieved with helium ions. In the prostate case, with a target depth of about 15-20 cm, the PTV location is deeper compared to the shallow target of patient D. At such range the dose ripple effect are less pronounced due to the increased range straggling, as demonstrated in Chapter 6.

7.5. Summary

From all the analyzed four beam geometry cases, advantages of helium ions over protons are evident in the meningioma patients for 1.8GyRBE fractionation, due to both physical (lateral and distal straggling) and biological advantages (RBE enhancement in the target with high LET at this fraction dose), particularly when using a variable RBE. However, in the AVM target tissue-type, helium ions do not clearly demonstrate the benefits for a 1.8GyRBE fractionation. As indicated in Grün et al. (2016), the advantages of one ion over the other ones can be discussed as a function of the tissue type, beam geometries and fractionation dose. However, our study indicates that when comparing helium ions and protons with a variable RBE, helium ions for 1.8GyRBE and 3GyRBE could provide better DVH characteristics in all meningioma cases, and appear promising with a 3GyRBE fractionation scheme for AVM. Furthermore, not using the RiFi could provide improved OAR dose sparing while maintaining optimal PTV coverage.

This chapter demonstrated the capabilities of the MCTP with proper constraints to provide sound plans, comparable in quality to those from the clinical TPS for protons with fixed RBE. For the meningioma cases with a fraction dose of 1.8 GyRBE, the plans optimized with MCTP show promising results for helium ions, with similar coverage to protons and better sparing of OAR for all beam configurations investigated, featuring two fields (from opposing to small angles) as well as single field. For the AVM cases, when using a higher fractionation dose of 3GyRBE, helium ions present improved DVH characteristics compared to helium ion with a fraction dose of 1.8GyRBE, and are advantageous in dose sparing compared to protons with a variable RBE. Irradiation without RiFi for helium ion beam therapy seems possible even at shallow depth, thus furthering the potential for OAR dose sparing. These results indicate than helium ions could be an alternative to proton therapy due to their favorable physical and biological characteristics. Helium ions could provide promising treatments for head low-grade meningioma, and prostate as seen in Appendix D. Further investigations using TCP/NCTP models or robust planning, to take into account the planning and delivery uncertainty, could also be of interest to support physicians and medical physicists for the introduction of helium therapy in the clinical routine.

Chapter 8. Conclusion & Outlooks

Helium ion beams have regained momentum over the last decades for patient treatment, after the discontinuation of the clinical trial in 1992 at the Berkeley National Laboratory. This renewed interest can be observed in the literature, with an increased number of publications related to both computational works, including studies based on Monte Carlo or analytical calculation engines, and experimental efforts, which focus on new physical and biological characterization of helium ion beams, as performed through this thesis.

The aim of this thesis was to provide and validate the key elements necessary to bring helium ions from initial measurements in phantoms to clinical treatment planning comparisons against other ions, particularly for the treatment of low-grade meningioma cases. Most of the studies presented in literature with helium ions were either (1) not supported by thorough dosimetric experiments or (2) not taking into account the complex mixed radiation field of helium irradiation or (3) not introducing complex biological modelling. This thesis overcomes these shortcomings as explained in the following.

Chapter 2 introduced the four steps needed in order to achieve the overall goal:

- The first step focused on the comparison of various dosimetric characteristics of the ions available at the Heidelberg ion beam therapy center, including protons, helium, carbon and oxygen ions. This step was achieved in Chapter 3 and Chapter 6, presenting the dosimetric advantages and drawbacks of the different ions, for irradiations performed with a state-of-the-art fully active beam delivery system. Particularly, these chapters demonstrated the potential of helium ions for further particle therapy improvements due to the observed favorable physical characteristics, intermediate between protons and heavier ions, with a smaller lateral and longitudinal straggling or a lower fragmentation tail, respectively.

- The second step was achieved in Chapter 4 and 6, where MC FLUKA predictions were found in good agreement with dosimetric measurements for the characterization of the helium ion pencil-beams at HIT as well as more complex clinical-like delivery scenarios. For the ion species available at HIT, the validation of a research MC-based treatment planning engine (MCTP) against measurements opened up the opportunity to proceed toward patient planning.

- The third step was related to the modelling of biological properties of helium ions. Through the physical validation of the MC predictions, as well as the MC-based generation of a physical database for input into an established analytical research TPS used for simple planning, biological experiment were carried out at HIT to verify the radiobiological model used in this thesis.

- The fourth step embodied the main goal of this thesis: treatment planning for meningioma patient cases with helium ions. Combining the improved simulation framework presented in Chapter 5 linked to a sound biological model, treatment planning comparisons between protons and helium ions presented in Chapter 7 for four meningioma cases demonstrated that helium ions could bring therapeutic benefits to patients by reducing dose to organs at risks.

Through this thesis, the first elements necessary to bring helium ions a step closer to a future therapeutic use at HIT have been completed. Nevertheless, additional studies are foreseen to proceed further toward clinical translation.

Deepest investigations on the biological side are a priority. New biological cells survival characterizations, in a similar fashion as in Mairani *et al* (2016) and Mairani *et al* (2016b), are ongoing at HIT with several cell lines to compare and verify different radiobiological models such as the LEM, MKM (Chapter 2, section 2.7) or the empirical biological model used in this thesis. Such work is needed to provide a sound model for treatment planning, validated for a wide range of cell types, hence α_x/β_x ratio, and representative of the different properties of tumor, and normal tissue. Following thorough cells experiments, animal experiments as in Saager *et al* (2016) or Karger et al (2006) will lead to more complex investigations, providing in-vivo validation of the different biological models, by analyzing the response of tissue (e.g. dose tolerance) to radiation. In complement to biological models predicting RBE, other models, e.g., based on TCP/NTCP modeling, could gain from such investigations. All these in-vitro and in-vivo studies will greatly benefit from the work of this thesis, namely the validation of the MC framework (including the MCTP), and the generated database for input to the research TPS, in order to create reliable physical or biologically optimized plans.

Besides the overall promising agreements found between FLUKA MC predictions and measurements for simple (e.g. depth dose distributions, lateral dose profiles) or complex (e.g. physically as well as biologically optimized SOBPs) cases, there is room for improvements of the MC code for modeling helium ions. As shown in Chapter 4 and Appendix B, disagreements against physical data sensitive to nuclear interaction were observed. Additional experimental physics data (e.g. cross sections, energy spectra, projectiles angular distribution) obtained in measurements such as Rovituso *et al* (2017) for ^{4}He ions or Dudouet *et al* (2014) for ^{12}C ions would be beneficial to guide the improvement of the MC models. Despite the fact that the MC code FLUKA is providing dosimetric results considered reliable enough to conduct studies toward the clinical level, improvement of specific nuclear models could lead to even stronger prediction capabilities of the MC code.

Additionally to the cases presented in this thesis for meningioma tumours and a preliminary study on a prostate cancer case, more clinical studies are foreseen to evaluate the anatomical localizations that would benefit the most from helium ion therapy. For that purpose reliable treatment planning engines are needed. Several approaches can be foreseen: (1) the development of MCTP toward a clinical version, featuring all improvements suggested in

Appendix C and allowing user-friendly interface and DVH constraints selections; (2) the adoption of an analytical TPS such as the SyngoPT system used clinically at HIT, integrating the database generated within the scope of this thesis with depth dose distributions, lateral Gaussian distributions (double or triple) and fragmentation spectra as in Mairani *et al* 2010 and Parodi *et al* (2012); (3) the use of fast GPU-MC simulation as developed for protons (Jia *et al* 2015) and carbon ions (Qin et al 2017);

To further enhance the quality of treatment planning, new features such as robust planning (Fredriksson 2013), taking into account during the optimization process all possible sources of uncertainties in patient positioning, beam delivery as well as radiation biology, could provide more reliable plans for clinical treatment and comparisons between ions. Other biological models, looking at different endpoints than the RBE model used in this thesis, could also be of interest for further treatment planning with ions, including helium ions. Additionally, the combination of different ions within the same treatment plan, such as helium and oxygen ions, could bring particle therapy a step further, taking advantages of their respective physical and biological properties.

The uncertainty in the Bragg peak position within the patient, described in Chapter 2, could benefit from in-vivo range monitoring techniques such as PET imaging. Investigations on the β+ emitters distribution of helium ions on several targets (PMMA, PE, gelatin as in Bauer *et al* 2013) have been started in the framework of this thesis. However, comparisons to MC results indicated that there was room for improvement of the MC code nuclear models, for reliable prediction of β+ emitter distributions.

Appendix

A-Supplementary material to Chapter 3

Additional information regarding topics discussed in Chapter 3 is provided in Appendix A.

Depth dose distributions with RiFi

Figure A.1 displays the depth dose distributions in water measured with the PeakFinder for irradiations with the ripple filter (RiFi). These measurements were used for the experimental comparisons presented in Chapter 3 (3.3.1.2.), the validation of Monte Carlo FLUKA dose predictions for helium ions (Chapter 4), as well as FLUKA input files refinement for protons, carbon and oxygen ions.

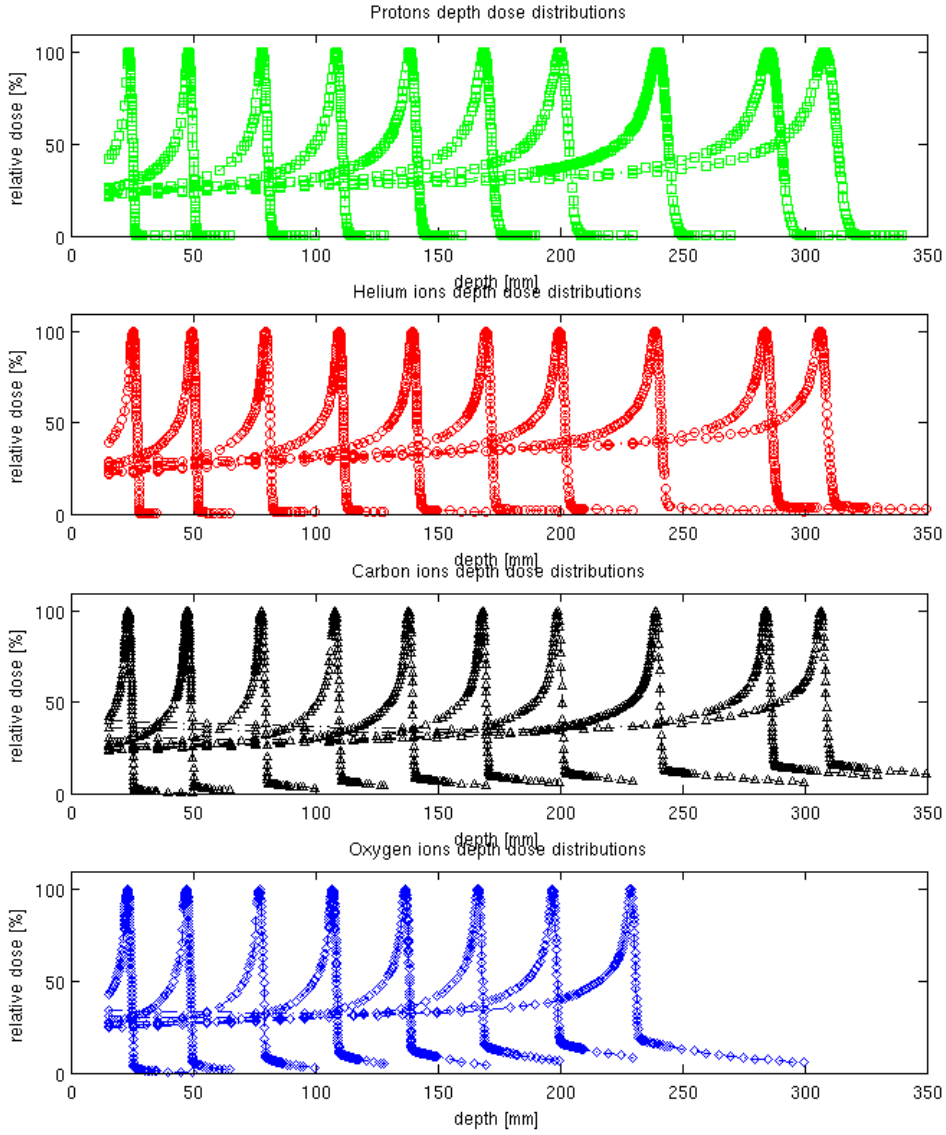

Figure A.1: Depth dose distribution measurements for protons, helium, carbon and oxygen ions, respectively, from the top to the bottom panels, in water with RiFi.

Relation between PW/R_{80} as function of R_{80}

Figure A.2 shows the relation between the ion peak-width presented in Chapter 3 (3.3.1.3.) over the range (R_{80}), times a factor F close to $\sqrt{M}$, with M the mass of the particles. At higher energies with R_{80}>120 mm, protons and helium ions exhibit a PW/R_{80} ratio 3.5 and 1.9 times larger than oxygen ions, respectively, while carbon ions exhibit a PW/R_{80} ratio 1.1 times larger than oxygen. As a function of particle mass *M*, the PW/R_{80} results, relative to oxygen ions, suggest a relationship for protons, helium and carbon ions, respectively, of about $0.85 \times (\sqrt{M_O}/\sqrt{M_p})$, $0.93 \times (\sqrt{M_O}/\sqrt{M_{He}})$ and $0.97 \times (\sqrt{M_O}/\sqrt{M_C})$. As described in section 3.3.1.3., the values are slightly inferior to the dependency on $1/\sqrt{M}$ described in Schardt et al. (2010). At higher energies, effects such as initial energy spread are less impacting the peak-width, dominated by range straggling.

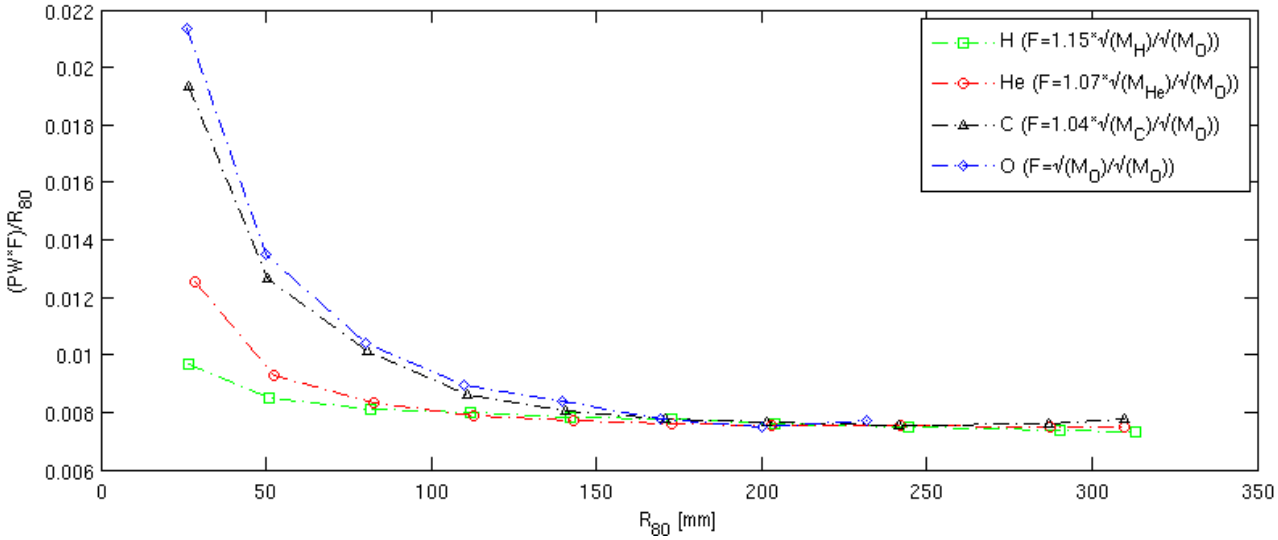

Figure A.2: Relation between the Peak-width (PW) sizes over the range (R_{80}), multiplied by a factor F, as a function of R_{80} for protons (squares), helium (circles), carbon (triangles) and oxygen ions (diamonds). The factor F is close to $\sqrt{M}$, with M the mass of the particles.

Ions σ_{0corr} evolution in water

As seen in figure A.3 and explained in section 3.3.2., the evolution of σ_{0corr} of the different ions before the Bragg-Peak has a dependency of $1/\sqrt{M}$ and therefore, the heavier the ion, the smaller the beam width. Figure A.3 presents the evolution of σ_{0corr} corrected by a factor F close to $\sqrt{M}$ (+/-10%). As a function of particle mass *M*, the width relative to carbon ions can be described by the following relations for protons, helium and oxygen ions respectively: $0.9 \times (\sqrt{M_c}/\sqrt{M_p})$, $\sqrt{M_C}/\sqrt{M_{He}}$, and $1.05 \times (\sqrt{M_C}/\sqrt{M_O})$.

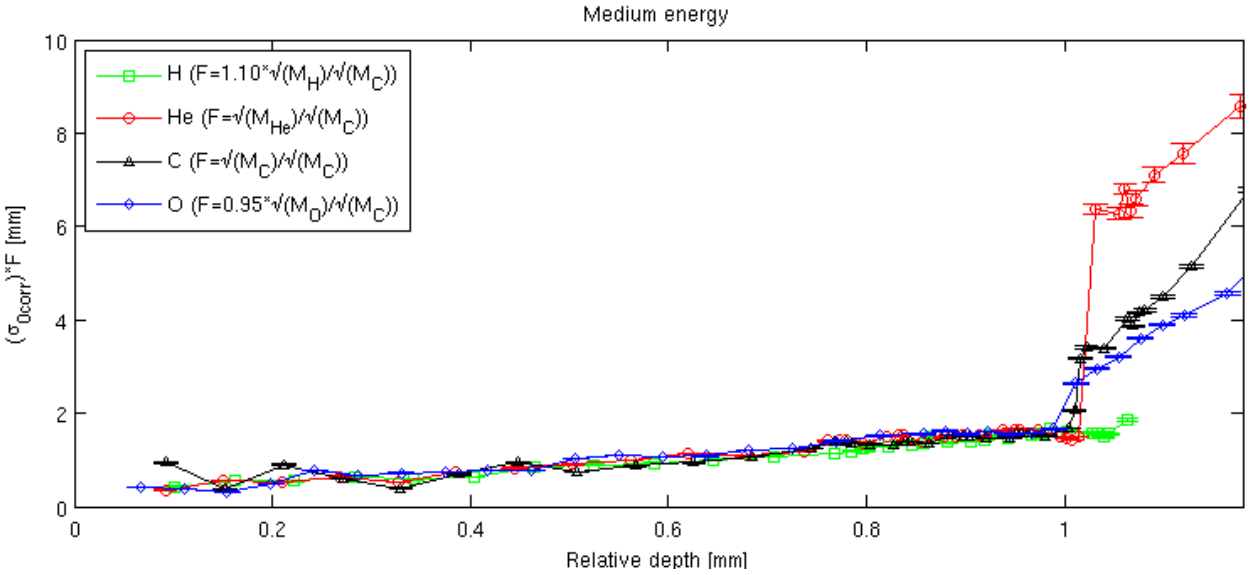

Figure A.3: Relation between the σ_{0corr} describing the central Gaussian core of the medium energy investigated (corrected for the Gaussian width size at 0 cm), multiplied by a factor F, as a function of R_{80} for protons (squares), helium (circles), carbon (triangles) and oxygen ions (diamonds). The factor F is close to $\sqrt{M}$, with M the mass of the particles.

B - Supplementary material to Chapter 4

Additional information regarding topics discussed in Chapter 4 is provided in Appendix B.

Momentum spread optimization

The figure B.1 illustrates the χ^2 reduction as a function of *dp/p* performed for the different energies presented in table 4.1. For all investigated energies, the value of *dp/p* minimizing the χ^2 is recorded. Subsequently with the obtained value, the relation between *dp/p* and the initial helium ions energy can be interpolated to the 255 energies available at HIT as seen in Figure 4.2.

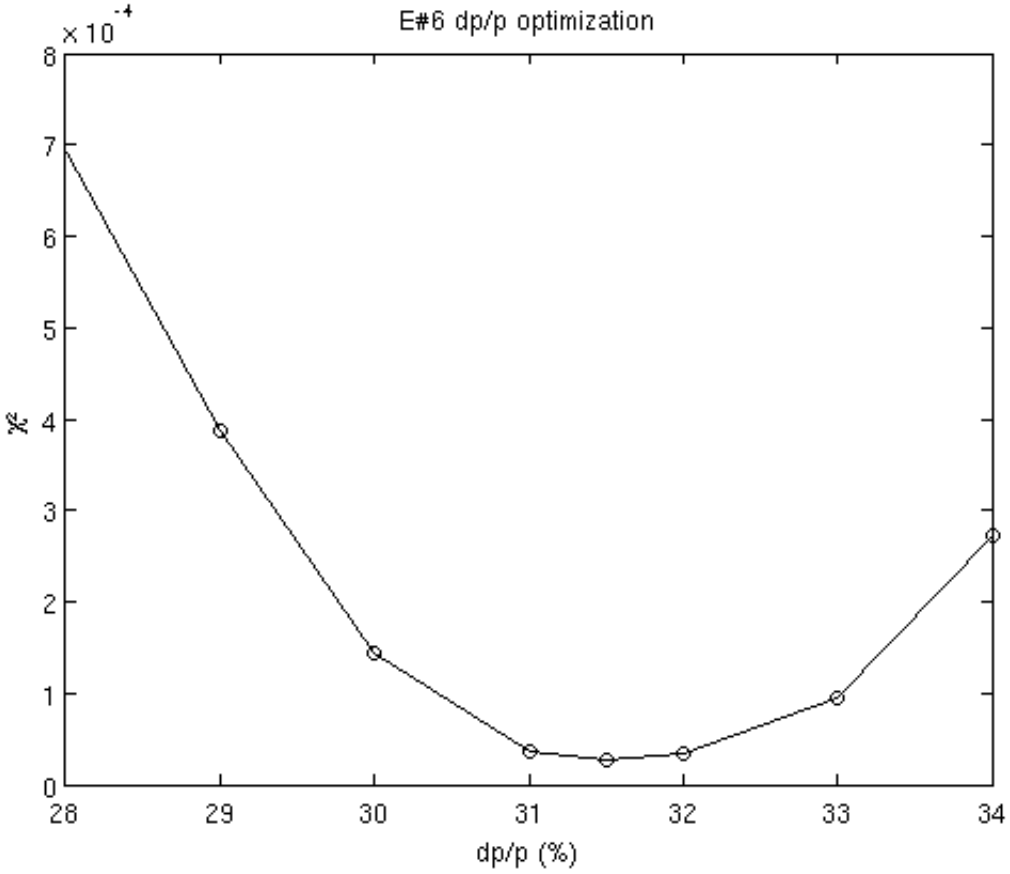

Figure B.1: Relative momentum spread (*dp/p*) optimization for ^{4}He (56.4MeV/u as seen in table 4.1, corresponding to an energy index of #6 on the HIT accelerator library). Points represent the χ^2 obtained for the corresponding *dp/p* values.

Triple Gaussian parametrizations for low and medium energies

The triple Gaussian parametrization of low and middle energies as shown in figure 4.8 and detailed in the results of section 4.3.2 are shown in figure B.2 and figure B.3. As explained in section 4.3.2, the different Gaussian widths corrected are in good agreement between simulations and measurements. For low energies, the different weights are not significantly different and within the error bars, however, for medium energies, as shown for high energies in figure 4.8, underestimation of the weight by FLUKA is seen. Further explanations are presented in section 4.4 and some tests weighting the dose contributions in FLUKA were performed for lateral profiles (figure B.4).

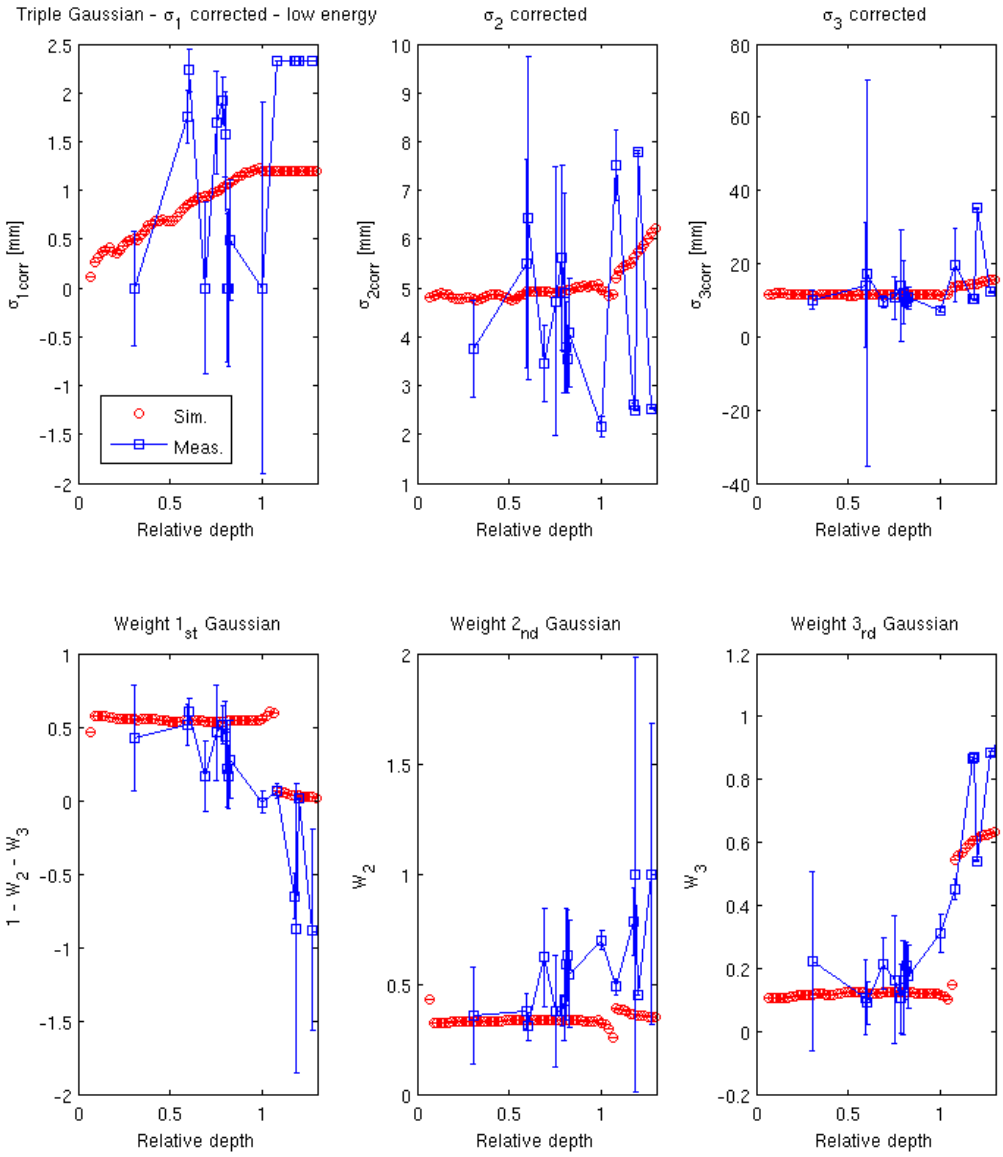

Figure B.2: Triple Gaussian parametrization for the lowest beam energy. Simulations are displayed with circles and measurements with squares. The top panels depict the Gaussian widths evolution in water (relative to the Bragg peak position), from the smallest Gaussian to the broader one from left to right. The bottom panel shows the corresponding weights.

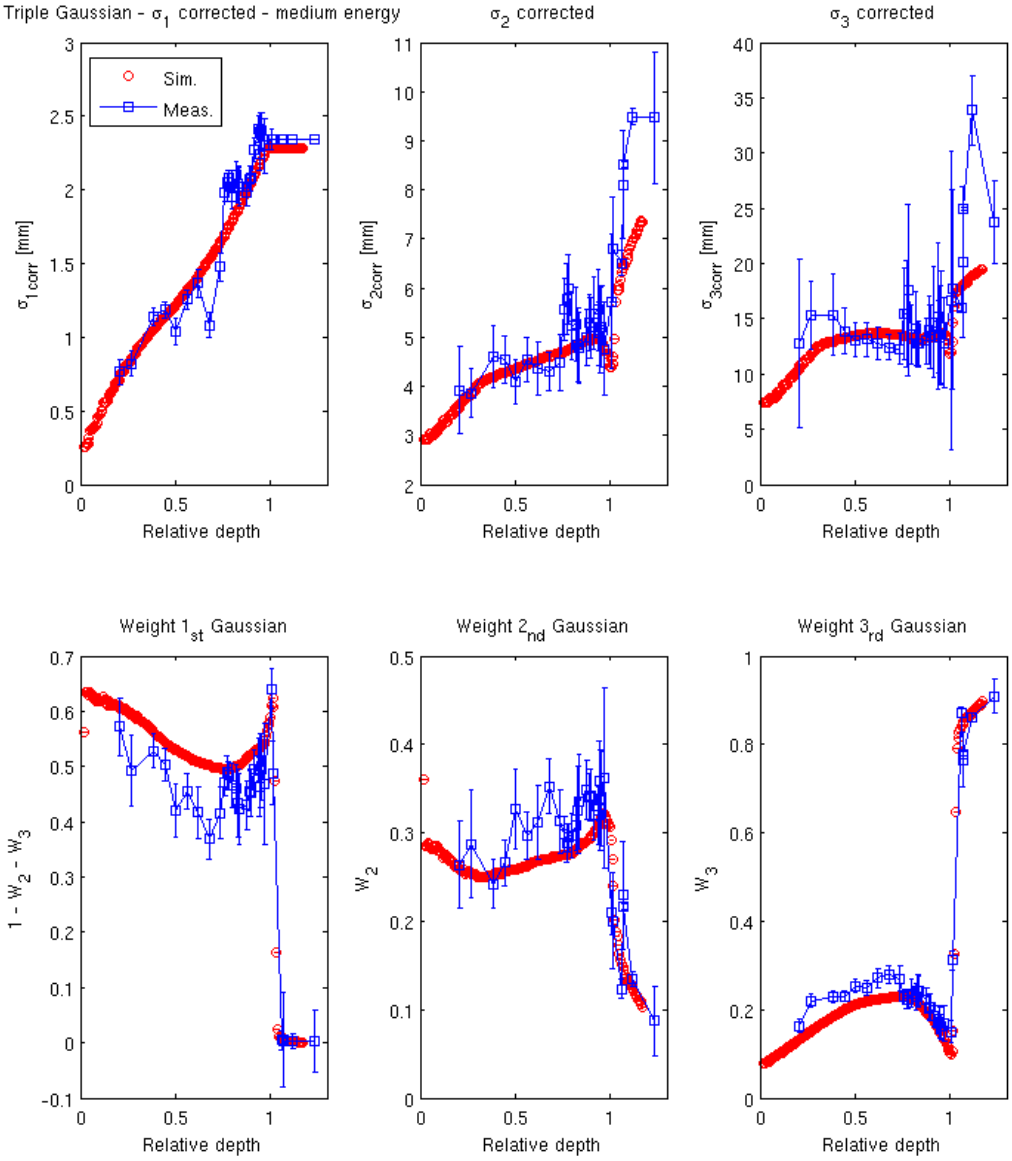

Figure B.3: Triple Gaussian parametrization for the medium beam energy. Simulations are displayed with circles and measurements with squares. The top panels depict the Gaussian width evolution in water (relative to the Bragg peak position), from the smallest Gaussian to the broader one from left to right. The bottom panel shows the corresponding weights.

Helium ions simulation modifications

In order to investigate the reasons behind the disagreements found in Chapter 4 between FLUKA predictions and dosimetric measurements for depth dose distributions and for lateral profiles, modifications to simulation parameters have been tested.

As explained in section 4.4, the possibility of a non-Gaussian beam in vacuum has been evaluated in order to explain the disagreement on the lateral dose distribution, particularly at high energy. For this purpose, lateral dose deposition in water as performed in section 4.2.3 was achieved for an initial double-Gaussian beam in vacuum. In addition to the primary Gaussian width, a secondary Gaussian was added with different widths of 9, 15 or 30 mm, applied with different weights of 3, 3 or 2%, respectively. These values are representative of the FWHM range for the second and third Gaussian, for a weight found after a trial and error process. As it can be seen in figure B.4, while these modifications improve the agreement at the phantom entrance with measurements (blue points), at further depths near the Bragg-peak, the difference remains consistent with the single Gaussian modeling in vacuum. These results indicate that beyond the possibility of a non-Gaussian beam in vacuum, improvements of the code can be foreseen to allow matching of the dose halo at large depth.

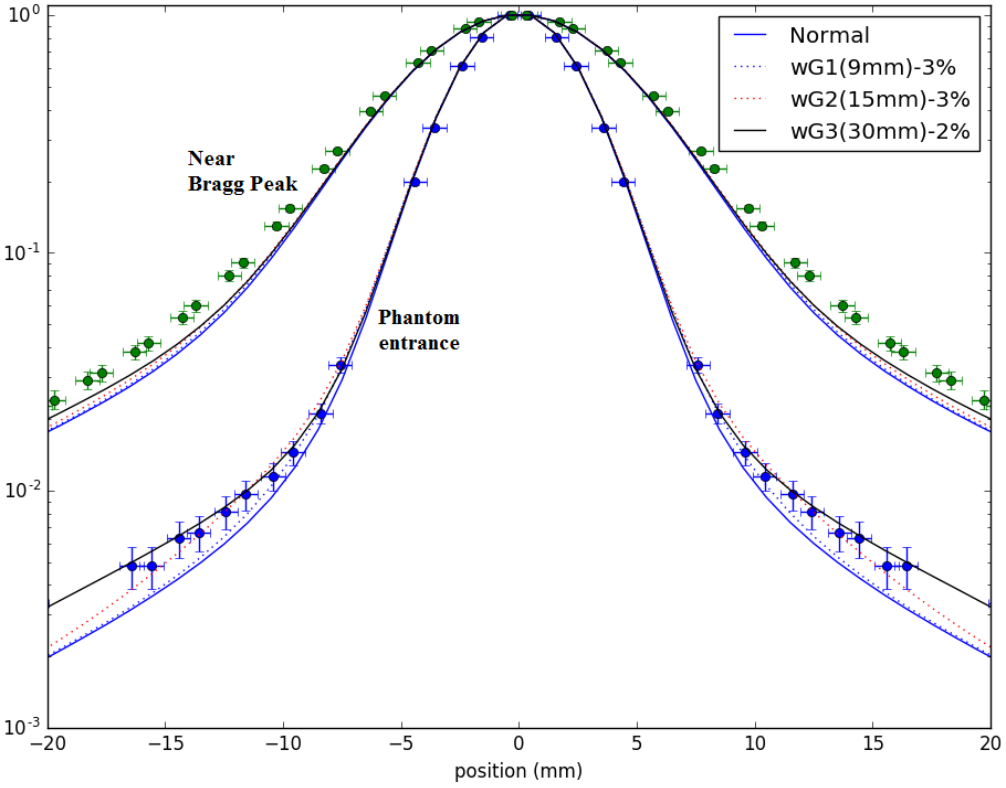

Figure B.4: Lateral dose distribution of the highest energy helium ion beam investigated, at the phantom entrance and near Bragg peak as explained in section 4.2.3. Simulation with just a normal single Gaussian beam in vacuum (“Normal”) or associated with an additional Gaussian with a larger width (9, 15 or 30mm) and a particular weight (3, 3 or 2% respectively).

In a second step, the dose contribution of each particle type (^{1}H, ^{2}H, ^{3}H, ^{3}He, ^{4}He) was recorded individually for the medium and high energy presented in Chapter 4 (158.1 MeV/u and 220.5MeV/u). Thus, it is possible to weight each dose contribution individually. For depth dose (Figure B.5 top panel) and lateral distributions (figure B.5 bottom), the dose contribution of protons was multiplied by a factor of 2. This leads to a reduced entrance-to-peak ratio for the depth dose distributions, as seen with the black curve ("Sim. mod."), affording better agreement between simulation and measurements for both investigating energies. The same conclusion is obtained with the lateral profiles where, with the modified simulations, better agreements are found at both the entrance and greater depths. These results could suggest that the dose contribution of large angles secondary particles such as protons could be underestimated by the FLUKA code. Either the underestimation of interactions of secondary particles, or their production angles, could be the cause of such effect. In figure B.6, at around the middle of the Bragg curves, some particles are underestimated at larger angles for both energies, such as deuterium for 120MeV/u or protons for 200MeV/u. Such experiments presented in figure B.6 and B.7 could help supporting the improvement of FLUKA model.

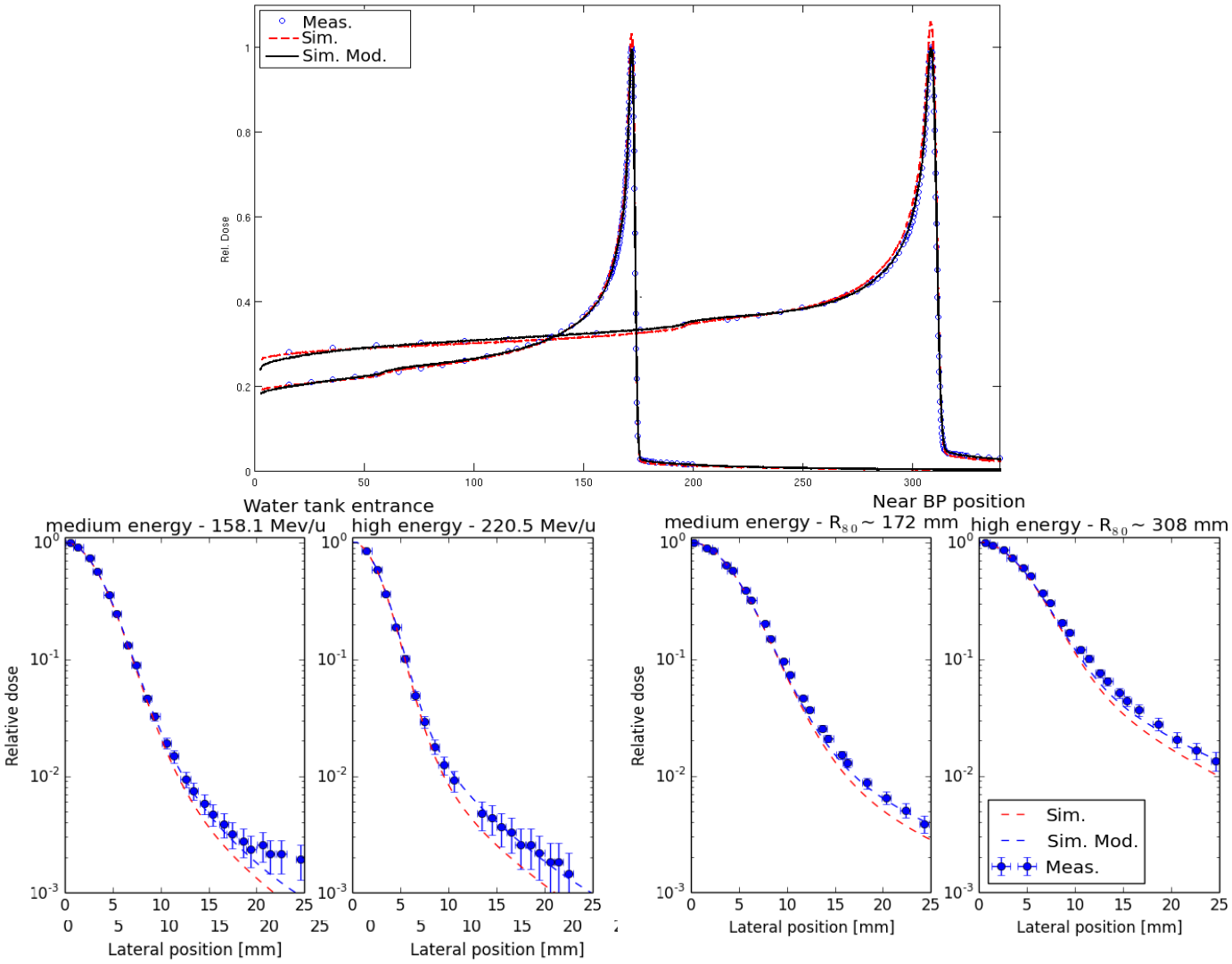

Figure B.5: Depth dose distributions (top) and lateral dose distributions at phantom entrance (bottom left panels) or near Bragg peak (bottom right panels) for the medium and high energy investigated. for the normal simulation ("Sim."), the modified simulation ("Sim. Mod."), and dosimetric measurements ("Meas.").

Comparison between FLUKA prediction and published physics experiment on ^{4}He attenuation

In order to understand the difference in dose and lateral dose distributions between simulations and dosimetric experiments, comparisons with published physics data acquired at HIT were performed. The energy telescope described in Krämer *et al* (2016) and in Rovituso *et al* (2017) was implemented into FLUKA. The detector configurations (energy telescope and composing materials) and the target (plastic flasks with their material composition) were reproduced with the same geometry described in details in Rovituso *et al* (2017). The scheme of the setup (top panel), the results for the 200MeV/u ^{4}He attenuation and the ^{3}He build up (middle panel), and build-up of H isotopes (bottom panel) are shown in figure B.6.

For each set-up configuration, with different thicknesses of water (0 to 25.7cm), 5×10^{7} particles were simulated in five independent runs. Phase space files were produced, recording information about the particles (e.g., type, energy, time of arrival from the center of the target) crossing the detector surface. After post-processing, the yield (number of particles per incoming ^{4}He) is displayed as a function of the target thickness in figure B.6.

As described in section 4.4, the attenuation and build-up of ^{4}He and ^{3}He, respectively, are consistent with experimental findings. Regarding the H isotopes, it seems that the FLUKA code is overestimating protons before 17cm and underestimating them afterwards, while overestimating tritons and deuterons. This finding could hint at a lack of large angles ^{1}H produced in the entrance, or lack of secondary production of ^{1}H from ^{3}H and ^{2}H at larger depth or a n underestimation of the H isotopes production at larger angles. However, the interpretation of these results is not straightforward, and needs more experimental data to bring a more conclusive understanding of the missing underlying physics processes within the FLUKA code.

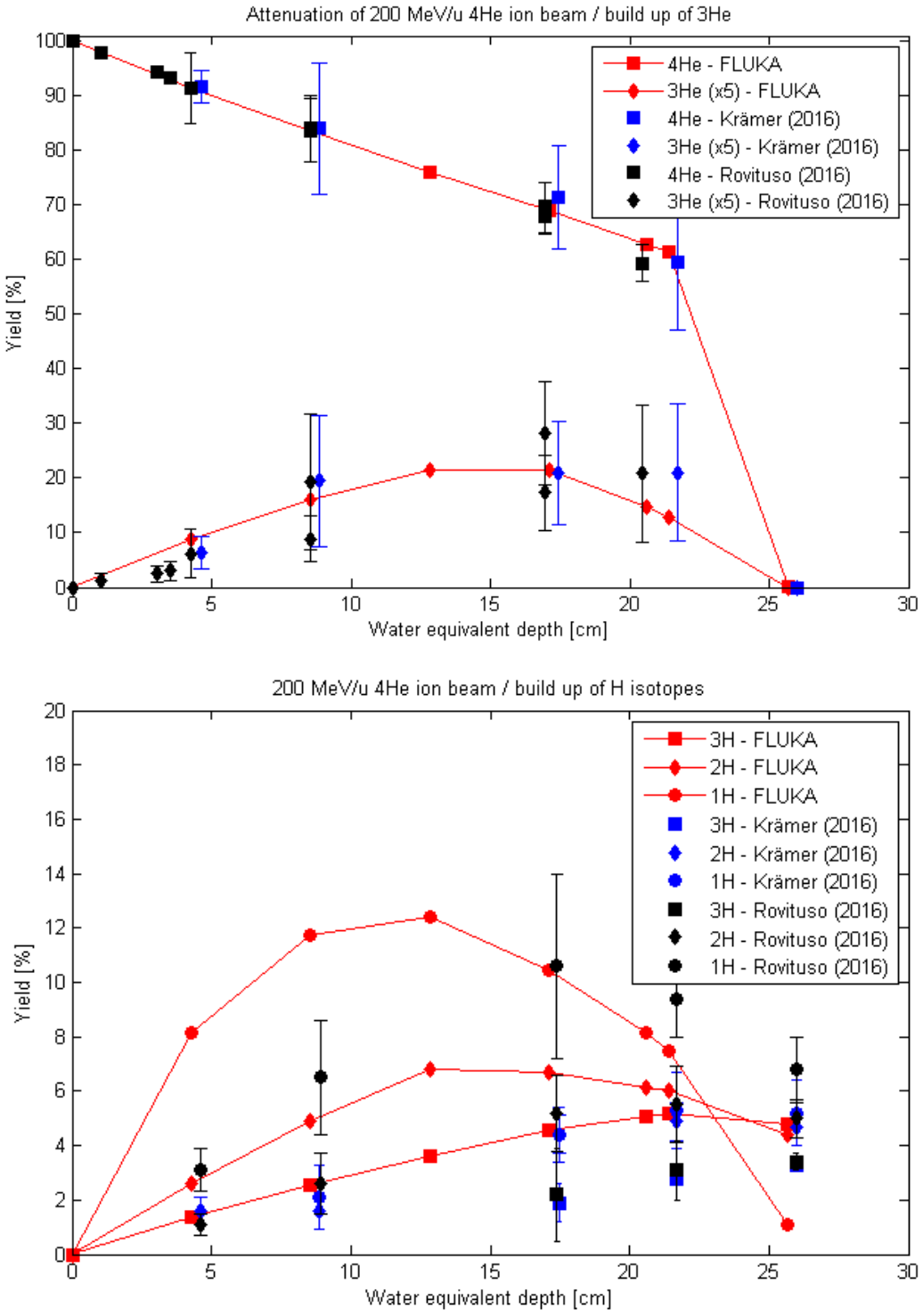

Figure B.6: Attenuation of 200MeV/u helium ions experiments: The experimental set-up is presented in Rovituso *et al* (2017). The results comparing measurements against FLUKA simulations reproducing the setup are plotted in the top (^{4}He attenuation and ^{3}He build up) and bottom panel (H isotopes). (Experimental data from Krämer *et al* (2016) and Rovituso *et al* (2017).

Comparison between FLUKA prediction and published physics experiment on ^{4}He and fragments angular distributions

For the same reason as the previously described study, comparisons with particle physics experiment on the angular distributions of 4He ions and their secondary particles were performed with FLUKA Monte Carlo code. The experiment described in Rovituso *et al* (2017) involved the irradiation of a target with a helium beam, with a range superior to the target size, and the collection of the escaping particles with a detector, at various angles (0 to 23°), in a similar fashion as in Haettner *et al* (2013). The detector is similar to the one used for the attenuation experiment previously described, only the geometry setup is changed as seen described in Rovituso *et al* (2017). The different geometry setups are reproduced in FLUKA. The two energies investigated are 120MeV/u and 200MeV/u, with water target thicknesses of 4.28 and 13.96cm, respectively. The targets are obtained using different combination of flasks and are modelled in FLUKA. For each angle/energy, 5×10^{7} particles were simulated in five independent runs.

It can be seen that for 120MeV/u the predicted surviving helium ions are in agreement with measurements, but present a smaller width than the measured distribution. All fragments at the 0° position are overestimated with FLUKA in comparison to the measurements. This could be explained considering that at this angle the dominant (by 2 orders of magnitude) proportion of ^{4}He compared to other particles could lead to shadowing of the fragments in the detection process. A measurement setup such as in Haettner *et al* (2013), stopping the primary beam inside the target, could overcome this potential measurement uncertainty. However, for larger angles (>4°), better agreement is found for both energies investigated. It can be mainly seen in the fragment distribution that for 120MeV/u, the secondary ^{2}H distribution is underestimated with FLUKA, as well as ^{1}H for the 200MeV/u. These underestimations could be an explanation for the disagreements found between dosimetric measurements and simulations (depth and lateral dose profiles). These measurements could be helpful in supporting FLUKA developments in the near future.

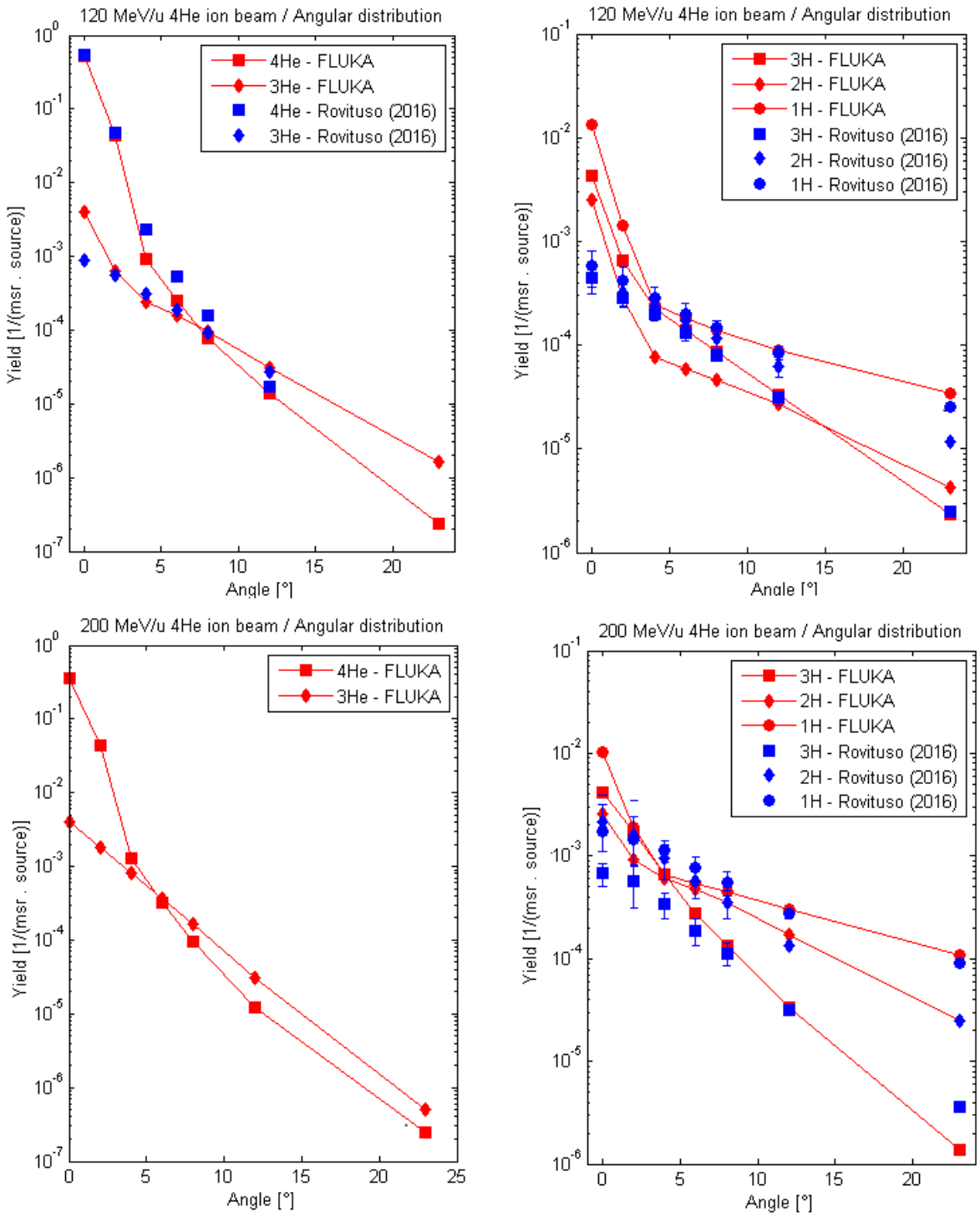

Figure B.7: Angular distributions of ^{4}He, ^{3}He (left panels) and ^{3}H, ^{2}H, ^{1}H (right panels) recorded at several angles after impinging on a water target (thickness 4.28 and 13.96 respectively) at an initial energy of 120 MeV/u (middle panels) or 200MeV/u (bottom panels), according to the experimental setup reported on the top panel (from Rovituso *et al* 2017). Results from FLUKA appear in red, results from experiments in Rovituso *et al* (2017) appear in blue.No data are displayed for ^{4}He, ^{3}He angular distribution at 200MeV/u.

C - Supplementary material to Chapter 6

Additional information regarding topics discusses in Chapters 6 is provided in Appendix C.

Monte Carlo Treatment Planning workflow

The general workflow of the Monte Carlo Treatment Planning tool (MCTP) used in Chapter 6, and then in Chapter 7, can be summarized as follows, as presented in figure C.1 (for patient cases):

1- Pre-optimization - Dose matrices creation

The initial steps aim to generate the dose matrices (physical or "biological") needed for the optimization with the MCTP. It can be divided in 3 sub-steps:

- Plan creation:

The plan creation corresponds to the generation of a set of pencil beams according to the position in depth of the target and its size.

In the case of the spread-out Bragg peaks (SOBP) targets presented in Chapter 6, knowing their positions, sizes, relation between energy and Bragg peak position from Chapter 3, a plan was created for each ion/SOBP depth to cover an area of 7 cm × 7 cm × 7 cm, in order to optimize afterwards either the 3 cm × 3 cm × 3 cm or the 6 cm × 6 cm × 6 cm SOBPs. The distance between two Bragg peaks in depth was kept the same for all ions, i.e., about ~2mm, for a lateral step size of 3mm, consistent with the focus size used (about 1/3 of the beam full-width at half-maximum at isocenter as recommended in Krämer et al 2000). The use of the ripple filter (RiFi) for heavy ions was foreseen, and thus the selected energies were adapted to compensate for the range reduction in the RiFi.

For the patient cases presented in Chapter 7, the initial plan from the clinical treatment planning system (TPS) was used. This plan was then extended with four additional energy slices (two inferiors and two superiors to the planned ones), and extended laterally in order to allow for higher freedom on pencil beam choices by the optimizer. The possibility of delivery with RiFi for helium ions was taken into account in the plan generation by introducing an offset in the selected energy index (corresponding to ~2 mm as seen in Chapter 3).

- ROI generation:

The optimization in the MCTP is not performed on the whole dose matrix but rather a region of interest (ROI). The ROI describes either the target (e.g. planning target volume (PTV) or the SOBP size and position) or normal tissues (e.g. organ at risk (OAR)). A ROI is defined in an in-house interface creating a file which delimitates a "box" around the ROI, including all voxels in the geometry. This "box" is characterized by its coordinates defining its position in the simulation geometry (position in water for the SOBP case, position in the patient geometry in case of clinical treatment plans, as presented in Chapter 7). Then, all voxels inside this "box" are characterized as part of the ROI or not.

- Input files generations and computation:

The MC FLUKA calculation is using the classical geometry presented in Chapter 5, with the detailed model of the beamline included in phase space files. For the SOBP target of Chapter 6, the geometry is assuming the water phantom as target, and for the patient cases of Chapter 7 the computed tomography (CT) is converted in FLUKA voxel geometry as described in Bauer et al 2014. The generated plan is divided according to the number of its energy slices, and an equal number of input files are created, each one linked to a particular energy slice.

For each ROI, an energy event scoring is selected for creation of a physical dose matrix. For biological scoring, using a selected biological model, an event scoring is created in a similar fashion and linked with a FLUKA routine to the model. For the model selected in this thesis (Mairani *et al* 2016b), an online calculation of the α and β terms of the linear quadratic model (cf. section 2.3 in Chapter 2) is performed, but other models and unique parameters can be linked as well. Event scoring implies that for a certain number N of primary histories, the (physical or biological) dose contribution to the ROI voxels will be known for every pencil beam. Hence, for each input file, hence for every energy slice, a dose matrix per ROI is created (together with the associated α and β matrices if needed), describing the contributions of each pencil beam to the ROI voxels. The number of primary histories was chosen at 10^5 for every case investigated. The resultant ROI matrices will be used for optimization in the MCTP.

- Matrix size:

Depending on the size of the ROIs for the targets considered in the planning process and the type of ion used, the matrix size can vary from about 50Mb for small targets with protons to 300Mb for the prostate case presented in Appendix D with helium ions. This huge memory requirement per energy slice represents one of the main limitations of the current approach with MCTP, e.g. when typically dealing with about 20 to 35 energy slices per beam. Further improvements can be foreseen by downsampling the voxel size, set in this study at 1 mm × 1 mm × 3 mm, to 2 mm × 2 mm × 3 mm, which is a value close to the voxel size used for dose calculation in clinical TPS. Another possibility would be, when working with patient cases, to improve the generation of the plan used for matrix creation. In the plan generator used in this study, the extreme lateral positions of the pencil beams, within an energy slice (maximum and minimum positions), were recorded and extended by 2 lateral step size. Subsequently, all pencil beams within these extreme values were allowed for matrices generation simulations (i.e., resulting in a large rectangular field for each energy slice). To improve this scenario, a new "smart" plan generator was created after the initial work presented in this thesis. Its process consists of the "dilation" of the initial plan for each energy slice, extending it by 2 lateral step sizes, but thus keeping a similar field morphology. For the prostate case, using such a method of "smart" plan creation could reduce the number of pencil beam by at least a factor 2. Associated to the voxel downsampling, it could bring the larger matrices to a reasonable size below 40Mb.

- Time:

The time needed to create the matrices is the second limitation of MCTPS. Depending on the energy, the number of pencil beams within one energy slice, and the selected number of primary histories for every pencil beam, the calculation time could rise to 4-5 days for the prostate case with helium ions (about 850 pencil beams for the largest energy slice, with 10000 primary history, for a deep seated target, with physical dose and biological matrices). With a reduction of the primary history and number of pencil beams, computational time could be reduced by a factor 4, then by splitting in two the energy slices with a high number of pencil beam, the largest matrices could be obtained within half a day with simulations running on a 100 nodes cluster. Despite such improvements in calculation performance, clinical implementation of MCTP remains a challenge.

2- MCTP optimization

- Optimization and constraints:

The optimization is performed according to Mairani *et al* (2013), using a dose-difference optimization algorithm, similar to the approach of Lomax (1999). Each voxel within the ROIs is given a dose constraint and corresponding weight. For the target, the constraint corresponds to the prescription dose, while for OAR the constraint corresponds to the maximum dose allowed. In addition to the planned dose constraint, a constraint on the maximum dose allowed of 107% of the planned dose was added to avoid hot spots within the target region. This constraint was not yet set for 6 cm × 6 cm × 6 cm SOBPs optimization, as could be seen in figure 6.6. The weights on the ROI are set to achieve the desired dose in the target while sparing the OAR. In the case of SOBP optimization, only the target was selected as the ROI. However, for the patient cases, PTV and OARs were selected as ROI. Dose constraints were set to respect dose volume histogram (DVH) objectives from the clinical TPS plan, as explained in Chapter 7. The calculation can be achieved either considering the physical dose only, or both biological doses, using physical and biological generated dose matrices.

A convergence criterion, which corresponds to the relative change brought to the plan (more specifically to the cost function) between two iterations, is set at 0.1%. When the optimizer reaches this point, result files are produced.

The optimizer work can be broke down into three steps per iteration:

  - Computing the steps: optimizing particle numbers per pencil beams
  - Computing the dose: calculating physical & biological dose
  - Computing the cost function to find the new cost values

- Additional constraints:

For the patient optimizations, in addition to the constraint on the maximum dose for the OAR, additional dose constraints were set to reduce the mean dose delivered to the OAR. The MCTP constraint for OAR is dealing only with maximum dose constraint in its current version. Consequently, to reduce the mean dose, a second maximum dose constraint needs to be added, for a dose level about 50% of the first maximum dose chosen, but with a lower weight. It allows reducing the overall dose received by the OAR, and thus reducing the OAR mean dose, by increasing the dose gradient around the target region.

- Results:

Once the convergence criterion is reached, the optimizer produces the new optimized plan. Other files are created such as 2D dose maps or DVH, allowing for quick checks on the optimization dose results. These results are only preliminary, based on the dose changes to the optimization matrixes with pencil beams weighting. Final calculations on the CT geometry are needed to obtain the dose predictions.

- Time:

The optimization with the above mentioned convergence setting and the matrices described previously is taking from below 1 minute, for simple plans with small targets and only physical dose optimization, to about 30 minutes for large plans with biological optimization, on a 12 GB RAM computer. This time could be reduced by reducing the matrix size as previously described and adding a dose threshold in the optimizer, where below a certain level of dose compared to the maximum delivered dose by a pencil, the matrix voxels are discarded for optimization.

3- Final dose calculation:

The final dose calculations are done in a similar way as in Chapter 5, using the phase space approach coupled with the newly obtained plans. For Chapter 6, the dose scoring was made in water phantom to be compared to measurements. In Chapter 7, dose (physical and biological) was computed in the patient voxelized geometry and then imported in the in-house framework for analysis (Bauer *et al* 2014). The number of primary histories was set to $5x10^7$ for patient cases and to $2x10^8$ for SOBPs final calculation.

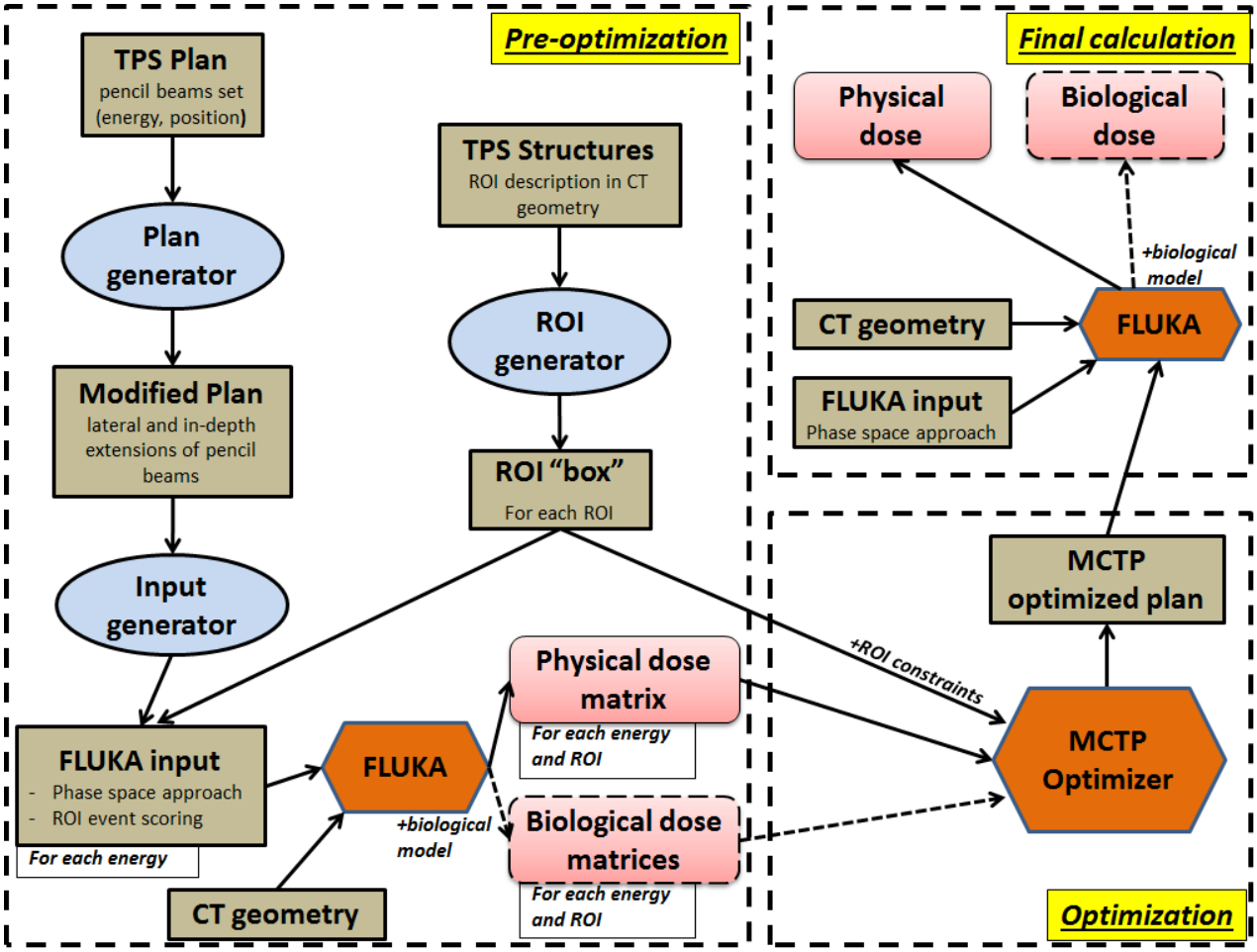

Figure C.1: Schema of the MCTP workflow for both physical (solid arrows) and biological (dashed arrows) optimization.

Forward calculation of SOBP from Chapter 3 for carbon ions

To investigate the difference in absolute deviation between measured and planned doses found in Chapter 3 and Chapter 6 for carbon ions, the dose calculation of the SOBP presented in Chapter 3 was performed with the MC code FLUKA. In Chapter 3, the difference in the SOBP region between measurements and planned dose (from analytical TPS) was about -1.8%, while in Chapter 6 the difference between measurements and planned dose (from MCTP) was found about +2.7%. Compared to the planned dose, the MC dose prediction in the high dose region, for the same SOBP presented in Chapter 3, shows deviations around -4.5%, and deviations to the measurements of about 3%. Figure C.2 shows that when correcting for the systematic offset of 3%, FLUKA predictions and measurements are well matching. This result is consistent with the findings of Chapter 6, pointing out the fact that the beam monitor calibration is tuned for the clinical and research analytical TPS.

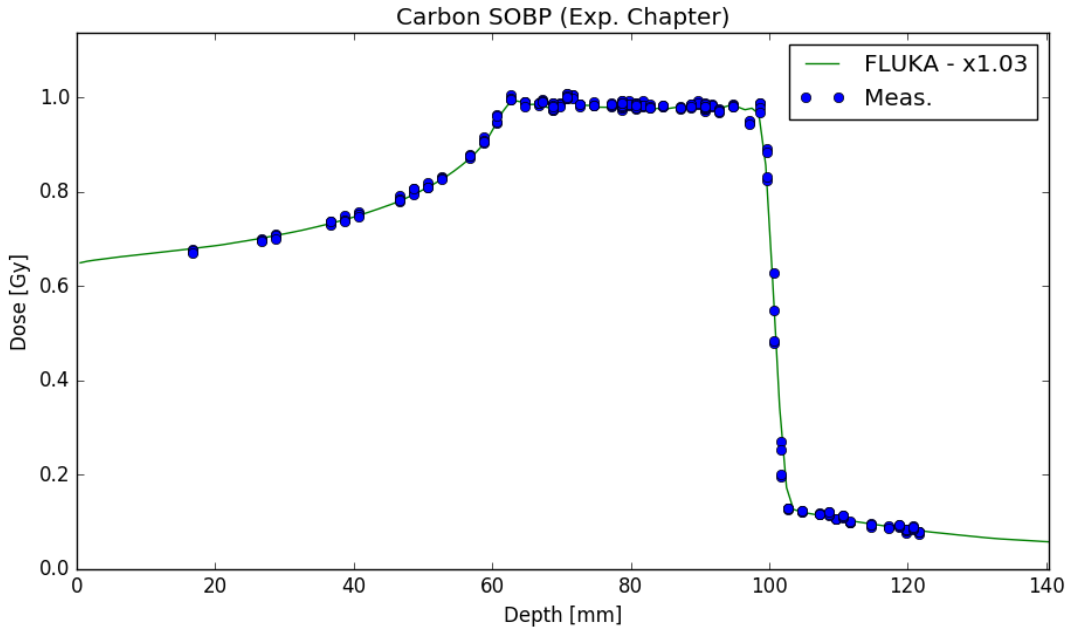

Figure C.2: Depth dose distribution of the Chapter 3 SOBP: Measurements are displayed with squares. The dose prediction from FLUKA multiplied by a factor 1.03 is represented by the solid line (green).

MCTP biological optimization and verifications

The MCTP system can be interfaced with experimentally validated biological models, such as phenomenological (Wedenberg *et al* 2013, Mairani et al. 2016a) or biophysical (Elsässer *et al* 2010, Inaniwa *et al* 2010) models. Thus, the MCTP tool can be used to calculate biologically optimized treatment plans. The model used in this thesis (Mairani *et al* 2016b, Mairani *et al* 2017a) is based on parametrizations of the RBE_{α} (= $\alpha_{ion}/\alpha_{photon}$) and R_{β} (= $\beta_{ion}/\beta_{photon}$), as a function of LET, with α and β being the parameters of the linear quadratic model (Chapter 2). The used RBE_{α} parametrization is based on a linear-exponential model for helium ions (Mairani *et al* 2016b) and a linear model for protons (Mairani *et al* 2017a) as a function of rescaled LET. Thus, online-computation of the dose-weighted average $\bar{\alpha}$ and $\bar{\beta}$ parameters with FLUKA can be achieved for every voxel *j* of the equation (2.15) in Chapter 2, with $\Delta d_{i,j}$, the dose from the *i*-th charged particles, associated to the corresponding $\alpha_{i,j}$ and $\beta_{i,j}$ obtained knowing their relation to $LET_{i,j}$ from the above-mentioned parametrization. Other models can also be linked by introducing their own biological database.

Using the data-driven biological model described in Mairani *et al* (2016a) and the experimentally validated MC engine fine-tuned to physical data in this thesis work, a 3.1 GyRBE helium ion SOBP was created for the investigations of Mairani *et al* (2016b) and then recalculated with an improved RBE model, as described in Mairani *et al* (2016b).

Prior to the cell irradiations performed in Mairani *et al* (2016b), pinpoint ionization chambers measurements in water were performed to verify the quality of the delivery. The agreement between measurements and FLUKA predictions was found within 2% for the whole dose distribution, and below 1% in the high dose region (figure C.3 bottom). The expected biological dose (figure C.3 bottom) calculated from the measured cells survival (figure C.3 top) is plotted against the predictions of the MC code FLUKA linked with both the previously mentioned models (Mairani *et al* 2016a and Mairani *et al* 2016b). For both models a good agreement within the uncertainties of the biological measurement was found.

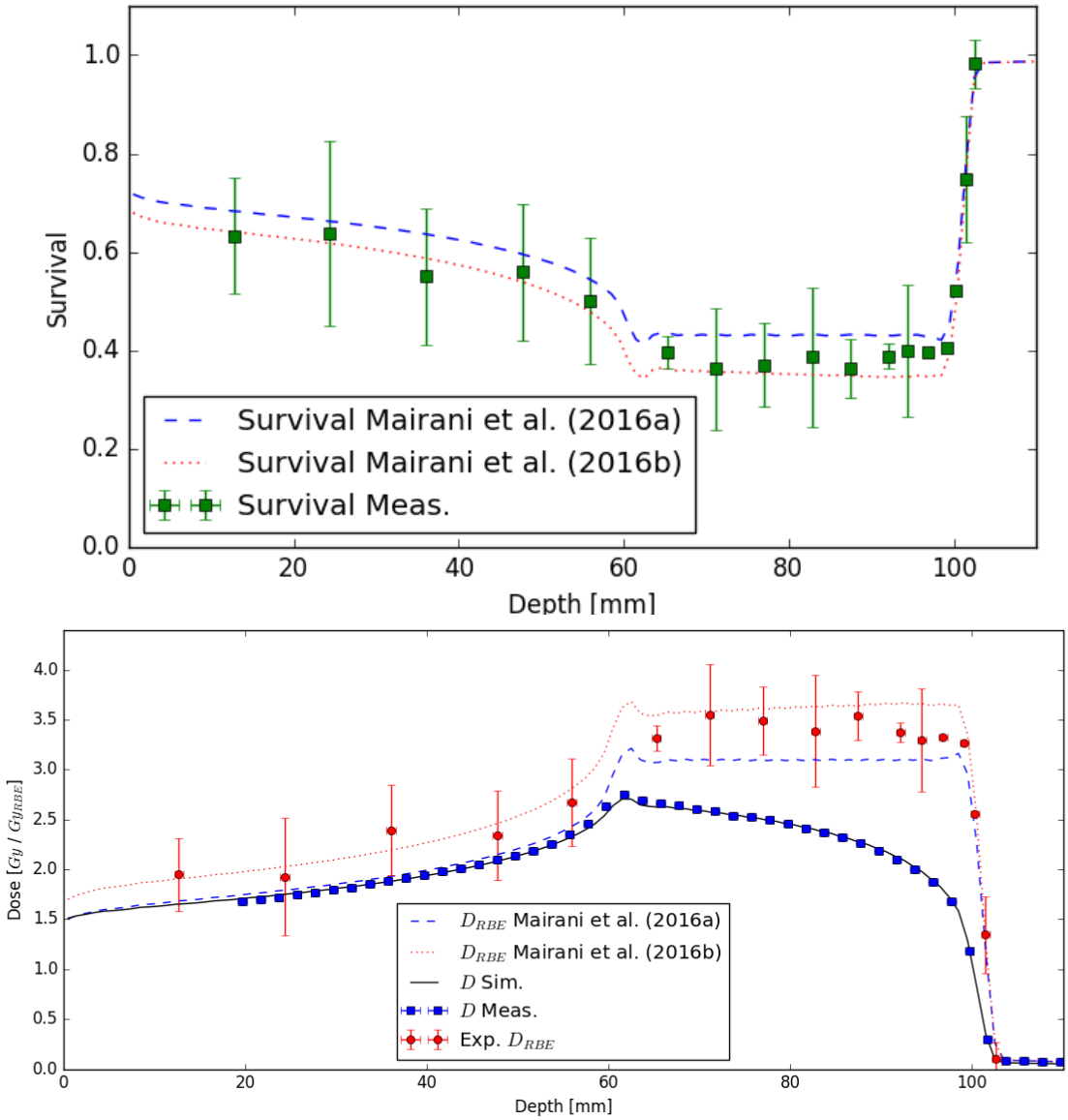

Figure C.3: *Top figure*: Cell survival as a function of depth into water. Cell survival prediction using the model described in Mairani *et al* (2016a) used for optimization is displayed in dashed lines, while in dotted line for the cell survival using the model from Mairani *et al* (2016b). Experimental cell survival is displayed with squares (adapted from Mairani *et al* (2016b)); *Bottom figure*: Depth dose distribution of a biologically optimized SOBP for helium ions. The physical dose is displayed in solid line. The biological dose appeared with dashed line for prediction using the model from Mairani *et al* (2016a) or with dotted lines for the model described in Mairani *et al* (2016b). Absorbed dose measurements are displayed as squares (blue) while the calculated biological dose extracted from experimental cell survival data with circles.

D- Supplementary material to Chapter 7

Additional information regarding topics discussed in Chapter 7 is provided in Appendix D.

Additional patient – a prostate patient case study

As in Chapter 7, this section presents the comparison between treatment plans of protons and helium ions for a prostate case. This patient was treated at the Heidelberg Ion Beam Therapy Center (HIT) with protons for a dose per fraction of 3.3 GyRBE for a total dose of 66GyRBE (with fixed RBE of 1.1), with two opposite beams as seen in table D.1 and figure D.1. Besides the PTV, the other regions of interests (ROI) are the rectum, the bladder and the femurs (left and right). The α_x/β_x ratio for the PTV is defined as 1.5 Gy and 3 Gy for the OAR, based on the rectum (late complication) from Fowler (2005). The selected α_x/β_x ratio for OAR is also within the range of α_x/β_x ratio presented in Fowler (2005) for bladder. The optimization dose matrices (physical and biological) were created for an irradiation of the patients without ripple filter for both ion species. This choice for helium ions is supported by the fact that prostate is a deep-seated organ, thus the effect of range straggling allows a peak wide enough to provide a good PTV coverage, without additional peak broadening, as performed in Chapter 6 for the deepest SOBP (~centered at 20cm). The generation of these matrices was performed following the same protocol presented in both Chapter 7 and Appendix C, for the PTV and the rectum, with FLUKA simulations using the phase approach of Chapter 5, with 10000 primary histories per pencil beam, a dose scoring coupled to a biological model (cf Appendix C) and for particle transport in the patient voxelized geometry (1x1x3 mm^3 voxel size). The optimization with MCTP was performed in a first step for protons (without variable RBE) with the dose constraints presented in table D.2, in order to reach comparable dose volume histograms (DVH) values as the ones of the clinical TPS. The DVH parameters values are presented in table D.2.

After defining these constraints, optimization was performed for both protons and helium ions using a variable RBE model. Using these final plans, including for protons both options with and without variable RBE model, final dose calculations were performed on a 1x1x3 mm^3 voxel grid for physical and biological dose matrices. The final calculations were performed using $50x10^6$ primary histories, in 50 independent runs.

		Dose constraint [GyRBE]	weight	Dose constraint [GyRBE]	weight
Patient E (H01949)	**PTV**	***3,3***	***14***	3,53	20
	Rectum	2,9	20	1,4	1

Table D.1: Patient proton plan characteristics from the clinical TPS for the considered prostate case. The information about the dose per fraction, number of fractions and beams are reported. It provides information on the angles between beams and the close by OAR used for optimization.

The comparison between the DVH parameters of the proton plans with fixed RBE, obtained from MCTP and TPS, is shown in table D.4. While a good agreement is found between the PTV coverage with difference below 1GyRBE, the MCTP plan does not provide the same sparing for the femoral heads, with higher delivered dose about 8-9 GyRBE. On the contrary, the rectum optimized with MCTP presents a dose lowered by about 6 to 13GyRBE in the D33-D22 DVH behavior. The bladder shows similar parameters for both MCTP and TPS plans. The reason behind the discrepancies in the dose to the femoral heads is ascribed to the optimization approach followed with the MCTP, in comparison to the TPS. Due to the large size of the optimization matrices (up to ~300Mb per energy slice), not enough RAM was available to combine several OAR in the optimizer. Thus, the critical OAR rectum was selected with priority. By reducing the matrices sizes as suggested in Appendix C, an optimization with all OAR could be possible, aiming to reproduce the TPS DVH results.

The FLUKA dose predictions for protons and helium ions using a variable RBE model are displayed in figure D.1 with the corresponding DVH in figure D.2. The difference, in GyRBE, of the DVH parameters between helium ions and protons with a fixed RBE are shown in table D.5, and in D.6 for helium ions against protons with a variable RBE.

	Planned dose / fraction [GyRBE]	Number of fractions	Number of beams	Angles between beams [°]	Critical organ at risks
Patient E (H01949)	3,3	20	2	180	*Rectum*
					Bladder
					Femur left
					Femur right

Table D.2: Optimal constraint parameters (per fraction) for PTV and OAR found with MCTP to reproduce similar values of the TPS proton DVH characteristics presented in table D.3.

		DVH analysis : H (RBE=1.1) TPS Plan							
		D5	D10	D20	D33	D50	D66	D75	D95
Patient E (H01949)	**PTV**	67,6	67,2	67,2	66,6	66,0	65,6	65,0	61,0
	Femur (L)	24,8	23,8	22,8	22,0	21,2	20,6	20,4	18,6
	Femur(R)	28,0	26,2	24,4	23,4	22,4	21,6	21,2	19,4
	Rectum	55,2	49,0	32,6	13,6	2,8	0,4	0,4	0,0
	Bladder	62,4	42,0	7,6	1,0	0,6	0,6	0,0	0,0

Table D.3: DVH parameters extracted from the TPS proton prostate plan. The dose volume parameters for each ROI, in GyRBE - D5, D10, D20, D33, D50, D66, D75 and D95 - are presented for a full plan delivery of 66GyRBE to the target. The MCTP optimization with protons at fixed RBE tries to reproduce these values.

		DVH analysis : H (MCTPS, RBE=1.1) - H (TPS, RBE=1.1)							
		D5	D10	D20	D33	D50	D66	D75	D95
Patient E (H01949)	**PTV**	0,6	0,4	0,0	0,0	0,0	0,4	0,4	0,0
	Femur (L)	9,0	9,6	9,6	9,6	9,6	9,4	9,2	9,4
	Femur(R)	7,4	7,8	7,8	6,8	6,2	5,6	5,0	0,6
	Rectum	-5,8	-11,0	-12,8	-6,2	-1,4	0,0	0,0	0,0
	Bladder	-0,4	1,2	1,4	0,0	0,0	0,0	0,0	0,0

Table D.4: Difference of DVH parameters for the ROIs of the prostate patient case, in GyRBE, between the MCTP optimized proton plan with fixed RBE and the TPS plan.

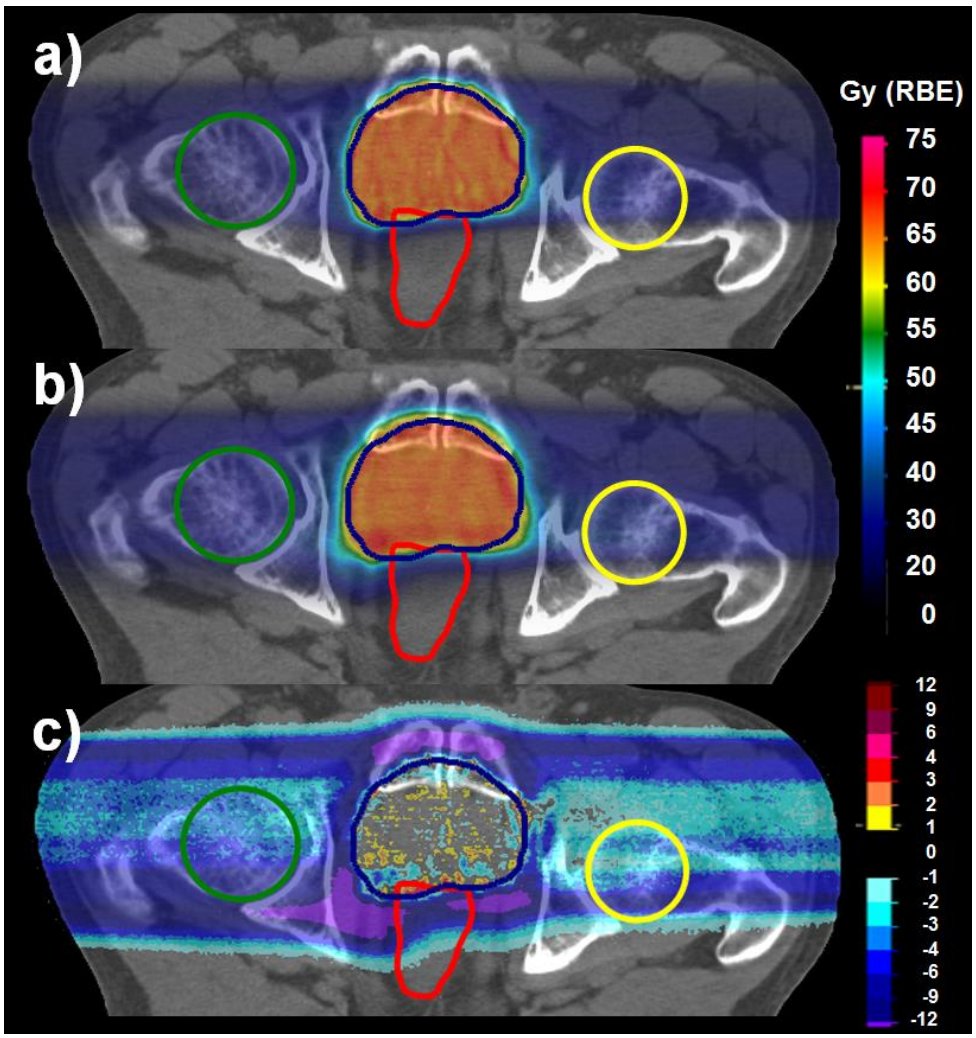

Figure D.1: Dose distributions superimposed onto the X-ray CT are shown for patient E, with helium ions on the top panel and protons in the middle panels for an axial slice, centered on the PTV. The bottom panels display the dose difference between the helium ions and proton dose predictions. (Displayed in *RayStation* (RaySearch Laboratories))

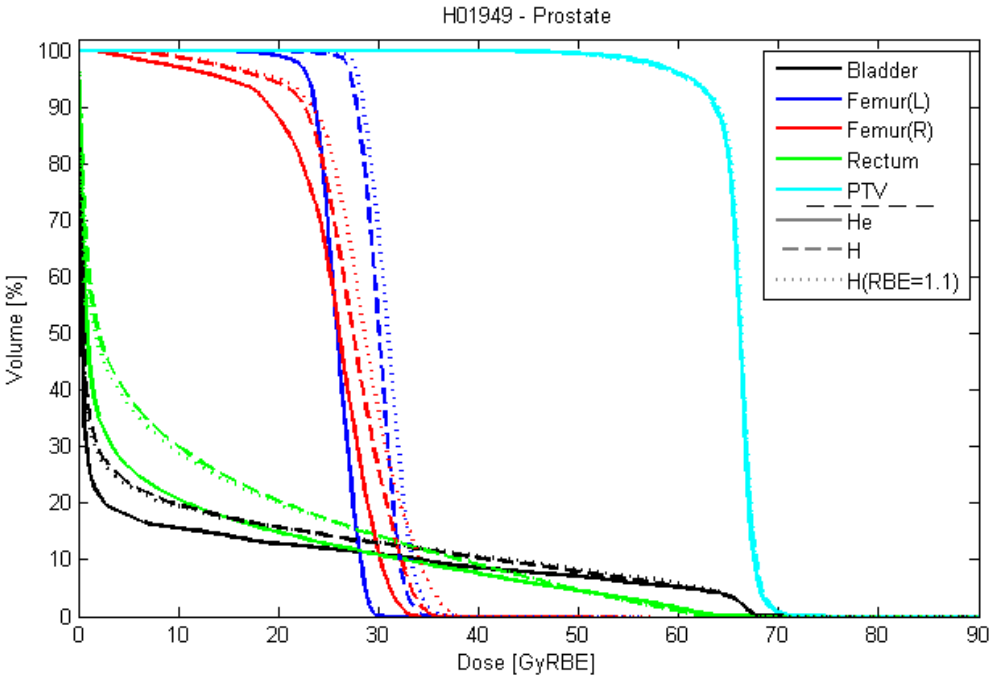

Figure D.2: DVH for the prostate patient case. The different ROIs investigated are displayed. Protons are shown for both fixed (dotted lines) and variable RBE (dashed lines). Helium ions are displayed with solid lines.

		DVH analysis : He (Prostate) - H (RBE=1.1)							
		D5	D10	D20	D33	D50	D66	D75	D95
Patient E (H01949)	**PTV**	0,2	0,2	0,0	0,0	0,2	-0,4	-0,4	0,2
	Femur (L)	-5,2	-5,2	-5,0	-4,8	-5,0	-4,8	-4,8	-5,0
	Femur(R)	-4,4	-4,0	-3,4	-2,6	-2,6	-2,6	-3,0	-5,4
	Rectum	-1,2	-5,4	-8,8	-4,8	-0,4	0,2	0,2	0,0
	Bladder	-1,4	-9,0	-6,2	-0,4	0,0	0,0	0,0	0,0

Table D.5: Difference of DVH parameters for the ROIs of the prostate patient case, in GyRBE, between the MCTP optimized helium ion plans and proton plans with fixed RBE.

		DVH analysis : He (Prostate) - H (Prostate)							
		D5	D10	D20	D33	D50	D66	D75	D95
Patient E (H01949)	**PTV**	0,2	0,2	0,2	0,0	0,2	0,2	-0,4	0,6
	Femur (L)	-4,2	-4,0	-4,0	-4,2	-4,4	-4,2	-4,0	-4,2
	Femur(R)	-2,4	-2,2	-2,2	-1,6	-1,4	-1,4	-1,6	-4,2
	Rectum	-0,8	-5,4	-9,8	-5,4	-1,0	0,2	0,2	0,0
	Bladder	0,2	-7,4	-6,6	-1,0	0,0	0,0	0,0	0,0

Table D.6: Difference of DVH parameters for the ROIs of the prostate patient case, in GyRBE, between the MCTP optimized helium ion plans and proton plans with variable RBE model.

It can be observed in figure D.2 that the proton plans (with or without RBE) provide the same dose results (within 1GyRBE). This is due to the high dose per fraction (3.3GyRBE), leading to a high physical dose. At a level of 3Gy physical dose the variation of RBE at the same LET level are reduced, as seen in figure 7.11, with values close to 1.1.

Helium ions compared to protons either with fixed or variable RBE present lower dose on all OARs up to 9GyRBE for the $D10_{bladder}$ of protons with fixed RBE and up to 9.8GyRBE for $D20_{rectum}$. The coverage of the PTV is similar in both comparisons with difference below 1GyRBE. Due to the higher LET, helium ions benefit from an increased therapeutic benefit in the tumor compared to the OARs. Associated to the physical advantages as such large penetration depth (in terms of reduced range and lateral straggling), helium ions allow better OAR and normal tissues dose sparing.

In addition, it can be observed that despite a delivery without RiFi, the PTV coverage and homogeneity with helium ions is similar to that of protons, indicating that such treatment could be performed without RiFi. This result was expected knowing that at such large depth (larger than 15cm), due to range straggling effect, the Bragg peak width for helium ions without RiFi is about the same than for carbon ions with RiFi, as seen in Chapter 3, figure 3.3.

Bibliography

Agostinelli S et al., 2003. G4-a simulation toolkit. Nuclear Instruments and Methods in Physics Research Section A: Accelerators, Spectrometers, Detectors and Associated Equipment , 506(3):250-303

Ahlen SP, 1980. Theoretical and experimental aspects of the energy loss of relativistic heavily ionizing particles. Rev. Mod. Phys., 52(1):121-173.

Allison J et al., 2006. Geant4 developments and applications. Nuclear Science, IEEE transactions on, 53(1):270 -278.

Andreo P, Wulff J, Burns DT, Palmans H, 2013. Consistency in reference radiotherapy dosimetry: resolution of an apparent conundrum when 60Co is the reference quality for charged-particle and photon beams, Phys Med Biol 58, 6593–6621. doi:10.1088/0031-9155/58/19/6593

Austin-Seymour M, Munzenrider J, Linggood R, Goitein M, Verhey L, Urie M et al., 1990.Fractionated proton radiation therapy of cranial and intracranial tumors. Am J Clin Oncol;13:327-30.

Barkas WH & Evans DA, 1963. Nuclear research emulsions. Academic Press New York.

Battistoni G, Bauer J, Böhlen T T, Cerutti F, Chin MPW, Dos Santos Augusto R, Ferrari A, Ortega G, Kozlowska W, Magro G, Mairani A, Parodi K, Sala P R, Schoofs P Tessonnier. T, Vlachoudis V, 2016. The FLUKA Code: An Accurate Simulation Tool for Particle Therapy, Front Oncol. doi: 10.3389/fonc.2016.00116

Bauer J, Unholtz D, Sommerer F, Kurz C, Haberer T, Herfarth K, et al, 2013a. Implementation and first clinical experience of offline PET/CT-based verification of scanned carbon ion treatment at the heidelberg ion beam therapy centre. Radiother. Oncol. 107 218–26. doi: 10.1016/j.radonc.2013.02.018

Bauer J, Unholtz D, Kurz C, Parodi K, 2013b. An experimental approach to improve the Monte Carlo modelling of offline PET/CT-imaging of positron emitters induced by scanned proton beams. Phys. Med. Biol. 58 5193–213. doi: 10.1088/0031-9155/58/15/5193

Bauer J, Sommerer F, Mairani A, Unholtz D, Farook R, Handrack J, Tessonnier T, et al, 2014. Integration and evaluation of automated Monte Carlo simulations in the clinical practice of scanned proton and carbon ion beam therapy. Phys. Med. Biol. 59 4635. doi:10.1088/0031-9155/59/16/4635

Bellinzona V E, Ciocca M, Embriaco A, Fontana A, Mairani A, Mori M, Parodi K, 2015. On the parametrization of lateral dose profiles in proton radiation therapy, Physica Medica , 31. doi:10.1016/j.ejmp.2015.05.004

Bethe HA, 1930. Zur Theorie des Durchgangs schneller Korpuskularstrahlen durch Materie. Ann. Phys., 397:325-400.

Bichsel H, Hiraoka T, Omata K, 2000. Aspects of fast-ion dosimetry. Radiat. Res., 153(2):208-219.

Bloch F, 1933. Bremsverm□gen von Atomen mit mehreren Elektronen. Z. Phys. A-Hadron. Nucl., 81:363-376.

Boag JW, 1975.The time scale in radiobiology. 12th Failla memorial lecture. In : Nygaard, Alder, Sinclair : Radiation research Proceedings of the 5th international congress of Radiation Research, New York : Academic Press, 9-29

Böhlen TT, Cerutti F, Chin MPW, Fassò A, Ferrari A, Ortega PG, Mairani A, Sala PR, Smirnov G, Vlachoudis V, 2014. The FLUKA Code: Developments and Challenges for High Energy and Medical Applications, Nuclear data sheets, 120. doi:10.1016/j.nds.2014.07.049

Böhlen TT, Bauer J, Dosanjh M, Ferrari A, Haberer T, Parodi K, Patera V, Mairani A, 2013. A Monte Carlo-based treatment-planning tool for ion beam therapy, J Radiat Res 54. doi: 10.1093/jrr/rrt050

Bohr N, 1913. On the Constitution of Atoms and Molecules. Phil. Mag., 26.

Bortfeld T, Bürkelbach J, Boesecke R, Schlegel W, 1990. Methods of image reconstruction from projections applied to conformation radiotherapy. Phys Med Biol 35: 1423–1434

Bortfeld T, 1997. An analytical approximation of the Bragg curve for therapeutic proton beams. Medical Physics 24(12):2024–33.

Bragg, W. and Kleeman, R. (1905). On the alpha particles of radium and their loss of range inpassing through various atoms and molecules. Philos. Mag.

Brahme A, 1988. Optimization of stationary and moving beam radiation therapy techniques. Radiother Oncol.12(2):129-40.

Brun R and Rademakers F, 1997. ROOT – an object oriented data analysis framework, Nucl. Instrum. Methods. Phys Res A. doi:10.1016/S0168-9002(97)00048-X

Burigo L, Pshenichnov I, Mishustin I, Bleicher M, 2015. Comparative study of dose distributions and cell survival fractions for 1H, 4He, 12C and 16O beams using Geant4 and Microdosimetric Kinetic model, Phys Med Biol, 60(8): 3313–3331. doi:10.1088/0031-9155/60/8/3313

Carabe A, Moteabbed M, Depauw N, Schuemann J, Paganetti H. Range uncertainty in proton therapy due to variable biological effectiveness. Physics in Medicine and Biology. 2012;57(5):1159-1172.

Castro JR, Quivey JM, Lyman JT, Chen GT, Phillips TL, Tobias CA, Alpen EL,1980. Current status of clinical particle radiotherapy at lawrence berkeley laboratory. Cancer 46.

Castro, J. R., Petti, P. L., Blakely, E. A. & Linstadt, D. E. Particle radiation therapy. Tech. Rep. LBL-36229, PA:W.B. Saunders Company (1994).

Cavinato M, Fabrici E, Gadioli E, Erba EG, Risi E, 1998. Boltzmann master equation theory of angular distributions in heavy-ion reactions, Nucl Phys A, 643(1):15–29. doi:10.1016/S0375-9474(98)00545-4

Char DH, Kroll SM and Castro J, 1998. Ten-year follow-up of helium ion therapy for uveal melanoma. Am. J. Ophthalmol 125.

Chen W, Bauer J, Kurz C, Tessonnier T, Handrack J, Haberer T, Debus J, Parodi K, 2017. A dedicated software application for treatment verification with off-line PET/CT imaging at the Heidelberg Ion Beam Therapy Center. J Phys: Conf. Ser., 777 012021

Combs S, Jäkel O, Haberer T, Debus J, 2010a. Particle therapy at the Heidelberg Ion Therapy Center (HIT) – Integrated research-driven university-hospital-based radiation oncology service in Heidelberg, Germany, Radiotherapy and Oncology, 95 41–44. doi:10.1016/j.radonc.2010.02.016

Combs SE, Hartmann C, Nikoghosyan A, Jakel O, Karger CP, Haberer T et al., 2010b. Carbon ion radiation therapy for high-risk meningiomas. Radiother Oncol;95:54-9.

D'Avila Nunes M, 2015. Protontherapy Versus Carbon Ion Therapy. Springer.

Dale E and Olsen DR, 1997. Specification of the dose to organs at risk in external beam radiotherapy, Acta Oncologica 36.

Dementyev AV and Sobolevsky NM, 1999. SHIELD - universal Monte Carlo hadron transport code: scope and applications. Radiat. Meas., 30(5):553 557.

Dobbs HJ, Parker RP, Hodson NJ, Hobday P, Husband JE, 1983. The use of CT in radiotherapy treatment planning. Radiother Oncol. 1983 Nov;1(2):133-41.

Dokic I, Mairani A, Niklas M, Zimmermann F, Chaudhri N, Krunic D, Tessonnier T, Ferrari A, Parodi K, Jäkel O, Debus J, Haberer T, Abdollahi A, 2016. Next generation multi-scale biophysical characterization of high precision cancer particle radiotherapy using clinical proton, helium-, carbon- and oxygen ion beams, Oncotarget. doi : 10.18632/oncotarget.10996

Dudouet J et al. 2014. Double-differential fragmentation cross-section measurements of 95 MeV/nucleon 12C beams on thin targets for hadron therapy, Phys. Rev. C 88, 024606

Durante M and Löffler JS, 2010. Charged particles in radiation oncology. Nat. Rev. Clin. Oncol. 7

Elsässer T, Weyrather W K, Friedrich T, Durante M, Iancu G, Krämer M, Kragl G, Brons S, Winter M, Weber KJ, Scholz M, 2010. Quantification of the relative biological effectiveness for ion beam radiotherapy: Direct experimental comparison of proton and carbon ion beams and a a novel approach for treatment planning, Int. J. Radiat. Oncol. 78(4), 1183.

Fano U, 1963. Penetration of protons, alpha particles and mesons. National Bureau of Standards

.

Ferrari A, Sala P, Fassò A, Ranft J. New Developments in FLUKA Modelling Hadronic and EM Interactions. Tsukuba: KEK (1997). p. 32–43.

Ferrari A, Sala PR. The physics of high energy reactions. In: Gandini A,Reffo G, editors. Proc Workshop on Nuclear Reaction Data and Nuclear ReactorsPhysics, Design and Safety. Miramare-Trieste, Italy: World Scientific (1998). 424 p. Available

Ferrari A, Sala PR, Fassò A,Ranft J, 2005. FLUKA: a multi-particle transport code, CERN-2005-10 (2005), INFN/TC_05/11, SLAC-R-773

Fowler, J. F., 1989, "The linear-quadratic formula and progressin fractionated radiotherapy," Br. J. Radiol. 62, 679–694.

Fowler JF, 2005. The radiobiology of prostate cancer including new aspects of fractionated radiotherapy. Acta Oncologica, 44:3.

Fredriksson A, 2013. Robust optimization of radiation therapyaccounting for geometric uncertainty. PhD thesis, Royal Institute of Technology, Stockholm, Sweden.

Frey K, Unholtz D, Bauer J, Debus J, Min CH, Bortfeld T, Paganetti H, Parodi K, 2014. Most-likely-shift method for an automated range analysis with uncertainty evaluation in PET-based in-vivo treatment verication. Phys. Med. Biol.

Fuchs H, Alber M, Schreiner T, Georg D, 2015. Implementation of spot scanning dose optimization and dose calculation for helium ions in Hyperion, Med. Phys. 42, 5157. doi:10.1118/1.4927789

Furusawa Y, Fukutsu K, Aoki M, Itsukaichi H, Eguchi-Kasai K, Ohara H, Yatagai F, Kanai T, Ando K, 2000. Inactivation of Aerobic and Hypoxic Cells from Three Different Cell Lines by Accelerated 3He-, 12C- and 20Ne-Ion Beams, Radiation Research, 154.

James F and Roos M, 1975. Minuit: A System for Function Minimization and Analysis of the Parameter Errors and Correlations, Comput Phys Commun 10,343-367. doi:10.1016/0010-4655(75)90039-9

Giovannini G, Böhlen T T, Cabal G, Bauer J, Tessonnier T, Frey K, Debus J, Mairani A , Parodi K, 2016. Variable RBE in proton therapy: comparison of model predictions and their influence on clinical-like scenarios, Radiation Oncology 11(1).

Grün R, Friedrich T, Krämer M, Zink K, Durante M, Egenhart-Cabillic R, Scholz M, 2015. Assessment of potential advantages of relevant ions for particle therapy: A model based study, Med Phys 42. doi:10.1118/1.4905374

Goldhaber AS and Heckman HH, 1978. High Energy Interactions of Nuclei. Annu. Rev. Nucl. Part. Sci., 28:161-205.

Goodhead, D. T. (1994). Initial events in the cellular effects of ionizing radiations: clustered damage in DNA. Int. J. Radiat. Biol., 65(1):7-17.

Goodhead D, 2006. Energy deposition stochastics and track structure: what about the target?; Radiat. Prot. Dosim. 122 3-15

Gottschalk B, Koehler AM, Schneider RJ, Sisterson JM,Wagner MS, 1993. Multiple Coulomb scattering of 160 MeV protons, Nucl. Instrum. Methods Phys. Res. B 74, 467–490.

Gottschalk B, Cascio E W, Daartz J, Wagner M S, 2015. On the nuclear halo of a proton pencil beam stopping in water, Phys. Med. Biol., 60. doi:10.1088/0031-9155/60/14/5627

Grassberger C, Lomax A, Paganetti H, 2015. Characterizing a proton beam scanning system for Monte Carlo dose calculation in patients, Phys. Med. Biol., 60. doi:10.1088/0031-9155/60/2/633

Gudowska I, Sobolevsky N, Andreo P, Belkic D, Brahme A, 2004. Ion beam transport in tissue-like media using the Monte Carlo code SHIELD-HIT. Physics in Medicine and Biology, 49(10):1933.

Gudjonsson O, Blomquist E, Nyberg G, Pellettieri L, Montelius A, Grusell E et al., 1999. Stereotactic irradiation of skull base meningiomas with high energy protons. Acta Neurochir; 141:933-40.

Grün R, Friedrich T, Krämer M, Zink K, Durante M, Egenhart-Cabillic R, Scholz M, 2015. Assessment of potential advantages of relevant ions for particle therapy: A model based study, Med. Phys 42. doi:10.1118/1.4905374

Haberer T, Becher W, Schardt D, Kraft G, 1993. Magnetic scanning system for heavy ion therapy, Nucl. Instrum. Methods. Phys. Res. A , 330 . doi:10.1016/0168-9002(93)91335-K

Haberer T, Debus J, Jäkel O, Schulz-Ertner D, Weber U, 2004. The Heidelberg ion therapy center, Radiotherapy and Oncology, 73, 186-190. doi: 10.1016/S0167-8140(04)80046-X

Hall EJ and Giaccia A, 2012. Radiobiology for the Radiologist. Lippincott Williams & Wilkins,Philadelphia, USA, 7th edition.

Haettner E, Iwase H, Krämer M, Schardt D, 2013. Experimental study of nuclear fragmentation of 200 and 400 MeV/u 12C ions in water for applications in particle therapy, Phys. Med. Biol., 58. http://dx.doi.org/10.1088/0031-9155/58/23/8265

Handrack J, 2016. Sensitivity of post-treatment PET/CT imaging to interfractional variations in ion therapy Master Thesis. University of Heidelberg, Heidelberg, Germany, 2016.

Held K D, Kawamura H, Kaminuma T, Paz A E S, Yoshida Y, Liu Q, Willers H, Takahashi A, 2016. Effects of Charged Particles on Human Tumor Cells, Front. Oncol.. http://dx.doi.org/10.3389/fonc.2016.00023

Highland, V. (1975). Some practical remarks on multiple scattering. Nucl. Instrum. Methods, 129(2):497-499.

Highland V., 1979, Erratum, Nucl. Instrum. Methods Phys. Res. 161, 171.

Hueso-Gonzalez F, Golnik C, Berthel M, Dreyer A, Enghardt W, Fiedler F,etal. 2014. Test of Compton camera components for prompt gamma imaging at the ELBE bremsstrahlung beam. J Instrum 9:05002. doi:10.1088/1748-0221/9/05/P05002

Hüfner J, 1985, Heavy fragments produced in proton nucleus and nucleus-nucleus collisions at relativistic energies, Phys. Rep. 125, 129–185.

Hughes et al , 1997. MCNPXTM - The LAHETTM/MCNPTM code merger. Proc. 3rd Workshop on Simulating Accelerator Radiation Environments (SARE 3) (Tsukuba, Japan, 7-9 May): KEK Proceedings.

Hünemohr N, Paganetti H, Greilich S, Jäkel O, Seco J, 2014. Tissue decomposition from dual energy CT data for MC based dose calculation in particle therapy. Medical physics, 41(6):061714. ISSN 0094-2405. doi: 10.1118/1.4875976.

org/content/aapm/journal/medphys/41/6/10.1118/1.4875976.

ICRU, 1993. Quantities and Units in Radiation Protection Dosimetry. ICRU Report N. 51.

ICRU, 1994. Stopping Powers and Ranges for Protons and Alpha Particles. ICRU Report N.49.

ICRU, 2007. Prescribing, Recording and Reporting Proton-Beam Therapy, ICRU Report N.78.

ICRU, 2009. Errata and Addenda for ICRU Report 73, Stopping of Ions Heavier than Helium.

Inaniwa T, Kanemastu N, Furukawa T, Fukahori M, Nakao M, Shirai T, 2014. Implementation of a triple Gaussian beam model with subdivision and redefinition against density heterogeneities in treatment planning for scanned carbon-ion radiotherapy, Phys. Med. Biol., 59. doi:10.1088/0031-9155/59/18/5361

Inaniwa T, Furukawa T, Kase Y, Matsufuji N, Toshito T, Matsumoto Y, Furusawa Y, Noda K, 2010. Treatment planning for a scanned carbon beam with a modified microdosimetric kinetic model, Phys. Med. Biol. 55(22), 6721. http://dx.doi.org/10.1088/0031-9155/55/22/008

Iwata et al. 2013. Superconducting Gantry and other developments at HIMAC. Proceedings od PAC2013, Pasadena, CA USA.

Jermann M, 2015. Particle therapy statistics in 2014. International Journal of Particle Therapy 2.

Jia x, Schumann J, Paganetti H, Jiang SB, 2012. GPU-based fast Monte Carlo dose calculation for proton therapy. Phys Med Biol. ;57(23):7783-97.

Jongen et al. 2010. BAJINR 400 MeV/u superconducting cyclotron for hadron therapy, Proceedings of 19th Int. Conf. on Cycl. and Their Appl., Lanzhou, China

Kaplan ID, Castro JR, Phillips TL, 1994. Helium charged particle radiotherapy for meningioma: Experience at UCLBL. Int.J.Radiat.Oncol Biol.Phys. 28: 257-261

Kantemiris I, Karaiskos P, Papagiannis P, Angelopoulos A, 2011. Dose and dose averaged LET comparison of 1H, 4He, 6Li, 8Be, 10B, 12C, 14N, and 16O ion beams forming a spread-out Bragg peak, Med. Phys. 38, 6585. doi:10.1118/1.3662911

Karger C P, Jäkel O, Palmans H, Kanai T, 2010. Dosimetry for ion beam radiotherapy, Phys. Med. Biol., 55. doi:10.1088/0031-9155/55/21/R01

Karger CP, Peschke P, Sanchez-Brandelik R, Scholz M, Debus J, 2006. Radiation tolerance of the rat spinal cord after 6 and 18 fractions of photons and carbon ions: Experimental results and clinical implications," Int. J. Radiat. Oncol., Biol., Phys. 66, 1488–1497.

Karger C P, Jäkel O, Hartmann G H, Heeg P, 1999. A system for three-dimensional dosimetric verification of treatment plans in intensity-modulated radiotherapy with heavy ions, Med. Phys., 26. doi:10.1118/1.598728

Kelleter L, Wronska A, Besuglow J, Konefal A, Laihem K, Leidner J, Magiera A, Parodi K, Rusiecka K, Stahl A, Tessonnier T, 2017. Spectroscopic study of prompt-gamma emission for range verification in proton therapy. Physica Medica.

Kempe J, Gudowska I, Brahme A, 2007. Depth absorbed dose and LET distributions of therapeutic H1, He4, Li7, and C12 beams, Med Phys 34, 183. doi:10.1118/1.2400621

Knäusl B, Fuchs H, Dieckmann K, Georg D, 2016. Can particle beam therapy be improved using helium ions? – a planning study focusing on pediatric patients, Acta Oncologica 55. doi:10.3109/0284186X.2015.1125016

Kraft G, 2000. Tumor therapy with heavy charged particles,Prog. Part. Nucl. Phys. 45, S473–S544.

Kramer M and Scholz M, 2000. Treatment planning for heavy-ion radiotherapy: calculation and optimization of biologically effective dose, Phys. Med. Biol., 45. http://dx.doi.org/10.1088/0031-9155/45/11/314

Krämer M, 2009. Swift ions in radiotherapy – Treatment planning with TRiP98. Nuclear Instruments and Methods in Physics Research Section B: Beam Interactions with Materials and Atoms, 267(6):989–992. ISSN 0168583X. doi: 10.1016/j.nimb.2009.02.015.

Kramer M, Jäkel O, Haberer T, Kraft G, Schardt D, Weber U, 2000. Treatment planning for heavy-ion radiotherapy: physical beam model and dose optimization, Phys. Med. Biol., 45. http://dx.doi.org/10.1088/0031-9155/45/11/313

Krämer M, Scifoni E, Schuy C, Rovituso M, Tinganelli W, Maier A, Kaderka R, Kraft-Weyrather W, Brons S,Tessonnier T, Parodi K, Durante M, 2016. Helium ions for radiotherapy ? Physical and biological verifications of a novel treatment modality, Med Phys. Apr;43(4):1995. doi:10.1118/1.4944593

Kraan AC, 2015. Range Verification Methods in Particle Therapy: Underlying Physics and Monte Carlo Modeling. Front Oncol;5:150

Kumazaki, Y, Akagi T, Yanou T, Suga D, Hishikawa Y, Teshima T, 2007. Determination of the mean excitation energy of water from proton beam ranges,Radiat. Meas. 42,1683–1691.

Kurz C, Mairani A, Parodi K, 2012. First experimental-based characterization of oxygen ion beam depth dose distributions at the Heidelberg Ion-Beam Therapy Center, Phys Med Biol., 57(15):5017-34. doi:10.1088/0031-9155/57/15/5017

Landry G, Reniers B, Granton PV, van Rooijen B, Beaulieu L, Wildberger JE, Verhaegen F, 2011. Extracting atomic numbers and electron densities from a dual source dual energy CT scanner: experiments and a simulation model. Radiother Oncol.

Landry G, Nijhuis R, Dedes G, Handrack J, Thieke C, Janssens G, Orbain de Xivry J, Reiner, M, Kamp F, Wilkens JJ, Paganelli C, Riboldi M, Baroni G, Ganswindt U, Belka C, Parodi K, 2015. Investigating CT to CBCT image registration for head and neck proton therapy as a tool for daily dose recalculation. Med. Phys. 42 (3),

Lawrence J H, Tobias C A, Born J L, Linfoot J A, Kling R P, Gottschalk A, 1964. Alpha and Proton Heavy Particles and the Bragg Peak in Therapy. Transactions of the American Clinical and Climatological Association, 75, 111–116. PMCID: PMC2279335

Levin WP, Kooy H, Loeffler JS, DeLaney TF, 2005. Proton beam therapy. Br J Cancer. 2005 Oct 17;93(8):849-54.

Löffler JS and Durante M, 2013. Charged particle therapy - optimization, challenges and future directions. Nature Reviews Clinical Oncology.

Lomax A, 1999. Intensity modulation methods for proton radiotherapy. Phys. Med. Biol. 44 185

Lyman JT and Howard J, 1977. Dosimetry and instrumentation for helium and heavy ions, Int J Radiat Oncol Biol Phys.,3:81-5. doi:10.1016/0360-3016(77)90231-0

Lynch WG, 1987. Nuclear fragmentation in proton- and heavy-ion-induced reactions, Annu. Rev. Nucl. Part. Sci. 37,493–535.

Magro G, Molinelli S, Mairani A, Mirandola A, Panizza D, Russo S, et al, 2015. Dosimetric accuracy of a treatment planning system for actively scanned proton beams and small target volumes: Monte Carlo and experimental validation. Phys. Med. Biol. 60 6865–6880. doi:10.1088/0031-9155/60/17/6865

Mairani A, 2008. Nucleus-Nucleus Interaction Modelling and its Impact on Treatment Planning in Ion Therapy-Physical and Biological Aspects. PhD thesis, University of Pavia.

Mairani A, Brons S, Cerutti F, Fassò A, Ferrari A, Krämer M, Parodi K, Scholz M and Sommerer F, 2010. The FLUKA Monte Carlo code coupled with the local effect model for biological calculations in carbon ion therapy Phys. Med. Biol. 55 4273–89

Mairani A, Dokic I, Magro G, Tessonnier T, Kamp F, Carlson DJ, Ciocca M, Cerutti F Sala P R, Ferrari A, Böhlen TT, Jäkel O, Parodi K, Debus J, Abdollahi A, Haberer T, 2016b. Biologically optimized helium ion plans: calculation approach and its in vitro validation, Phys. Med. Biol. , 61. doi:10.1088/0031-9155/61/11/4283

Mairani A, Dokic I, Magro G, Tessonnier T, Bauer J, Böhlen T, Ciocca M, Ferrari A, Sala P, Jäkel O, Debus J, Haberer T, Abdollahi A, Parodi K, 2017a. A phenomenological relative biological effectiveness approach for proton therapy based on an improved description of the mixed radiation field. Phys. Med. Biol.

Mairani A, Böhlen T, Schiavi A, Tessonnier T, Molinelli S, Brons S, Battistoni G, Parodi K,Patera V, 2013. A Monte Carlo based-treatment tool for proton therapy, Phys. Med. Biol. 58 2471–90, doi:10.1088/0031-9155/58/8/2471

Mairani A, Magro G, Dokic I, Valle SM, Tessonnier T, Galm R, Ciocca M, Parodi K, Ferrari A, Jäkel O, Haberer T, Pedroni P, Böhlen TT, 2016b. Data-driven RBE parameterization for helium ion beams.Phys Med Biol. 2016 Jan 21;61(2):888-905. doi: 10.1088/0031-9155/61/2/888.

Mairani A., Tessonnier T, Mein S, Böhlen T T, Magro G, Bauer J, Chen W, Kamp F, Carlson D J, Ferrari A, Parodi K, Debus J, Haberer T, 2017b. RBE models in 4He ion beam therapy: predictions in clinically-relevant scenarios. To be submitted

Meyer S, Gianoli C, Magallanes L, Kopp B, Tessonnier T, Landry G, Dedes G, Voss B, Parodi K, 2017. Comparative Monte Carlo study on the performance of integration- and list-mode detector configurations for carbon ions computed tomography. Phys Med Biol 62(3)

Min CH, Kim CH, Youn MY, Kim JW, 2006. Prompt gamma measurements for locating the dose fall off region in the proton therapy. ApplPhysLett, 89(18):183517. doi:10.1063/1.2378561

Moliere, G. (1948). Theorie der Streuung schneller geladener Teilchen I - Einzelstreuung am abgeschirmten Coulomb-Feld. Z. Naturforsch. 3a.

Molinelli S, Mairani A, Mirandola A, Freixas GV, Tessonnier T, Giordanengo S, et al, 2013. Dosimetric accuracy assessment of a treatment plan verification system for scanned proton beam radiotherapy: one-year experimental results and Monte Carlo analysis of the involved uncertainties. Phys. Med. Biol. 58 3837. doi: 10.1088/0031-9155/58/11/3837

Niita K, Sato T, Iwase H, Nose H, Nakashima H, Sihver L. PHITS-a particle and heavy ion transport code system. Radiation Measurements, 41(9-10):1080 1090

Noda K,2016. Beam Delivery Method for Carbon-ion Radiotherapy with the Heavy-ion Medical Accelerator in Chiba. International Journal of Particle Therapy.

Noel G, Bollet MA, Calugaru V, Feuvret L, Haie-Meder C, Dhermain F et al Functional outcome of patients with benign meningioma treated by 3D conformal irradiation with a combination of photons and protons. Int.J Radiat.Oncol Biol.Phys. 2005;62:1412-22.

Ondreka D and Weinrich U, 2008. The Heidelberg Ion Therapy (HIT) accelerator coming into operation. Proceeding of EPAC08, Genoa, Italy

Owen H, Lomax A, Jolly S, 2016. Current and future accelerator technologies for charged particle therapy. Nuclear Instruments and Methods in Physics Research Section A: Accelerators, Spectrometers, Detectors and Associated Equipment

Palmans H, Thomas R, Kacperek A, 2006. Ion recombination correction in the Clatterbridge Centre of Oncology clinical proton beam, Phys. Med. Biol., 51, http://dx.doi.org/10.1088/0031-9155/51/4/010

Paganetti H, Jiang H, Parodi K, Slopsema R, Engelsman M, 2008. Clinical implementation of full Monte Carlo dose calculation in proton beam therapy. Phys. Med. Biol. 53 4825. doi: 10.1088/0031-9155/53/17/023

Paganetti H, Jiang H, Lee SY, Kooy H, 2004. Accurate Monte Carlo for nozzle design, commissioning, and quality assurance in proton therapy. Med. Phys. 31 2107–18. doi: 10.1118/1.1762792

Paganetti H, Niemierko A, Ancukiewicz M, Gerweck LE, Loeffler JS, Goitein M, Suit HD, 2002. Relative biological effectiveness (RBE) values for proton beam therapy. Int J Radiat Oncol Biol Phys.;53:407–21

Parodi K, 2004. On the feasibility of dose quantication with in-beam PET data in radiotherapy with 12C and proton beams. PhD thesis, Technische Universit□at Dresden, Germany.

Parodi K, Ferrari A, Sommerer F, Paganetti H, 2007. Clinical CT-based calculations of dose and positron emitter distributions in proton therapy using the FLUKA Monte Carlo code. Phys. Med. Biol. 52 3369–87. doi:10.1088/0031-9155/52/12/004

Parodi K, Mairani A, Brons S, Naumann J, Krämer M, Sommerer F, Haberer T, 2010. The influence of lateral beam profile modifications in scanned proton and carbon ion therapy: a Monte Carlo study, Phys. Med. Biol. 55, 5169–87; doi:10.1088/0031-9155/55/17/018

Parodi K, Mairani A, Brons S, Hasch BG, Sommerer F, Naumann J, Jäkel O, Haberer T, Debus J, 2012. Monte Carlo simulations to support start-up and treatment planning of scanned proton and carbon ion therapy at a synchrotron-based facility, Phys. Med. Biol., 57, doi:10.1088/0031-9155/57/12/3759

Parodi K, Mairani A, Sommerer F, 2013. Monte Carlo-based parameterization of the lateral dose spread for clinical treatment planning of scanned proton and carbon ion beams, J. Radiat. Res., 54. doi:10.1093/jrr/rrt051

Pedroni E, Bacher R, Blattmann H, Bhringer T, Coray A, Lomax A, Lin S, Munkel G, Scheib S, Schneider U, Tourovsky A, 1995. The 200MeV proton therapy project at the Paul Scherrer Institute: Conceptual design and practical realization. Med. Phys., 22(1):37-53.

Pedroni E, Scheib S, Böhringer T, Coray A, Grossmann M, Lin S, Lomax A, 2005. “Experimental characterization and physical modelling of the dose distribution of scanned proton pencil beams, Phys Med Biol., 50. doi:10.1088/0031-9155/50/3/011

Peeler C, Mirkovic D, Titt U, Blanchard P, Gunther JR, Mahajan A, Mohan R, Grosshans DR, 2016. Clinical evidence of variable proton biological effectiveness in pediatric patients treated for ependymoma. Radiotherapy and Oncology.

Phillips T L, Fu K K, Curtis S B, 1977. Tumor biology of helium and heavy ions, Int J Radiat Oncol Biol Phys., 3:109-13. doi:10.1016/0360-3016(77)90236-X

Podgorsak E B, 2005. Radiation Oncology Physics (Vienna: IAEA)

Polster L, Schuemann J, Rinaldi I, Burigo L, McNamara AL, Stewart RD, Attili A, Carlson DJ, Sato T, Ramos Méndez J, Faddegon B, Perl J, Paganetti H, 2015. Extension of TOPAS for the simulation of proton radiation effects considering molecular and cellular endpoints. Phys Med Biol. 2015 Jul 7;60(13):5053-70

Poole B, Blackfield D, Nelson S, 2007. Particle simulations of a linear dielectric wall proton accelerator. In Particle Accelerator Conference. PAC. IEEE, pages 1790-1792.

Qin N, Pinto M, Tian Z, Dedes G, Pompos A, Jiang S, Parodi K, Jia X, 2017. Initial development of goCMC: a GPU-oriented fast cross-platform Monte Carlo engine for carbon ion therapy. Phys Med Biol.

Ramos-Méndez JR, Perl J, Schümann J, Shin J, Paganetti H, Faddegon B, 2015. Improved efficiency in Monte Carlo simulation for passive-scattering proton therapy. Phys Med Biol. 60 :5019-35. doi: 10.1088/0031-9155/60/13/5019

Rao M, Yang W, Chen F., Sheng K, Ye J, Mehta V, Shepard D, Cao D, 2010. Comparison of Elekta VMAT with helical tomotherapy and _xed _eld IMRT: Plan quality, delivery e_ciency and accuracy. Med. Phys., 37(3):1350{1359.

Richter D, Schwarzkopf A, Trautmann J, Kramer M, Durante M, Jakel O, Bert C, 2013. Upgrade and benchmarking of a 4D treatment planning system for scanned ion beam therapy. Med. Phys., 40(5).

Richter C, Pausch G, Barczyk S, Priegnitz M, Keitz I, Thiele J, Smeets J, Stappen FV, Bombelli L, Fiorini C, Hotoiu L, Perali I, Prieels D, Enghardt W, Baumann M, 2016. First clinical application of a prompt gamma based in vivo proton range verification system. Radiother Oncol. ;118(2):232-7

Rietzel E, Schardt D, Haberer T, 2007. Range accuracy in carbon ion treatment planning based on CT-calibration with real tissue samples. Radiation Oncology, 2(1):14

Rinaldi I. Investigation of novel imaging methods using therapeutic ion beams. PhD Thesis. University of Heidelberg, Heidelberg, Germany, 2011.

Rinaldi I, Brons S, Gordon J, Panse R, Voss B, 2013. Experimental characterization of a prototype detector system for carbon ion radiography and tomography.

Rossomme S, Hopfgartner J, Lee N D, Delor A, Thomas R A S, Romano F, Fukumura A, Vynckier S, Palmans H, 2016. Ion recombination correction in carbon ion beams, Med. Phys. 43, 4198. http://dx.doi.org/10.1118/1.4953637

Rovituso M, Schuy C, Weber U, Brons S, Cortés-Giraldo MA, La Tessa C, Piasetzky E, Izraeli D, Schardt D, Toppi M, Scifoni E, Krämer M, Durante M, 2017. Fragmentation of 120 and 200 MeVu-1 4He ions in eater and PMMA targets. Phys Med Biol (62).

Sánchez-Parcerisa D, Gemmel A, Jäkel O, Parodi K, Rietzel E, 2012. Experimental study of the water-to-air stopping power ratio of monoenergetic carbon ion beams for particle therapy, Phys Med Biol., 57. doi:10.1088/0031-9155/57/11/3629

Santacroce A, Kamp MA, Budach W, Häanggi D, 2013. Radiobiology of Radiosurgery for the Central Nervous System. Biomed Res Int, 13, doi:10.1155/2013/362761

Schardt D, Elsässer T , Schulz-Ertner D, 2010. Heavy-ion tumor therapy: Physical and radiobiological benefits, Rev. Mod. Phys. 82, 383. doi:10.1103/RevModPhys.82.383

Scheib S and Pedroni E, 1992. Dose calculation and optimization for 3D conformal voxel scanning, Radiat. Environ. Biophys., 31.doi:10.1007/BF01214833

Schlaff C, Krauze A, Belard A, O'Connel JJ, Camphausen KA, 2014. Bringing the heavy: carbon ion therapy in the radiobiological and clinical context, Radiation Oncology 9:88.

Schneider U, Pemler P, Besserer J, Pedroni E, Lomax A & Kaser-Hotz B 2005 Medical Physics 32(1), 195–199

Schulte R, Bashkirov V, Li T, Liang Z, Mueller K, Heimann J, Johnson L, Keeney B, Sadrozinski H W, Seiden A, Williams D, Zhang L, Li Z, Peggs S, Satogata T & Woody C 2004 Nuclear Science, IEEE Transactions on 51(3), 866–872.

Schulz-Ertner D, Karger CP, Feuerhake A, Nikoghosyan A, Combs SE, Jäkel O, Edler L, Scholz M, Debus J, 2007. Effectiveness of carbon ion radiotherapy in the treatment of skull-base chordomas. Int J Radiat Oncol Biol Phys, 68(2):449-457.

Schümann J, Paganetti H, Shin J, Faddegon B, Perl J, 2012. Efficient voxel navigation for proton therapy dose calculation in TOPAS and Geant4. Phys Med Biol. 57 3281-93. doi:10.1088/0031-9155/57/11/3281

Schwaab J, Brons S, Fieres J, Parodi K, 2011. Experimental characterization of lateral profiles of scanned proton and carbon ion pencil beams for improved beam models in ion therapy treatment planning, Phys Med Biol., 56. doi:10.1088/0031-9155/56/24/009

Schwoerer H, Pfotenhauer S, Jackel O, Amthor KU, Liesfeld B, Ziegler W, Sauerbrey R, Ledingham KWD, Esirkepov T. Laser-plasma acceleration of quasimonoenergetic protons from microstructured targets. Nature, 439(7075):445-448.

Scifoni E, Tinganelli W, Weyrather W K, Durante M, Maier A, Krämer M, 2013. Including oxygen enhancement ratio in ion beam treatment planning: model implementation and experimental verification, Phys. Med. Biol., 58. doi:10.1088/0031-9155/58/11/3871

Serber R, 1947. Nuclear reactions at high energies. Phys. Rev., 72(11):1114{1115.

Shakirin G, Braess H, Fiedler, F., Kunath D, Laube K, Parodi K, Priegnitz M, Enghardt W, 2011. Implementation and workow for PET monitoring of therapeutic ion irradiation: a comparison of in-beam, in-room, and o_-line techniques. Phys. Med. Biol., 56(5):1281-1298.

Sorge H, Stocker H, Greiner W, 1989. Relativistic quantum molecular dynamics approach to nuclear collisions at ultrarelativistic energies. Nucl Phys A 498(3):567–76. doi:10.1016/0375-9474(89)90641-6

Stankovskiy A, Kerhoas-Cavata S, Ferrand R, Nauraye C, Demarzi L, 2009. Monte Carlo modelling of the treatment line of the Proton Therapy Center in Orsay. Phys Med Biol. 54 2377-94. doi: 10.1088/0031-9155/54/8/008

Suit H, DeLaney T, Goldberg S, Paganetti H, Clasie B, Gerweck L, Niemierko A, Hall E, Flanz J, Hallman J, Trofimov A, 2010. Proton vs carbon ion beams in the definitive radiation treatment of cancer patients, Radiotherapy and Oncology, 3-22

Tessonnier T, Mairani A, Cappucci F, Mirandola A, Vilches Freixas G, Molinelli S, et al, 2014. Development and application of tools for Monte Carlo based simulations in a particle beam radiotherapy facility. Appl Radiat Isot. 83 155-8. doi: 10.1016/j.apradiso.2012.12.019

Tessonnier T, Marcelos T, Mairani A, Brons S, Parodi K, 2016. Phase Space Generation for Proton and Carbon Ion Beams for External Users' Applications at the Heidelberg Ion Therapy Center, Front. Oncol. doi:10.3389/fonc.2015.00297

Tessonnier T., Mairani A., Brons S., Haberer T., Debus J., Parodi K., 2017a. Experimental dosimetric comparison of 1H, 4He, 12C and 16O scanned ion beams, Phys. Med. Biol., under revision

Tessonnier T, Mairani A, Brons S, Sala P, Cerutti F, Ferrari A, Haberer T, Debus J, Parodi K, 2017b. Helium ions at the Heidelberg Ion Beam Therapy Center: Comparisons between FLUKA Monte Carlo code predictions and dosimetric measurements, Phys. Med. Biol., under revision

Tessonnier T, Böhlen TT, Cerutti F, Ferrari A, Sala P, Brons S, Haberer T, Debus J, Parodi K, Mairani A, 2017c. Dosimetric verification in water of a Monte Carlo treatment planning tool for proton, helium, carbon and oxygen ion beams at the Heidelberg Ion Beam Therapy Center. Phys. Med. Biol., submitted

Tobias CA, Lawrence JH, Born JL, McCombs RK, Roberts JE, Anger HO, Low-Beer BVA, Huggins CB, 1958. Pituitary Irradiation with High-Energy Proton Beams A Preliminary Report. Cancer Res., 18:121{134.

Tsai YS, 1974 .Pair production and bremsstrahlung of charged leptons, Rev. Mod. Phys. 46, 815–851.

Tsujii H, Mizoe J, Kamada T, Baba M, Tsujii H, Kato H, Kato S, Yamada S, Yasuda S, Ohno T, Yanagi T, Imai R, Kagei K, Kato H, Hara R, Hasegawa A, Nakajima M, Sugane N, Tamaki N, Takagi R, Kandatsu S, Yoshikawa K, Kishimoto R, Miyamoto T, 2007. Clinical Results of Carbon Ion Radiotherapy at NIRS. J Radiat Res, 48(Suppl.A):A1-A13.

Unkelbach J, Craft D, Salari E, Ramakrishnan J, Bortfeld T. The dependence of optimal fractionation schemes on the spatial dose distribution. Phys Med Biol.;58(1):159-67

Vernimmen FJ, Harris JK, Wilson JA, Melvill R, Smit BJ, Slabbert JP, 2001. Stereotactic proton beam therapy of skull base meningiomas. Int J Radiation Oncology Biol Phys 49.

Vernimmen FJ and Slabbert JP, 2010. Assessment of the α/ß ratios for arteriovenous malformations, meningiomas, acoustic neuromas, and the optic chiasma. Int J Radiation Biology, 86:6, 486-498, DOI:10.3109/09553001003667982

Webb S, 2003. The physical basis of IMRT and inverse planning. Br. J. Radiol., 76(910):678-689.

Weber DC, Schneider R, Goitein G, Koch T, Ares C, Geismar JH et al Spot Scanning based Proton Therapy for Intracranial Meningioma: Long-term Results from the Paul Scherrer Institute. Int.J.Radiat.Oncol Biol.Phys. 2011.

Weber U and Kraft G, 1999. Design and construction of a ripple filter for a smoothed depth dose distribution in conformal particle therapy, Phys Med Biol 44. doi:10.1088/0031-9155/44/11/306

Wedenberg M, Lind BK, Hardemark B, 2013. A model for the relative biological effectiveness of protons: The tissue specific parameter of photons is a predictor for the sensitivity to let changes, Acta Oncologica 52(3), 580-588. DOI: 10.3109/0284186X.2012.705892

Wilson RR, 1946. Radiological use of fast protons, Radiology. doi:10.1148/47.5.487

Würl M, Englbrecht F, Parodi K, Hillbrand M, 2016. Dosimetric impact of the low-dose envelope of scanned proton beams at a ProBeam facility: comparison of measurements with TPS and MC calculations, Phys. Med. Biol., 61. doi:10.1088/0031-9155/61/2/958

Yang M, Virshup G, Clayton J, Zhu XR, Mohan R, Dong L, 2010. Theoretical variance analysis of single- and dual-energy computed tomography methods for calculating proton stopping power ratios of biological tissues. Phys Med Biol. 7;55(5):1343-62

Acknowledgements

There would be not enough words to thank all the persons who support me along this *PhD journey*.

At first, I would like to thank Prof. Katia Parodi for this unique opportunity to work in the field I was striving for since I discovered the world of particle therapy. With your strong support and scientific expertise, you helped me progress in the right direction. Despite the distance between Munich and Heidelberg I enjoyed your supervision, your availability and your honesty.

I am very grateful to my committee members: Prof. Kuhr, Prof. Rädler, Prof. Weller, Prof. Burkert, and particularly Prof. Rühm who kindly accepted to be me second referee and to review this work.

A special thanks to Dr. Andrea Mairani, who shared his insights with me, most of the time around a coffee, since my master thesis at CNAO. Through all the events that happened during these three years, you were there, giving me your help, kindness and support. For me the *Stack Team*, and its new *smallina* member, has been like a family, and I am very grateful for all this time.

I would like to thank Prof. Thomas Haberer and Prof. Jürgen Debus, for letting me work in this great environment, providing me all the beam-time needed to perform my experiments. *Un grand merci* to Dr. Stephan Brons who taught me so many things from how to perform measurements to how to make the best coffee, which was indispensable for all these night shifts. Your advice has always been precious to me. I thank all the colleagues from the HIT medical physics team and the accelerator team for the fruitful exchanges and projects, particularly Benjamin, Hannah, Katrin, Beata, Julian…

Work is hard, but a nice atmosphere makes things easier, and I am so thankful for all my office colleagues. Many left, many came, now it's my turn. A particular thank to Dr. Julia Bauer who took care of me when I arrived in Heidelberg, teaching me all the small details needed to work on my own. All my gratitude to all of you: Christopher, Chiara, Ilaria, Jakob, Sodai, Guillaume, Josefine, Lorena. Many thanks to Mac and Ben who gave me their strong help at the end of this PhD.

To all my friends who encouraged me, either from Heidelberg (Eva, Giulia, Kai, Jule …) or from France (Greg, Coralie, Anais, Loriane …). Special thanks to Simon who brought so much fun from France each time. And a special thought to Line.

I do not forget the way that brought me here, and I would address my regards to Denis Porcheron and Dr. Bardia Farman who made me discover medical physics and particle therapy. Thank you to Dr. Mario Ciocca for welcoming me at CNAO, which paved the way to my current and future situation.

My deep thank to my family, supporting me through this whole journey and giving me the mean to achieve my goals.

This work was supported by the German Research foundation DFG (KFO214).